Experimental study of shape evolution in nuclei near Z=82

By

Soumen Nandi

Enrolment No: PHYS04201504014

Variable Energy Cyclotron Centre, Kolkata

A thesis submitted to the
Board of Studies in Physical Sciences

In partial fulfillment of requirements

for the Degree of

DOCTOR OF PHILOSOPHY

of

HOMI BHABHA NATIONAL INSTITUTE

Feb, 2021

Homi Bhabha National Institute[1]

Recommendations of the Viva Voce Committee

As members of the Viva Voce Committee, we certify that we have read the dissertation prepared by **Shri Soumen Nandi** entitled **"Experimental study of shape evolution in nuclei near Z=82"** and recommend that it may be accepted as fulfilling the thesis requirement for the award of Degree of Doctor of Philosophy.

Chairman - Name & Signature with date

Dr. Chandana Bhattacharya, VECC C. Bhattacharya 19.4.2021

Guide / Convener - Name & Signature with date

Dr. Gopal Mukherjee, VECC Gopal Mukherjee 19/04/2021

Co-guide - Name & Signature with date (if any) **X X X X X X X**

Examiner - Name & Signature with date

Prof. Ajay Kr. Singh, IIT Kharagpur 19.4.21

Member 1- Name & Signature with date

Prof. Gautam Gangopadhyay. Calcutta University G. Gangopadhyay 19.4.2021

Member 2- Name & Signature with date

Dr. Tilak Kr. Ghosh, VECC T. Ghosh 19/04/21

Member 3- Name & Signature with date

Dr. Jhilam Sadhukhan, VECC Jhilam Sadhukhan 19/4/21

Final approval and acceptance of this thesis is contingent upon the candidate's submission of the final copies of the thesis to HBNI.

I/We hereby certify that I/we have read this thesis prepared under my/our direction and recommend that it may be accepted as fulfilling the thesis requirement.

Date: 19/04/2021

Place: Kolkata

Signature **Co-guide (if any)**

Gopal Mukherjee 19/04/2021

Signature **Guide**

[1] This page is to be included only for final submission after successful completion of viva voce.

STATEMENT BY AUTHOR

This dissertation has been submitted in partial fulfillment of requirements for an advanced degree at Homi Bhabha National Institute (HBNI) and is deposited in the Library to be made available to borrowers under rules of the HBNI.

Brief quotation from this dissertation are allowable without special permission, provided that accurate acknowledgement of source is made. Requests for permission for extended quotation from or reproduction of this manuscript in whole or in part may be granted by the Competent Authority of HBNI when in his or her judgement the proposed use of the material is in the interests of scholarship. In all other instances, however, permission must be obtained from the author.

Soumen Nandi

Soumen Nandi

DECLARATION

I, here by declare that the investigation presented in the thesis has been carried out by me. The work is original and has not been submitted earlier as a whole or in part for a degree/diploma at this or any other Institution/University.

Soumen Nandi

Soumen Nandi

List of Publications arising from the thesis

In Journal :

1. **Effect of neutron alignments on the structure of ^{197}Tl**
   S. Nandi, G. Mukherjee, T. Roy, R.Banik, A. Dhal, Soumik Bhattacharya, S. Bhattacharyya, C. Bhattacharya, Md. A. Asgar, H. Pai, S. Rajbanshi, Pratap Roy, T. K. Ghosh, K. Banerjee, T. K. Rana, Samir Kundu, S. Manna, R. Pandey, A. Sen, S. Pal, S. Mukhopadhyay, D. Pandit, D. Mandal, and S. R. Banerjee
   Phys. Rev. C Vol. **99**, 054312 (2019).

2. **First Observation of Multiple Transverse Wobbling Bands of Different Kinds in ^{183}Au**
   S. Nandi, G. Mukherjee, Q. B. Chen, S. Frauendorf, R. Banik, Soumik Bhattacharya, Shabir Dar, S. Bhattacharyya, C. Bhattacharya, S. Chatterjee, S. Das, S. Samanta, R. Raut, S.S. Ghugre, S. Rajbanshi, Sajad Ali, H. Pai, Md. A. Asgar, S. Das Gupta, P. Chowdhury, A. Goswami
   Phys. Rev. Lett. **125**, 132501 (2020).

In Conferences/Symposia :

1. **Study of multi-quasiparticle band structures in ^{197}Tl using α beam**
   G. Mukherjee, **S. Nandi**, H. Pai, T. Roy, Md.A. Asgar, A. Dhal, R. Banik, Soumik Bhattacharya, A. Saha, S. S. Alam, S. Bhattacharyya, C. Bhattacharya, Pratap Roy, T.K. Ghosh , S. Kundu, K. Banerjee, T.K. Rana, R. Pandey, S. Manna, A. Sen, S. Pal, S. Mukhopadhyay, D. Pandit, D. Mondal, T. Bhattacharjee, A. Dey, J.K. Meena, A.K. Saha, J.K. Sahoo, R. Mandal Saha, A. Choudhury, and S.R. Banerjee.

Proceedings of the DAE Symposium on nuclear physics, Vol. **61**, 270 (2016).

2. **Nuclear structure near N =108 deformed shell gap: case of ^{187}Os**
S. Nandi, G. Mukherjee, A. Dhal, R. Banik, S. Bhattacharya, C. Bhattacharya, S. Bhattacharyya, S. Kundu, D. Paul, Sajad Ali, S. Rajbanshi, H. Pai, P. Ray, S. Chatterjee, S. Das, S. Samanta, A. Goswami, R. Raut, S. Ghugre, S. Biswas.
Proceedings of International Symposium on Nuclear Physics, DAE, Vol. **63**, 114 (2018).

3. **Shape evolution in nuclei with Z in A $\sim$ 180 190 region**
S. Nandi and G. Mukherjee.
Proceedings of International Symposium on Nuclear Physics, DAE, Vol. **63**, 336 (2018).

4. **VECC-INGA: An exploration of nuclear structure with light ions**
Soumik Bhattacharya, R. Banik, **S. Nandi**, Sajad Ali, S. Chatterjee, S. Das, S. Samanta, K. Basu, A. Choudhury, A. Adhikari, S. S. Alam, Shabir Dar, B. Das, Sangeeta Das, A. Dhal, A. Mondal, K. Mondal, P Mukhopadhyay, H. Pai, P. Ray, A. Saha, I. Shaik, C. Bhattacharya, G. Mukherjee, R. Raut, S. S. Ghugre, A. Goswami, S. Bhattacharyya.
Proceedings of International Symposium on Nuclear Physics, DAE, Vol. **63**, 1156 (2018).

5. **Presence of transverse and longitudinal wobbling in ^{183}Au**
S. Nandi, G. Mukherjee, Q.B. Chen, R. Banik, S. Bhattacharya, Shabir Dar, S. Bhattacharyya, C. Bhattacharya, S. Rajbanshi, Sajad Ali, H. Pai, S. Chatterjee, S. Das, S. Samanta, R. Raut, S.S. Ghugre, S. Das Gupta, P. Chowdhury.
Proceedings of the DAE Symposium on nuclear physics Vol. **64**, 68 (2019).

(B) Other publications (in refereed journals)

1. **Yrast and non-yrast spectroscopy of ^{199}Tl using α-induced reactions**
   Soumik Bhattacharya, S. Bhattacharyya, R. Banik, S. Das Gupta, G. Mukherjee, A. Dhal, S. S. Alam, Md. A. Asgar, T. Roy, A. Saha, **S. Nandi**, T. Bhattacharjee, A. Choudhury, Debasish Mondal, S. Mukhopadhyay, P. Mukhopadhyay, S. Pal, Deepak Pandit, I. Shaik, and S. R. Banerjee.
   Phys. Rev. C Vol. **98**, 044311 (2018).

2. **Band structures in ^{169}Tm and the structures of Tm isotopes around N = 98**
   Md.A. Asgar, G. Mukherjee, T. Roy, **S. Nandi**, G.H. Bhatt, J.A. Sheikh, R. Palit, S. Bhattacharyya, Soumik Bhattacharya, C. Bhattacharya, A. Dhal, T.K. Ghosh, A. Chaudhuri, K. Banerjee, Samir Kundu, T.K. Rana, Pratap Roy, R. Pandey, S. Manna, J.K. Meena, S. Saha, S. Biswas, J. Sethi, P. Singh, and D. Choudhury.
   Eur. Phys. J. A Vol. **55**, 175 (2019).

3. **Revealing multiple band structures in ^{131}Xe from α-induced reactions**
   R. Banik, S. Bhattacharyya, S. Biswas, Soumik Bhattacharya, G. Mukherjee, S. Rajbanshi, Shabir Dar, **S. Nandi**, Sajad Ali, S. Chatterjee, S. Das, S. Das Gupta, S. S. Ghugre, A. Goswami, A. Lemasson, D. Mondal, S. Mukhopadhyay, H. Pai, S. Pal, D. Pandit, R. Raut, Prithwijita Ray, M. Rejmund, and S. Samanta.
   Phys. Rev. C Vol. **101**, 044306 (2020).

4. **Quasi-γ-band in ^{114}Te**
   Prithwijita Ray, H. Pai, Sajad Ali, Anjali Mukherjee, A. Goswami, S. Rajbanshi, Soumik Bhattacharya, R. Banik, **S. Nandi**, S. Bhattacharyya, G. Mukherjee, C. Bhattacharya, S. Chakraborty, G. Gangopadhyay, Md. S. R. Laskar, R. Palit, G. H. Bhat, S. Jehangir, J. A. Sheikh, A. K. Sinha, S. Samanta, S. Das, S. Chatterjee, R. Raut, and S. S. Ghugre.
   Phys. Rev. C Vol. **101**, 064313 (2020).

5. **Investigation of different possible excitation modes in neutron-rich ^{78}As**

   A. K. Mondal, A. Chakraborty, K. Mandal, U. S. Ghosh, Aniruddha Dey, Saumyajit Biswas, B. Mukherjee, S. Rai, Krishichayan, S. Chatterjee, S. K. Das, S. Samanta, R. Raut, S. S. Ghugre, R. Banik, S. Bhattacharyya, **S. Nandi**, S. Bhattacharya, G. Mukherjee, S. Ali, A. Goswami, R. Chakrabarti, S. Mukhopadhyay, A. K. Sinha, V. Kumar and A. Kumar.

   Phys. Rev. C Vol. **102**, 064311 (2020).

6. **Exploring the structure of Xe isotopes in A $\sim$ 130 region: Single particle and collective excitations**

   R. Banik, S. Bhattacharyya, S. Biswas, S. Bhattacharya, G. Mukherjee, S. Rajbanshi, S. Dar, **S. Nandi**, S. Ali, S. Chatterjee, S. Das, S. Das Gupta, S. S. Ghugre, A. Goswami, D. Mondal, S. Mukhopadhyay, H. Pai, S. Pal, D. Pandit, R. Raut, P. Ray, and S. Samanta

   EPJA Web of Conferences Vol. **232**, 04001 (2020).

7. **Complex fragment emission in dissipative binary decay of ^{74,76}Kr**

   T. K. Rana, Samir Kundu, C. Bhattacharya, S. Manna, Pratap Roy, R. Pandey, Arijit Sen, T. K. Ghosh, G. Mukherjee, K. Banerjee, S. Mukhopadhyaya, Dipen Pal, Moin Shaikh, **S. Nandi**, Vishal Srivastava, J. K. Sahoo, J. K. Meena, A. K. Saha, R. M. Saha, Somnath Dalal, and S. Bhattacharya

   Phys. Rev. C Vol. **103**, 034614 (2021).

Other results reported in Conferences/Symposia :

1. **High Spin Structure in** $208, 209$**Rn**

   Soumik Bhattacharya, S. Bhattacharyya, R. Banik, R. Raut, A. Dhal, **S. Nandi**, S. Das Gupta, Debasish Mondal, G. Mukherjee, A. Sharma, Indu Bala, S. Muralithar, R. P. Singh, S. S. Bhattacharjee,V. Srivastava.

   Proceedings of the DAE Symposium on nuclear physics, Vol. **62**, 138 (2017).

2. **Performance of CsI(Tl) detector array for digital INGA**

   Md. S. R. Laskar, R. Palit, S. Biswas, C.S. Palshetkar, F. S. Babra, S. Jadhav, B. S. Naidu, R. Donthi, A. Thomas, A. Jhingan, E. Ideguchi, M. Kumar Raju, G. Mukherjee, **S. Nandi**, T. Trivedi, S. Bhattacharya.

   Proceedings of the DAE Symposium on nuclear physics, Vol. **62**, 1058 (2017).

3. **Study of 116Sb: an ensemble of single particle as well as collective structure**

   Shabir Dar, Soumik Bhattacharya, S. Bhattacharyya, R. Banik, **S. Nandi**, G. Mukherjee, S. Das Gupta, Sajad. Ali, S. Chatterjee, S. Das, A. Dhal, S. S. Ghugre, A. Goswami, D. Mondal, S. Mukhopadhyay, S. Pal, D. Pandit, R. Raut, P. Ray, S. Samanta.

   Proceedings of the International Symposium on nuclear physics, DAE, Vol **63**, 78 (2018).

4. **γ-ray spectroscopy of ^{131}Xe from α-induced reaction**

   R. Banik, S. Bhattacharyya, S. Biswas, Soumik Bhattacharya, G. Mukherjee, Shabir Dar, S. Das Gupta, **S. Nandi**, Sajad Ali, P. Ray, S. Chatterjee, S. Samanta, S. Das, A. Goswami, S. Ghugre, R. Raut, H. Pai, A. Lemasson, A. Navin, M. Rejmund, D. Mondal, S. Mukhopadhyay, S. Pal, D. Pandit, S. Rajbanshi.

   Proceedings of the International Symposium on nuclear physics, DAE, Vol **63**, 82 (2018).

5. **In-beam γ- ray spectroscopy of ^{63}Zn**

   U. S. Ghosh, S. Rai, B. Mukherjee, A. Biswas, A. K. Mondal, K. Mandal, A. Chakraborty, G. Mukherjee, **S. Nandi**, S. Chakraborty, A. Sharma, S. S. Bhattacharjee, I. Bala, R. Garg, S. Muralithar, R. P. Singh.

   Proceedings of the International Symposium on nuclear physics, DAE, Vol **63**, 130 (2018).

6. **In-beam γ- ray spectroscopy of ^{66}Zn**

   S. Rai, B. Mukherjee, U.S. Ghosh, A. Biswas, A.K. Mondal, K. Mondal, A. Chakraborty, S. Chakraborty, A. Sharma, G. Mukherjee, **S. Nandi**, S.S. Bhattacharjee, I. Bala, R.

Garg, S. Muralithar, R.P. Singh.

Proceedings of the International Symposium on nuclear physics, DAE, Vol **63**, 240 (2018).

7. **Search for γ-band in ^{114}Te**

   Prithwijita Ray, H. Pai, S. Ali, S. Rajbanshi, S. Chakraborty, R. Banik, **S. Nandi**, G. Mukherjee, S. Bhattacharya, C. Bhattacharya, S. Bhattacharyya, S. Samanta, S. Das, S. Chatterjee, R. Raut, S.S. Ghugre, Md.S.R. Laskar, R. Palit, A. Goswami.

   Proceedings of the International Symposium on nuclear physics, DAE, Vol **63**, 260 (2018).

8. **Isotopic yield and mass distributions of neutron-rich fragment nuclei produced in α induced fission of ^{232}Th**

   Aniruddha Dey, S. Mukhopadhyay, D.C. Biswas, A. Chakraborty, A.K. Mondal, K. Mondal, B.N. Joshi, S. Chatterjee, S. Samanta, S. Das, Soumik Bhattacharya, R. Banik, **S. Nandi**, R. Raut, G. Mukherjee, S. Bhattacharyya, S.S. Ghugre, A. Goswami.

   Proceedings of the International Symposium on nuclear physics, DAE, Vol **63**, 268 (2018).

9. **Investigation of the medium-spin level structure of ^{78}Se**

   K. Mandal, A.K. Mondal, A. Chakraborty, S. Ali, R. Banik, S. Bhattacharya, S. Bhattacharyya, D.C. Biswas, S. Biswas, S. Chattarjee, S.K. Das, A. Dey, U.S. Ghosh, S.S. Ghugre, A. Goswami, Krishi chayan, A. Kumar, V. Kumar, B. Mukherjee, G. Mukherjee, S. Mukhopadhyay, **S. Nandi**, S. Rai, R. Raut, S. Samanta.

   Proceedings of the International Symposium on nuclear physics, DAE, Vol **63**, 274 (2018).

10. **Band structure of the ^{132}Xe nucleus above the 5^{-} $\hbar$ state**

    Suresh Kumar, Neelam, Papinder Singh, A. Sharma, S. Chatterjee, S. Samanta, S. Das, R. Raut, S. S. Ghugre, Soumik Bhattacharya, **S. Nandi**, R. Banik, Sajad Ali, G. Mukherjee, A. Goswami, S. Bhattacharyya.

Proceedings of the International Symposium on nuclear physics, DAE, Vol **63**, 308 (2018).

11. **Lifetime measurement of low lying states of ^{27}Si**

    Sathi Sharma, Sangeeta Das, Arkajyoti De, Rashika Gupta, A. Gupta, A. Adhikari, A. Das, Y. Sapkota, A. Saha, S. S. Alam, S. Bhattacharya, R. Banik, **S. Nandi**, S. Das, S. Samanta, S. Chatterjee, S. Bhattacharyya, B. Dey, D. Pramanik, A. Bisoi, T. Bhattacharjee, M. Nandy, S. Sarkar, M. Saha Sarkar.

    Proceedings of the International Symposium on nuclear physics, DAE, Vol **63**, 320 (2018).

12. **Spectroscopy of ^{160,161}Ho**

    A. Adhikari, D. Pramanik, S. Das, Arkabrata Gupta, Y. Sapkota, Ananya Das, S. Sharma, A. De, A. Saha, S.S. Alam, S. Das, S. Samanta, S. Chatterjee, S. Bhattacharya, R. Banik, **S. Nandi**, R. Raut, S.S. Ghugre, S. Bhattacharyya, G. Mukherjee, T. Bhattacharjee, A. Bisoi, M. Saha Sarkar, S. Sarkar.

    Proceedings of the International Symposium on nuclear physics, DAE, Vol **63**, 332 (2018).

13. **Cluster emission studies in ^{28,29}Si***

    S. Manna, C. Bhattacharya, T.K. Rana, S. Kundu, R. Pandey, A. Sen, D. Paul, Pratap Roy, T.K. Ghosh, G. Mukherjee, S. Mukhopadhyay, **S. Nandi**, J.K. Meena, R.M. Saha, A.K. Saha, J.K. Sahoo, Somnath Dalal.

    Proceedings of the International Symposium on nuclear physics, DAE, Vol **63**, 678 (2018).

14. **Digital Pulse Processing and DAQ System for INGA at VECC**

    S. Chatterjee, S. Das, S. Samanta, K. Basu, R. Raut, S. S. Ghugre, A. K. Sinha, R. Banik, S. Bhattacharya, **S. Nandi**, A. Dhal, A. Choudhury, P. Mukhopadhyay, S. Imran, S. Bhattacharyya, G. Mukherjee, C. Bhattacharya, S. Ali, P. Ray,S. Rajbanshi, H. Pai, A. Goswami, H. Tan.

    Proceedings of the International Symposium on nuclear physics, DAE, Vol **63**, 1100

(2018).

15. **A LYSO-based compact detector system for nuclear science applications**
A. Banerjee, S. Mandal, Pratap Roy, S. Mukhopadhyay, S. Bhattacharyya, G. Mukherjee, **S. Nandi**, M. Kumar, A. Jhingan, R. Palit.
Proceedings of the International Symposium on nuclear physics, DAE, Vol **63**, 1180 (2018).

16. **Revisiting the high-spin states in ^{54}Mn reveals its new structure**
S. Basu, G. Mukherjee, **S. Nandi**, A. Dhal, R. Banik, S. Bhattacharya, S. Bhattacharyya, C. Bhattacharya, S. Kundu, D. Paul, Sajad Ali, S. Rajbanshi, H. Pai, P. Ray, S. Chatterjee, S. Das, S. Samanta, A. Goswami, R. Raut, S.S. Ghugre, S. Biswas.
Proceedings of the DAE Symposium on nuclear physics, Vol. **64**, 66 (2019).

17. **Band structures in ^{116}Sb**
Shabir Dar, Soumik Bhattacharya, S. Bhattacharyya, R. Banik, S. Nandi, G. Mukherjee, S. Das Gupta, Sajad. Ali, S. Chatterjee, S. Das, A. Dhal, S. S. Ghugre, A. Goswami, D. Mondal, S. Mukhopadhyay, S. Pal, D. Pandit, R. Raut, P. Ray, S. Samanta.
Proceedings of the DAE Symposium on nuclear physics, Vol. **64**, 152 (2019).

18. **Spectroscopic study of ^{197}Hg**
S. Das Gupta, Soumik Bhattachraya, S. Bhattacharyya, R. Banik, G. Mukherjee, R. Raut, S. Ghugre, S. Das, S. Samanta, S. Chatterjee, S. Rajbanshi, **S. Nandi**, Shabir Dar, Sneha Das, A. Goswami, Sajad Ali, Sudatta Ray, Rupsa Banik, Sangeeta Majumdar.
Proceedings of the DAE Symposium on nuclear physics, Vol. **64**, 182 (2019).

19. **High states and band structures in Yb isotopes**
Saket Suman, S.K. Tandel, S.G. Wahid, Poulomi Roy, A. Chakraborty, K. Mandal, A.K.

Mondal, G. Mukherjee, S. Bhattacharyya, Soumik Bhattacharya, R. Banik, **S. Nandi**, Shabir Dar, A. Asgar, S. Samanta, S. Das, S. Chatterjee, R. Raut, S.S. Ghugre, A. Sharma, Sajad Ali, P. Chowdhury.
Proceedings of the DAE Symposium on nuclear physics, Vol. **64**, 226 (2019).

20. **Spectroscopy of ^{126}Te**
Atreyee Dey, Anwesha Basu, A. K. Singh, S. Nag, G. Mukherjee, S. Bhattacharyya, R. Banik, **S. Nandi**, S. Bhattacharya, R. Raut, S. S. Ghugre, S. Das, S. Samanta, S. Chatterjee, A. Goswami, S. Ali, H. Pai, S. Rajbanshi.
Proceedings of the DAE Symposium on nuclear physics, Vol. **64**, 248 (2019).

21. **High spin spectroscopy of ^{90}Zr**
P. Dey, R. Palit, Md S. R. Laskar, F. S. Babra, S. Biswas, N. Chaudhury, B. Das, Biswajit Das, R. Gala, C. S. Palshetkar, L. P. Singh, P. Singh, R. P. Singh, S. Muralithar, E. Ideguchi, K. Raja, S. Kumar, K. Rojeeta Devi, Neelam, T. Trivedi, S. Bhattacharya, G. Mukherjee, **S. Nandi**, S. Sihotra, A. Sharma, R. Raut, S. S. Ghugre, S. Nag, A. K. Singh, P. C. Srivastava.
Proceedings of the DAE Symposium on nuclear physics, Vol. **64**, 258 (2019).

22. **Spectroscopy of ^{196}Hg**
S. Das, S. Chatterjee, S. Samanta, R. Raut, S. S. Ghugre, A. K. Sinha, S. Ali, P. Ray, A. Goswami, **S. Nandi**, R. Banik, S. Bhattacharya, S. Bhattacharyya, G. Mukherjee, S. Rajbanshi, S. Dasgupta, H. Pai.
Proceedings of the DAE Symposium on nuclear physics, Vol. **64**, 274 (2019).

23. **Near-yrast exotic structure in ^{199}Hg**
Soumik Bhattacharya, S. Bhattacharyya, S. Das Gupta, R. Banik, G. Mukherjee, A. Dhal, **S. Nandi**, Md. A. Asgar, T. Roy, R. Raut, S. S. Ghugre, S. K. Das, S. Chatterjee,

S. Samanta, Shabir Dar, A. Goswami, Sajad Ali, S. Mukhopadhyay, Debasish Mondal, S. S. Alam, T. Bhattacharjee, A. Saha, Deepak Pandit, Surajit Pal, S. R. Banerjee, S. Rajbanshi.

Proceedings of the DAE Symposium on nuclear physics, Vol. **64**, 276 (2019).

24. Fission dynamics at energies far above the Coulomb barrier

Md Moin Shaikh, T. K. Ghosh, A. Sen, D. Paul, K. Atreya, C. Bhattacharya, S. Kundu, T. K. Rana, **S. Nandi**, G. Mukherjee, J. K. Meena, S. Manna, Pratap Roy, R. Pandey, S. Mukhopadhyay, Raj Kumar Santra.

Proceedings of the DAE Symposium on nuclear physics, Vol. **64**, 321 (2019).

25. Fission fragment mass distribution of ^{225}Pa

K. Atreya, T. K. Ghosh, A. Sen, MD. Moin Shaikh, D. Paul, C. Bhattacharya, Samir Kundu, S. Manna, G. Mukherjee, **S. Nandi**, R. Pandey, T. K. Rana, Pratap Roy, S. Mukhopadhyay, Raj Kumar Santra.

Proceedings of the DAE Symposium on nuclear physics, Vol. **64**, 399 (2019).

Soumen Nandi

Soumen Nandi

DEDICATIONS

Dedicated to my 'Parents',

Smt. Bandana Nandi and Shri Hare Krishna Nandi,

and my 'Better half', Priya

ACKNOWLEDGMENTS

In my Ph.D journey, I have gathered lots of experiences from my supervisor, teachers, seniors and friends, which helped me to grow as a researcher. I highly acknowledge the constant support that I have received from my supervisor Dr. Gopal Mukherjee throughout my Ph.D tenure. He has constantly guided me through the period and supported me by boosting my moral. The guidence from Gopal sir in various fields were very helpful for me. I have enjoyed and learnt a lot from the scientific discussions that I had with him. I am extremely thakful to sir for addressing all of my stupid questions always and encourage me to ask questions. I am really thankful to sir for believing me throughout my tenure. It would never have been possible to complete this thesis without his expert supervision. I will really miss the disscussions with sir.

Thank you very much sir.

I am extremely grateful to Dr. Sarmistha Bhattacharyya for her kind support in my research work. Thank you mam.

I am deeply indebted to Prof. Dinesh Kumar Srivastava, former Director, Variable Energy Cyclotron Centre (VECC), Prof. Sudhee Ranjan Banerjee, Former Head, experimental nuclear physics group, VECC, for giving me the encouragement and kind support.

I express my special gratitude to our Division Head, Dr. Chandana Bhattacharya, for her caring support and expert guidance through out my Ph.D tenure.

I am grateful to our Group Head and Former dean, HBNI Prof. Jane Alam sir for his kind support and providing a healthy research environment in VECC campus.

I would also like to acknowledge the sincere help from present dean, HBNI Prof. Parnika Das mam for her immense help to complete my thesis work. The extreme support from Director, Dr. Sumit Som for providing a vibrant working atmosphere is highly acknowlwdge.

I am extremely grateful to dean, student affairs, Dr. T. K. Ghosh (sir) for his kind support and various valuable suggestions in different academic and administrative processes.

I would like to express my special thanks to my friend cum room mate Santanu for supporting me in various ups and downs throughout my Ph.D life. The disscussion on various topics in almost every area and also the mental support provided by him are highly acknowledged. Thank you bhai.

I am highly thankful to Sarajit da for his immense help starting from my Ph.D joining days to till now.

The unconditional help starting form my Ph.D interview at VECC throughout my Ph.D tenure from Prof. Subhasis Chattopadhyay sir is highly acknowledged.

The excellent support and encouragement received from Mrs. Anindita Chowdhury, Mr. Pulak Mukhopadhyay and Imran Seikh of Physics Lab, VECC, is very much appreciated.

It was great opportunity to participate in various experiments occured in CPDA group with Dr. T. K. Ghosh, Dr. Supriya Mukhopadhyay, Dr. Pratap Roy, Dr. S. Kundu, Dr. T.K. Rana, Dr. K. Banerjee, Arijit da, Santu da, Ratnesh ji, Jai da, Jayanta da, Amiya da, Ratan da, and Pintu da.

I am highly grateful Prof. Partha Chowdhury, Lowell University, Dr. Rajarshi Raut and Dr. S. S. Ghugre from UGC, DAE CSR, Kolkata center for their encouragement and kind support. I have really enjoyed the discussion with them on various physics issues.

I would also like to acknowledge the immense help from Abhilash sir and Dr. Debdulal Kabiraj sir at IUAC target lab for their kind help to prepare ^{186}W target using their electron gun system. This target was used in one of my thesis experiments.

The kind guidance from my seniors Hari da, Soumik da, Ranbir da, Subhendu da, Saikat da, Tanmoy da, Asgar da, Soumya da, Saradindu da and Shinjinee di in early stage of my Ph.D life is very much appreciated. Specially, the scintific discussions with Hari da, Soumik da, Subhendu da (boss), Ranabir da and Saikat da is very much appreciated to understand the different aspects of nuclear structure physics.

The late night discussions along with the food made by Subhendu da (boss) in our mess is highly acknowledged. Thank you boss.

I am really thankful to my seniors.

I would like to give my sincere thanks to Late Professor Asimananda Goswami from Saha Institute of Nuclear Physics for his helps and suggestions at various stages of my work. I miss you very much sir. Your useful suggestions and experience in Physics as well as in experimental aspects will be missed.

I am really thankful to Arghya da for his guidence starting from my M.Sc. days. I am really grateful to Mitali, Shreyasi, Sumit, Sanchari, and Mahfuzur for their encouragement and inspiration. I am very much thankful to Prasun da, Abhishek and all other members in the grid lab for addressing various computer related issues at various stage of my Ph.D tenure. I was extremely fortunate to have friends like Noor da, Rajendra da, Suvroneel, Dipen, Shabir, Kirti, Sansaptak, Shefali, Sudipta, Sudip, Sneha, Tousif, Joy, Vivek, Chandrani, Satya with whom I have spent moments in last few years.

I would like to mention special thanks to my school friends Samapan and Avik with whom I have startred my journey in Physics.

I would like to mention special thanks to our librarian and specially Anindita di for arranging books and journal papers for me in my early days of Ph.D.

I am highly indebted and grateful to my Maa-Baba, Bon and my wife Priya and all of my family members. The unlimited encouragement and full of support at every stage of my life from Maa-Baba is higly appreciated. I would have nothing without their support. The sacrifices did by Maa-Baba for giving me a good life is highly acknowledged. The beating (mar) from my mother in my childhood is highly acknowledged. It helps me lot in my life.

Thank you for your trust.

Thank you Maa-Baba.

Finally and most importantly, I would like to acknowledge the heartiest support and help from my better half Priya. Without your encouragement and support that you did for me, I would not have been able to complete my thesis. I believe this is your degree too.

Thank you for your constant support and love.

I sincerely apologize inadvertent omission of any name from the above list of acknowledgment.

Contents

List of Publications **5**

Summary **v**

List of Figures **xvi**

List of Tables **xvii**

1 Introduction **1**

1.1 γ Vibrational Band . . . 4

1.1.1 Experimental Signatures of γ Vibrational Band . . . 5

1.2 Chiral Band . . . 6

1.2.1 Experimental Signatures of Chiral Band . . . 7

1.3 Magnetic Rotational Band . . . 7

1.3.1 Experimental Signatures of Magnetic Rotational Band . . . 8

1.3.2 Shears Mechanism . . . 9

1.4 Wobbling Band . . . 9

1.4.1 Experimental Signatures of Wobbling Band . . . 10

2 Nuclear Models **17**

2.1 Nuclear Deformation Parameters . . . 18

2.2 Shell Model 21
2.3 Nilsson Model 23
2.4 Cranking Model 27
2.5 Strutinsky Shell Correction 29
2.6 Total Routhian Surface (TRS) Calculations 30
2.7 Shears Mechanism with the Principal Axis Cranking for Magnetic Rotational Band 31
2.8 Particle-Rotor Model 33
2.9 Comparison of Experimental Results with the Theoretical Calculations 34

3 Experimental Techniques and Data Analysis **39**
3.1 Fusion Evaporation Reaction 40
3.2 γ Ray Detection 44
3.2.1 Photoelectric Effect 45
3.2.2 Compton Scattering 46
3.2.3 Pair Production 46
3.3 High-Purity Germanium (HPGe) Detectors 47
3.3.1 Clover Detector 48
3.3.2 Low Energy Photon Spectrometer (LEPS) 50
3.4 Experimental Setups and Performed Experiments 51
3.4.1 VECC array for NUclear Spectroscopy (VENUS) 51
3.4.2 Indian National Gamma Array (INGA) 52
3.4.3 Experiment 1 (^{197}Tl) 52
3.4.4 Experiment 2 (^{183}Au) 53
3.4.5 Experiment 3 (^{187}Os) 54
3.5 Data Analysis Technique 55
3.5.1 Calibration and Efficiency 56
3.5.2 γ Ray Coincidence Relation and Intensity Arguments 58
3.5.3 Angular Distribution of γ-ray Transition 60

3.5.4 Directional Correlation from the Oriented (DCO) states ratio (R_{DCO}) . . 61

3.5.5 Linear Polarization (P) and Polarization Asymmetry (Δ_{PDCO}) 62

4 Band Structures in ^{197}Tl **68**

4.1 **Introduction** 68

4.2 Experimental Results 72

4.3 Discussions 81

4.4 Theoretical Calculations 91

4.4.1 TRS Calculations 91

4.4.2 SPAC Calculations 93

4.5 Summary 95

5 Wobbling Bands in ^{183}Au **100**

5.1 **Introduction** 100

5.2 Experimental Results 102

5.3 Discussions 111

5.4 Theoretical Calculations and Conclusions 114

5.5 Summary 117

6 Different Modes of Excitations in ^{187}Os **120**

6.1 **Introduction** 120

6.2 Experimental Results 125

6.2.1 Bands 1 and 2 129

6.2.2 Band 3 130

6.2.3 Bands 4, 5, 6, 7 and 8 132

6.3 Discussions 135

6.4 Theoretical Calculations 144

6.4.1 TRS Calculations 144

6.5 Summary 145

7 Summary and Future Outlook **149**

7.1 Summary 149

7.2 Study of ^{197}Tl Nucleus 151

7.3 Study of ^{183}Au Nucleus 152

7.4 Study of ^{187}Os Nucleus 153

7.5 Future Outlook 154

Table 2.1: Different rotation axis of a triaxial nucleus with deformation parameter γ

Rotation axis	Deformation parameter γ
Medium axis	$0^\circ > \gamma > -60^\circ$
Short axis	$0^\circ < \gamma < +60^\circ$
Long axis	$-60^\circ > \gamma > -120^\circ$

From eq^n's (2.4) and (2.5), we get

$$\sum_\mu \mid \alpha_{2\mu} \mid^2 = a_{20}^2 + 2a_{22}^2 = \beta_2^2 \tag{2.6}$$

$$R(\theta, \phi) = R_0 \left[1 + \beta_2 \sqrt{\frac{5}{16\pi}} (\cos\gamma(3\cos^2\theta - 1) \quad + \sqrt{3}\sin\gamma\cos^2\theta\cos 2\phi) \right] \tag{2.7}$$

The parameters β_2 and γ represent the degree of axial deformation and axial asymmetry, respectively. The increments of the three semi-axes along the $x-$, $y-$ and $z-$axes in the body-fixed frame are given by

$$\delta R_x = R(\frac{\pi}{2}, 0) - R_0 = R_0 \frac{5}{4\pi} \beta_2 \cos(\gamma - \frac{2\pi}{3}) \tag{2.8}$$

$$\delta R_y = R(\frac{\pi}{2}, \frac{\pi}{2}) - R_0 = R_0 \frac{5}{4\pi} \beta_2 \cos(\gamma + \frac{2\pi}{3}) \tag{2.9}$$

$$\delta R_z = R(0, 0)) - R_0 = R_0 \frac{5}{4\pi} \beta_2 \cos\gamma \tag{2.10}$$

Different nuclear shapes can be described in a $\beta_2 - \gamma$ plane using Lund convention [5]. For example, $\gamma = 0^\circ$ and -60° represent collective prolate and oblate shapes, respectively. On the other hand, the even multiple of 60° represents noncollective prolate and odd multiple of 60° represents noncollective oblate shapes. Otherwise, any other value of γ indicate axially asymmetric shapes. The different nuclear shapes in the $\beta_2 - \gamma$ plane in the Lund convention are shown in Fig. 2.1. The asymmetric nuclear shape has three unequal moments of inertia with respect to the three unequal axes (medium, short, long). Different values of the deformation parameter γ represent different rotation axis of a triaxial nucleus. The range of values applicable for medium axis, short axis and long axis rotations are tabulated in Table 2.1.

4.2 Experimental Results

A total spectrum projected from the γ-γ symmetric matrix has been shown in Fig. 4.1. It contains mostly the known peaks of ^{197}Tl nucleus. A few stronger peaks from other neighboring nuclei, which were also populated in the reaction, are also marked in the spectrum.

A new and improved level scheme of ^{197}Tl has been obtained in the present work and is shown in Fig. 4.2. The level scheme has been extended upto the excitation energy of 5.14 MeV and angular momentum of 19.5 $\hbar$ with the placement of 28 new γ transitions which have been placed for the first time. The level scheme, shown in Fig. 4.2, is based on the $9/2^-$ isomer ($\pi h_{9/2}$ configuration) with half life of $T_{1/2} = 0.54(1)$ sec at 608 keV of excitation energy [28]. The experimental results of γ-ray transition energies (E_γ), level energies (E_i), spins and parities of the initial (I_i^π) levels, R_{DCO} and Δ_{PDCO} values along with the adopted multipolarities of the γ-rays have been tabulated in Table 4.1. Different gated spectra were used for the determination of the relative intensities of the γ rays and all the intensities quoted in Table 4.1 are after proper normalization. The intensities of the nearly-degenerate γ rays could be separately determined using various single gated spectra.

Table 4.1: List of γ rays belonging to ^{197}Tl with their energies (E_γ) and intensities (I_γ). The placement of these γ rays in the level scheme are denoted by the energy (E_i) and spin-parity (I_i^π) of the decaying state. The measured values of R_{DCO} and Δ_{PDCO} along with the adopted multipolarities are also given.

$E_\gamma(keV)$	$E_i(keV)$[9]	I_i^π	I_γ	R_{DCO}	Δ_{PDCO}	Multipolarity
102.5(2)	3166.9(6)	$27/2^-$	1.22(5)	0.65(6)[1]		M1+E2
107.1(2)	3273.9(7)	$29/2^-$	1.05(5)	0.46(6)[1]		M1+E2
113.4(3)	3871.4(7)	$29/2^+$	0.63(3)	0.61(5)[6]		M1+E2
152.3(2)	2264.9(4)	$17/2^+$	5.02(9)	1.04(2)[5]		M1+E2
161.1(4)	2542.7(7)	$17/2^+$	0.16(1)	1.05(13)[4]		M1+E2

Table 4.1: Continued....

$E_\gamma(keV)$	$E_i(keV)$[9]	I_i^π	I_γ	R_{DCO}	Δ_{PDCO}	Multipolarity
170.9(1)	2594.8(3)	$21/2^-$	7.04(11)	0.53(2)[1]		M1+E2
176.2(5)	4881.8(11)	$37/2^+$	0.65(3)	0.51(4)[6]		M1+E2
178.9(3)	3141.6(5)	$23/2^+$	1.31(5)	0.64(5)[8]		M1+E2
192.1(4)	3758.1(5)	$27/2^+$	1.36(5)	1.00(7)[5]		M1+E2
194.2(4)	2818.5(10)	$19/2^+$	0.075(1)	1.06(12)[4]		M1+E2
195.5(2)	2460.5(4)	$19/2^+$	5.02(9)	0.90(2)[5]	-0.05(2)	M1+E2
197.1(3)	4563.9(8)	$35/2^+$	0.11(1)			(M1+E2)
204.5(3)	4075.9(8)	$31/2^+$	2.51(8)	0.58(6)[6]	-0.30(12)	M1(+E2)
204.7(2)	3310.9(7)	$27/2^+$	0.63(2)	0.50(7)[5]	-0.13(8)	M1(+E2)
204.7(3)	3614.1(7)	$27/2^+$	0.25(1)	0.51(6)[8]		M1+E2
206.6(5)	3064.4(6)	$25/2^-$	3.14(9)	0.64(4)[2]	-0.23(5)	M1(+E2)
210.9(3)	2753.6(8)	$19/2^+$	0.11(1)	0.96(10)[4]		M1+E2
241.1(2)	2353.9(4)	$17/2^+$	2.99(7)	1.01(5)[5]	-0.28(8)	M1(+E2)
242.8(6)	2624.4(9)	$17/2^+$	0.18(1)	1.06(16)[4]		M1+E2
247.9(3)	3106.2(6)	$25/2^+$	0.95(4)	0.47(5)[2]	0.16(9)	E1
258.3(6)	5140.1(12)	$39/2^+$	0.30(2)	0.51(6)[6]		M1+E2
260.1(4)	2624.4(9)	$17/2^+$	0.05(2)			(M1+E2)
262.2(3)	4338.1(8)	$33/2^+$	2.42(8)	0.53(5)[6]	-0.22(7)	M1(+E2)
263.6(4)	2858.4(5)	$23/2^-$	8.60(20)	0.44(2)[1]	-0.14(5)	M1(+E2)
262.9(3)	3404.5(6)	$25/2^+$	0.61(2)	0.43(6)[8]	-0.22(8)	M1(+E2)
263.1[10]	2528.0(2)	$19/2^+$	0.17(6)			M1+E2
267.8(3)	3409.4(6)	$25/2^+$	0.79(4)	0.89(7)[5]	-0.1(1)	M1+E2
273.1(3)	3584.1(7)	$29/2^+$	0.68(2)	0.50(5)[2]	-0.14(8)	M1(+E2)
286.2(3)	3560.2(7)	$31/2^-$	0.91(7)	0.55(5)[2]	-0.33(12)	M1(+E2)
288.9(4)	2962.7(4)	$21/2^+$	2.33(6)	0.91(5)[5]	-0.12(5)	M1(+E2)
298.9(2)	2016.9(3)	$17/2^-$	6.05(9)	0.38(5)[1]	-0.11(4)	M1+E2
307.6(3)	1302.6(2)	$13/2^-$	19.53(3)	0.31(1)[2]	-0.10(4)	M1+E2

Table 4.1: Continued....

$E_\gamma(keV)$	$E_i(keV)$[9]	I_i^π	I_γ	R_{DCO}	Δ_{PDCO}	Multipolarity
319.8(1)	2673.7(4)	$19/2^+$	2.56(8)	0.91(4)[5]	-0.09(4)	M1(+E2)
320.5(2)	2038.8(3)	$17/2^-$	3.41(8)	0.39(5)[1]	-0.03(10)	M1+E2
338.9(2)	2799.4(4)	$21/2^+$	5.73(11)	0.46(2)[6]	-0.04(5)	M1+E2
345.8(3)	3145.2(4)	$23/2^+$	3.15(9)	1.00(6)[5]	-0.15(17)	M1+E2
348.1(2)	2460.5(4)	$19/2^+$	0.72(2)	1.02(7)[6]		E2
360.9(3)	3323.5(5)	$23/2^+$	0.95(4)	1.18(6)[8]	-0.09(8)	M1+E2
362.8(3)	3946.8(8)	$31/2^+$	0.54(3)	0.45(5)[2]		M1+E2
367.5(6)	4705.6(9)	$35/2^+$	0.95(1)	0.49(6)[6]	-0.11(5)	M1(+E2)
385.2(2)	2423.9(3)	$19/2^-$	6.08(34)	0.56(1)[1]	-0.03(3)	M1+E2
387.2(3)	995.1(2)	$11/2^-$	100.0(1)	0.33(4)[2]	-0.05(1)	M1+E2
394.4(2)	2112.5(3)	$15/2^+$	0.90(5)	0.93(14)[6]		E1
407.0(2)	2423.9(3)	$19/2^-$	5.70(11)	0.26(2)[1]	-0.19(4)	M1(+E2)
412.3(4)	3972.4(7)	$33/2^-$	0.36(3)	0.46(3)[2]		M1+E2
411.2(6)	2363.8(7)	$15/2^+$	0.61(3)	0.72(4)[4]		M1+E2
415.5(6)	1718.1(2)	$15/2^-$	12.67(16)	0.25(1)[1]	-0.08(4)	M1+E2
420.9(3)	3566.1(5)	$25/2^+$	1.97(8)	0.38(2)[7]		M1+E2
420.7(2)	4367.3(8)	$33/2^+$	0.34(1)	0.58(5)[2]		M1+E2
429.1(3)	2381.6(7)	$15/2^+$	0.66(3)	0.76(3)[4]	-0.05(5)	M1+E2
434.7(4)	3758.1(5)	$27/2^+$	0.48(3)	1.41(20)[5]		E2
469.6(5)	3064.4(6)	$25/2^-$	1.51(5)	0.98(8)[1]	0.07(7)	E2
478.0 (2)	3584.2(7)	$29/2^+$	0.05(1)			
534.5(2)	2799.4(4)	$21/2^+$	1.72(4)	0.87(11)[6]	0.02(1)	E2
555.7(2)	2594.8(3)	$21/2^-$	3.73(11)	1.09(6)[1]	0.11(4)	E2
556.9(8)	1552.3(4)	$13/2^-$	47.31(3)	0.23(1)[7]	0.05(3)	M1+E2
560.1(1)	2112.5(3)	$15/2^+$	47.13(6)	0.53(2)[7]	0.15(3)	E1
562.3(4)	2673.7(4)	$19/2^+$	1.43(5)	1.89(20)[5]	0.15(5)	E2
578.1(4)	2594.8(3)	$21/2^-$	4.19(11)	0.92(5)[1]	0.09(4)	E2

Table 4.1: Continued....

$E_\gamma(keV)$	$E_i(keV)$[9]	I_i^π	I_γ	R_{DCO}	Δ_{PDCO}	Multipolarity
608.8(2)	2962.7(4)	$21/2^+$	1.25(7)	1.73(28)[5]	0.2(1)	E2
612.8(7)	3758.1(5)	$27/2^+$	1.40(5)	1.89(22)[5]	0.1(1)	E2
616.5(4)	4563.9(8)	$35/2^+$	0.18(1)	0.92(22)[3]		E2
635.9(6)	3946.8(8)	$31/2^+$	0.09(1)	0.86(14)[3]		E2
684.7(4)	3145.2(4)	$23/2^+$	1.36(7)	1.69(10)[5]	0.2(1)	E2
694.6(3)	1302.6(2)	$13/2^-$	35.30(8)	1.09(3)[2]	0.12(4)	E2
698.4(4)	3972.4(7)	$33/2^-$	2.08(20)	1.0(2)[1]	0.22(11)	E2
705.8(2)	2423.9(3)	$19/2^-$	15.77(23)	1.09(3)[1]	0.12(3)	E2
714.4(4)	2016.9(3)	$17/2^-$	12.54(22)	1.04(2)[1]	0.08(2)	E2
723.0(1)	1718.1(2)	$15/2^-$	15.77(3)	1.04(2)[3]	0.07(2)	E2
736.2(2)	2038.8(3)	$17/2^-$	12.67(16)	1.00(2)[1]	0.12(6)	E2
766.6(6)	3566.1(5)	$25/2^+$	2.28(9)	1.67(10)[5]	0.2(1)	E2
773.1(3)	1381.1(3)	$11/2^-$	0.44 (2)			
782.3(6)	4367.3(8)	$33/2^+$	0.14(1)	1.05(14)[3]		E2
809.8(3)	2112.5(3)	$15/2^+$	7.60(16)	0.55(2)[1]	0.09(3)	E1
871.2(5)	1866.3(6)	$13/2^-$	0.63(4)		-0.27(18)	M1+E2
957.4(6)	1952.5(7)	$13/2^+$	8.58(10)		0.13(4)	E1

The spin and parity of the level at 1953 keV was assigned as $13/2^+$ in the previous work [13]. This assignment was based on the proposed dipole nature of the 957-keV γ ray based on the measured R_{DCO} value. However, the R_{DCO} value of this transition was extracted gated by

[1]From the 695-keV (E2) gate.
[2]From the 737-keV (E2) gate.
[3]From the 706-keV (E2) gate.
[4]From the 957-keV (E1) gate.
[5]From the 560-keV (E1) gate.
[6]From the 767-keV (E2) gate.
[7]From the 685-keV (E2) gate.
[8]From the 609-keV (E2) gate.
[9]least square fit using the GTOL code of ENSDF [29]

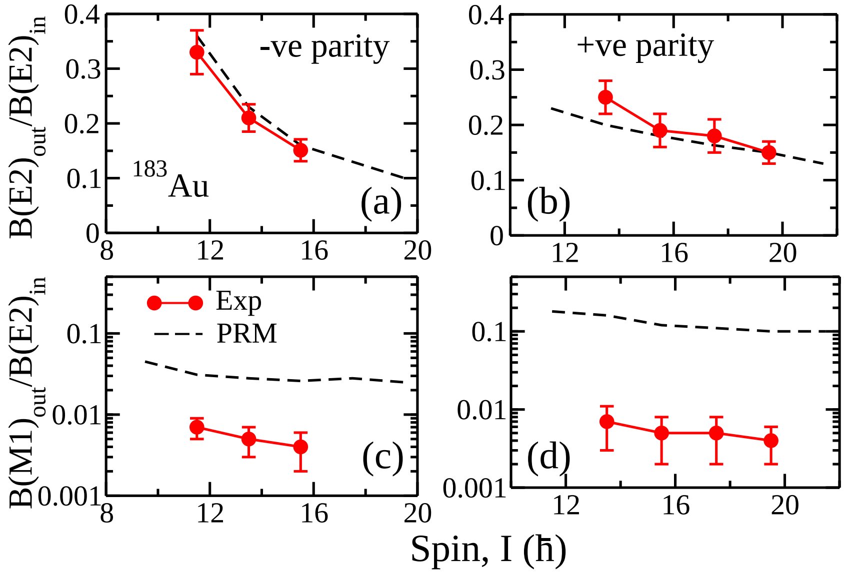

Figure 5.6: Measured values of the ratio of transition probabilities, $B(E2)_{\text{out}}/B(E2)_{\text{in}}$ and $B(M1)_{\text{out}}/B(E2)_{\text{in}}$, determined from the γ-ray intensities, as a function of angular momentum I for the negative parity (a and c) and the positive parity (b and d) bands in ^{183}Au. The theoretical values calculated from PRM are also shown.

of $B(E2)_{\text{out}}/B(E2)_{\text{in}}$ and smaller values of $B(M1)_{\text{out}}/B(E2)_{\text{in}}$ have been obtained for both the configurations, which suggest that the bands 3 and 5 are of wobbling nature [18].

Table 5.1: Energy (E_γ) and intensity (I_γ) of the γ rays, the spin and parity of the initial (I_i^π) and the final (I_f^π) states and the energy of the initial state (E_i) (GTOL fit) of ^{183}Au. The measured values of R_{DCO} and Δ_{PDCO} of the γ rays are also tabulated.

$E_\gamma(keV)$	$E_i(keV)$	$I_i^\pi \rightarrow I_f^\pi$	I_γ [1]	R_{DCO}	Δ_{PDCO}	Multipolarity
12.4 [2]	12.4	$9/2^- \rightarrow 5/2^-$	-	-	-	(E2)
164.6	866.9	$17/2^+ \rightarrow 13/2^+$	27.3(8)	1.03(3) [3]	-	E2
195.9	898.1	$15/2^+ \rightarrow 13/2^+$	12.5(14)	0.58(4) [4]	-	M1+E2
205.3	274.0	$11/2^- \rightarrow 7/2^-$	57.8(1)	1.04(2) [3]	-	E2
219.7	232.1	$13/2^- \rightarrow 9/2^-$	100.0(1)	0.99(3) [3]	-	E2
261.6	274.0	$11/2^- \rightarrow 9/2^-$	42.5(1)	0.64(3) [5]	-0.17(5)	M1+E2
266.4	866.9	$17/2^+ \rightarrow 15/2^-$	59.0(2)	0.55(2) [5]	0.24(3)	E1

Table 5.1: Continued....

$E_\gamma(keV)$	$E_i(keV)$	$I_i^\pi \rightarrow I_f^\pi$	I_γ [1]	R_{DCO}	Δ_{PDCO}	Multipolarity
283.5	1150.6	$21/2^+ \rightarrow 17/2^+$	82.1(1)	1.07(2) [5]	0.11(3)	E2
300.5	866.9	$17/2^+ \rightarrow 17/2^-$	4.3(1)	0.94(7) [3]	-0.02(4)	E1
315.4	1213.4	$19/2^+ \rightarrow 15/2^+$	16.3(14)	1.43(11) [6]	0.25(6)	E2
326.4	600.5	$15/2^- \rightarrow 11/2^-$	61.9(1)	0.97(2) [3]	0.14(2)	E2
334.2	566.4	$17/2^- \rightarrow 13/2^-$	67.5(4)	1.04(2) [4]	0.28(5)	E2
346.6	1213.4	$19/2^+ \rightarrow 17/2^+$	4.9(2)	1.01(5) [6]	-0.17(5)	M1+E2
368.5	600.5	$15/2^- \rightarrow 13/2^-$	18.5(3)	0.64(3) [3]	-0.15(5)	M1+E2
379.2	1529.8	$25/2^+ \rightarrow 21/2^+$	79.7(9)	0.94(2) [3]	0.25(2)	E2
423.4	1023.9	$19/2^- \rightarrow 15/2^-$	21.1(6)	0.91(5) [7]	0.25(3)	E2
423.8	990.3	$21/2^- \rightarrow 17/2^-$	49.8(3)	0.96(2) [8]	0.19(2)	E2
428.3	702.3	$13/2^+ \rightarrow 11/2^-$	45.8(4)	0.68(2) [3]	0.15(4)	E1
432.2	1488.5	$23/2^- \rightarrow 19/2^-$	7.0(5)	0.98(5) [4]	0.26(5)	E2
439.2	2178.4	$27/2^+ \rightarrow 23/2^+$	4.3(4)	0.98(7) [3]	0.13(4)	E2
453.1	1982.8	$29/2^+ \rightarrow 25/2^+$	63.5(8)	0.95(2) [3]	0.13(2)	E2
456.1	1056.5	$19/2^- \rightarrow 15/2^-$	4.0(2)	0.95(12) [9]	0.14(8)	E2
456.8	1670.1	$23/2^+ \rightarrow 19/2^+$	4.5(3)	1.40(17) [6]	0.16(8)	E2
457.4	1023.9	$19/2^- \rightarrow 17/2^-$	6.3(3)	0.62(4) [4]	-0.16(5)	M1+E2
464.5	1488.5	$23/2^- \rightarrow 19/2^-$	9.2(8)	0.96(7) [9]	0.20(6)	E2
470.3	702.3	$13/2^+ \rightarrow 13/2^-$	11.5(2)	1.10(6) [3]	-0.19(6)	E1
477.9	2540.5	$31/2^- \rightarrow 29/2^-$	1.1(1)	0.52(8) [10]	-	M1+E2
490.3	1056.5	$19/2^- \rightarrow 17/2^-$	3.13(9)	0.49(5) [4]	-	M1+E2
494.7	1986.9	$27/2^- \rightarrow 25/2^-$	3.5(1)	0.50(4) [4]	0.07(4)	M1+E2
497.8	1488.5	$23/2^- \rightarrow 21/2^-$	5.2(5)	0.49(6) [11]	0.08(5)	M1+E2
498.1	1986.9	$27/2^- \rightarrow 23/2^-$	14.8(15)	0.95(5) [12]	0.25(3)	E2
502.2	1492.2	$25/2^- \rightarrow 21/2^-$	30.2(3)	1.04(3) [8]	0.16(2)	E2
505.4	2683.9	$31/2^+ \rightarrow 27/2^+$	4.9(5)	1.01(12) [3]	0.27(8)	E2
509.2	2492.1	$33/2^+ \rightarrow 29/2^+$	53.4(7)	0.88(2) [3]	0.22(2)	E2

Table 5.1: Continued....

$E_\gamma(keV)$	$E_i(keV)$	$I_i^\pi \rightarrow I_f^\pi$	I_γ [1]	R_{DCO}	Δ_{PDCO}	Multipolarity
519.3	1670.1	$23/2^+ \rightarrow 21/2^+$	1.8(1)	0.70(5) [3]	-	M1+E2
520.3	1544.2	$23/2^- \rightarrow 19/2^-$	3.6(7)	1.06(9) [9]	0.20(5)	E2
535.6	2205.7	$(27/2^+) \rightarrow 23/2^+$	< 0.6	-	-	(E2)
553.5	2540.5	$31/2^- \rightarrow 27/2^-$	13.5(1)	1.08(8) [12]	0.17(8)	E2
556.9	3049.1	$37/2^+ \rightarrow 33/2^+$	35.8(6)	1.03(2) [3]	0.19(4)	E2
559.7	3243.5	$35/2^+ \rightarrow 31/2^+$	2.0(3)	1.03(12) [3]	-	E2
570.7	2062.8	$29/2^- \rightarrow 25/2^-$	23.7(2)	0.97(3) [8]	0.26(3)	E2
573.7	2117.9	$27/2^- \rightarrow 23/2^-$	2.2(4)	0.95(9) [9]	0.23(7)	E2
588.6	1739.2	$23/2^+ \rightarrow 21/2^+$	6.6(1)	0.50(6) [3]	0.06(4)	M1+E2
597.0	3840.3	$39/2^+ \rightarrow 35/2^+$	2.6(1)	0.83(6) [3]	0.21(8)	E2
606.5	3655.5	$41/2^+ \rightarrow 37/2^+$	26.2(5)	1.00(3) [3]	0.23(4)	E2
607.2	3147.7	$35/2^- \rightarrow 31/2^-$	11.7(13)	0.94(10) [12]	0.20(7)	E2
623.7	4464.1	$43/2^+ \rightarrow 39/2^+$	< 0.6	-	-	(E2)
624.5	2742.4	$31/2^- \rightarrow 27/2^-$	2.1(4)	0.87(12) [9]	-	E2
627.1	2689.9	$33/2^- \rightarrow 29/2^-$	12.8(2)	0.94(5) [8]	0.22(4)	E2
646.3	3388.7	$35/2^- \rightarrow 31/2^-$	0.84(16)	-	-	(E2)
648.3	3796.0	$39/2^- \rightarrow 35/2^-$	6.6(8)	1.05(14) [12]	0.23(8)	E2
648.5	2178.4	$27/2^+ \rightarrow 25/2^+$	8.2(3)	0.52(5) [3]	0.06(4)	M1+E2
652.3	4307.8	$45/2^+ \rightarrow 41/2^+$	11.3(2)	1.02(6) [5]	0.16(4)	E2
661.4	4457.4	$43/2^- \rightarrow 39/2^-$	1.8(4)	1.12(14) [12]	-	E2
667.8	3357.7	$37/2^- \rightarrow 33/2^-$	5.9(1)	0.94(8) [8]	0.28(6)	E2
675.5	5132.9	$47/2^- \rightarrow 43/2^-$	1.1(4)	1.04(12) [12]	-	E2
678.5	4986.3	$49/2^+ \rightarrow 45/2^+$	6.5(2)	1.03(8) [5]	0.26(8)	E2
690.8	5677.1	$53/2^+ \rightarrow 49/2^+$	2.4(1)	1.10(13) [5]	0.24(8)	E2
692.1	4049.8	$41/2^- \rightarrow 37/2^-$	3.1(1)	0.99(9) [8]	0.17(8)	E2
698.3	6375.5	$57/2^+ \rightarrow 53/2^+$	1.2(1)	0.93(11) [13]	-	E2
701.3	2683.9	$31/2^+ \rightarrow 29/2^+$	5.2(4)	0.53(6) [14]	0.06(4)	M1+E2

Table 5.1: Continued....

$E_\gamma(keV)$	$E_i(keV)$	$I_i^\pi \rightarrow I_f^\pi$	I_γ [1]	R_{DCO}	Δ_{PDCO}	Multipolarity
710.4	4760.2	$45/2^-\rightarrow41/2^-$	1.5(1)	0.98(9) [8]	0.17(11)	E2
727.2	7102.7	$61/2^+\rightarrow57/2^+$	1.2(1)	0.93(13) [13]	-	E2
736.4	5496.6	$49/2^-\rightarrow45/2^-$	1.0(1)	0.99(18) [8]	-	E2
745.5	6242.1	$53/2^-\rightarrow49/2^-$	0.60(3)	-	-	(E2)
745.7	7848.4	$65/2^+\rightarrow61/2^+$	0.8(1)	1.03(14) [13]	-	E2
751.3	3243.5	$35/2^+\rightarrow33/2^+$	1.7(1)	0.55(6) [14]	0.05(4)	M1+E2
779.1	5912.0	$51/2^-\rightarrow47/2^-$	0.7(4)	1.04(15) [12]	-	E2
791.0	3840.3	$39/2^+\rightarrow37/2^+$	1.7(2)	0.53(9) [14]	-	M1+E2
808.7	4464.1	$43/2^+\rightarrow41/2^+$	1.4(1)	0.50(10) [14]	-	M1+E2

5.3 Discussions

In ^{183}Au (Z = 79), the proton Fermi level lies just below the Z = 82 shell closure. However, Ω components of the high-j proton orbitals $\pi h_{9/2}$ and $\pi i_{13/2}$ come down in energy with deformation and intrudes in to the region of the proton fermi level in Au isotopes. Rotational bands have, accordingly, been observed in different Au isotopes based on the above configurations

[1]Relative γ-ray intensities are estimated from prompt spectra and normalized to 100 for the total intensity of 220-keV γ-rays.

[2]Adopted from [19];

[3]From 283 keV (E2) gate;

[4]From 220 keV (E2) gate;

[5]From 379 keV (E2) gate;

[6]From 428 keV (E1) gate;

[7]From 326 keV (E2) gate;

[8]From 334 keV (E2) gate;

[9]From 205 keV (E2) gate;

[10]From 571 keV (E2) gate;

[11]From 465 keV (E2) gate substracted from 334 keV (E2) gate;

[12]From 465 keV (E2) gate;

[13]From 557 keV (E2) gate;

[14]From 453 keV (E2) gate;

Table 5.2: The moments of inertia along medium ($\mathcal{J}_m$), short ($\mathcal{J}_s$) and long ($\mathcal{J}_l$) axes obtained for the wobbling bands in ^{183}Au, ^{135}Pr and ^{105}Pd. The values for the later two nuclei are taken from Ref. [14] and [9], respectively. The estimated values of I_m based on HFA approximation are also given.

	^{183}Au	^{183}Au	^{135}Pr	^{105}Pd
	$\pi i_{13/2}$ band	$\pi h_{9/2}$ band	$\pi h_{11/2}$ band	$\nu h_{11/2}$ band
$\mathcal{J}_m$	50.00	36.85	21.0	9.24
$\mathcal{J}_s$	37.52	25.70	13.0	5.87
$\mathcal{J}_l$	2.38	5.45	4.0	1.99
$\mathcal{J}_m/\mathcal{J}_s$	1.33	1.43	1.61	1.57
I_m ($\hbar$)	16.5	7.5	5.5	6.5

mation parameters on the angular momentum also been checked and it change only within 0.01 for β and 1° for γ from the bandhead to the highest spin for both the negative and positive parity band. It justifies the stability of triaxial shape for both the wobbling bands. The three moment of inertia for the negative and positive parity bands have been extracted by fitting the experimental energy spectra and the values are $\mathcal{J}_{m,s,l} = 36.85, 25.70, 5.45$ $\hbar^2$/MeV and $\mathcal{J}_{m,s,l} = 50.00, 37.52, 2.38$ $\hbar^2$/MeV, respectively. In both calculations, the pairing gap $\Delta = 12/\sqrt{A} = 0.89$ MeV is adopted. It should be noted that the calculations can reproduce the experimental $B(E2)$ values [27], which justifies the correct prediction of the deformation parameters by CDFT. The experimental values are compared with the calculations as shown in Fig. 5.8. The wobbling energies for both the positive and the negative parity wobbling bands have been well reproduced by the calculations. Also the experimental $B(E2)_{\mathrm{out}}/B(E2)_{\mathrm{in}}$ values whcih are highly sensitive to the nuclear triaxiality, agree well with the calculated ones (Fig. 5.6). It also justifies the correct inputs of triaxiality by CDFT calculation. The over estimation of the $B(M1)_{\mathrm{out}}/B(E2)_{\mathrm{in}}$ values is attributed to the absence of scissors mode in the calculations [28]. The large values of $B(E2)_{\mathrm{out}}/B(E2)_{\mathrm{in}}$ and small values of $B(M1)_{\mathrm{out}}/B(E2)_{\mathrm{in}}$ obtained in the calculations, further support the wobbling interpretation for both the bands.

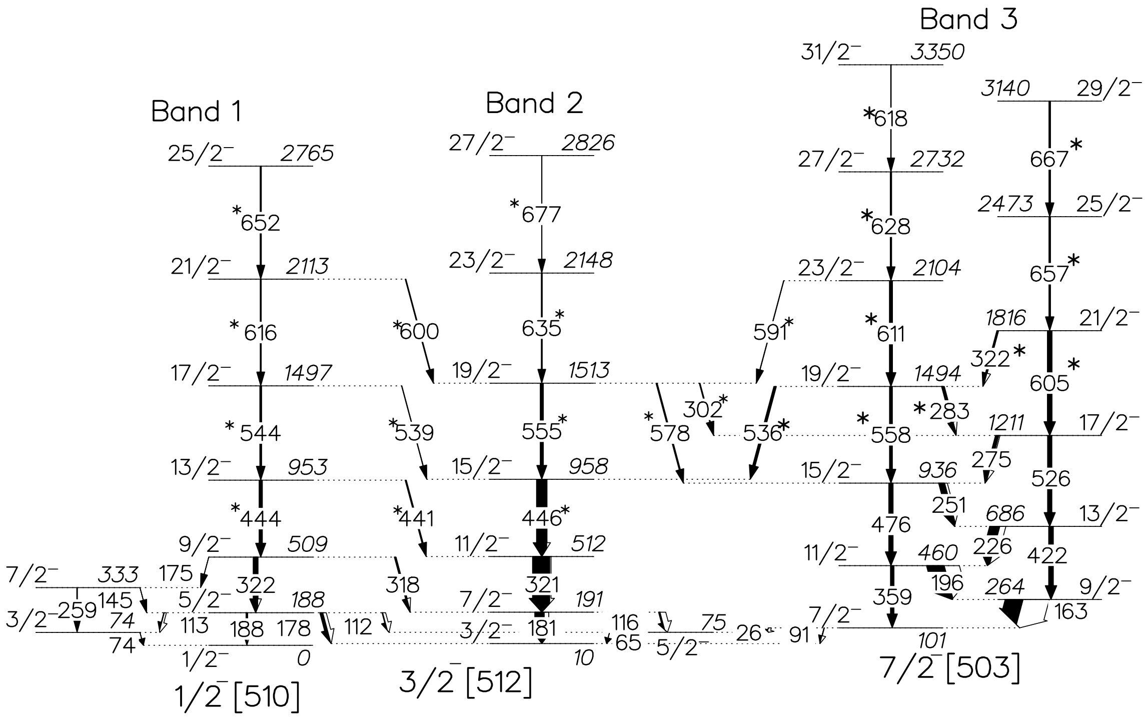

Figure 6.1: Negative parity states of level scheme of ^{187}Os, proposed from the present work. The width of the transitions are proportional to their intensity and new γ transitions are marked by asterisks(*)

Table 6.1: List of γ rays belonging to negative parity bands of ^{187}Os with their energies (E_γ) and intensities (I_γ). The placement of these γ rays in the level scheme are denoted by the energy (E_i) and spin-parity (I_i^π) of the decaying state. The measured values of R_{DCO} and Δ_{PDCO} along with the adopted multipolarities are also given.

E_γ (keV)	E_i (keV)	I_i^π	I_γ^a	R_{DCO}	Δ_{PDCO}	Multipolarity
25.9(2)	101	7/2⁻	38(12)[1]			(M1+E2)
65.31(2)	75	5/2⁻				(M1+E2)
74.3(2)	74	3/2⁻				(M1+E2)
91.1(2)	101	7/2⁻	1.6(11)[1]			(E2)
112.4(2)	188	5/2⁻	3.9(1)			(M1+E2)
113.3(2)	188	5/2⁻	2.9(3)			(M1+E2)
115.8(2)	191	7/2⁻	8.17(3)	0.49(6)[2]		M1+(E2)

Table 6.1: Continued....

E_γ (keV)	E_i (keV)	I_i^π	I_γ^a	R_{DCO}	Δ_{PDCO}	Multipolarity
145.3(2)	333	$7/2^-$	0.46(6)			(M1+E2)
162.9(2)	264	$9/2^-$	100.0(18)	0.62(3)[3]	-0.06(4)	M1+E2
175.4(2)	509	$9/2^-$	0.57(8)			(M1+E2)
177.8(2)	188	$5/2^-$	16.8(2)	0.76(4)[4]		M1+(E2)
181.0(2)	191	$7/2^-$	54.7(2)	0.93(3)[2]	0.13(10)	E2
187.7(2)	188	$5/2^-$	6.5(2)	0.99(7)[4]		E2
196.4(2)	460	$11/2^-$	99.9(16)	0.58(3)[5]	-0.07(5)	M1+E2
225.6(2)	686	$13/2^-$	57.0(16)	0.48(2)[6]	-0.14(9)	M1+E2
250.6(2)	936	$15/2^-$	34.1(8)	0.52(3)[3]	-0.11(8)	M1+E2
259.1(2)	333	$7/2^-$	3.11(4)			(E2)
275.2(2)	1211	$17/2^-$	19.1(10)	0.59(4)[5]	-0.06(2)	M1+E2
282.6(2)	1494	$19/2^-$	4.0(2)	0.60(6)[5]		M1+(E2)
302.2(2)	1513	$19/2^-$	3.9(1)	0.62(9)[5]		M1+(E2)
318.1(2)	509	$9/2^-$	7.7(10)	0.67(7)[7]	-0.17(14)	M1+E2
321.3(2)	512	$11/2^-$	100(1)	0.95(2)[2]	0.13(5)	E2
321.6(2)	509	$9/2^-$	26.0(5)	1.01(3)[8]	0.17(11)	E2
321.9(2)	1816	$21/2^-$	8.2(13)	0.53(7)[5]		M1+(E2)
359.3(2)	460	$11/2^-$	18.8(5)	1.03(7)[5]	0.11(8)	E2
421.9(2)	686	$13/2^-$	26.8(5)	0.92(5)[6]	0.09(8)	E2
440.8(2)	953	$13/2^-$	6.4(2)	0.69(2)[9]	-0.15(12)	M1+E2
443.5(2)	953	$13/2^-$	18.0(15)	0.93(9)[8]	0.18(14)	E2
445.8(2)	958	$15/2^-$	58.6(8)	1.07(4)[9]	0.10(5)	E2
476.3(2)	936	$15/2^-$	24.5(8)	1.03(7)[10]	0.09(4)	E2
525.8(2)	1211	$17/2^-$	24.2(4)	1.07(5)[3]	0.12(7)	E2
536.1(2)	1494	$19/2^-$	14.0(6)	1.04(9)[10]	0.17(13)	E2
539.4(2)	1497	$17/2^-$	2.1(1)	0.70(10)[2]	-0.11(5)	M1+E2
544.4(2)	1497	$17/2^-$	10.0(3)	1.04(12)[8]	0.17(13)	E2

Table 6.1: Continued....

E_γ (keV)	E_i (keV)	I_i^π	I_γ^a	R_{DCO}	Δ_{PDCO}	Multipolarity
555.4(2)	1513	$19/2^-$	17.4(4)	0.99(7) [9]	0.14(8)	E2
557.7(2)	1494	$19/2^-$	16.2(4)	0.98(10) [3]	0.12(7)	E2
577.7(2)	1513	$19/2^-$	6.9(3)	1.04(14) [5]	0.13(11)	E2
591.3(2)	2104	$23/2^-$	1.9(2)			(E2)
599.5(2)	2113	$21/2^{(-)}$	4.1(4)	0.57(13) [2]		M1+(E2)
604.5(2)	1816	$21/2^-$	26.3(5)	1.02(7) [3]	0.09(6)	E2
610.5(2)	2104	$23/2^-$	17.3(4)	1.00(10) [3]	0.16(11)	E2
616.0(2)	2113	$21/2^{(-)}$	<5.72	1.10(13) [4]		(E2)
618.0(2)	3350	$31/2^-$	2.6(2)	1.02(12) [11]	0.11(10)	E2
627.9(2)	2732	$27/2^-$	7.6(3)	1.03(16) [5]	0.22(12)	E2
635.0(2)	2148	$23/2^-$	5.2(2)	1.04(10) [5]	0.14(12)	E2
652.0(2)	2765	$25/2^{(-)}$	<6.72(11)	1.02(13) [4]		(E2)
657.1(2)	2473	$25/2^-$	8.8(2)	0.98(4) [3]	0.19(13)	E2
667.1(2)	3140	$29/2^-$	8.7(2)	0.91(14) [6]	0.19(16)	E2
677.2(2)	2826	$27/2^{(-)}$	1.6(1)	1.07(21) [5]		E2

[1] From LEPS data, not normalized to clovers

[2] From the 446-keV (E2) gate.
[3] From the 422-keV (E2) gate.
[4] From the 322-keV (E2) gate.
[5] From the 476-keV (E2) gate.
[6] From the 526-keV (E2) gate.
[7] From the 444-keV (E2) gate.
[8] From the 188-keV (E2) gate.
[9] From the 181-keV (E2) gate.
[10] From the 610-keV (E2) gate.
[11] From the 628-keV (E2) gate.

Table 6.2: List of γ rays belonging to positive parity bands of ^{187}Os with their energies (E_γ) and intensities (I_γ). The placement of these γ rays in the level scheme are denoted by the energy (E_i) and spin-parity (I_i^π) of the decaying state. The measured values of R_{DCO} and Δ_{PDCO} along with the adopted multipolarities are also given.

E_γ (keV)	E_i (keV)	I_i^π	I_γ^a	R_{DCO}	Δ_{PDCO}	Multipolarity
86.4(2)	1647.3	$21/2^+$	1.22(1)			(M1+E2)
132.8(2)	2029.9	$25/2^+$	0.21(1)			(M1+E2)
162.4(2)	418.4	$13/2^+$	100.0(9)	0.41(1)[1]		M1+E2
178.5(2)	1825.6	$25/2^+$	1.09(4)	0.44(6)[1]		M1+E2
179.9(2)	1561.4	$21/2^+$	0.96(7)			(M1+E2)
199.1(2)	617.4	$15/2^+$	37.6(3)	0.49(1)[2]		M1+E2
200.8(2)	817.7	$17/2^+$	21.9(6)	0.68(2)[3]		M1+E2
203.0(2)	1286.5	$21/2^+$	4.11(13)	0.47(5)[1]	-0.25(16)	M1+E2
214.1(2)	1340.5	$19/2^+$	4.23(4)	0.61(7)[4]	-0.13(11)	M1+E2
220.9(2)	1561.4	$21/2^+$	15.92(2)	0.73(4)[4]	-0.06(4)	M1+E2
232.7(2)	1126.5	$17/2^+$	5.80(1)	0.59(3)[5]	-0.15(10)	M1+E2
246.4(2)	2202.1	$25/2^+$	2.6(1)	0.72(8)[6]		M1+E2
253.9(2)	2283.8	$27/2^{(+)}$	1.71(4)	0.84(11)[7]		M1+E2
254.8(2)	1381.6	$19/2^+$	3.66(9)	0.54(5)[8]	-0.14(10)	M1+E2
265.9(2)	1647.3	$21/2^+$	1.29(4)	0.67(11)[8]	-0.07(5)	M1+E2
266.3(2)	1083.9	$19/2^+$	13.2(3)	0.48(1)[1]	-0.11(6)	M1+E2
296.3(2)	2326.2	$29/2^+$	7.6(5)	0.90(10)[8]	0.24(13)	E2
301.8(2)	2628.0	$33/2^+$	4.0(4)	0.95(5)[7]	0.17(10)	E2
305.3(2)	2202.1	$25/2^+$	6.01(7)	0.75(10)[1]	-0.18(10)	M1+E2
308.5(2)	1955.5	$23/2^+$	1.06(5)	0.69(10)[8]		M1+E2

Table 6.2: Continued....

E_γ (keV)	E_i (keV)	I_i^π	I_γ^a	R_{DCO}	Δ_{PDCO}	Multipolarity
320.8(2)	1832.6	$21/2^+$	0.90(14)			(M1+E2)
321.1(2)	2949.1	$37/2^+$	3.5(4)	1.00(9)[7]	0.23(11)	E2
335.7(2)	1897.4	$23/2^+$	18.3(7)	0.66(5)[1]	-0.14(10)	M1+E2
345.4(2)	2242.8	$25/2^+$	1.27(2)	0.51(7)[5]	-0.17(11)	M1+E2
353.6(2)	3327.0	$31/2^+$	3.70(2)	0.67(11)[5]	-0.23(11)	M1+E2
360.9(2)	1647.0	$23/2^+$	4.74(19)	0.52(4)[1]	-0.13(8)	M1+E2
361.0(2)	617.4	$15/2^+$	21.3(2)	0.88(6)[9]	0.09(8)	E2
363.8(2)	2973.3	$29/2^+$	3.89(4)	0.52(6)[5]	-0.14(9)	M1+E2
371.3(2)	2203.9	$(23/2^+)$	0.80(2)			(M1+E2)
376.5(2)	2274.4	$27/2^+$	1.88(3)	0.91(12)[5]	0.15(12)	E2
381.8(2)	2656.2	$(31/2^+)$	0.55(2)			(E2)
385.4(2)	1511.9	$19/2^+$	2.5(2)	0.50(4)[8]	-0.20(9)	M1+E2
399.0(2)	817.7	$17/2^+$	27.7(2)	0.99(4)[9]	0.22(5)	E2
407.3(2)	2609.4	$27/2^+$	11.6(2)	0.65(9)[5]	-0.09(7)	M1+E2
434.9(2)	1561.4	$21/2^+$	14.5(2)	0.93(6)[4]	0.26(9)	E2
440.3(2)	2642.4	$27/2^+$	5.1(2)	0.63(6)[5]	-0.17(10)	M1+E2
446.5(2)	1340.5	$19/2^+$	5.5(1)	0.83(9)[7]	0.15(9)	E2
451.0(2)	1832.6	$21/2^+$	2.17(2)	0.54(15)[8]	-0.14(11)	M1+E2
466.5(2)	1083.9	$19/2^+$	18.9(9)	1.0(2)[9]	0.12(7)	E2
468.2(2)	2029.9	$25/2^+$	11.8(5)	1.01(11)[2]	0.13(11)	E2
468.9(2)	1286.5	$21/2^+$	29.0(5)	1.00(4)[1]	0.09(3)	E2
475.7(2)	893.8	$15/2^+$	9.8(1)	0.53(5)[5]	-0.09(6)	M1+E2
476.9(2)	1561.4	$21/2^+$	5.5(8)	0.62(6)[1]	-0.16(11)	M1+E2
488.3(2)	1381.6	$19/2^+$	3.35(9)	1.03(10)[6]	0.24(12)	E2
508.9(2)	1126.5	$17/2^+$	13.7(10)	0.58(2)[5]	-0.11(7)	M1+E2
520.6(2)	1647.3	$21/2^+$	3.8(1)	0.98(8)[8]	0.22(12)	E2
523.0(2)	1340.5	$19/2^+$	2.6(2)	0.62(11)[4]	-0.14(12)	M1+E2

Table 6.2: Continued....

E_γ (keV)	E_i (keV)	I_i^π	I_γ^a	R_{DCO}	Δ_{PDCO}	Multipolarity
538.7(2)	3181.1	$29/2^{(+)}$	0.65(3)	0.62(8)[5]		M1+E2
539.0(2)	1825.6	$25/2^{+}$	10.8(3)	1.00(4)[1]	0.11(4)	E2
553.1(2)	2836.9	$31/2^{(+)}$	1.15(8)	0.91(10)[7]		E2
554.3(2)	2202.1	$25/2^{+}$	17.0(2)	0.79(5)[1]	-0.19(11)	M1+E2
562.2(2)	3399.1	$(35/2^{+})$	0.44(6)			(E2)
563.5(2)	1647.0	$23/2^{+}$	23.1(2)	0.92(2)[2]	0.08(4)	E2
563.7(2)	1381.6	$19/2^{+}$	9.7(2)	0.42(3)[6]	-0.12(8)	M1+E2
573.9(2)	1955.5	$23/2^{+}$	3.0(1)	1.02(11)[1]	0.22(13)	E2
590.6(2)	3200.0	$31/2^{+}$	1.49(3)	1.08(15)[5]	0.19(8)	E2
611.8(2)	1897.4	$23/2^{+}$	0.19(2)			(M1+E2)
617.6(2)	2443.2	$29/2^{+}$	12.0(2)	1.05(8)[1]	0.19(5)	E2
624.5(2)	2136.4	$23/2^{(+)}$	1.30(3)	0.96(15)[8]		E2
627.6(2)	2274.4	$27/2^{+}$	0.27(2)			(M1+E2)
637.7(2)	893.8	$15/2^{+}$	8.5(1)	0.93(6)[5]	0.22(10)	E2
654.6(2)	2301.9	$27/2^{+}$	6.0(1)	0.95(5)[2]	0.15(6)	E2
668.7(2)	1955.5	$23/2^{+}$	2.14(5)	0.69(11)[8]		M1+E2
686.6(2)	3129.8	$33/2^{+}$	3.7(1)	1.00(11)[1]	0.19(9)	E2
708.0(2)	1126.5	$17/2^{+}$	7.1(1)	0.91(4)[5]	0.18(10)	E2
717.8(2)	3327.0	$31/2^{+}$	0.82(1)	0.92(19)[5]		E2
722.9(2)	1340.5	$19/2^{+}$	3.55(2)	0.94(11)[4]	0.24(9)	E2
725.1(2)	3854.9	$37/2^{+}$	0.58(4)	1.10(14)[1]		E2
732.2(2)	3034.1	$31/2^{+}$	1.5(1)	1.02(17)[2]	0.29(17)	E2
743.8(2)	1561.4	$21/2^{+}$	1.4(2)	1.04(14)[1]		E2
783.3(2)	3817.4	$35/2^{+}$	0.50(6)	0.90(16)[2]		E2
922.0(2)	1340.5	$19/2^{+}$	7.2(1)	0.99(7)[7]	-0.05(3)	M3+E4

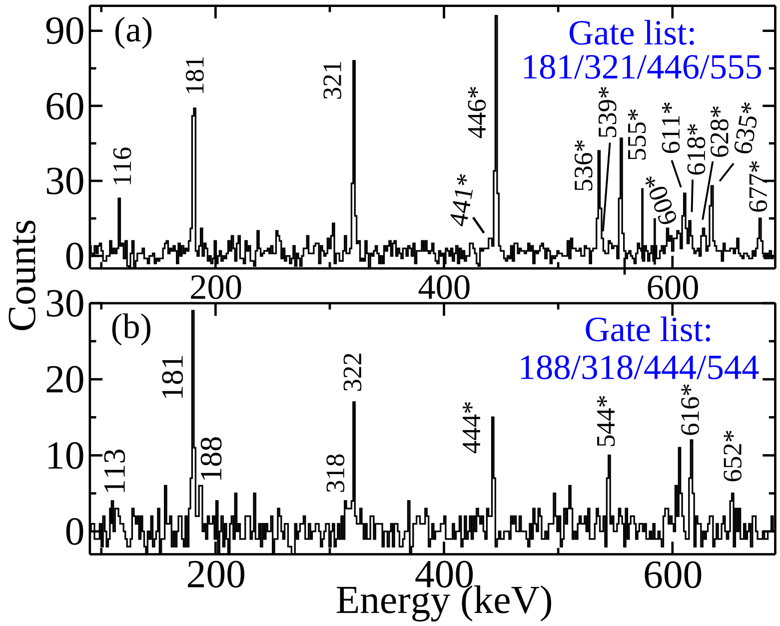

Figure 6.3: Double gated spectra of gatelist of (a) 181, 321, 446, 555 keV and (b) 188, 318, 444, 544 keV transitions in band 2 and 1, respectively. Newly observed transitions are marked by (*).

6.2.1 Bands 1 and 2

The spin and parity of the band heads of bands 1 and 2 were assigned as $1/2^-$ and $3/2^-$ and were known upto the level energy at 509 keV and 511 keV, respectively, from the previous work of Sodan et al. [7]. However, the levels at 509 keV, 511 keV and the low lying level 341 keV were tentatively placed in the level scheme. In the present analysis bands 1 and 2 have been extended upto the excitation energies of 2765 and 2826 keV and angular momentum of $25/2^-$ and $27/2^-$, respectively. The tentatively placed 509-keV level of band 1 has been confirmed in the present analysis. All the γ rays of band 1 along with the newly observed transitions are shown in the double gated spectra of Fig. 6.3. The spin and parity for most of the levels of band 1 have been assigned using R_{DCO} and Δ_{PDCO} measurements of the decaying γ rays.

[1]From the 399-keV (E2) gate.
[2]From the 466-keV (E2) gate.
[3]From the 539-keV (E2) gate.
[4]From the 361-keV (E2) gate.
[5]From the 435-keV (E2) gate.
[6]From the 574-keV (E2) gate.
[7]From the 468-keV (E2) gate.
[8]From the 708-keV (E2) gate.
[9]From the 539-keV (E2) gate.

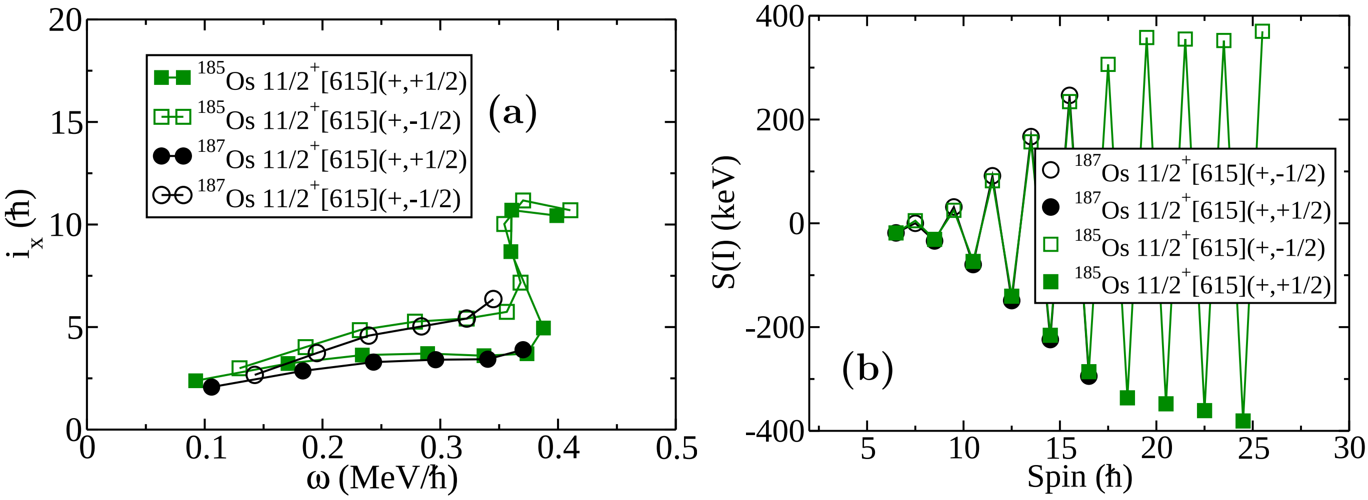

Figure 6.13: (a) Aligned angular momentum i_x as a function of rotational frequency (ω) for the $\nu i_{13/2}$ band in ^{185,187}Os. (b) Energy staggering (S(I)) vs. spin ($\hbar$) for the $\nu i_{13/2}$ band in ^{185,187}Os.

Table 6.3: The systematic comparison of γ and $\gamma\gamma$ band head excitation energies for ^{186,187,188}Os

Nucleus	$K_{1\gamma}$	$E_{1\gamma}$(keV)	$K_{2\gamma}$	$E_{2\gamma}$(keV)	$E_{2\gamma}/E_{1\gamma}$
^{186}Os	2^+	768	4^+	1353	1.76
^{187}Os	$15/2^+$	637	$19/2^+$	1125	1.77
^{188}Os	2^+	633	4^+	1280	2.02

the positive parity bands based on high Ω orbital in ^{185}Os and ^{187}Os can be a menifestation of triaxial nuclear shape.

The band head excitation energies of γ-band and γ-γ band in even-even neighbouring ^{186,188}Os [3, 5] isotopes are mentioned in Table. 6.3. It shows that the band head excitation energy of second 2^+ state of the γ band decreases for heavier Os isotopes. The decrease of band head excitation energy means that the heavier Os isotopes are much more γ deformed as discussed in details at chapter-1. In case of odd-A ^{187}Os, a new γ-band (band 5) and a new γ-γ band (band 6) at the excitation energy of 637 and 1125 keV have been observed with respect to the band head excitation energy of the positive parity main band 4. The generation of γ-band and γ-γ band in ^{187}Os can be represented by a coupling of odd neutron in $11/2^+$[615] orbital with the γ-band and γ-γ band at even-even ^{186}Os. The $11/2^+$ state in positive parity main band

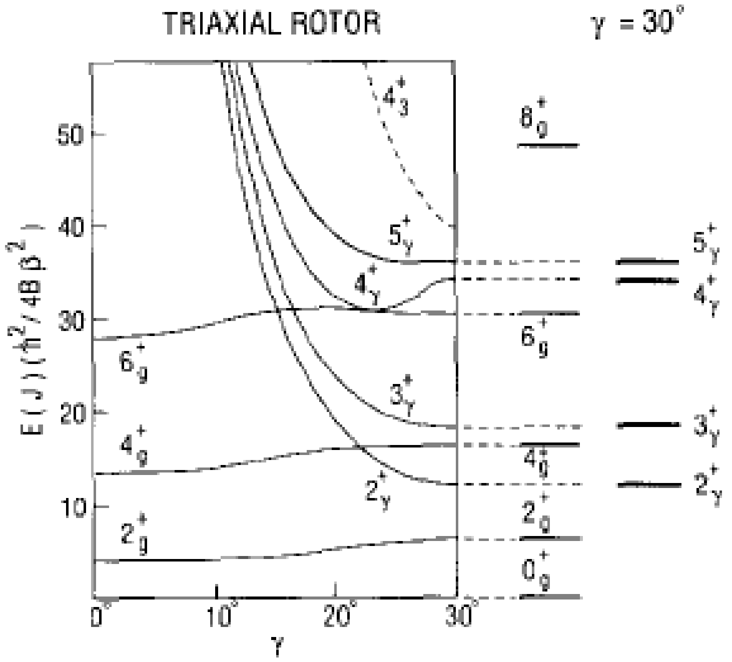

Figure 1.1: Calculated energy levels of a γ band using Davydov model [17, 18].

- **wobbling band**

1.1 γ Vibrational Band

The deformed vibration in atomic nuclei for quadrupole shape can be classified into two types

- β vibration for an axially deformed nucleus
- γ vibration for a non-axial nucleus

The quadrupole phonons carry two units of angular momentum with projections K=0 and K=2. The K=0 vibration, called the β vibration, is along the symmetry axis and preserves the axial symmetry of the nucleus. On the other hand, K = 2 corresponds to γ vibration which represents the fluctuation of nuclear shape from its axial symmetry. When an even-even nucleus has non-axial deformation, a new set of levels of spins 2, 3, 4, 5 ... etc. are generated in addition to the ground state rotational band (0, 2, 4,...etc.). Also, a slight change in the energies of this main ground state rotational band occur compared to the axially symmetric

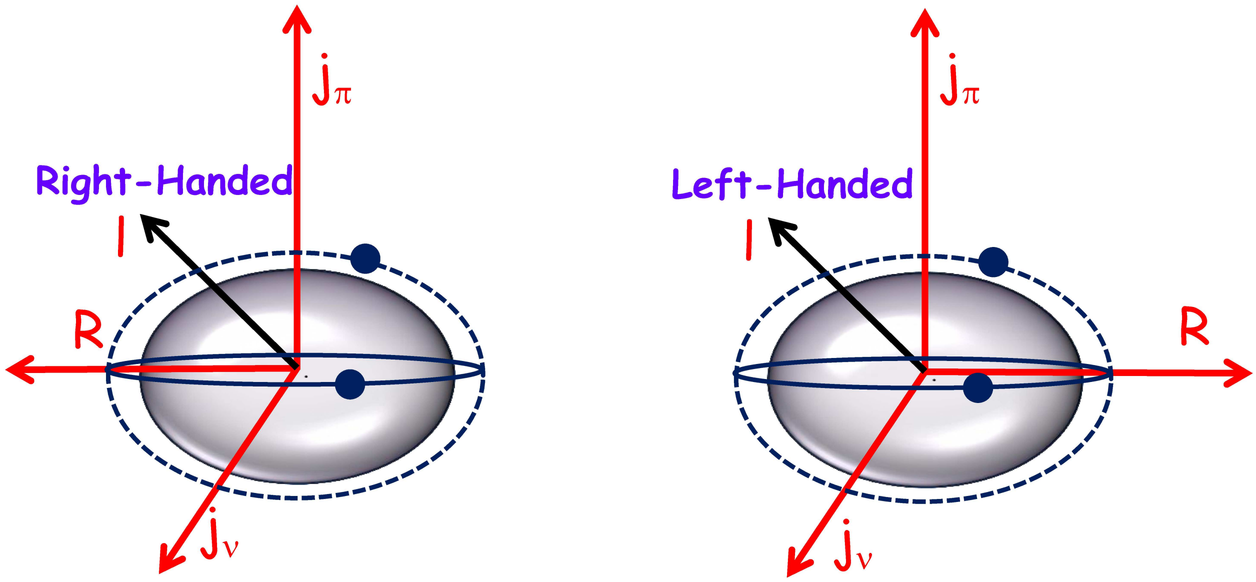

Figure 1.2: Geometrical representation of right-handed and left-handed chiral geometry

$\sim$ 180 region, multiphonon $\gamma\gamma$ vibrational bands are reported in even-even ^{186,188}Os nuclei [30] but, has not been observed in any of the odd-A isotopes in this mass region.

1.2 Chiral Band

The doubly degenerate chiral band was first predicted by Frauendorf and Meng [31] for a nucleus with stable triaxial shape and having a particle-hole configuration. The particle angular momentum, the hole angular momentum and the angular momentum of the triaxial core can be arranged with a right hand - left hand symmetry and form the chiral geometry as shown in Fig. 1.2. A triaxial nucleus has three unequal principal axes: short, long and medium. The unpaired particle aligns along the short axis to maximise the overlap to the core. On the other hand, the hole aligns along the long axis to minimise the overlap to the core and the core angular momentum (R) is perpendicular to both particle and hole angular momenta. The right-handed and the left-handed systems are related with each other by $R_y(\pi))T$ symmetry.

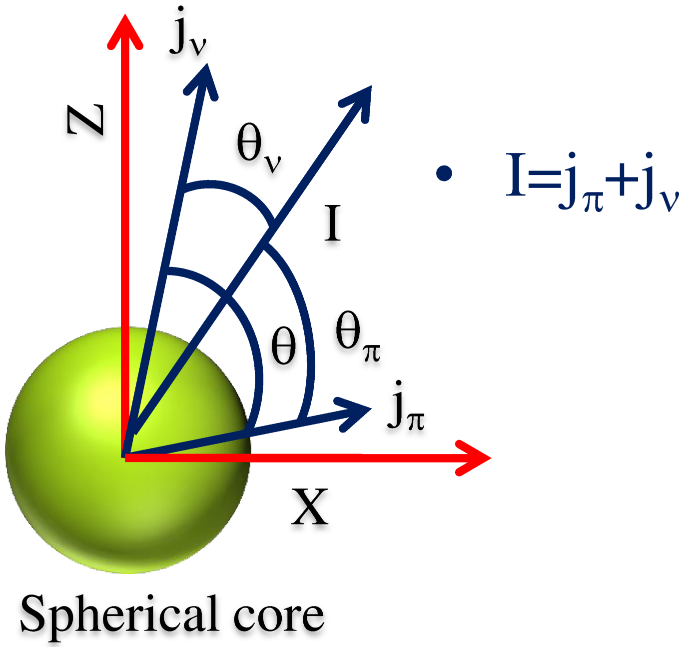

Figure 1.3: Schematic representation of shears mechanism for magnetic rotational band

almost perpendicular to each other. In MR bands, the angular momenta are generated when the particle and hole angular momentum blades align along the total angular momentum axis. The angular momentum generation of an MR band in weakly deformed nuclei in this way is known as shears mechanism [39].

1.3.1 Experimental Signatures of Magnetic Rotational Band

The experimental signatures of the magnetic rotational bands are as follows:

- The level energies in MR band follow $E(I) - E(I_0) = A(I - I_0)^2$, where $E(I_0)$ and I_0 are the bandhead excitation energy and spin, respectively.
- The MR band consists of intraband $\Delta I = 1$ magnetic dipole transitions with weak or no E2 cross-over.
- The dipole transition strengths [B(M1)] are large generally of the order of 1-10 μ_N^2.
- The experimental B(M1) value decreases with spin. Therefore, the $\frac{B(M1)}{B(E2)}$ ratio decreases for a band with fixed B(E2) value.

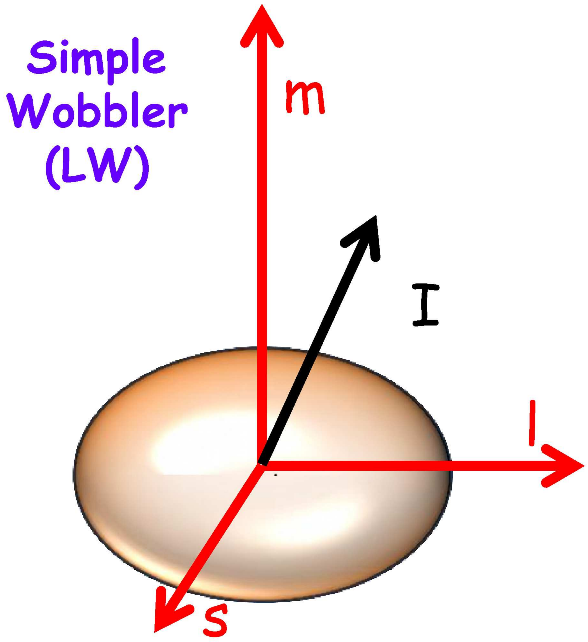

Figure 1.4: Geometrical representation of Simple wobbler in even-even nucleus

wobbling band can be expressed as

$$E = E_{\mathrm{rot}} + (n_w + 1/2)\hbar\omega_{\mathrm{wob}}$$

where, E_{rot} is the rotational energy due to the rotation around the medium axis, n_w is the wobbling quanta and $\hbar\omega_{\mathrm{wob}}$ is the wobbling frequency with wobbling energy $E_{\mathrm{wob}} = \hbar\omega_{\mathrm{wob}}$. However, such "simple" wobbling motion for the even-even nuclei (with zero quasi-particle configuration) has not been observed till date.

But, wobbling motion has been observed in very few odd-A nuclei in the nuclear chart [41, 42, 43, 44, 45, 46, 47, 48, 49, 50]. The wobbling motion in odd-A nuclei can be classified into the following two types based on the coupling of the odd particle with the triaxial core [51]:

I. Transverse wobbling (TW)

II. Longitudinal wobbling (LW)

1.4.1 Experimental Signatures of Wobbling Band

As mentioned before, the wobbling motion is realized in a deformed rotational nucleus. Therefore, the nucleus must possesses a primary rotational band as in a normal deformed nucleus.

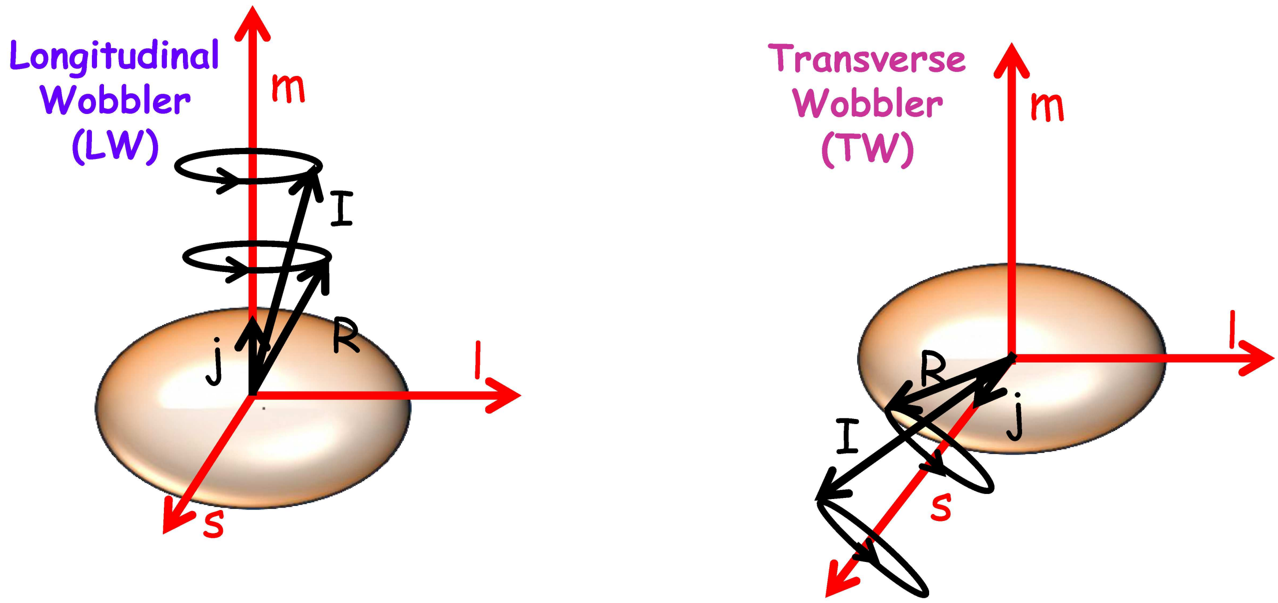

Figure 1.5: Geometrical representation of longitudinal and transverse wobbling motion in odd-A nucleus

The wobbling is manifested as a collective vibration on top of this rotational motion. Following are the specific signatures of wobbling motion in nuclei:

- The wobbling motion is manifested by a series of rotational bands on top of the vibrational states of wobbling quanta n_w.
- These wobbling bands are connected to the primary rotational band via $\Delta I = 1$ E2 transitions.
- The ratio of the strengths of the interband to intraband E2 transitions, i.e $\dfrac{B(E2)_{out}}{B(E2)_{in}}$ is large.

The two different types of wobbling motions for odd-A nuclei can be distingushied from the coupling of the odd particle with triaxial core. In case of LW, the particle angular momentum aligns along the medium axis while it aligns along the short or long axes for TW motion (Fig. 1.5). The measured wobbling frequency has been found to increase with angular momentum, I for LW, while in case of all the TW identified so far, prior to the present work, the wobbling frequency has been observed to decrease with I. Also, multiple wobbling bands like multiple chiral bands [52] in a triaxial nucleus still not been found in any nuclei in the nuclear chart. The experimental wobbling frequency $E_{\rm wob} = \hbar\omega_{\rm wob}$ can be obtained from the

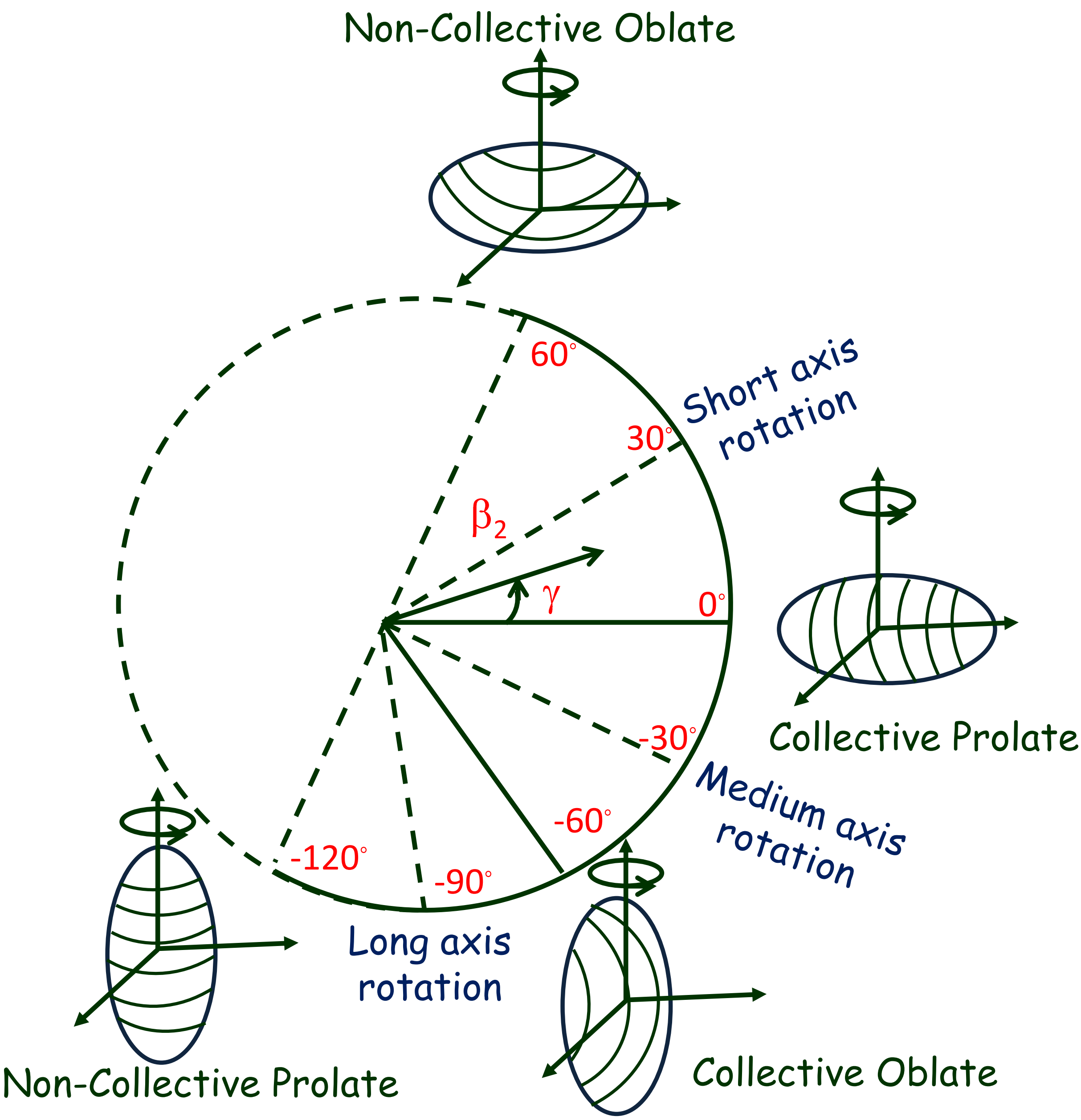

Figure 2.1: Different nuclear shapes in (β_2-γ) plane using Lund convention[5].

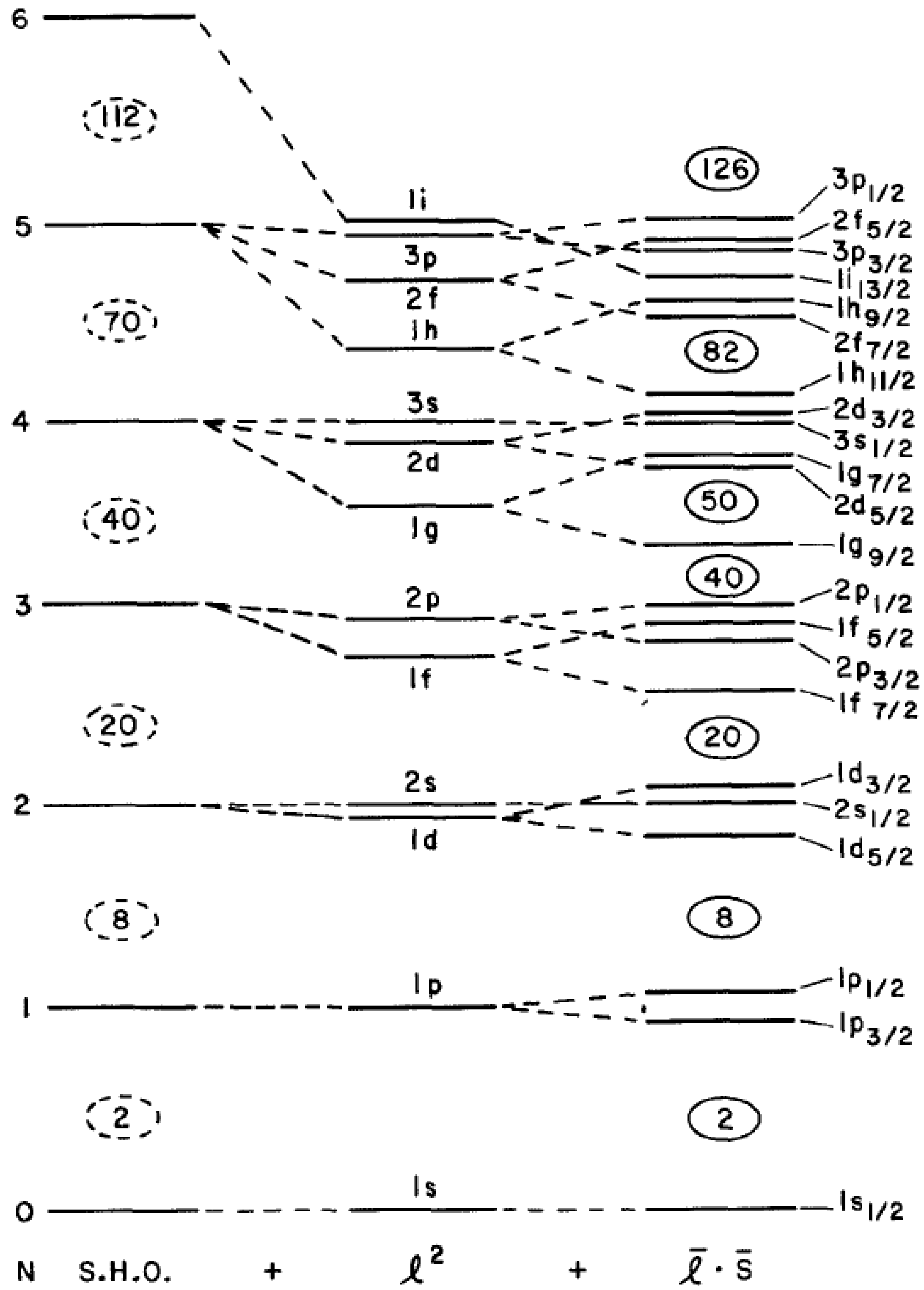

Figure 2.2: Spherical shell model diagram of single particle states with spin orbit term reproducing magic numbers 2, 8, 20, 28, 50, 82, 126 [6].

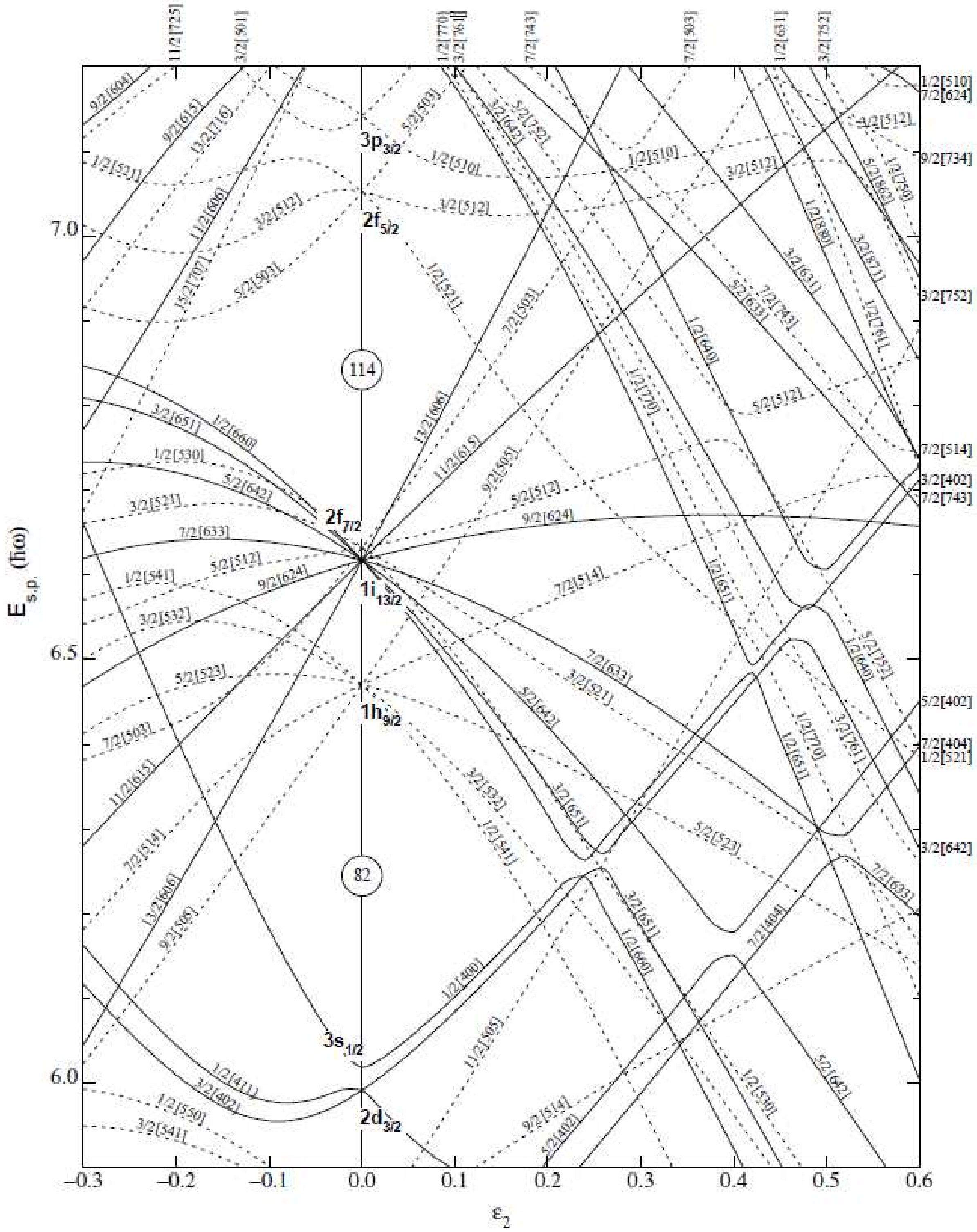

Figure 2.3: Nilsson diagram for proton (Z $\sim$ 82) single particle energy states as a function of axial deformation parameter ϵ_2 (ϵ_2=δ). Solid and dashed lines represent positive and negative parity orbitals, respectively [7].

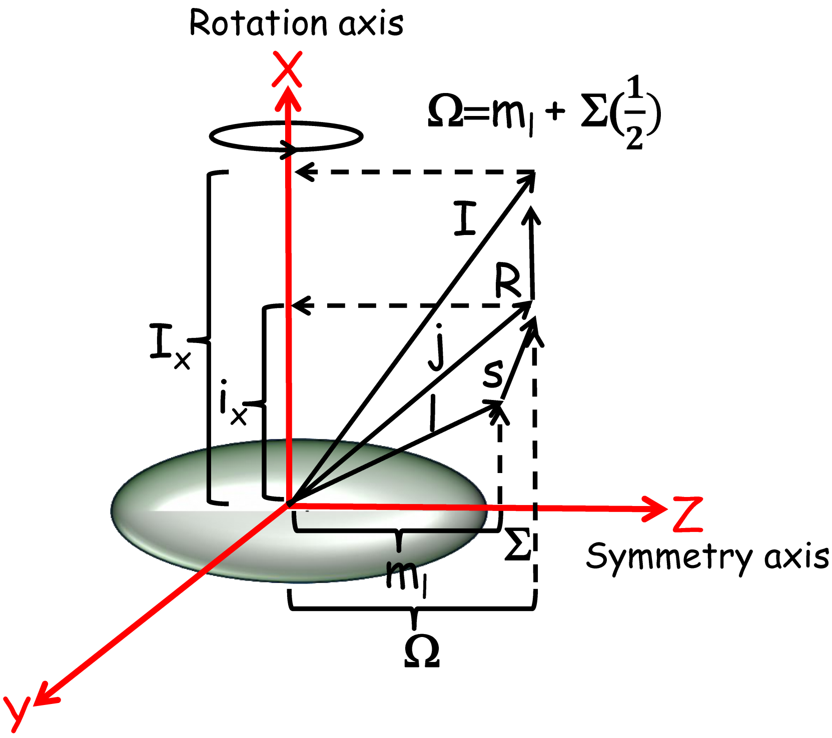

Figure 2.4: Asymptotic quantum numbers m$_l$, Σ, Ω for the Nilsson model are shown

where N is the principal quantum number, Ω is projection of single-particle angular momentum on the symmetry axis (z), m_l is projection of the orbital angular momentum on the symmetry axis and n_z is number of oscillator quanta along the symmetry axis (Fig. 2.4. The z-projection of the total angular momentum of the particle satisfies

$$\Omega = (m_l \pm \frac{1}{2}), \tag{2.30}$$

where, $\pm\frac{1}{2}$ are the projections of the spin angular momentum. These quantum numbers are known as asymptotic quantum numbers. The z-projection of total angular momentum of the particle (Ω) and the parity π are the only two good quantum numbers for a nucleus with large deformation. One of the features in Nilsson model is that the 2j+1 fold degeneracy of the shell model states are lifted and each level splits into (2j+1)/2 number of states. Each level has only two fold degeneracy $\pm\Omega$.

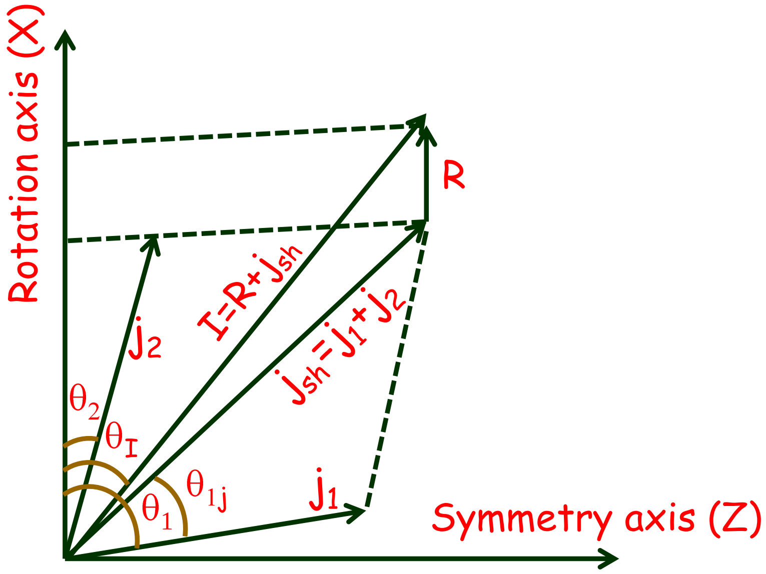

Figure 2.5: Schematic diagram of the shears mechanism in the principal axis cranking picture

angular momentum ($\overrightarrow{R}$) with the shears angular momentum ($\overrightarrow{j_{sh}}$)[17, 18, 19]. The level energy of an MR band of spin I can be expressed as

$$E(I) = E(core) + E(shears) + constant.$$

Where,

$$E(core) = \frac{R^2\,(\mathrm{I},\,\theta_1,\,\theta_2)}{2J(I)}$$

is the contribution to the total energy E(I) from core rotation, and

$$E(shears) = v_2 P_2(cos(\theta_1 - \theta_2))$$

is the shears energy due to the interaction between the shear blades $\overrightarrow{j_1}$ and $\overrightarrow{j_2}$. The particle and hole angular momenta $\overrightarrow{j_2}$ and $\overrightarrow{j_1}$ make angle θ_2 and θ_1 with respect to the rotational axis $\hat{x}$. The reduced transition probabilities of dipole ($B(M1)$) and quadrupole ($B(E2)$) transitions, with the classical approximation for Clebsch-Gordon coefficients, can be written as [18, 19, 20, 21, 22],

$$B(M1) = \frac{3}{8\pi}[j_1 g_1^* sin(\theta_1 - \theta_I) - j_2 g_2^* sin(\theta_I - \theta_2)]^2$$

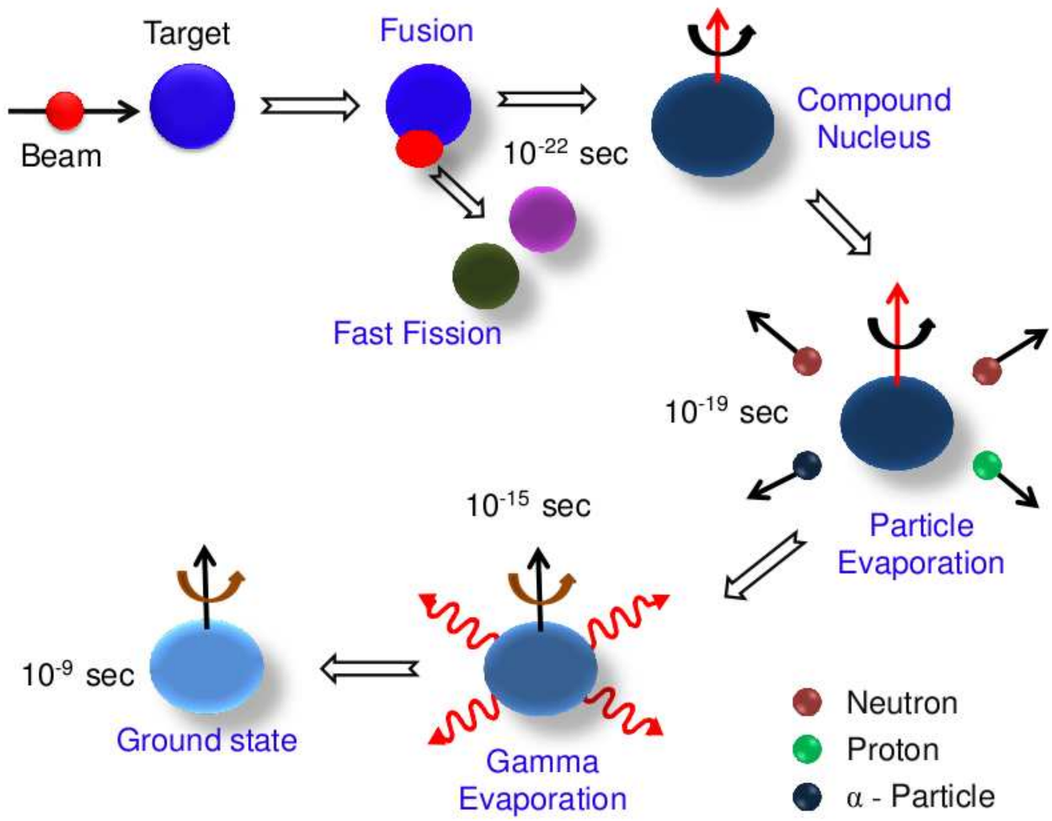

Figure 3.1: Schematic diagram of fusion evaporation reaction. This figure is taken from Ref. [1].

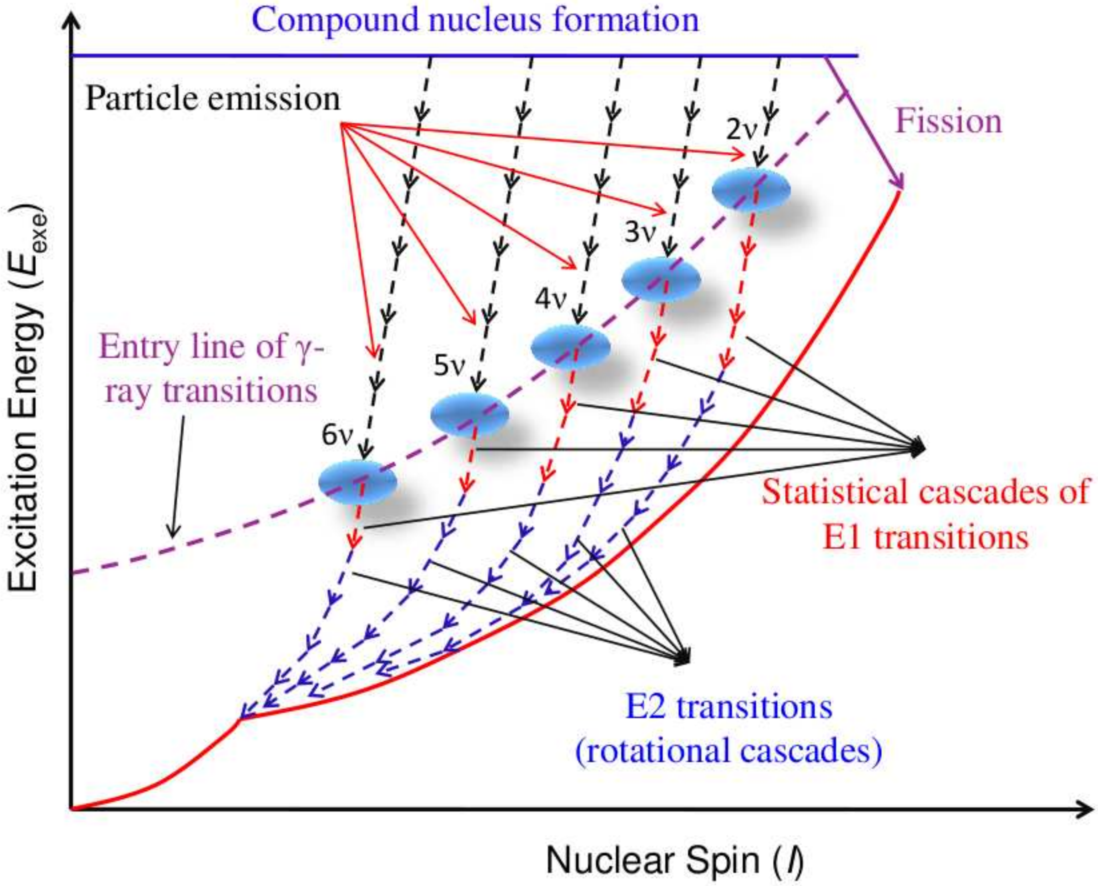

Figure 3.2: Excitation energy as a function of nuclear spin is shown. This figure is taken from Ref. [1].

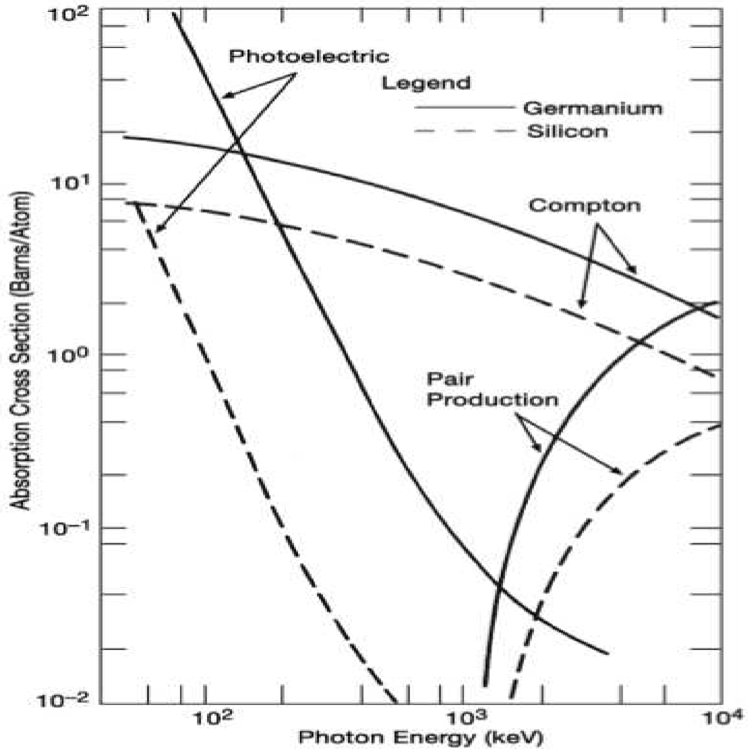

Figure 3.3: Cross section for each of the three types of γ-ray interactions in Ge (Z = 32) and Si (Z = 14) as a function of γ energy. This figure is taken from Ref. [3].

3.2 γ Ray Detection

In a fusion-evaporation reaction, the compound nucleus, in an excited state below the particle separation threshold, decays predominantly through the emission of γ rays until it reaches to the ground state. In this way, the compound nucleus and/or residual nucleus decay through mainly γ rays before reaching to the ground state. The gamma rays interact with material by three major processes, photoelectric effect, Compton scattering and pair production. In all the three interaction mechanisms gamma ray deposits its energy either completely or partially and the electrons inside the material takes this energy. In a detector medium these energetic electrons ultimately generate an electric pulse which is proportional to the energy deposited by the gamma ray.

Figure 3.4: Clover HPGe (left) and LEPS HPGe (right) detector at Laboratory.

3.2.1 Photoelectric Effect

The most desirable interaction to obtain the full energy of gamma transition is the photoelectric effect. In the photoelectric effect, the γ-ray photons interact with the bound atomic electrons and transfer full energy to the electrons. Due to the absorption of energy the bound electron emits with kinetic energy E_e, such that,

$$E_e = E_\gamma - E_b \tag{3.7}$$

Where E_γ is the γ-ray energy and E_b is the electron binding energy. The dependence of the photoelectric cross section with the energy of the incident γ ray is shown in Fig. 3.3 [3]. The photoelctric effect cross-section decreases with the increase of the γ-ray energy. Along with the energy dependence, the photoelctric cross-section also depends on the atomic number (Z) of the interacting material which can be calculated using born aproxiamtion for non-relativistic case. It can be shown that the dependence of the photoelectric effect cross-section (σ_{photo}) on Z follows the equation

$$\sigma_{photo} \propto Z^n,$$

where n varies from 4 to 5 over the γ-ray energy region of interest.

Figure 3.5: VENUS setup at VECC.

packing (Ge-Ge distance of about 0.2 mm). The detector is housed inside an aluminium vacuum chamber. A picture of a Clover detector is shown in Fig. 3.4. Due to the thick aluminium cover in front of the crystals the detection efficiency for low energy γ rays (E_γ<100 keV) is reduced. The clover detectors, used in the present thesis work, were equipped with Anti-Compton shields (ACS) consisted of Bismuth Germanate ($Bi_4Ge_3O_{12}$) scintillation detectors (BGO). The ACS detects the Compton scattered γ rays which escape from the HPGe crystals after depositing a partial energy to the HPGe detector. The energy signals of such γ rays are vetoed out and are not registered as they contribute to the Compton background. This way, the Compton background is minimized. In a clover HPGe detector full energies of some of these Compton scattered events could be recovered by the process called addback. In this addback process, the energy deposited by a γ ray in the neighboring crystals of a clover detector, following a Compton scattering event, are added up in the offline analysis. Therefore, the partial energy deposition in two (or more) crystals of a clover detector detector are added up to give full energy peak, which would otherwise contribute to the Compton background. In this way, a double advantage of an increase of full energy peak as well as a decrease of Compton background is achieved. The "addback factor" can be expressed as the ratio of the total count of a peak in a clover detector after doing "addback" (addition of photo peaks of four crystals and additional count in the photo peak due to "addback") to the sum of the photoelectric counts of the four individual crystals of the clover.

$$\text{Addback factor} = \frac{\text{Addback counts of the clover detector}}{\text{Sum of photoelectric counts of the 4 crystals}}$$

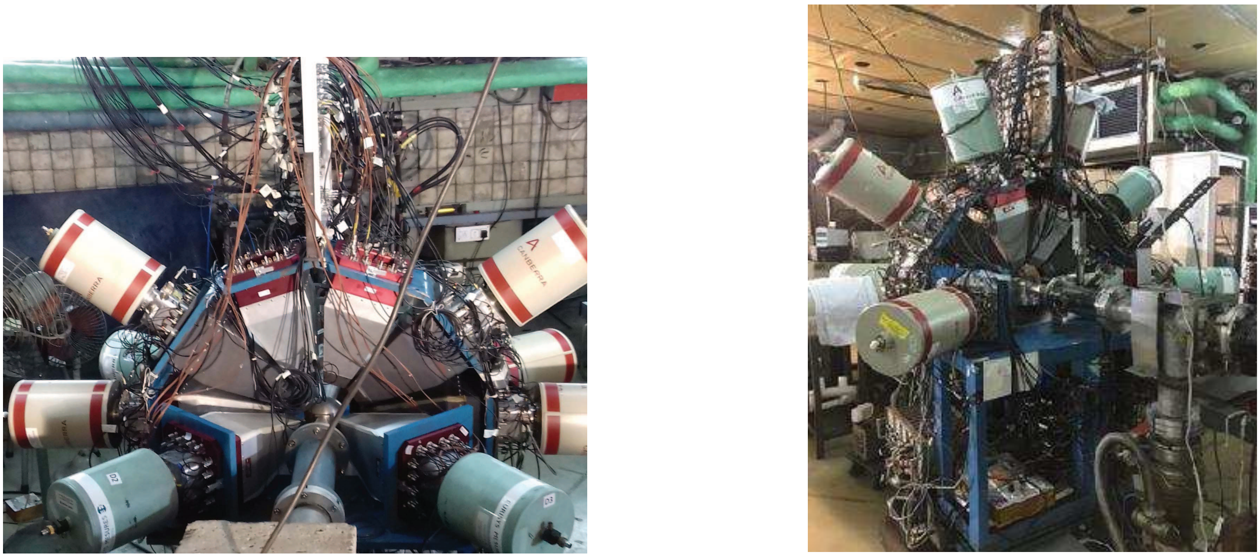

Figure 3.6: INGA setup at VECC (Phase I (left) and II (right)).

This addback factor is close to unity for low energy γ rays because of the large photo electric cross-section for such γ rays. But it increases with energy as the photo electric cross section decreases (but Compton scattering cross section almost remains same) and attains a maximum value ~ 1.5 at about 1.4 MeV γ ray.

3.3.2 Low Energy Photon Spectrometer (LEPS)

Low Energy Photon Spectrometer (LEPS) is a planer HPGe detector (Fig. 3.4) which is specially designed for the detection of low energy transitions with higher efficiency compared to the clover detector. The LEPS detector used in this work has a planar HPGe crsytal which has four electronically separated segments and a very thin Berilium window at the entry face. The thin Berilium window compared to the thick aluminium cover for clover detector allows the low energy γ transitions to enter the detector medium with much less attenuation. However, due to its small size, the effciency of the LEPS detector is very poor for high energy ($>\sim$ 400 keV) γ rays.

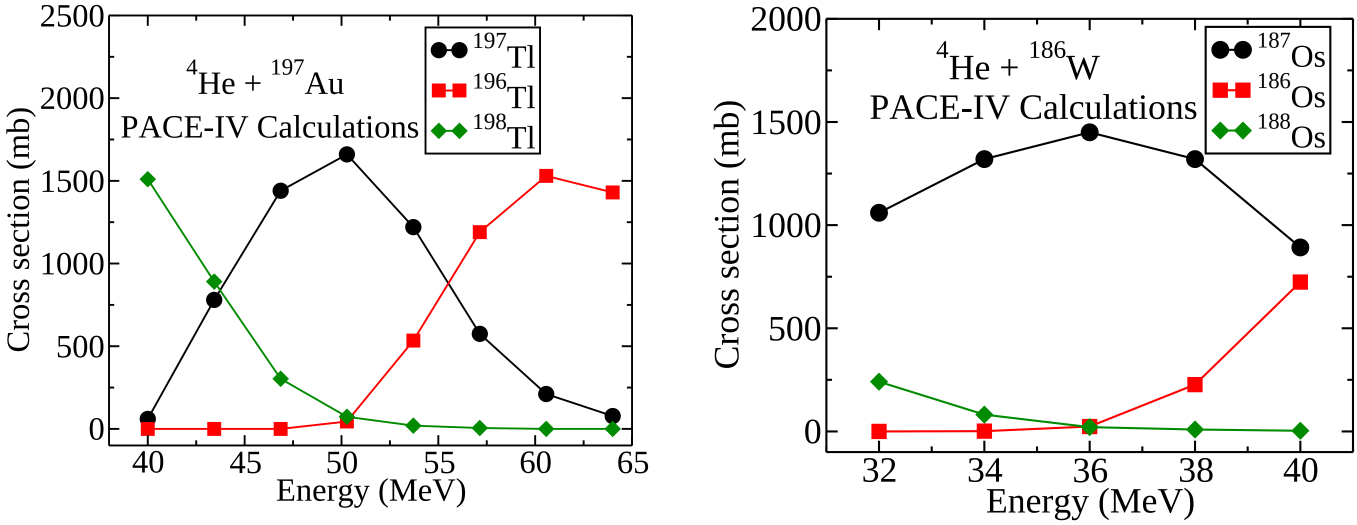

Figure 3.7: The excitation function of ^{4}He+^{197}Au (left) and ^{4}He+^{186}W (right) reactions as calculated from PACE-IV.

3.4 Experimental Setups and Performed Experiments

In this thesis work, the γ ray spectroscopic studies have been performed using the VECC array for NUclear Spectroscopy (VENUS) and Indian National Gamma Array (INGA) at Variable Energy Cyclotron Centre, kolkata. The detail discussions about the experimental setups have been discussed below:

3.4.1 VECC array for NUclear Spectroscopy (VENUS)

VECC array for NUclear Spectroscopy (VENUS) [6] at VECC is an array of Clover HPGe detectors, which consisted of 6 Compton-suppressed Clover detectors (at the time of the experiment) and arranged in four different angles (θ) in the median plane (ϕ=0° and 180°). Two detectors each were placed at θ = 150° and 90° angles with respect to the beam direction and the other two were placed at 45° and 55° angles (shown in Fig. 3.5). VME-based data acqusition system was used for VENUS with conventional electronics at the time of the experiment performed in the present thesis work. The data were collected in the list-mode format which were further analysed in the offline.

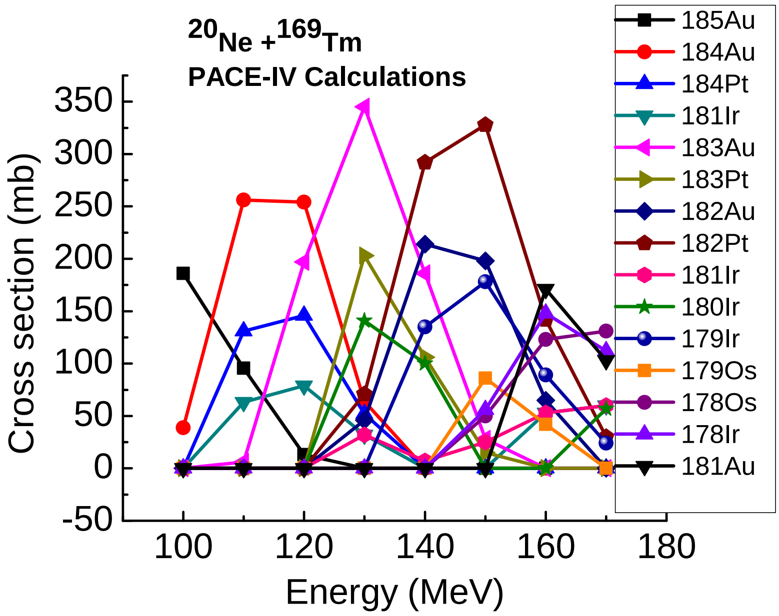

Figure 3.8: The excitation function of ^{20}Ne+^{169}Tm reaction as calculated from PACE-IV.

about 55° with respect to the beam direction. The gamma rays were detected using the VENUS setup [6, 9] as described above. The energy and efficiency calibration of all the detectors were done using the known radioactive sources of ^{133}Ba and ^{152}Eu. The γ-γ coincidence data were recorded using VME based data aqusition system in the list-mode format. The time-difference data between the master gate and the RF signal of cyclotron was also recorded in a time to amplitude converter (TAC) module. Also, experimental data in singles mode were taken for the intensity and angular distribution measurements of the γ rays.

3.4.4 Experiment 2 (^{183}Au)

The heavy-ion induced fusion evaporation reaction ^{169}Tm(^{20}Ne, 6n)^{183}Au at 146 MeV has been used to populate the excited states of the neutron deficient nucleus ^{183}Au. The beam was delivered from the K-130 cyclotron at VECC. A self supporting target of thickness ~23 mg/cm^2 has been used for this experiment. The excitation function, as calculated from the PACE-IV code, is shown in Fig. 3.8. It shows that several nuclei have been populated in this reaction and the population cross section of ^{183}Au is maximum at the beam energy 130 MeV which can be achived in the middle of the target by the incident beam energy of 146 MeV. In this experiment INGA phase II setup with eight Compton-suppressed clover and two LEPS detectors were used

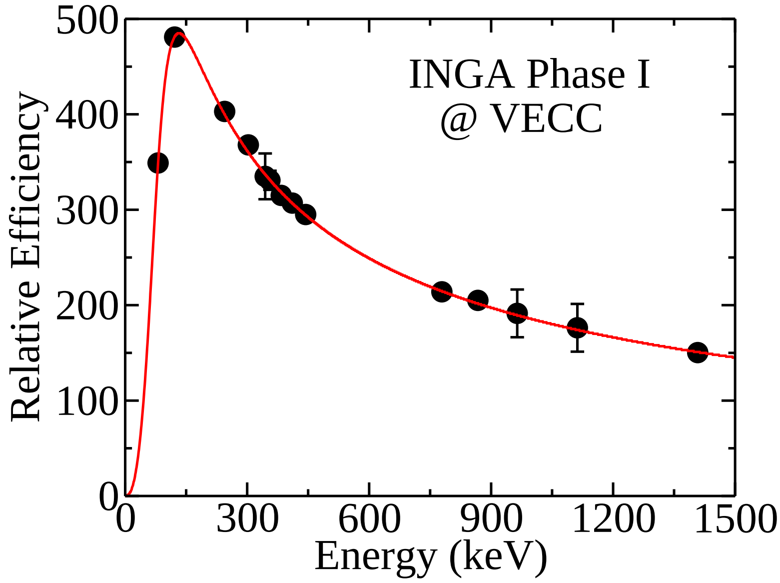

Figure 3.9: Relative efficiency of INGA phase I array at VECC.

to detect the gamma rays. The energy and efficiency calibration of all the detectors have been done using known radioactive source of ^{133}Ba and ^{152}Eu. The γ-γ coincidence data were recorded in two- and higher-fold coincidence mode with time stamp in a fast (250 MHz) digital data acquisition system based on Pixie-16 modules of XIA [8].

3.4.5 Experiment 3 (^{187}Os)

The excited states in heavier Os isotopes can only be populated using light-ion induced reaction or deep inealstic scattering. In the present study, the excited states of ^{187}Os were populated by the alpha-induced fusion evaporation reaction ^{186}W(^{4}He, 3n)^{187}Os at 36 MeV of beam energy delivered from the K-130 cyclotron at VECC. The excitation function, calculated from the PACE-IV code, is shown in Fig. 3.7. It shows that the population cross section of ^{187}Os is $\sim$ 96% of the total reaction cross section at the beam energy of 36 MeV. A stack of 3 ^{186}W foils, each of 300μg/cm^2 thick on 20μg/cm^2 ^{12}C backing, was used as target which was placed at an angle $\sim$ 55° with respect to the beam direction. The γ rays were detected using the INGA phase I setup [7] with seven Compton-suppressed clover HPGe detectors and one LEPS detetctor. The energy and efficiency calibrations of clover detectors were done using radioactive ^{133}Ba and ^{152}Eu sources. Two and higher fold data were recorded using PIXIE-16 digitizer based system devoloped by UGC-DAE-CSR Kolkata centre [8] with the requirement

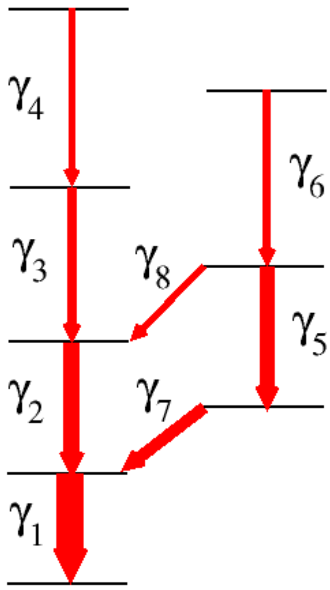

Figure 3.10: Example of level scheme for γ-ray coincidence demonstration.

of γ-γ coincidence master trigger. Some of the data files were recorded in singles mode for the intensity measurement of the γ rays.

3.5 Data Analysis Technique

The raw data files were sorted and analysed using Linux Advanced MulitParameter System (LAMPS) [10], IUCPIX [8], RADWARE [11] and INGASORT [12] analysis packages. The data from each crystal of clover detectors were calibrated and gain matched and addback data were generated on event-by-event basis. These addback data were used to generate several γ-γ matrices and a three dimensional γ-γ-γ cube for further analysis. Similarly, the data from the LEPS detectors were used to generate a LEPS vs. Clover asymmetric matrix for further analysis. The level schemes of the nuclei of interest have been constructed using the coincidence relation of the γ rays and their intensity arguments. The spin and parity of a nuclear level have been assigned from the multipolarity (λ) and type (E/M) of the γ ray decaying from that level. The measurements of directional correlation from the oriented states (DCO) ratio [13], angular distribution and the polarization asymmetry ratio (along with the linear polarizatioom,

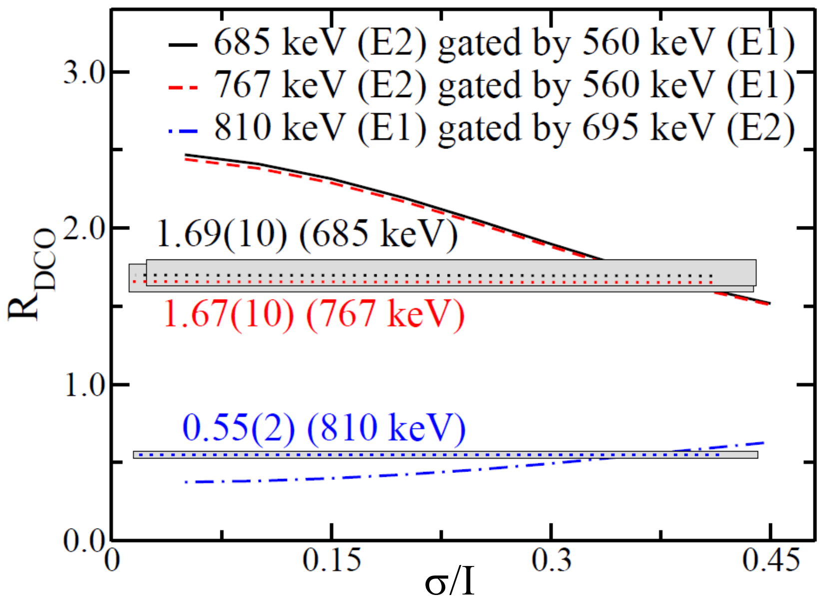

Figure 3.11: Theoretical (solid, dashed and dashed-dot lines) and measured (dotted lines with shaded regions encompass the uncertainties) R_{DCO} values for different values of σ/I for the three stretched γ rays. The σ/I values for the present experiment were determined from the crossing point of the theoretical lines and the experimental ones.

P) were used to determine the λ and E/M of the γ rays. The detail discussions on different data analysis techniques are discussed below.

3.5.1 Calibration and Efficiency

The energy calibration represents the relation between the channel number, as recorded by the data acquisition, and the corresponding energy of the γ-ray peak in the spectrum. This can be determined using the known γ-ray energies from the radioactive sources. The energies and channel numbers of the known γ-lines can be fitted using the following polynomial.

$$E_\gamma = \sum_{i=1}^{n}(a_0 + a_i x^i) \tag{3.11}$$

where the coefficients a_0 and a_i are known as the calibration constants and n represents the order of the polynomial. The energy of an unknown photopeak can be obtained from the corresponding channel number using the calibration constants. In the present thesis work, ^{152}Eu and ^{133}Ba radioactive sources have been used for to determine the calibration constants

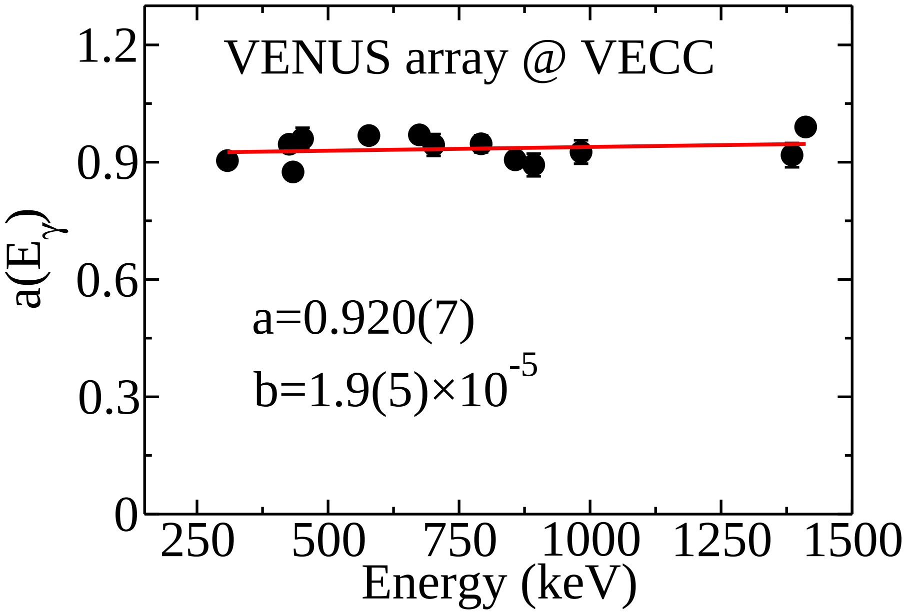

Figure 3.12: Asymmetric correction factor $a(E_\gamma)$ for the detectors at 90° (VENUS). solid line is the linear fit of the experimental data points. The values of coefficients, a and b, are also given.

from second order polynomial using the following equation:

$$E_\gamma = a_0 + a_1 x + a_2 x^2 \tag{3.12}$$

where E_γ and x are the energy and channel number, respectively, corresponding to the incident γ ray while a_0, a_1 and a_2 are the calibration parameters. The values of these parameters have been obtained from the fitting of the known-energy source data.

In order to determine the intensity of a gamma ray, one needs to know the efficiency of the detection system. In γ-ray spectroscopic study, the relative intensities of the γ rays are essential to build the level scheme and also to determine the branching ratios. The efficiency of the γ rays is energy dependent and therefore, the relative efficiencies of the γ rays as a function of the γ-ray energy need to be determined. The relative efficiency curves as a function of γ-ray energy of INGA and VENUS array has been obtained using ^{152}Eu source. Similarly, the relative efficiency of the LEPS detector has been obtained using the known low energy γ rays from ^{133}Ba source. The experimental data were fitted with the following equation, using the "effit" program of the RADWARE package [11].

$$\ln(\epsilon) = \{(A + Bx + Cx^2)^{-G} + (D + Ey + Fy^2)^{-G}\}^{-1/G} \tag{3.13}$$

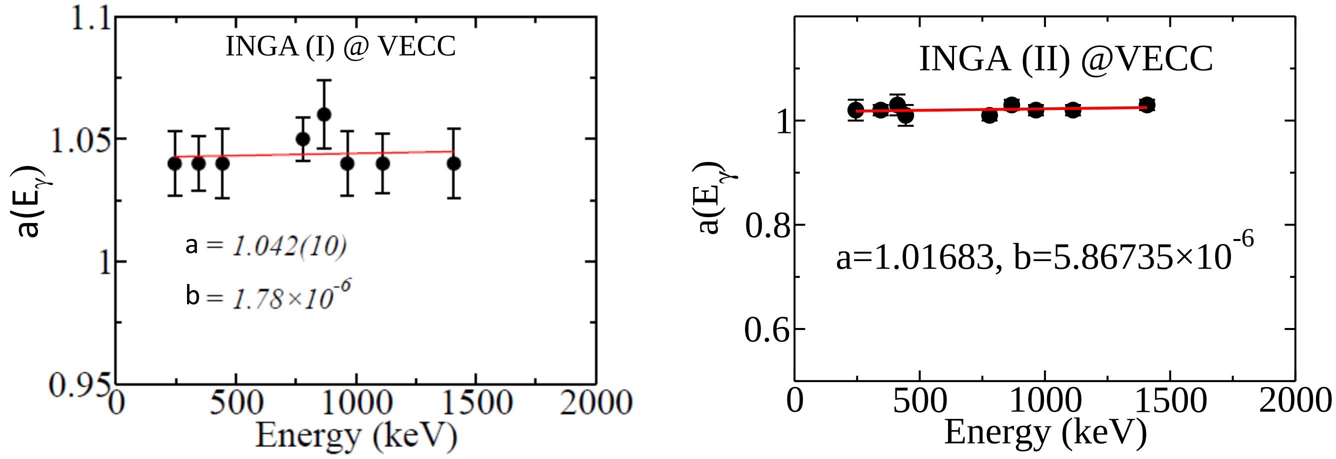

Figure 3.13: Asymmetric correction factor $a(E_\gamma)$ for the detectors at 90° (INGA I (left) and INGA II (right)). solid line is the linear fit of the experimental data points. The values of coefficients, a and b, are also given.

where ϵ is the efficiency, $x = \ln(\frac{E_\gamma}{100})$, $y = \ln(\frac{E_\gamma}{1000})$ and E_γ is the γ-ray energy in keV. A, B, C, D, E, F and G are the fitting parameters. A typical relative efficiency curve, obtained from the present work, is shown in Fig.3.9.

3.5.2 γ Ray Coincidence Relation and Intensity Arguments

The level scheme of a nucleus is a pictorial representation of its excited states. Construction of the level scheme is the primary building block to understand the structure of a nucleus. As mentioned above one of the methods to construct a level scheme is the coincidence relation between the γ rays. This can be performed by analysing the gated spectra projected from a $\gamma - \gamma$ matrix and/or a $\gamma - \gamma - \gamma$ cube. The concept of coincidence and parallel γ rays are important for this analysis. As an example, to construct the level scheme as shown in Fig. 3.10, if one puts a "single-gate" on the γ-ray energy γ_2 in the $\gamma - \gamma$ coincidence matrix, then the gated spectrum will show the peaks at γ_1, γ_3, γ_4, γ_6 and γ_8 energies as these γ rays are in "coincidence" with γ_2. But the γ rays γ_7 and γ_5 will not appear in that spectrum as these two γ rays are not in coincidence with γ_2. Therefore, the γ_2 is "parallel" with γ_7 and γ_5. Similarly, if one puts a "double-gate" on the γ-ray energies γ_7 and γ_5 in the $\gamma - \gamma - \gamma$ coincidence cube, then the gated spectrum will contain only the γ_1 and γ_6 peaks which are in coincidence with both

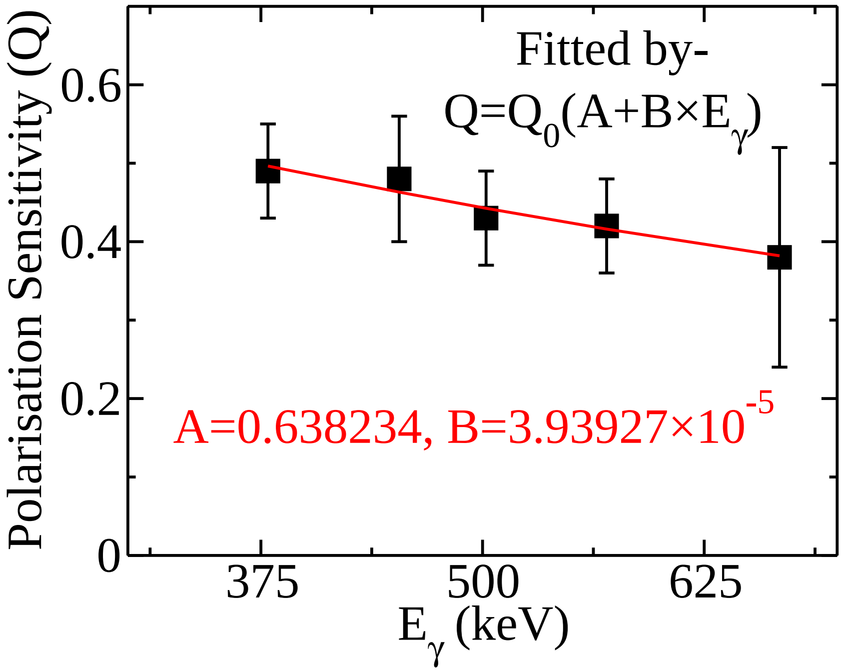

Figure 3.14: Polarization Sensitivity of INGA (phase II) array at VECC

the gating γ rays γ_7 and γ_5. Therefore, by putting "double-gate" on a $\gamma - \gamma - \gamma$ cube, one can uniquely identify a band. However, the number of counts in a "double-gated" spectrum is much less than a "single-gated" spectrum. In this way by analysing various single- and double-gated coincidence spectra, the level scheme of a nucleus can be established. In the fusion evaporation reaction, the CN is produced at high excitation energy and high angular momentum and since the residual nucleus (which is the nucleus of interest) retains much of its angular momentum, but loses a large amount of excitation energy because of particle evaporation, the entry point remains close to the yrast line and its decay follows mostly the yrast line. Moreover, the produced CN and, hence, the residual nucleus has a large distribution in angular momentum. Therefore, the intensity of the γ rays increases with the decrease of angular momentum and hence, with the excitation energy of the residual nucleus. This implies that the low-lying γ rays will have larger intensities. So, in order to maintain the proper ordering of the γ rays in the level scheme, the intensity balance are checked at each energy level such that the feed-in intensity of a level is lower (or may be similar but not larger) than the feed-out intensity.

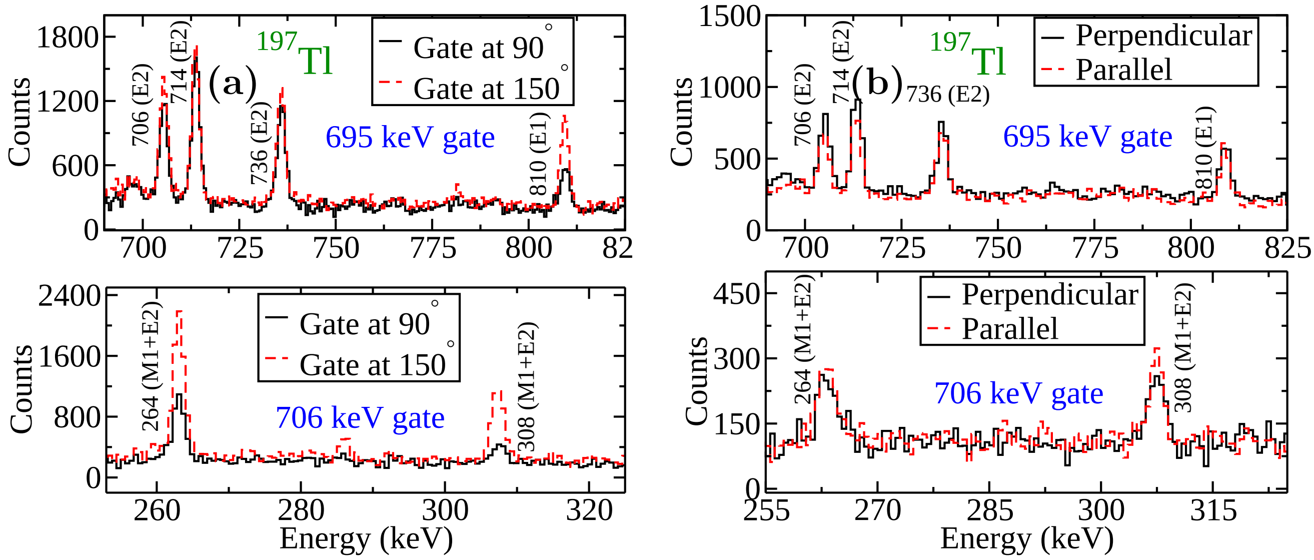

Figure 3.15: Typical gated spectra of DCO ratio (a) and polarization asymmetry (b) measurements in ^{197}Tl.

3.5.3 Angular Distribution of γ-ray Transition

In a heavy-ion fusion evaporation reaction the linear momentum of the projectile brings the orbital angular momentum in to the compound nucleus and, hence, the residual nucleus (the nucleus of interest) is aligned in a particular (perpendicular) direction. Now, the γ-rays emitted from such aligned states follow angular distributions depending on their multipolarities [14, 15]. Therefore, by measuring the angular distribution of the γ-rays, their multipolarities can be determined, and hence, the angular momentum (spin) of the initial nuclear state, from which the γ ray is being emitted, if the spin of the final state is known. In case of complete alignment of the nuclear excited states, the angular distribution of γ-rays is expressed as [16, 17]:

$$W(\theta) = \sum_{k=0}^{\lambda} a_k^{max} P_k(\cos\theta) \quad \text{where k = 0, 2, 4,...} \tag{3.14}$$

where $P_k(\cos\theta)$ are the Legendre polynomials and a_k^{max} are the angular coefficients for the completely aligned nuclear state. In the actual cases, the nuclear oriented states are partially aligned. Therefore, the angular coefficients are expressed as

$$a_k(I_i L_1 L_2 I_f) = \alpha_k(I_i) a_k^{max}(I_i L_1 L_2 I_f) \tag{3.15}$$

Where $\alpha_k(I_i) = \frac{\rho_k(I_i)}{B_k(I_i)}$ are the attenuation coefficient of alignment. $\rho_k(I)$ is the degree of alignment of $I-$spin state and is expressed as,

$$\rho_k(I) = \sqrt{2I+1} \sum_m (-1)^{I-m} (ImI-m|k0) P_m(I) \tag{3.16}$$

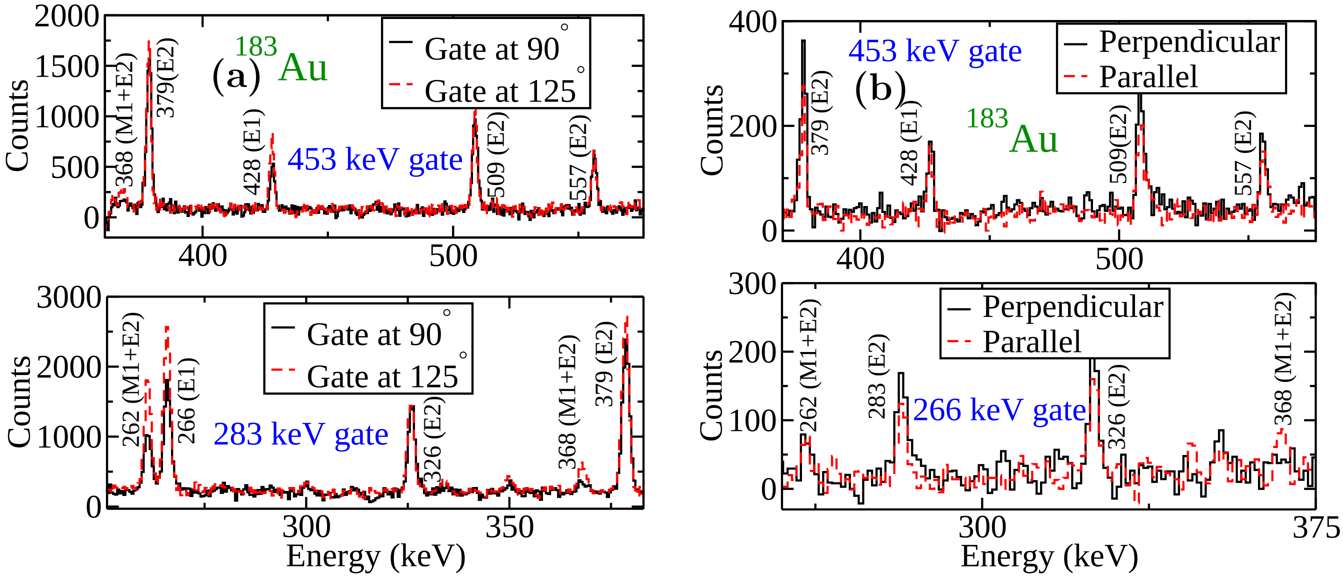

Figure 3.16: Typical gated spectra of DCO ratio (a) and polarization asymmetry (b) measurements in ^{183}Au.

measurement, an angle-dependent asymmetric $\gamma - \gamma$ matrix (DCO matrix) was formed using the coincidence data from the 150° (θ_1) detectors and the 90° (θ_2) detectors in the VENUS array setup and for the INGA array, θ_1 and θ_2 were 125° and 90°, respectively. The R_{DCO} of a γ ray (γ_1) is obtained from the ratio of its intensities (I_γ) gated by a transition (γ_2) with known multipolarity at the above two angles from the DCO matrix. This ratio is obtained from the experimental data using the following relation:

$$R_{DCO} = \frac{I_{\gamma_1} \text{ at } \theta_1, \text{ gated by } \gamma_2 \text{ at } \theta_2}{I_{\gamma_1} \text{ at } \theta_2, \text{ gated by } \gamma_2 \text{ at } \theta_1} \tag{3.18}$$

In the present geometry of VENUS and INGA arrays, theoretical value of DCO ratio of a γ transition gated by the same multipolarity transition is unity whereas, DCO ratio of a pure dipole transition gated by a stretched quadrupole transition is ~ 0.5 and that of stretched quadrupole transition gated by pure dipole transition is ~ 2. Representative gated spectra for DCO ratio measurements in ^{197}Tl, ^{183}Au and ^{187}Os nuclei have been shown in Fig. 3.15, 3.16 and 3.17.

3.5.5 Linear Polarization (P) and Polarization Asymmetry (Δ_{PDCO})

The geometrical advantage of a clover detector has been used as a polarimeter to measure the polarization asymmetry (Δ_{PDCO}) of a γ ray. Out of the four crystals of a clover, any one them

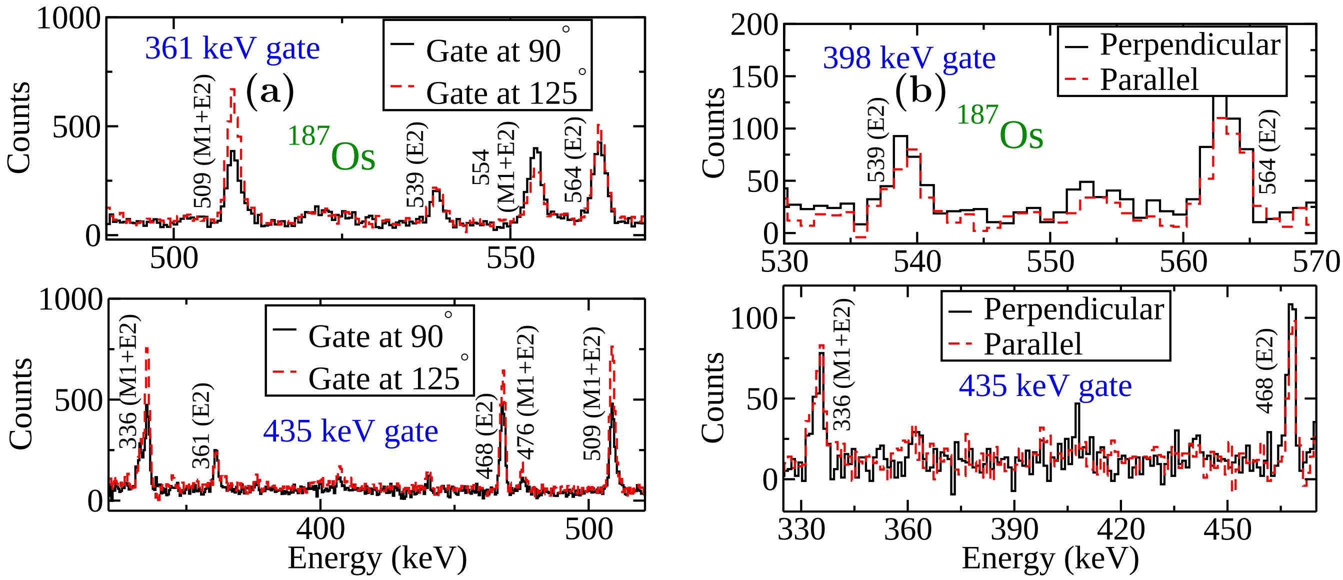

Figure 3.17: Typical gated spectra of DCO ratio (a) and polarization asymmetry (b) measurements in ^{187}Os.

acts as a scatterer and the two adjacent crystals act as analyzers for the Compton scatter of a γ ray inside the detector. The type (E/M) of a transitions can be obtained from the polarization asymmetry measurement [19, 20]. The polarization asymmetry (Δ_{PDCO}) is defined as

$$\Delta_{PDCO} = \frac{a(E_\gamma)N_\perp - N_\parallel}{a(E_\gamma)N_\perp + N_\parallel} \tag{3.19}$$

where, $N_\perp$ and $N_\parallel$ are the perpendicular and parallel scattered counts of a γ-ray transition in the 90° detectors with respect to the reaction plane. $a(E_\gamma)$ is a geometrical correction factor for the array. To measure $N_\perp$ and $N_\parallel$, two asymmetric matrices of $N_\perp$ vs. all detectors and $N_\parallel$ vs. all detectors were generated. The asymmetric response of the clover segments was corrected by the factor $a(E_\gamma)$ $(=\frac{N_\parallel}{N_\perp})$ which needs to be determined for an unpolarized radioactive source. In the VENUS experment, we have used the decay radiations (during beam-off period) from the target foil to estimate the exact value of $a(E_\gamma)$ in order to avoid any uncertainty due to the positioning of external sources. The values of $a(E_\gamma)$ are shown in Fig. 3.12 along with the fit using the equation, $a(E_\gamma) = a + bE_\gamma$. The fitting gives the values of the coefficients as, $a = 0.920(7)$ and $b = 1.9(5) \times 10^{-5}$. Positive and negative values of the polarization asymmetry Δ_{PDCO} indicate electric (E) and magnetic (M) types of the transitions, respectively. But, in the experiment 2 and 3, ^{152}Eu radioactive source has been used to obtain $a(E_\gamma)$ as shown in Fig. 3.13 due to the lack of enough radioactive decay gamma rays. Typical gated spectra for polarization asymmetry measurements in ^{197}Tl, ^{183}Au and ^{187}Os nuclei are shown in Fig. 3.15, 3.16 and 3.17. The linear polarization (P) can be obtained from the measured polarization

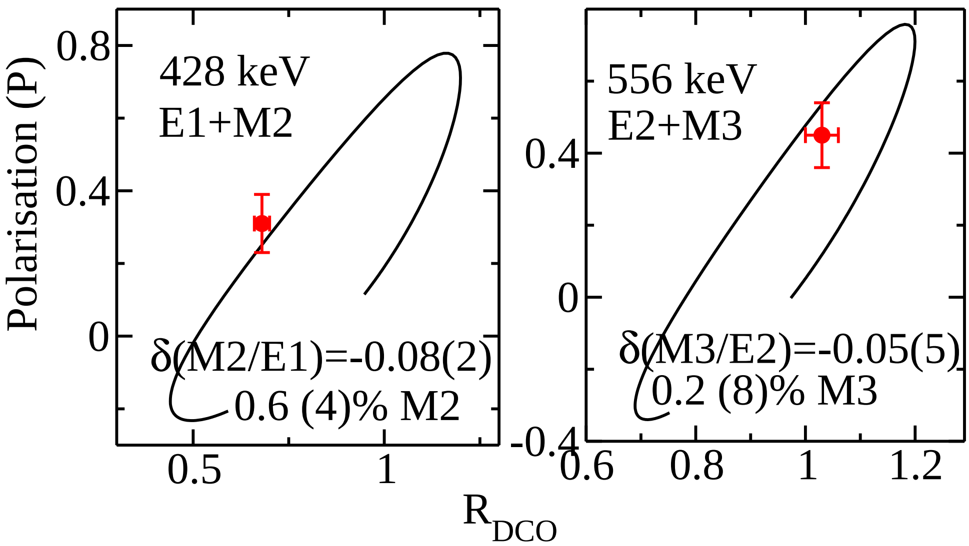

Figure 3.18: The experimental (symbol) and calculated (solid line) values of R_{DCO} and P of two of the transitions in ^{183}Au. The 557 keV is a known $E2$ transition decaying from $37/2^+$ to $33/2^+$ in band (4) and 428 keV is a known $E1$ transition from $13/2^+$ to $11/2^-$ between band (4) and band (1). These transitions show very small mixing ratios (δ) as they should be.

asymmetry (Δ_{PDCO}) as:

$$P = \frac{\Delta_{PDCO}}{Q} \tag{3.20}$$

Where, Q is the polarization sensitivity. It depends on the incident γ-ray energy and the geometry of the polarimeter. The polarization sensitivity can be expressed as:

$$Q(E_\gamma) = (A + BE_\gamma)Q_0(E_\gamma) \tag{3.21}$$

with

$$Q_0(E_\gamma) = \frac{\alpha + 1}{\alpha^2 + \alpha + 1} \tag{3.22}$$

where $\alpha = E_\gamma / m_e c^2$, E_γ is the incident γ-ray energy and $m_e c^2$ is the electron rest mass energy. The parameters A and B, and $Q(E_\gamma)$ can be experimentally determined using γ-rays with known polarizations. The polarization sensitivity (Q) has been obtained for the INGA array (experiment 2) using the known stratched E2 transitions as shown in Fig. 3.14.

The mixing ratio δ can be obtaind for a mixed transition from the simultaneous measurement of DCO ratio and polarization (P) measurement. The experimental linear polarization (P) and

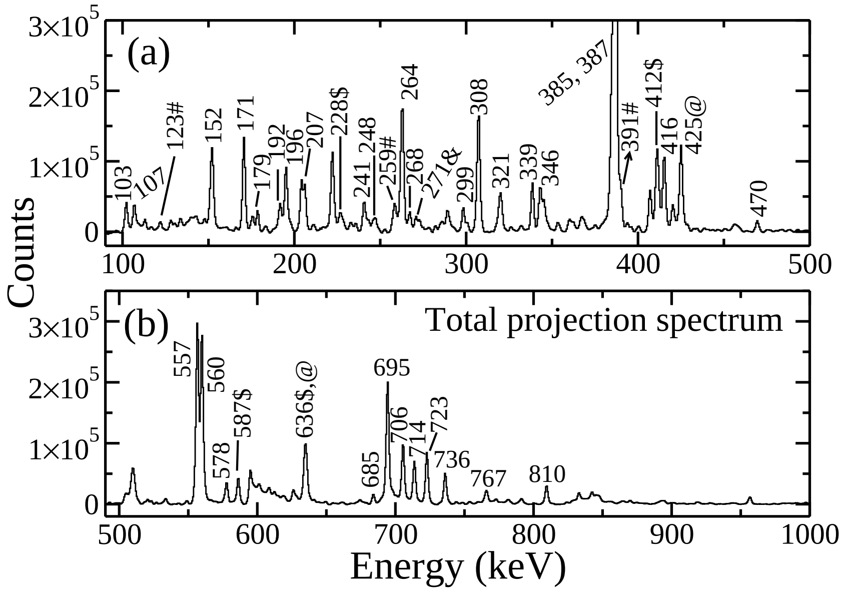

Figure 4.1: The total projection spectrum from the $\gamma - \gamma$ matrix for the lower (a) and the higher (b) energy parts. The known γ-ray peaks from different nuclei are shown. The peaks with no symbol are the known peaks in ^{197}Tl while the symbols correspond to #: ^{198}Tl, &: ^{196}Tl, \$: ^{198}Hg, and @: ^{196}Hg.

induced fusion evaporation reactions [12, 13, 27] with the help of a very limited number of Ge detectors. In these studies, two rotational bands, based on an 1-quasiparticle (qp) and a 3-qp configurations were reported. However, no band crossing phenomenon has been observed in any of these bands. So, the effect of the alignment of a pair of neutrons in these rotational-like bands could not be studied. It may be noted that the doubly degenerate bands in ^{195}Tl were observed after neutron alignments in the $i_{13/2}$ orbital. Apart from the $i_{13/2}$, the negative parity $f_{5/2}$, $p_{3/2}$ and $p_{1/2}$ neutron orbitals are also available near the Fermi level for the nuclei with neutron number $N > 114$. Therefore, it is important to study the higher spin states in ^{197}Tl beyond the neutron alignments in order to understand the type of band structures generated due to the neutron alignments in the positive and in the negative parity orbitals.

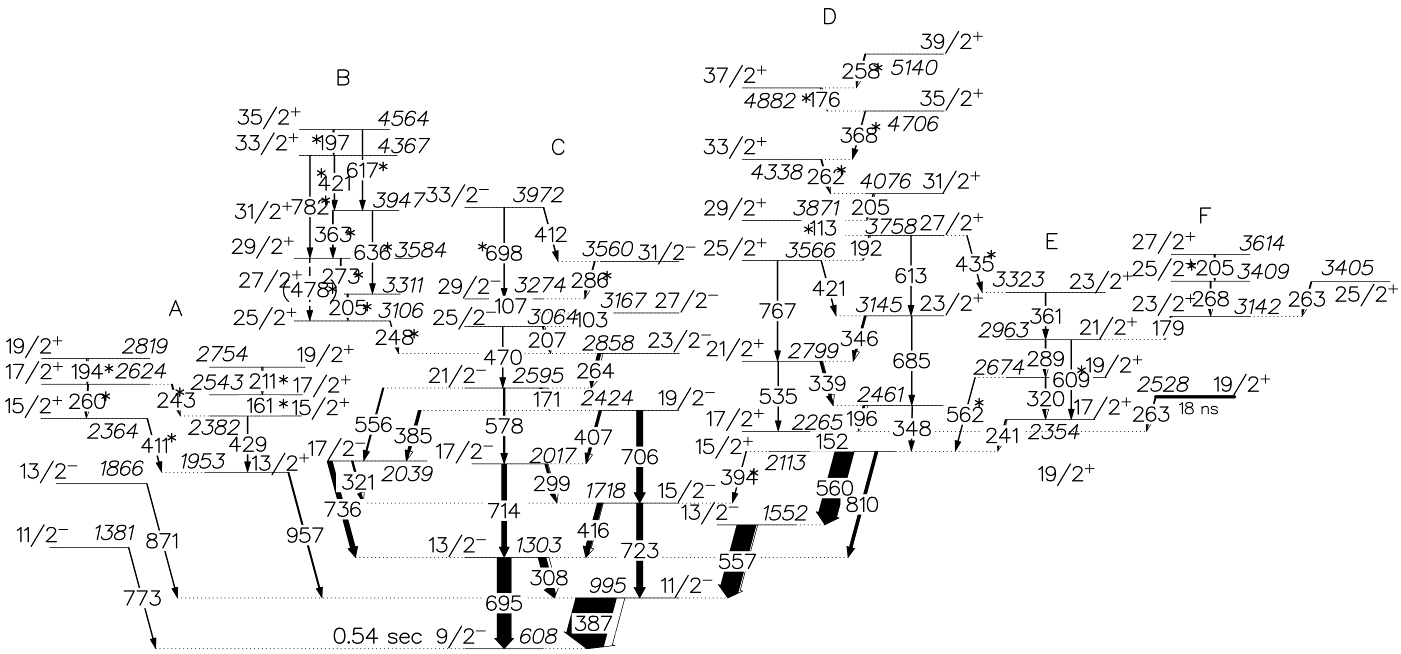

Figure 4.2: Proposed level scheme of ^{197}Tl from the present work. Levels above the 0.54-sec isomer at 608 keV are shown. The new γ transitions are marked by asterisks (*)

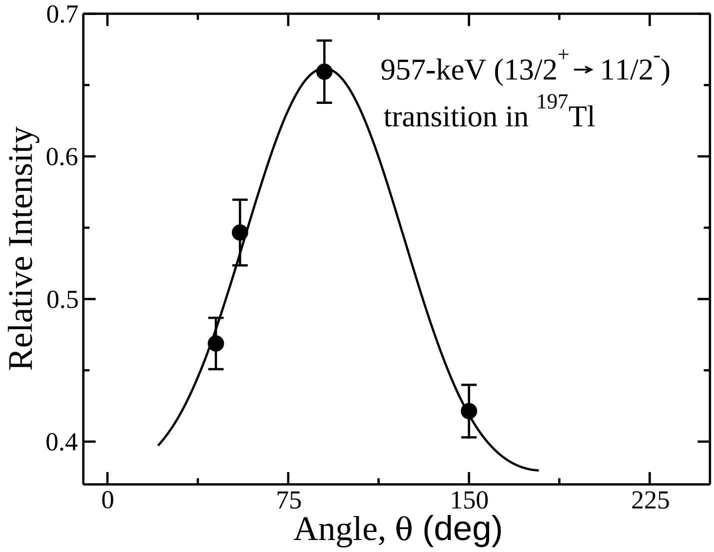

Figure 4.3: Angular distribution of the 957-keV transition in ^{197}Tl from the singles-data. The solid line is the fitted curve for a dipole transition.

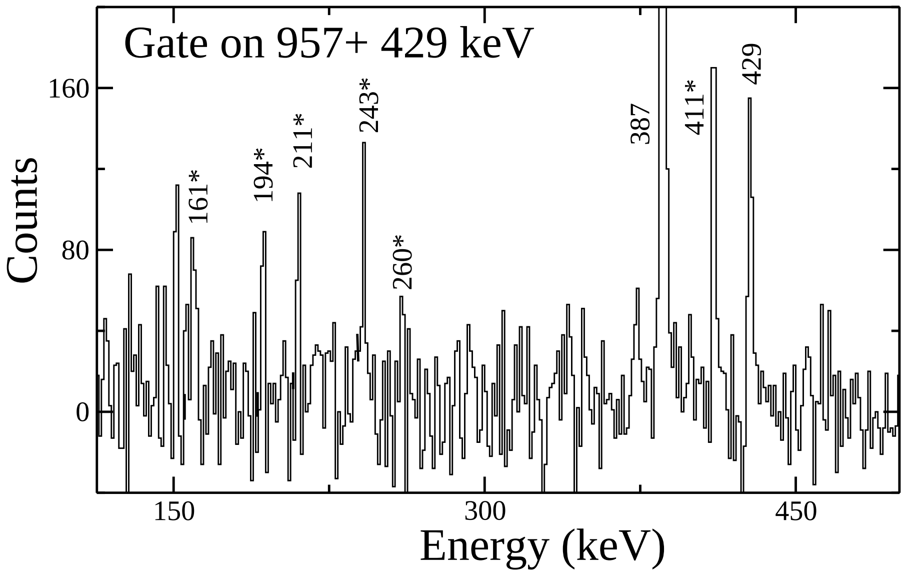

Figure 4.4: Sum-gated spectrum with gates on 957-keV and 429-keV transitions corresponding to the band-like structure A in ^{197}Tl; new γ rays are marked by asterisks (*).

a mixed ($M1 + E2$) transition (387 keV) and hence, the dipole assignment of the 957-keV γ ray was tentative. But the nature of the transition was confirmed as an Electric (E) from the Δ_{PDCO} value in the previous measurement [13]. The information about the multipolarity of the transition can be obtained from the angular distribution measurement, which could not be performed in the earlier work due to the lack of detectors at different angles. In the present work, the angular distribution measurement has been performed using the clover detectors at four different angles in the VENUS setup [30]. Data for the angular distribution measurement were taken in singles mode. The result of angular distribution measurement has been ploted in Fig. 4.3. It confirms the dipole nature of the transition. The electric (E) nature of this γ has also been confirmed in the present work from the Δ_{PDCO} measurement. Therefore, the spin and parity assignment of $13/2^+$ state has been confirmed form the $E1$ nature of the 957-keV γ-ray.

The 429-keV γ-ray, on top of the $13/2^+$ state and decaying from the 2382-keV level, was known earlier [13] but without any spin-parity assignment. In the present work, several new γ-ray transitions on top of 1953-keV and 2382-keV levels have been observed. These new γ-rays formed a single-particle like structure A. All the new γ rays are confirmed in the sum-gated spectrum with gates on 957- and 429-keV γ-rays as shown in Fig. 4.4. The R_{DCO} values of the new transitions have been obtained in the gate of pure E1 transition of 957-keV.

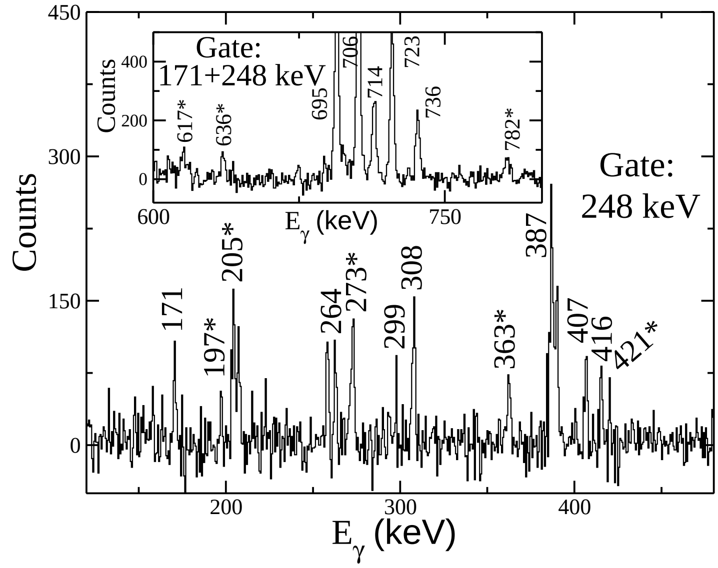

Figure 4.5: A spectrum gated by 248-keV transition showing the γ rays in band B. The higher energy γ-lines in band B are shown in the sum gated (171+248 keV) spectrum in the inset. The new γ-rays are marked by asterisks (*).

A new band B has been observed in the present work which deacays to the main rotational band C. All the new transitions of band B has been confirmed in the single gate of the 248-keV connecting transition (Fig. 4.5). The week E2 cross-over transitions of band B have been confirmed in the sum gate of 171- and 248-keV transitions. The connecting transition 248-keV has been observed in the sum-gated spectrum of Fig. 4.6 along with the other transitions of band C. The placement of the 248-keV γ-ray has been made from the fact that the 470-keV γ ray decaying from the 3064-keV, $25/2^-$ level and the ones above it in band C are not observed in the 248-keV gated spectrum of Fig. 4.5. But the 171- and 264-keV γ-rays and the ones below it are observed in that spectrum. The band-head spin and parity of band B has been assigned by the R_{DCO} and polarization asymmetry measurements of the 248 keV connecting transition and the nature of the transitions has been found to be a pure $E1$ type. Therefore, the spin-parity (I^π) of the band head of the band B at 3106-keV has been assigned as $I^\pi = 25/2^+$.

In case of the band C, most of the transitons were previously known and have been verifed in the present work. All the gamma rays belonging to band C are shown in Fig. 4.6. In one of the earlier works by Lieder et al., [12], a 412-keV γ ray was placed on top of the 3274-keV level. The placement of this transition has been changed in the present analysis. A new 286-keV,

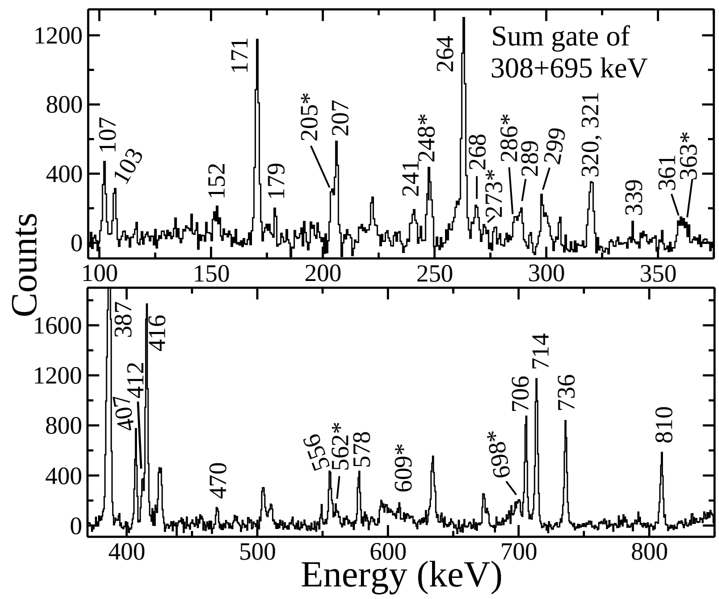

Figure 4.6: Sum gated spectrum with gates on 695-keV and 308-keV transitions corresponding to band C in ^{197}Tl; new γ rays are marked by asterisks (*).

and a cross-over 698-keV transition have been identified and placed in this band for the first time from this work. The R$_{DCO}$ values of 286 and 412-keV transitions indicate predominantly dipole in nature and the cross-over 698 keV is a quadrupole one.

Most of the transitions of the band structures D, E and F are confirmed in the single gate of 560 keV as shown in Fig. 4.7(a). The transitions in the lower part of the band D were known earlier [13]. This band has been extended in the present work beyond the first paticle alignment and up to $39/2^{+}\hbar$ of angular momentum with the observation of several new transitions above the $27/2^{+}$ state. The new γ transitions of band D have been confirmed in the sum gates on 767-keV and 339-keV transitions as shown in Fig. 4.7(b). The measured R$_{DCO}$ and the Δ_{PDCO} values of the 557-, 560- and the 810-keV transitions are consistent with the positive parity assignment for this band. It is interesting to note that no cross-over $E2$ transition has been observed above $J^{\pi} = 27/2^{+}$ in this band.

In the earlier work [13], a new band ($B3$) was observed at the band-head excitation energy of 2376 keV with six transitions of energy 179, 241, 267, 289, 320 and 361 keV. This band decays to the lower levels by a 262-keV transition. However, due to insufficient statistics coincidence relation among these transitions could not be checked in the ealier work and the placements of the transitions were somewhat tentative. In the present work, coincidence relation between

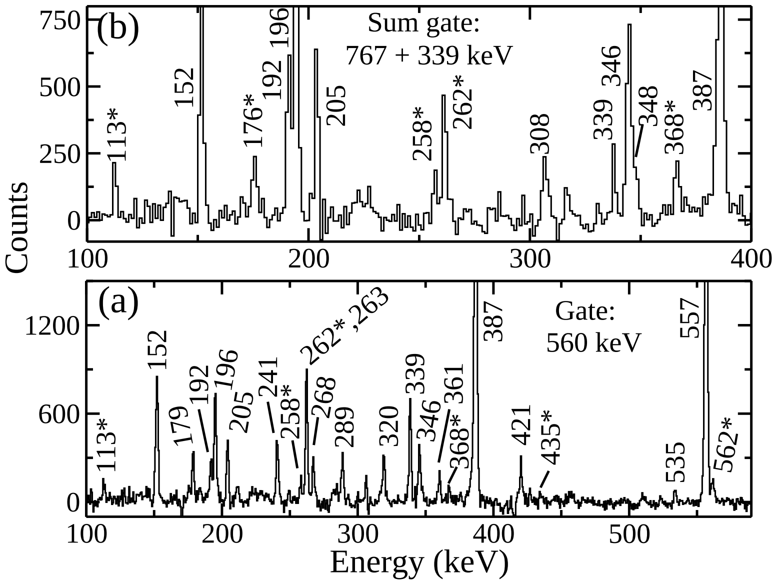

Figure 4.7: (a) Coincidence spectrum gated by 560-keV γ ray and (b) sum coincidence spectrum gated by 767-keV and 339-keV γ rays showing the transitions in the sequences D and E. The new γ-rays are marked by asterisks (*).

the transitions have been checked due to better statistics and it has been observed that the placements of the γ rays need to be modified. These sequences are built above a 2354-keV level which is connected to the known lower-lying levels by a 241-keV transition. Fig. 4.8 shows the coincidence relation for the transitions in the sequences E and F. The spectrum in Fig. 4.8(a) is gated by the 241-keV transition which shows all the γ-rays in the E and F bands. Moreover, the intensity of the 241-keV transition is the largest among the transitions in the two sequences as can be seen from the spectrum in Fig. 4.7(a). Therefore, the 241-keV transition is placed at the bottom of the two sequences E and F.

The 263-keV γ ray is not observed in the 268-keV gated spectrum [see Fig. 4.8(b)] whereas, it is observed to be in coincidence with both 241-keV and 179-keV transitions (see Fig. 4.8(a) and Fig. 4.8(c), respectively). Therefore, there must be a 263-keV transition which is in coincidence with both 241- and 179-keV transitions but in parallel with the 268-keV one. A new level at 3405 keV, in parallel to the sequence F, has been placed (see Fig.4.2) that decays to the 3142 keV level by a 263-keV γ ray which satisfies the above coincidence conditions. There is another transition of exactly similar energy in the level scheme of ^{197}Tl which decays from an 18-ns isomer at 2528 keV ($19/2^-$). The peak at 263-keV has been found to have a larger intensity in the spectrum gated 560-keV transition (Fig.4.7(a) in which both the 263-keV transitions will

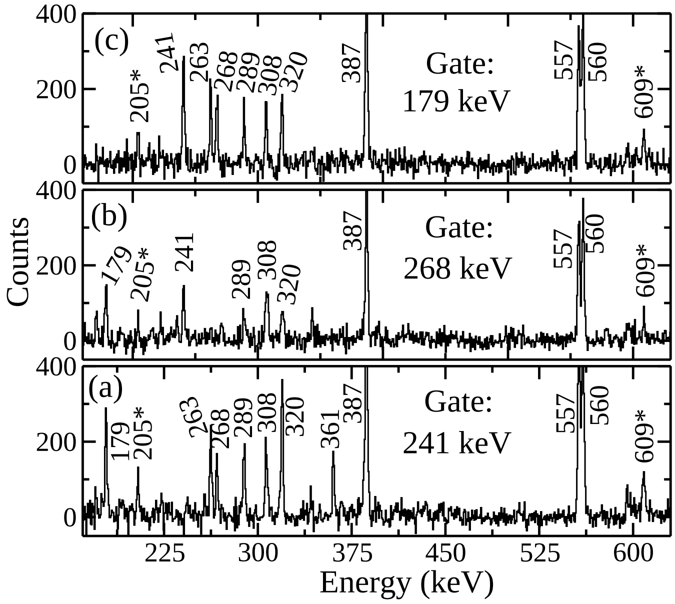

Figure 4.8: Coincidence spectra gated by 241-keV (a), 268-keV (b) and 179-keV (c) transitions showing the γ-lines placed in sequence E and F in the level scheme. New γ rays are marked by asterisks (*).

contribute to the peak. Also, the ratios of intensities of 263 keV and 268 keV peaks observed in Fig. 4.8(a) and (c) (in which only the newly placed 263-keV transition at higher excitation energy will only contribute to the peak) are found to be much smaller compared to that observed in Fig.4.7(a)). This supports the multiple placement of the 263-keV transition. However, it is interesting to note that no transitions above the newly placed $25/2^+$, 3405-keV state could be identified although the intensity of the 263-keV peak corresponding to the decay of this state is relatively large. This might indicate the presence of a long-lived high-spin isomer in ^{197}Tl.

The 361-keV transition is observed in 241-keV gate but it is not present in the spectra gated by 268-keV or 179-keV transitions. Therefore, the 179-keV, 268-keV and the newly observed 205-keV transitions are placed to form the sequence F, parallel to the 361-keV transition. A new 609-keV cross-over transition has also been observed in the sequence E but no other such cross-over transition is observed in these two sequences.

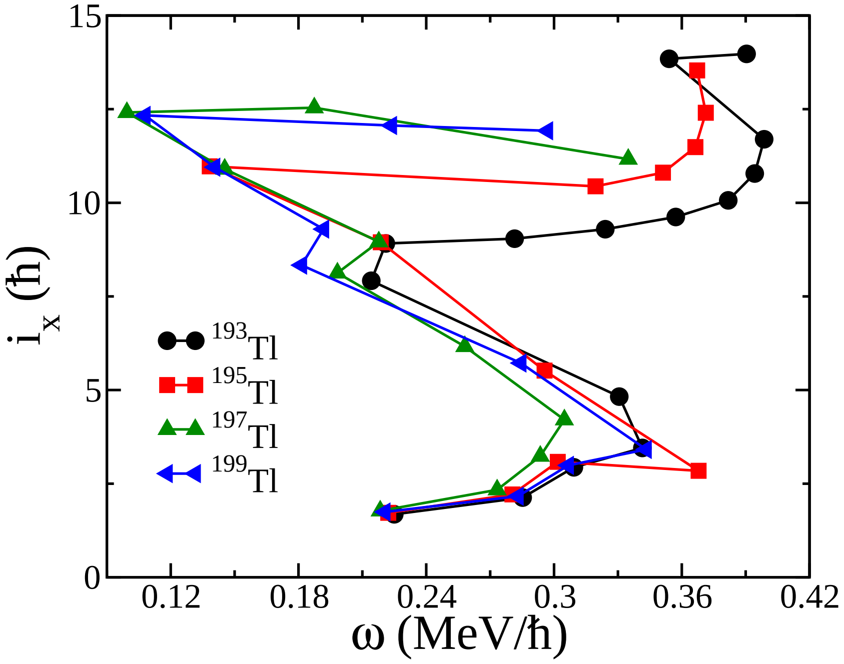

Figure 4.9: Aligned angular momentum i_x as a function of rotational frequency (ω) for the $\pi h_{9/2}$ band in ^{193,195,197,199}Tl. The Harris reference parameters are chosen to be j_0=8$\hbar^2 MeV^{-1}$ and j_1=40$\hbar^4 MeV^{-3}$.

4.3 Discussions

As mentioned before, the ground state spin-parity of odd-A Tl isotopes are $I^\pi = 1/2^+$ corresponding to the occupation of the odd-proton in the $3s_{1/2}$ orbital below the $Z = 82$ shell closure. The first excited state with $I^\pi = 3/2^+$ is obtained by the excitation of the odd proton to the $2d_{3/2}$ orbital. The second excited state in the odd-A Tl isotopes is $9/2^-$, corresponding to the occupation of the intruder $\pi h_{9/2}$ orbital by the odd proton. It is an isomeric state in all the odd-A Tl isotopes. Rotational band based on this configuration has been observed up to ^{201}Tl [17] and indication of a band-like structure has been observed in ^{203}Tl [16]. This indicates that the shape driving effect of the $\pi h_{9/2}$ orbital still competes with the spherical shell closures even up to the neutron number $N = 122$. The observation of these rotatonal bands has been interpreted as the coupling of the intruder $\pi h_{9/2}$ orbital with the deformed core of neighboring even-even Hg.

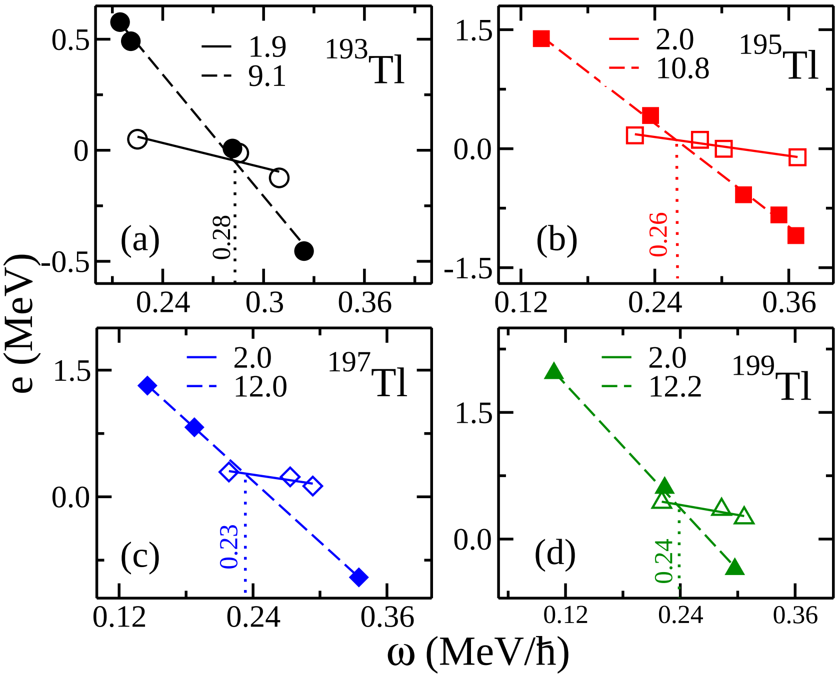

Figure 4.10: Experimental Routhians (e) as a function of rotational frequency (ω) for the $\pi h_{9/2}$ band in ^{193}Tl (a) ,^{195}Tl (b), ^{197}Tl (c) and ^{199}Tl (d). The open and filled symbols correspond to the experimental data before and after the band crossing. The solid (dashed) lines are the linear fit to the data points before (after) the band crossing. The dotted lines denote the crossing point with the associated number is the crossing frequency, ω_c. The values of the slopes of the two linear fits are also given for each isotope.

The band C in ^{197}Tl is based on the aforementioned intruder $\pi h_{9/2}$ orbital and it has been extended in the present work beyond its spin region where band crossing takes place. The band crossing of this band can be explained as the alignment of a pair of $i_{13/2}$ neutrons. The newly observed band crossing phenonmena of ^{197}Tl has been compared with the other neighbouring odd-A Tl isotopes. The aligned angular momentum (i_x) as a function of rotational frequency (ω) for the $\pi h_{9/2}$ band in ^{197}Tl along with its other neighbouring isotopes are plotted in Fig. 4.9. Similar behavior is observed in all these isotopes which indicates a common phenomenon of the alignment of two neutrons in $i_{13/2}$ orbital for the Tl isotopes. From the similarities of band crossing frequency and gain in alignment the configuration of band C in ^{197}Tl after the band crossing has been assigned as $\pi h_{9/2} \otimes \nu i^2_{13/2}$. However, there are certain differences in the gain

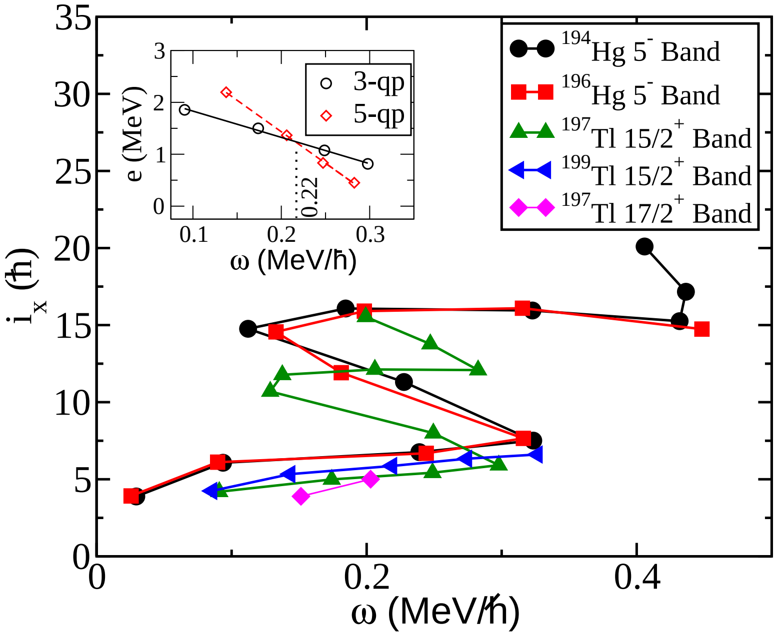

Figure 4.11: Aligned angular momentum i_x as a function of rotational frequency (ω) for the bands D and E, based on the $15/2^+$ and $17/2^+$ states, respectively, in ^{197}Tl. Same quantities for the 3-qp band in the neighboring isotope ^{199}Tl and for the 5^- bands in ^{194,196}Hg are also shown. (inset) the experimental routhian (e) vs. rotational frequency for the band D in ^{197}Tl. The solid and the dashed lines are the linear fits to the 3-qp and the 5-qp parts of the band D. The crossing frequency is indicated by the dotted line.

in alignment for the different odd-A Tl isotopes. In order to get a better quantitative values of the crossing frequency and the alignment gain, the experimental energy Routhians (e) are plotted as a function of rotational frequency (ω) in Fig. 4.10. In this plot, the intersections between the two energy Routhians, corresponding to before and after the particle alignment, defines the crossing frequency. In order to plot the two Routhians, the two regions were easily identified and separated from Fig. 4.9.

The slopes of the Routhians give the aligned angular momentum (i_x) which can be obtained by a linear fit of the data points in Fig. 4.10. The initial gain in alignment for all the isotopes remain constant at a value of $i_x \sim 2\hbar$ which has been otained using linear fitting of the energy Routhians before particle alignment (Fig. 4.10). Similarly, the values of i_x for the Tl isotopes after the alignments have also been obtained from the fitted slope of the 3-qp Routhians, i.e,

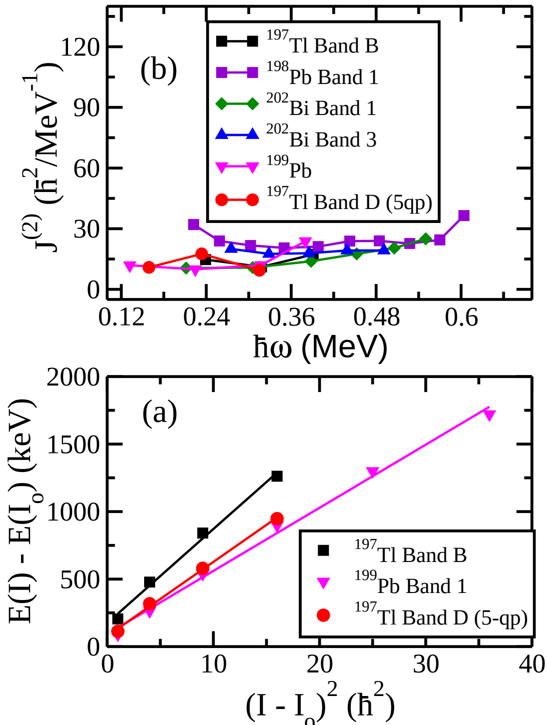

Figure 4.12: (a) Level energy E(I) with respect to the band head energy ($E_\circ$) as a function of the square of spin difference and (b) dynamic moment of inertia ($J^{(2)}$) as a function of rotational frequency ($\hbar\omega$) for the band B in ^{197}Tl and some other MR bands in the neighboring nuclei. The solid lines in (a) are the linear fits to the respective data points (symbol). Data for ^{199}Pb, ^{198}Pb and ^{202}Bi are taken from Ref. [31] [32] and [33], respectively.

the Routhian after the particle alignments, and has been compared with the other neighbouring Tl isotopes. The i_x values have been found to increase from $\sim 9\hbar$ in N = 112 isotope ^{193}Tl to $\sim 12\hbar$ in N = 116 isotope ^{197}Tl which remains constant thereafter for N = 118 isotope ^{199}Tl. On the other hand, crossing frequency, ω_c, has been observed to decrease with the increase in neutron number until ^{197}Tl and remains almost same in ^{199}Tl. This can be understood from the fact that as the neutron number increases, the neutron Fermi level moves from higher- Ω to lower-Ω orbitals (corresponding to small to large values of j_x, respectively, where j_x is the projection of particle angular momentum on to the rotation axis) in the Nilsson diagram for oblate deformation and, as a result, the required Coriolis force ($\omega_c j_x$) can be achieved to align a pair of neutrons at a lower ω_c. It may be noted that the maximum gain in alignment can be obtained as $12\hbar$ from the alignment of a pair of neutrons in $i_{13/2}$ orbital, which seems to be the value for neutron number $N \geq 116$ in Tl isotopes and below which the $i_{13/2}$ neutrons are only partially aligned.

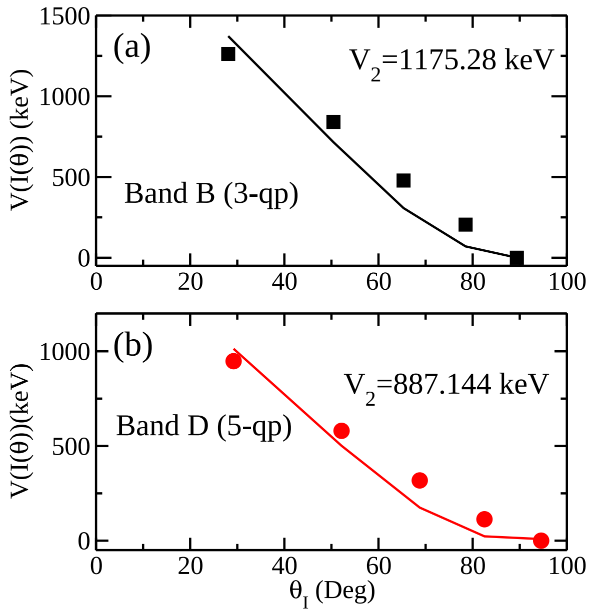

Figure 4.13: Plot of V(I(θ)) as a function of shears angle θ for the band B (a) and the band D (b) in ^{197}Tl. The solid lines are the fits to the data points from which the effective interaction V_2 between the proton and neutron angular momentum vectors has been obtained.

The present results of the 3-qp and 5-qp bands in ^{197}Tl, discussed above, imply an interesting shape transtion in odd-A Tl isotopes at higher excitation energy. Two doubly degenerate bands of chiral nature were obseved in the $N = 114$ isotope ^{195}Tl, Where as, MR bands are observed in case of ^{197}Tl with neutron number $N = 116$. Therefore, the increase in neutron number in Tl isotopes modifies the aplanar configuration, corresponding to chiral band, of the three angular momentum vectors of proton, neutron, and core in ^{195}Tl to a planar one in ^{197}Tl. Similar transition from an aplanar to a planar configuration was also observed in Cs isotopes in $A \sim 130$ mass region [43].

The band E has been modifed compared to that proposed in [13] and a new level structure F has been observed in this study. Very similar excitation energy of the bands D and E suggests a 3-qp nature of the band E. This band E decays to the $15/2^+$ state of the band D. The band E may be interpreted as a multiplet of band D of configuration $\pi h_{9/2} \otimes \nu i_{13/2}(fp)$. Similar values of their aligned angular momenta, i_x, as shown in Fig. 4.11, support this configuration assignment of band E. Level structure similar to that in band E has also been observed in the next heavier odd-A isotope ^{199}Tl [14]. The MR band B and the 5-qp part of band D were further investigated in the framework of a semiclassical model of magnetic rotation [44] to extract the particle-hole interaction strength. In this semiclassical model, the proton blade (j_π) and the

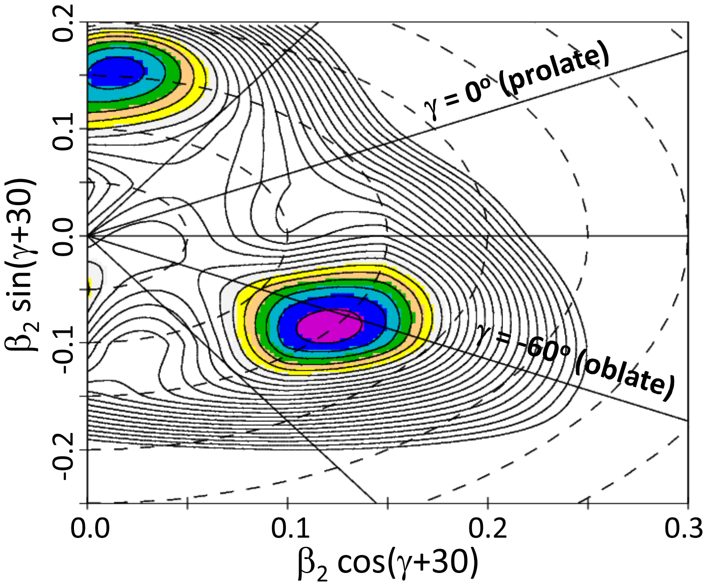

Figure 4.14: The total Routhian surfaces calculated for ^{197}Tl for the configuration of $\pi h_{9/2} \otimes \nu i^{-2}_{13/2}$, that is after the band crossing in band C. The contours are 250 keV apart.

neutron blade (j_ν) are coupled together to produce the total angular momentum (I). The angle between the proton and the neutron angular momentum blades is called the shears angle and it can be represented in a semiclassical way with the formula [44]:

$$\cos\theta_I = \frac{I(I+1) - j_\pi(j_\pi+1) - j_\nu(j_\nu+1)}{2\sqrt{j_\pi(j_\pi+1)j_\nu(j_\nu+1)}} \tag{4.4}$$

Where, I is the total angular momentum of a state. Considering the values of j_π and j_ν as $5.5\hbar$ and $11\hbar$, respectively, for the proposed 3-qp configuration $\pi i_{13/2} \otimes \nu i^{-2}_{13/2}$ for the band B, the band head spins of $12.5\hbar$ is well reproduced. similarly, for the 5-qp part of the band D, $j_\pi = 4.5$ and $j_\nu = 13$ are considered and the band head spin of $13.5\hbar$ is well reproduced by assuming perpendicular coupling between j_π and j_ν. The maximum angular momentum that can be generated by the complete alignment of the proton and the neutron angular momentum blades along the total angular momentum axis would be $16.5\hbar$ and $17.5\hbar$ for the 3-qp and 5-qp bands, respectively. The levels above $I^\pi = 33/2^+$ and $37/2^+$ in the 3- and 5-qp bands, respectively, show irregular level spacings which indicates the initiation of another band crossing for both the bands. Thus, the maximum possible spins which can be generated in these two bands by shears mechanism are also well reproduced.

According to the prescription of Macchiavelli et al. [44] in the case of shears mechanism, the neutron and proton angular momenta are coupled to spin I and interact via a term of the form

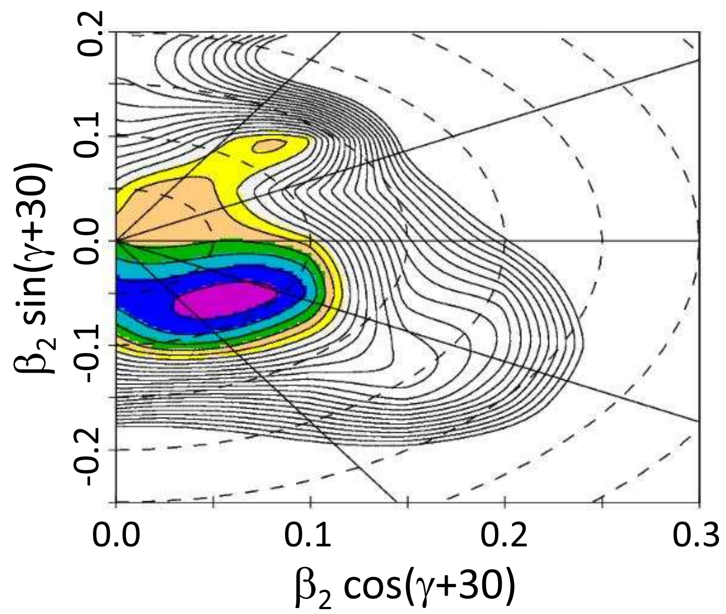

Figure 4.15: 3-qp configuration of $\pi i_{13/2} \otimes \nu i_{13/2}^{-2}$ corresponding to the band B in ^{197}Tl.

$V_2P_2(\cos\theta)$. The energy along the band is given only by the change in potential energy due to the angular momentum coupling, and accordingly, the excitation energies of the states in the MR bands, with respect to the band head energy, can be written as

$$V(I(\theta)) = E_I - E_b = (3/2)V_2\cos^2(\theta_I), \tag{4.5}$$

where E_I and E_b are the level energies corresponding to the angular momentum I and the band head energy, respectively; θ_I is the shears angle related to the angular momentum I, and V_2 is the total interaction strength between the proton and the neutorn blades. The experimental $V(I(\theta))$ and θ_I have been extracted and are plotted in Fig. 4.13 for the two MR bands in ^{197}Tl. The experimental data points are fitted by using Eqn.(4.5) to extract the value of the interaction strength V_2. The fitted values of V_2 are also shown in the Fig. 4.13. We have obtained V_2 = 1175 keV for the 3-qp MR band and V_2 = 887 keV for the 5-qp MR band. These lead to the interaction strength per particle-hole pair as V_2^{ph} = 587.5 keV and 221.8 keV, respectively, for the 3-qp and 5-qp bands. The value of V_2^{ph} for the 3-qp band is similar to the values reported in the Pb region [45], but it is some what less for the 5-qp band. It is to be noted that the 5-qp configuration also includes low-j negative parity orbitals, hence, it seems that not all of the neutron holes are taking part in the shears mechanism and the interaction strength may not be equally divided among all the particle-hole pairs.

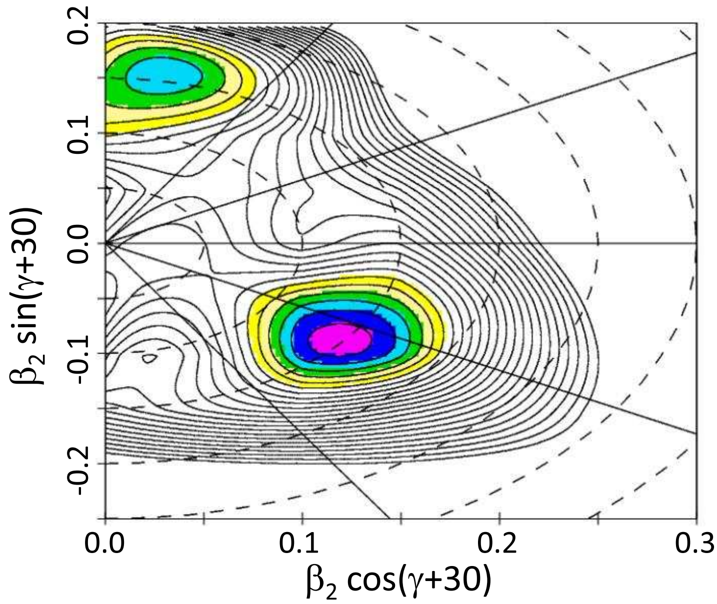

Figure 4.16: 3-qp configuration of $\pi h_{9/2} \otimes \nu i^{-1}_{13/2}(fp)^{-1}$ corresponding to the lower part of band D in ^{197}Tl.

4.4 Theoretical Calculations

4.4.1 TRS Calculations

In order to understand the different shapes in ^{197}Tl and the effects of the high-j active proton and neutron orbitals on shapes, the total Routhian surface (TRS) calculations have been performed, as discussed in Chapter 2.5 and 2.6. The formalism of Nazarewicz et al., as depicted in Ref. [46, 47], has been used and the detail technical procedure has been given in Ref. [48] (and references there in). As mentioned before, the deformation of a nucleus for a particular configuration at a particular rotational frequency corresponds to the minimum in the contour plots of the potential energies in β_2 and γ ($\gamma = 0°$ = prolate and $\gamma = -60°$ = oblate) mesh points. The energy minimization on β_4 was done for each value of β_2 and γ. Several TRSs have been calculated for different configurations and at several rotational frequencies ($\hbar\omega$). The TRS calculation for the 1-qp, $\pi h_{9/2}$ and $\pi i_{13/2}$, configurations in ^{197}Tl were earlier calculated in Ref. [13] using the same procedure. It showed oblate shapes for the $\pi h_{9/2}$ configuration and nearly spherical shape for the $\pi i_{13/2}$ configuration.

The TRS calculations, performed for the configuration corresponding to the band C in ^{197}Tl after the band crossing, is shown in Fig. 4.14. It shows energy minimum at near-oblate defor-

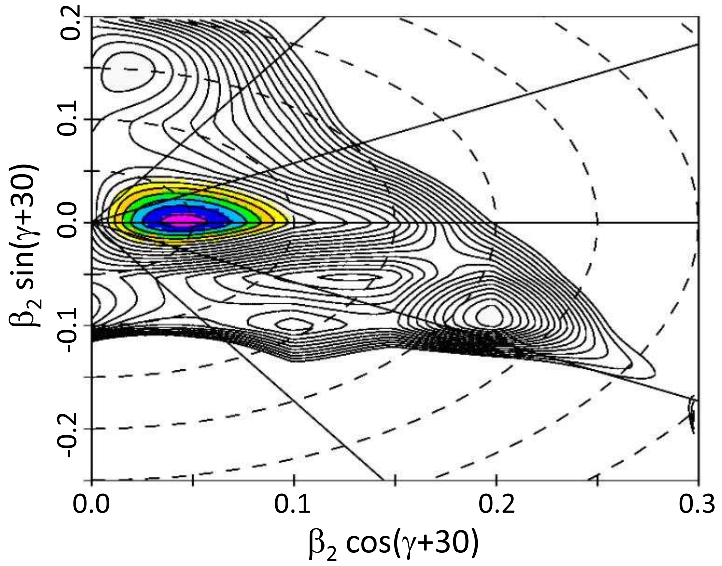

Figure 4.17: 5-qp configuration of $\pi h_{9/2} \otimes \nu i_{13/2}^{-3}(fp)^{-1}$ corresponding to the upper part of the band D in ^{197}Tl.

mation with $\beta_2 \sim 0.15$ and $\gamma \sim -62^\circ$ which is similar to the 1-qp $\pi h_{9/2}$ configuration. The TRS plot for the 3-qp band B of configuration $\pi i_{13/2} \otimes \nu i_{13/2}^{-2}$ in ^{197}Tl are shown in Fig. 4.15. The minimum of the TRS for this configuration indicates a near-spherical shape with $\beta_2 \sim 0.08$ and $\gamma \sim -72^\circ$. Similar near spherical shape was obtained for the 1-qp $\pi i_{13/2}$ configuration in ^{197}Tl as well [13].

The TRS calculations were also performed for the 3-qp and 5-qp part of the band D and are shown in Fig. 4.16 and 4.17, respectively. An oblate shape with $\beta_2 \sim 0.14$ and $\gamma \sim -66^\circ$ has been obtained for the 3-qp part of band D. On the other hand, the calculations for the configuration $\pi h_{9/2} \otimes \nu i_{13/2}^{-3}(fp)^{-1}$, corresponding to the upper part of band D (5-qp), shows a near-spherical minimum at a very low deformation with $\beta_2 \sim 0.05$ and $\gamma \sim -30^\circ$. The near-spherical shape for the band B and the 5-qp part of the band D, obtained from the TRS calculations, are consistent with the observed MR nature of these bands. In the TRS plot for the 3-qp configuration of band D (Fig. 4.16), a secondary minimum appears at about 400 keV above the first primary minimum. The observation of the band E (Fig. 4.2) at about the similar excitation energy relative to the band D provides an impression that the band E may correspond to this second minimum.

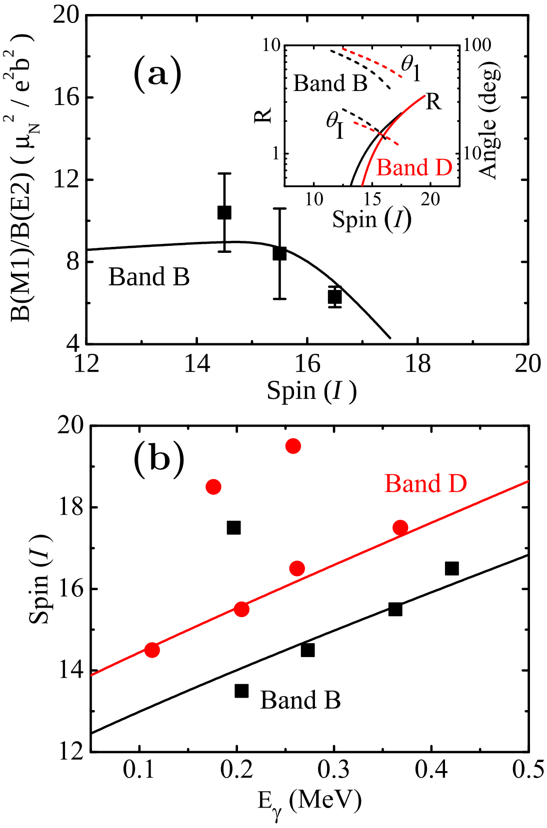

Figure 4.18: Comparison of the experimental results for the dipole bands B (represented by the black filled squares) and the upper part of D (represented by the red filled solid circles) in ^{197}Tl with the SPAC model (solid black and red lines for the bands B and upper part of D, respectively). The $B(M1)/B(E2)$ transition strengths against spin (I) have been depicted in (a) and the variation of spin (I) with the level energy difference (E$_\gamma$) is shown in (b). The variation of R and θ_1 with spin (I) are shown in the inset of (a).

4.4.2 SPAC Calculations

As discussed in Chapter 2.7, the Shears mechanism with the Principal Axis Cranking (SPAC) model [49, 50, 51, 52, 53] has been successfully applied to explain the MR bands. This model can be used as a powerful tool to extract the intrinsic character, quasiparticle configurations, and contribution of (deformed) core rotation in shears sequences. The SPAC model calculation has been performed to understand the shears mechanisms in the 3-qp and 5-qp (ΔI=1) dipole bands in^{197}Tl identified as a MR bands on top of the $25/2^+$ and the $27/2^+$ states, respectively.

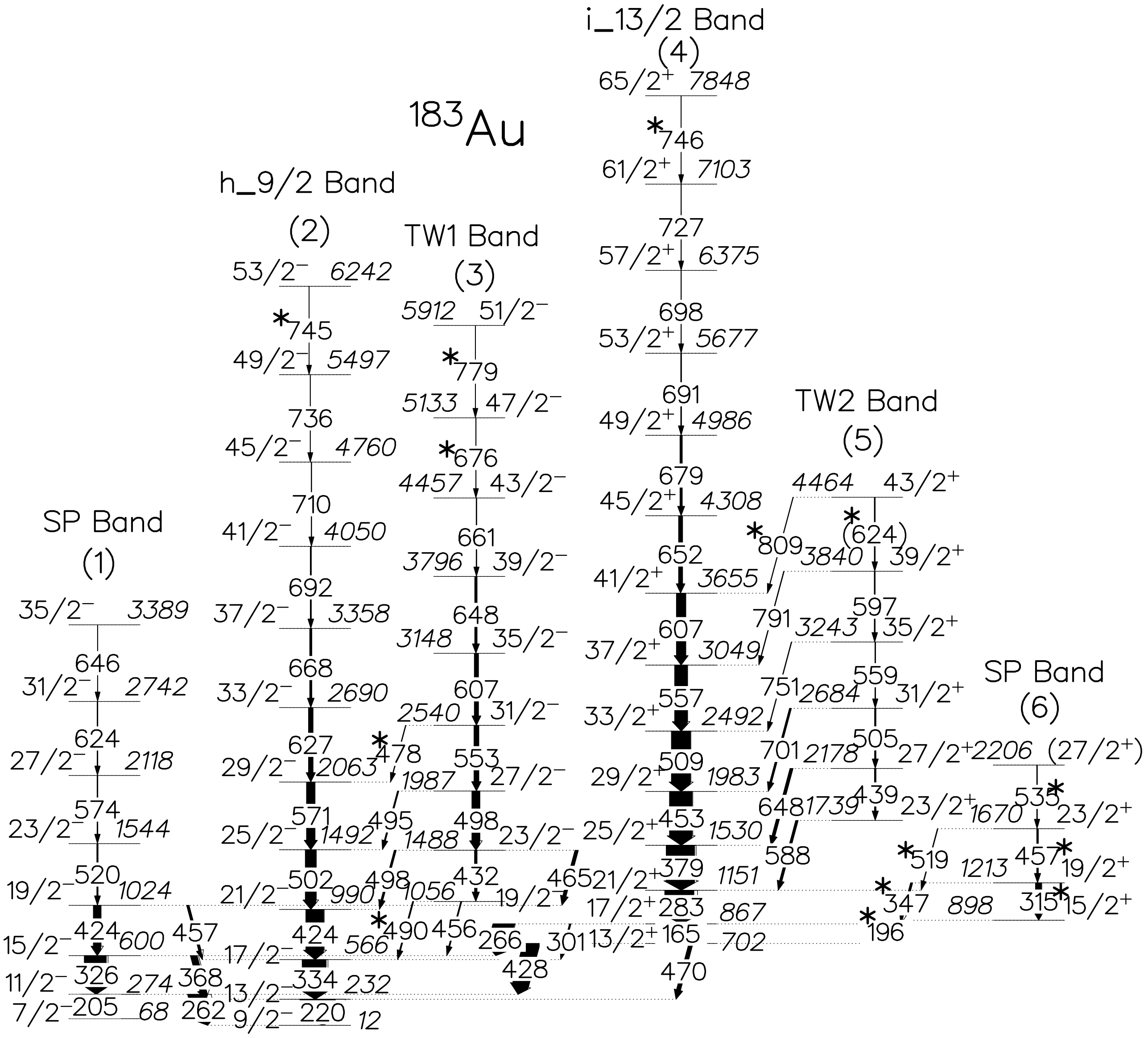

Figure 5.1: New level scheme of ^{183}Au from the present work. Line widths are proportional to their intensities. The level energies are obtained by fitting the γ-ray energies using the code *GTOL* [17]. The new transitions in the level scheme are marked by asterisks.

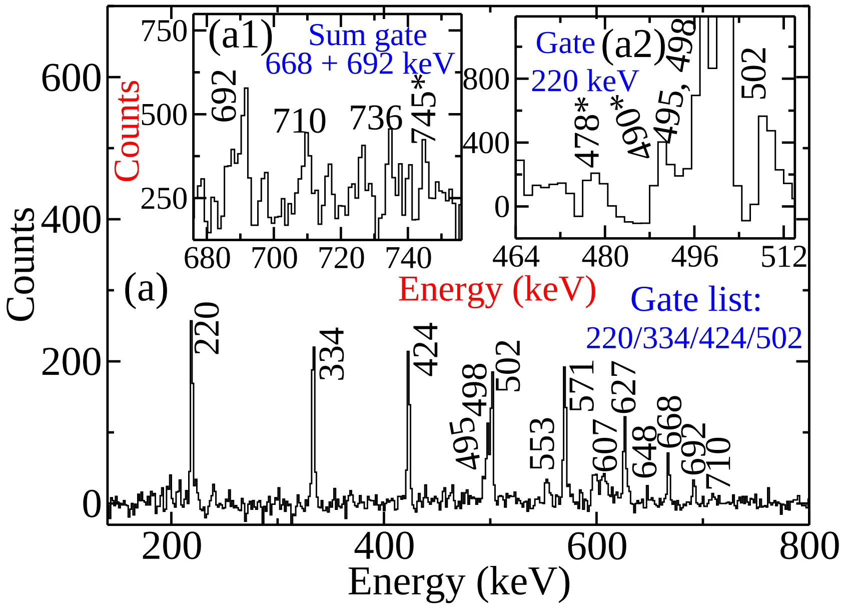

Figure 5.2: Summed double-gated γ-ray spectra projected from the γ-γ-γ cube and the γ-γ matrix. In (a) the gates were put in the cube on all the 6 pair combinations from the gatelist of 220, 334, 424, 502 keV γ rays in band (2) of ^{183}Au. The higher energy γ rays at the top of this band are shown in the sum gated (668- and 692-keV) spectrum projected from the matrix (a1). The connecting transitions between the band (3) and the band (2) are shown in the spectrum gated by 220-keV (a2).

gamma rays of energy 624 and 809 keV, decaying form that level, have been identified in the present work. In the present analysis, a new band 6 has been identified and extended up to the excitation energy of 2206 keV. The gamma rays belong to this band have been confirmed in the sum gate of 196 and 428 keV as shown in Fig. 5.4.

As mentioned before, the nature of the connecting transitions between the main and the side bands are crucial in identifying the wobbling or signature partner band. Between the wobbling partner bands, the connecting transitions are predominantly $E2$ in nature, that is their M1+E2 mixing ratios are large; whereas, in case of signature partner bands, the mixing ratios of the connecting transitions should be small. Simultaneous measurements of linear polarisation (P) and DCO ratio (R_{DCO}) were performed in the present work for the determination of mixing ratio (δ) of a mixed M1+E2 transition. For this, the measured linear polarisation (P) and R_{DCO} values were compared with the ones calculated for different mixing ratio (δ). The measured mixing ratio δ is close to 0 for pure transitions, which has been obtained for a pure $E1$ and a pure $E2$ transition as shown in Fig. 3.18 in Chapter 3. The negative parity band 2 and the

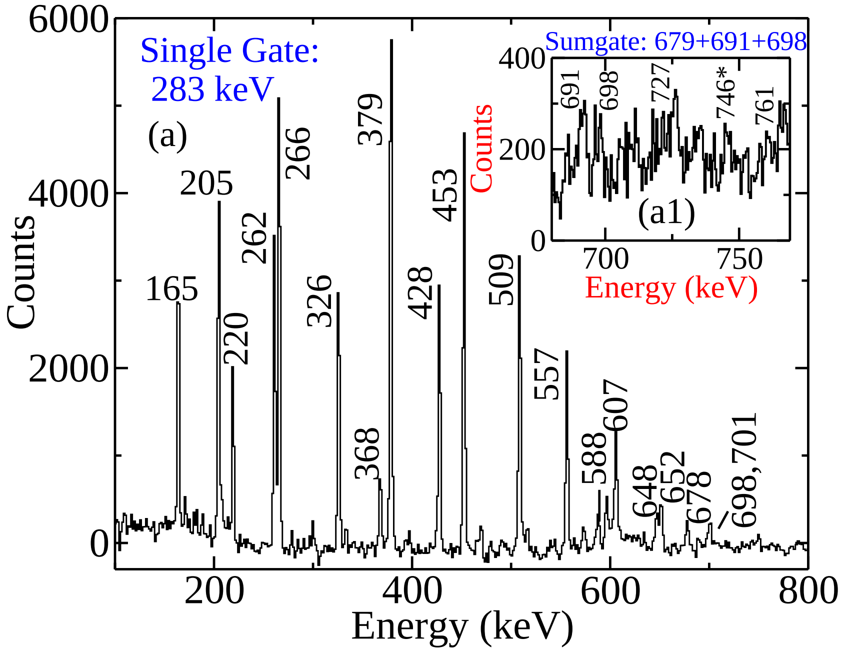

Figure 5.3: Single gated γ-ray spectra projected from the γ-γ-γ cube and the summed gated spectra from γ-γ matrix. In (a) the single gate was put in 283 keV transition in the cube from band (4) of ^{183}Au. The higher energy γ rays at the top of this band are shown in the sum gated (679, 691 and 698-keV) spectrum projected from the matrix (a1).

positive parity band 4 have two E2 rotational side bands each of which decay to the yrast main band by $\Delta I = 1$ M1+E2 transitions. The measured values of P and R_{DCO} has been compared with the calculated ones for these connecting transitions and are shown in Fig. 5.5. The low values of δ for the conecting transitions between band 1 and band 2 suggest that the transitions are mostly $M1$ in nature. Therefore, the assignment of band 1 as the signature partner of the negative parity yrast band is justified.

Similarly, the polarization and R_{DCO} measurements were done for the 490, 495,and 498 keV connecting transitions between band 3 and band 2. It may be noted that there are two 498 keV transitions and the 495 keV transition is parallel to both of them. Therefore, the 495-keV transition can easily be seperated by putting a gate on 502 keV (E2). In case of 498 keV transiton, it is difficult to seperate the in-band 498-keV transition of band 3 from the inter-band connecting 498 keV one. So, we have measured the P and R_{DCO} of the connecting 498 keV transition in the following way: the 334-keV (E2) gate includes both the 498-keV transitions whereas, a gate on the 465-keV (E2) transition, (connecting transition from $23/2^{-}$ in band 3 to $19/2^{-}$ in band 1) contanis only the contribution of the in-band 498 keV transition. Therefore, a spectrum, obtained by subtracting the 465-keV gate to the 334-keV gate was used to determine

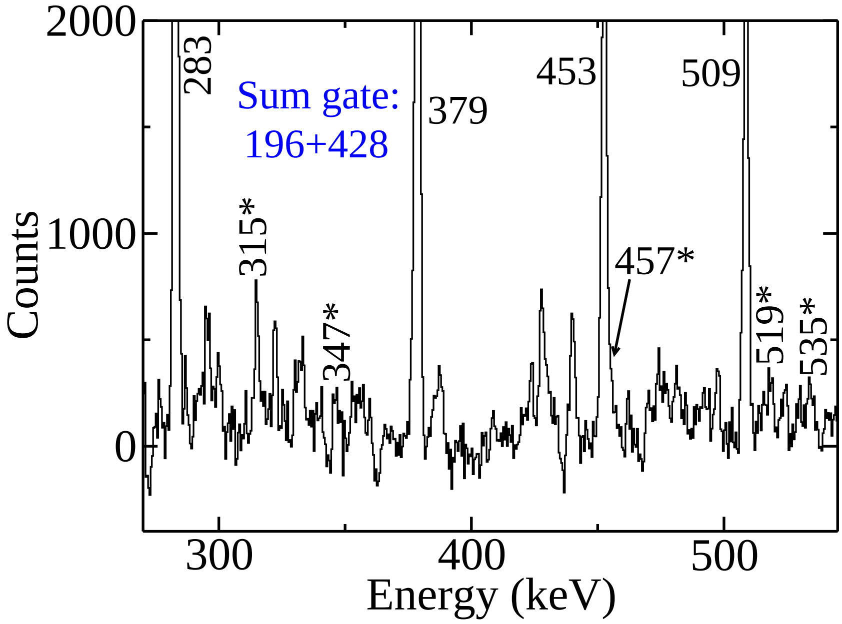

Figure 5.4: Summed single-gated γ-ray spectra projected from γ-γ matrix. All the new gamma rays of band 6 are shown in the sum gated (196 and 428-keV) spectrum projected from the matrix.

the R$_{DCO}$ and P of the connecting 498-keV γ-ray. The R_{DCO} value of the 498-keV in-band transition gated by 465-keV γ ray comes out to be 1.01(4), as it should be as both of them are stretched quadrupole transitions. It may be noted that this procedure could be adopted because both the 334-keV and the 465-keV gating transitions are of same (E2) type.

It can be seen from Fig. 5.5 that the values of δ are quite large for all the connecting transitions from band 3 to the main band 2 (in contrast to the connecting transitions between band 1 and band 2). Similarly, the δ values of the connecting transitions between the bands 5 and 4 are large whereas, the δ values for the connecting transitions from band 6 to band 4 are small. The large values of δ indicate that the transitions from band 3 to band 2 and also from band 5 to band 4 are predominantly $E2$ ($\sim$ 90%) in nature. Hence, the bands 3 and 5 may be considered as the wobbling partner bands of band 2 and band 4, respectively. On the other hand, the bands 1 and 6 are the signature partner bands of band 2 and band 4, respectively.

The branching ratios, $B(E2)_{\mathrm{out}}/B(E2)_{\mathrm{in}}$ and $B(M1)_{\mathrm{out}}/B(E2)_{\mathrm{in}}$ are also extracted from the measured intensities and the δ values of the corresponding transitions as suggested in [18]. These are shown in Fig. 5.6 for both the negative and the positive parity configurations. Larger values

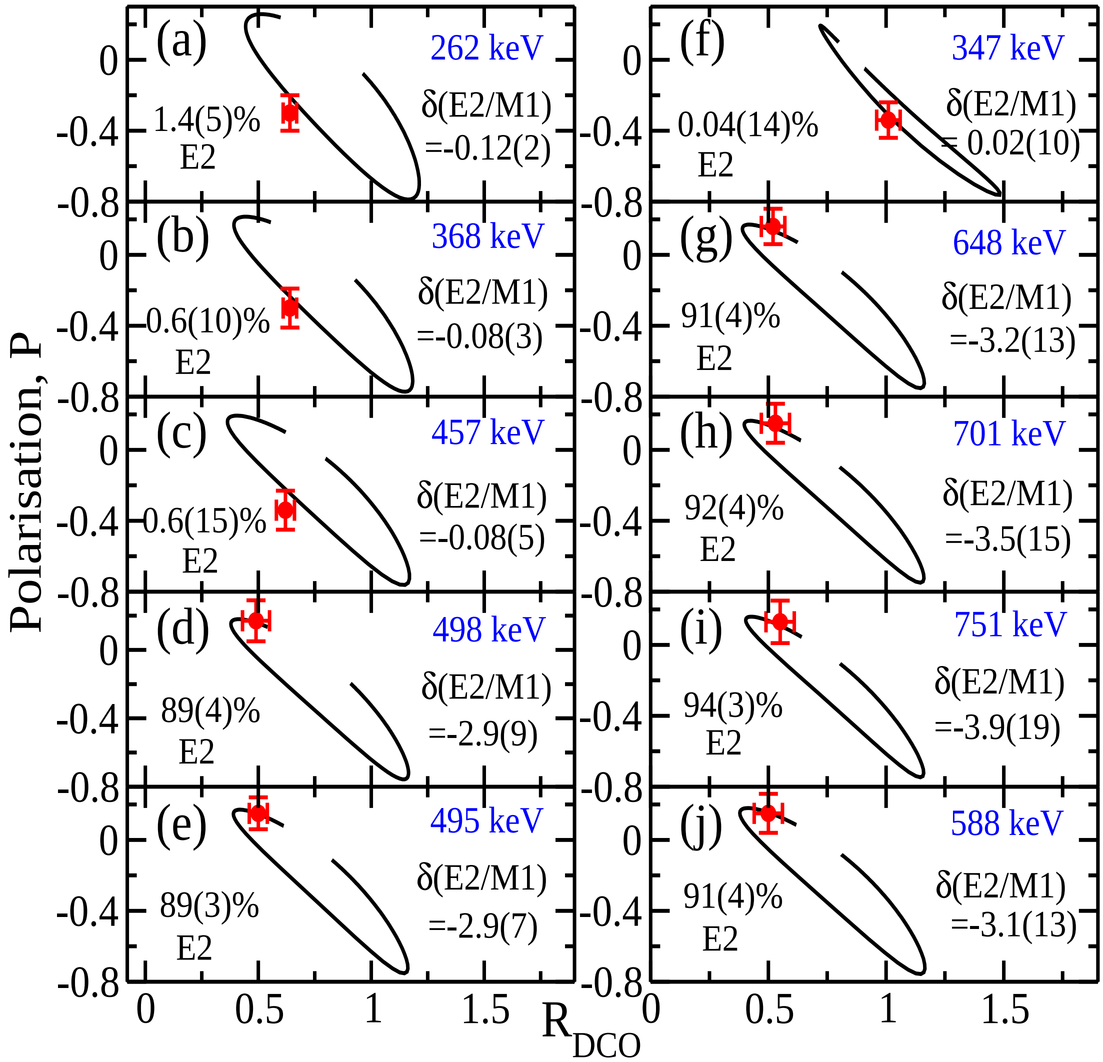

Figure 5.5: Experimental (symbol) and calculated (solid line) values (for different mixing ratios δ) of DCO ratios (R_{DCO}) and linear polarization (P) of the connecting transitions that decay to the negative parity band (2) (a − e) and to the positive parity band (4) (f − j).

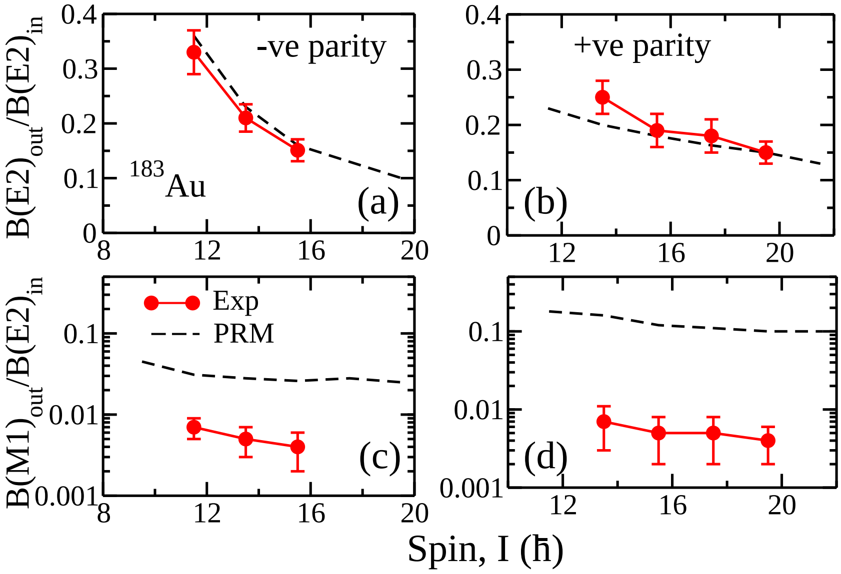

Figure 5.6: Measured values of the ratio of transition probabilities, $B(E2)_{\text{out}}/B(E2)_{\text{in}}$ and $B(M1)_{\text{out}}/B(E2)_{\text{in}}$, determined from the γ-ray intensities, as a function of angular momentum I for the negative parity (a and c) and the positive parity (b and d) bands in ^{183}Au. The theoretical values calculated from PRM are also shown.

of $B(E2)_{\text{out}}/B(E2)_{\text{in}}$ and smaller values of $B(M1)_{\text{out}}/B(E2)_{\text{in}}$ have been obtained for both the configurations, which suggest that the bands 3 and 5 are of wobbling nature [18].

Table 5.1: Energy (E_γ) and intensity (I_γ) of the γ rays, the spin and parity of the initial (I_i^π) and the final (I_f^π) states and the energy of the initial state (E_i) (GTOL fit) of ^{183}Au. The measured values of R_{DCO} and Δ_{PDCO} of the γ rays are also tabulated.

$E_\gamma(keV)$	$E_i(keV)$	$I_i^\pi \rightarrow I_f^\pi$	I_γ [1]	R_{DCO}	Δ_{PDCO}	Multipolarity
12.4 [2]	12.4	$9/2^- \rightarrow 5/2^-$	-	-	-	(E2)
164.6	866.9	$17/2^+ \rightarrow 13/2^+$	27.3(8)	1.03(3) [3]	-	E2
195.9	898.1	$15/2^+ \rightarrow 13/2^+$	12.5(14)	0.58(4) [4]	-	M1+E2
205.3	274.0	$11/2^- \rightarrow 7/2^-$	57.8(1)	1.04(2) [3]	-	E2
219.7	232.1	$13/2^- \rightarrow 9/2^-$	100.0(1)	0.99(3) [3]	-	E2
261.6	274.0	$11/2^- \rightarrow 9/2^-$	42.5(1)	0.64(3) [5]	-0.17(5)	M1+E2
266.4	866.9	$17/2^+ \rightarrow 15/2^-$	59.0(2)	0.55(2) [5]	0.24(3)	E1

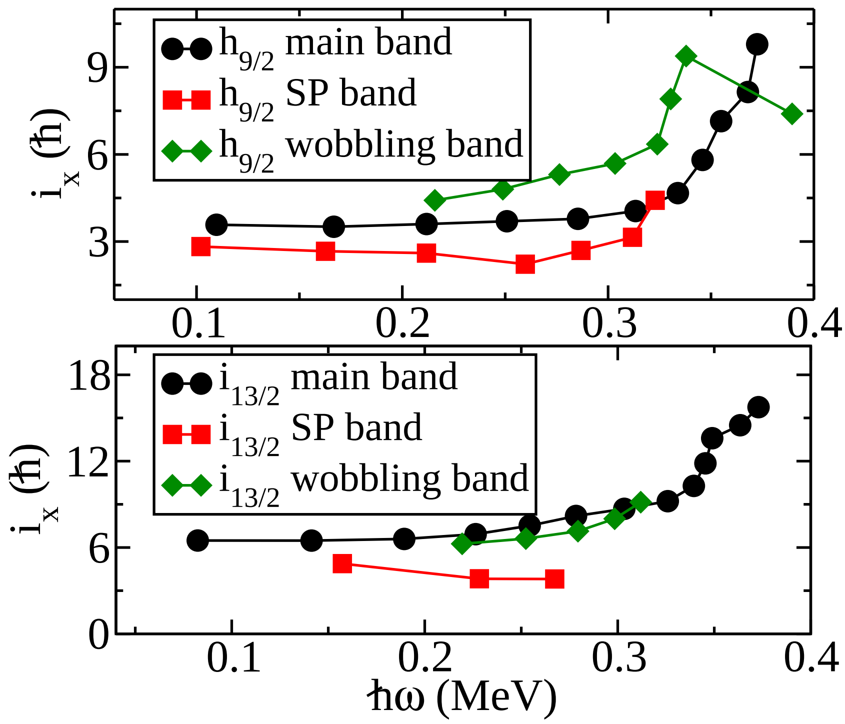

Figure 5.7: Aligned angular momentum i_x as a function of rotational frequency (ω) for the $\pi h_{9/2}$ and $\pi i_{13/2}$ band in ^{183}Au. The Harris reference parameters j_0=29.4 $\hbar^2 MeV^{-1}$ and j_1=121 $\hbar^4 MeV^{-3}$, from Ref. [16] have been used.

[15, 16, 20, 21]. The configurations of negative and positive parity bands in ^{183}Au were already known as $\pi h_{9/2}$ and $\pi i_{13/2}$, respectively [15, 16]. The invlovement of the Ω components for these high-j configurations can be obtained from the quasiparticle aligned angular momentum i_x of the observed rotational bands. The plot of i_x as a function of rotational frequency ($\hbar\omega$) is shown in Fig. 5.7. It can be seen that in case of the positive parity main band, $i_x \approx 6.5\hbar$ at the begining of the band. This indicates the involvement of the fully aligned $\Omega = 1/2$, $i_{13/2}$ configuration for this positive parity band. In case of the negative parity band, the estimated value of i_x ($\approx 3.5\hbar$) is somewhat less than the fully aligned value ($= 4.5\hbar$) corresponding to $\Omega = 1/2$ and, suggesting small mixing with other Ω orbitals, but nevertheless, still the low-Ω components are involved in generating the negative parity band. The involvement of low-Ω component indicates that the odd-particle is aligned along the short axis of a prolate-like triaxial nucleus. Therefore, the geometrical arrangement of odd particle and the core is similar to a Transverse Wobbler as shown in Fig. 1.5 in Chapter 1. So, both the wobbling bands in ^{183}Au are suggested as Transverse wobbling (TW) bands.

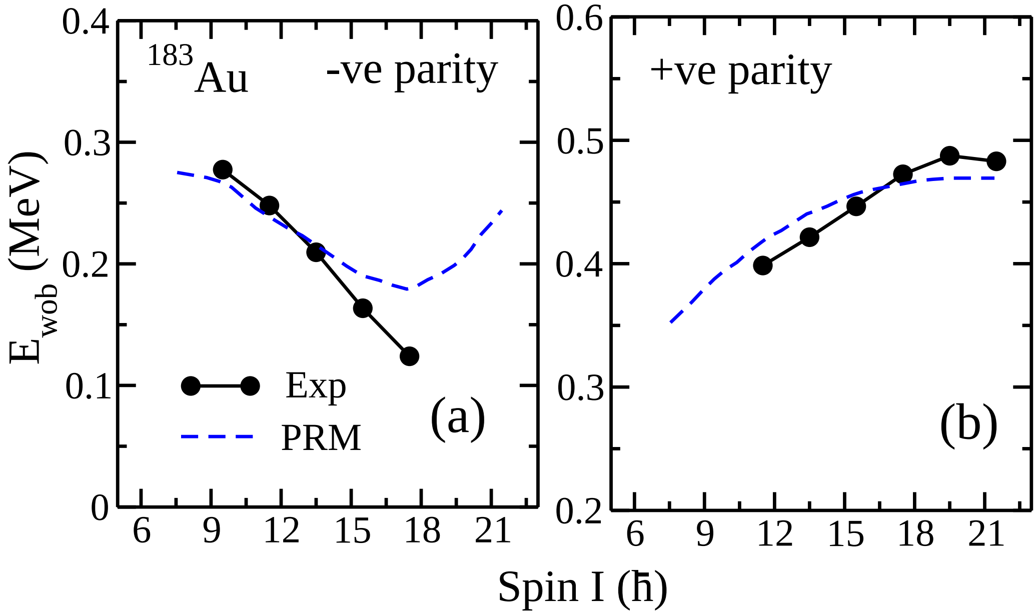

Figure 5.8: Experimental wobbling energy E_{wob} as a function of angular momentum I for the negative parity (a) and the positive parity (b) bands in ^{183}Au. The theoretically calculated values are also shown. The error bars on experimental values are within the size of the data points.

It was shown in Ref. [14] that the variation of the wobbling energy with spin (I) depends on the type (LW or TW) of wobbling motion. Experimentally, the wobbling energy $E_{\mathrm{wob}} = \hbar\omega_{\mathrm{wob}}$ can be obtained from the energy differences between the $n_w = 1$ wobbling partner band and $n_w = 0$ yrast band using the relation [9, 10, 11, 12]:

$$E_{\mathrm{wob}} = E(I, n_w = 1) - [E(I-1, n_w = 0) + E(I+1, n_w = 0)]/2,$$

where $E(I)$ is the level energy with angular momentum I. The experimental values of E_{wob} for both the wobbling bands have been obtained in the present work and the wobbling frequency are plotted with spin (I) as shown in Fig. 5.8. It has been observed that the wobbling frequency decreases with spin for the negative parity wobbling band whereas, it increases for the positive parity wobbling band. The general understanding suggest that the increase (decrease) of wobbling frequency with spin I is the manifestation of LW (TW). However, the the low-Ω, $i_{13/2}$ configuration for the positive parity band is in contradiction to the LW geometry of the coupling of the odd quasiparticle. Therefore, more in depth analysis is needed to understand the nature of these two bands. It is worth pointing out that Frauendorf and Dönau showed that it is possible, in case of TW, that the wobbling frequency increases with the increase of spin for initial lower values of spin for a special condition on the ratio of moments of inertia

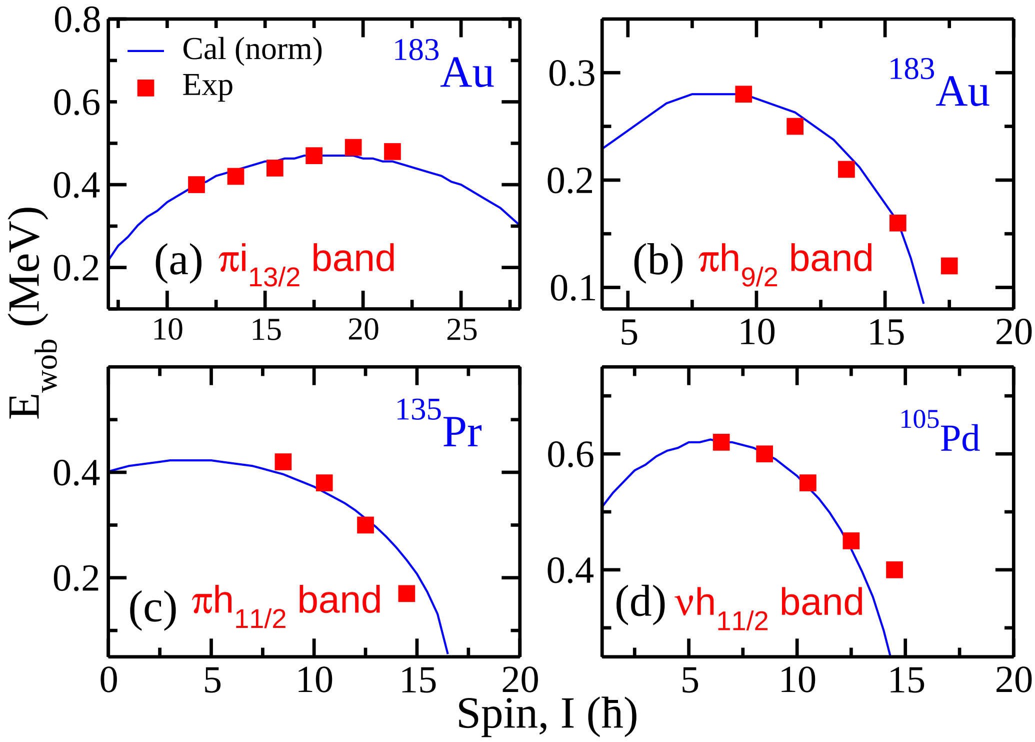

Figure 5.9: Experimental and calculated values (see text for details) of wobbling energies as a function of angular momentum (I) for the (a) positive ($i_{13/2}$) and (b) negative ($h_{9/2}$) parity wobbling bands in ^{183}Au. For comparison, the same for the normal deformed TW bands in ^{135}Pr (c) and ^{105}Pd (d) are also shown. Data for the later two nuclei are obtained from Ref.[11] and [9], respectively.

along short, long and medium axes [14]. However, that feature has not been observed in any of the wobbling bands observed so far, prior to this work and it is likely that the wobbling band based on $\pi i_{13/2}$ orbital observed in ^{183}Au in this work, is that special mode of TW as predicted in Ref.[14].

5.4 Theoretical Calculations and Conclusions

In order to understand the observation of multiple wobbling bands in ^{183}Au, theoretical calculations have been performed in the frame work of particle rotor model (PRM) [14, 22, 23, 24, 25]. The input deformation parameters of $\beta_2 = 0.30$ and $\gamma = 20.0°$ have been obtained for the negative parity band while for the the positive parity band the β_2 and γ values are 0.29 and 21.4°, respectively as obtained from CDFT calculations [26]. The dependence of the defor-

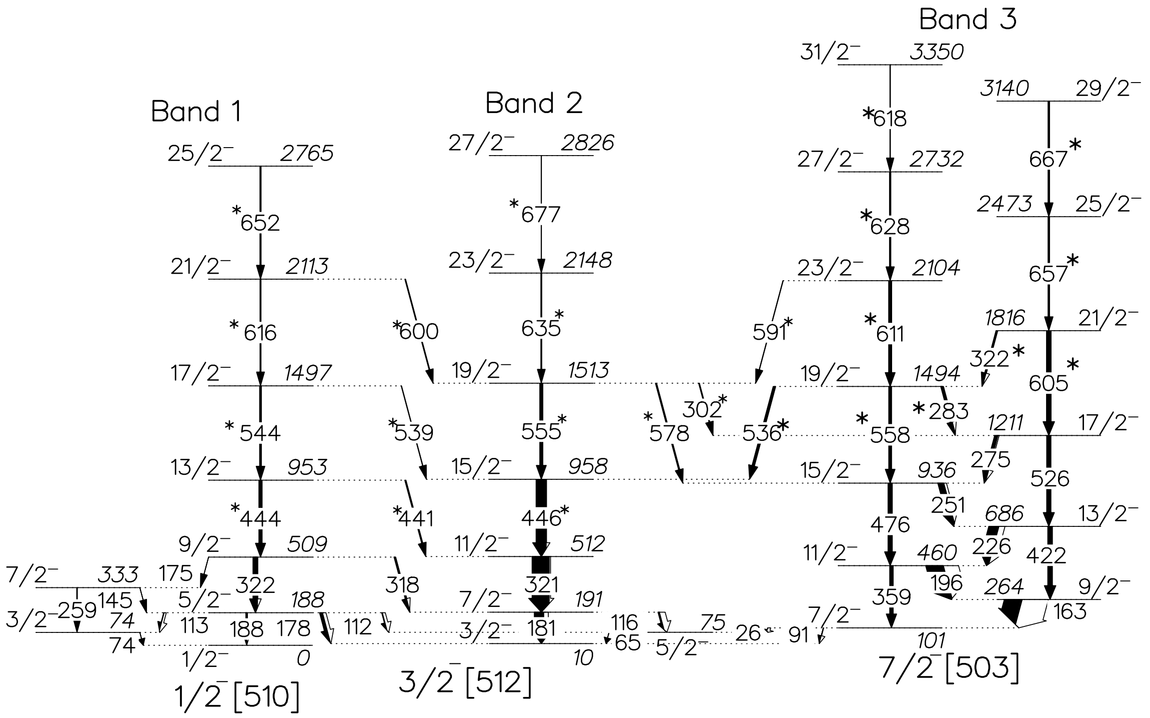

Figure 6.1: Negative parity states of level scheme of ^{187}Os, proposed from the present work. The width of the transitions are proportional to their intensity and new γ transitions are marked by asterisks(*)

Table 6.1: List of γ rays belonging to negative parity bands of ^{187}Os with their energies (E_γ) and intensities (I_γ). The placement of these γ rays in the level scheme are denoted by the energy (E_i) and spin-parity (I_i^π) of the decaying state. The measured values of R_{DCO} and Δ_{PDCO} along with the adopted multipolarities are also given.

E_γ (keV)	E_i (keV)	I_i^π	I_γ^a	R_{DCO}	Δ_{PDCO}	Multipolarity
25.9(2)	101	$7/2^-$	38(12)[1]			(M1+E2)
65.31(2)	75	$5/2^-$				(M1+E2)
74.3(2)	74	$3/2^-$				(M1+E2)
91.1(2)	101	$7/2^-$	1.6(11)[1]			(E2)
112.4(2)	188	$5/2^-$	3.9(1)			(M1+E2)
113.3(2)	188	$5/2^-$	2.9(3)			(M1+E2)
115.8(2)	191	$7/2^-$	8.17(3)	0.49(6)[2]		M1+(E2)

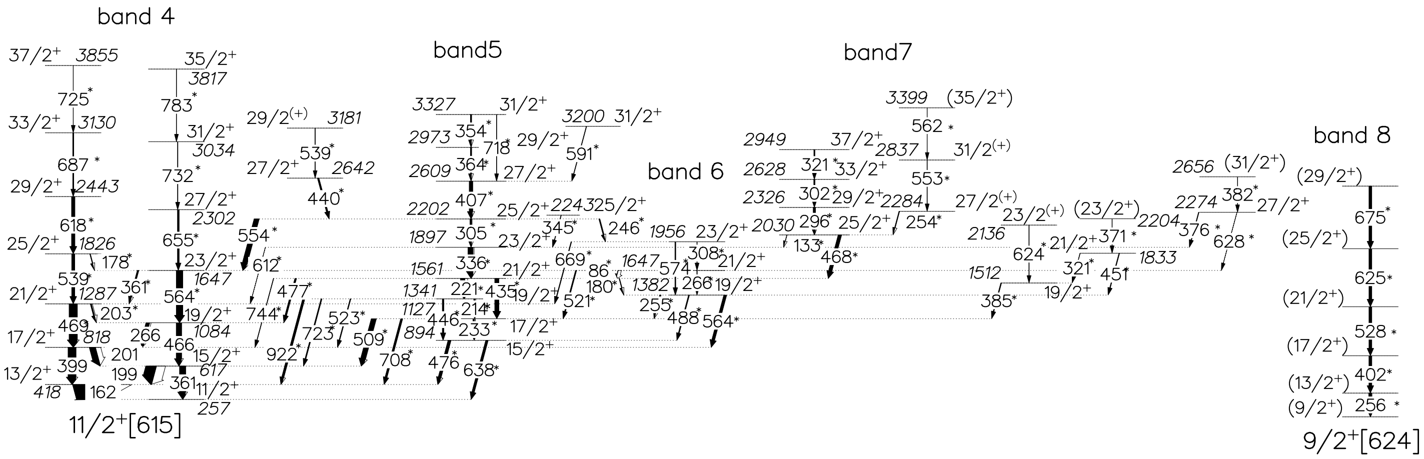

Figure 6.2: Positive parity states of level scheme of ^{187}Os, proposed from the present work. The width of the transitions are proportional to their intensity and new γ transitions are marked by asterisks(*)

6.2 Experimental Results

The proposed negative and positive parity parts of the level scheme of ^{187}Os, as obtained using coincidence relation and intensity argument is shown in Fig. 6.1 and 6.2. The experimental γ-ray transition energies (E_γ), the level energies (E_i), the spins and parities of the initial (I_i^π) levels, the R_{DCO} and Δ_{PDCO} values along with the adopted multipolarities of the γ-rays belong to the negative and positive parity parts have been tabulated in Table. 6.1 and Table. 6.2. A total of 94 new γ ray transitions have been identified for the first time and are placed in the level scheme. These are marked by asterisks (*) in the level schemes. All the bands have been extended upto first pair alignment.

The relative intensities of the γ rays were measured from different single and double-gated spectra to remove contamination from similar γ ray energies of other bands in ^{187}Os as well as γ rays coming from the other nuclei produced in this reaction. All the intensities quoted in the above table are after proper normalization.

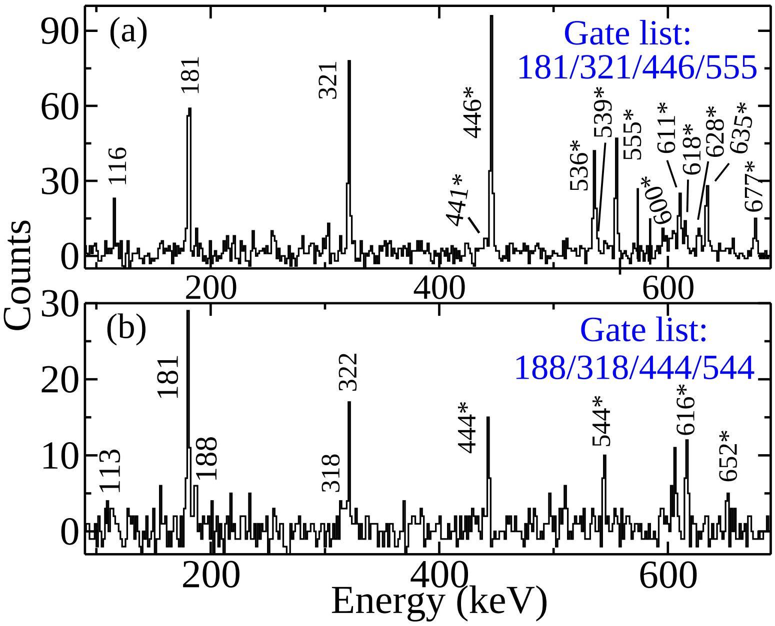

Figure 6.3: Double gated spectra of gatelist of (a) 181, 321, 446, 555 keV and (b) 188, 318, 444, 544 keV transitions in band 2 and 1, respectively. Newly observed transitions are marked by (*).

6.2.1 Bands 1 and 2

The spin and parity of the band heads of bands 1 and 2 were assigned as $1/2^-$ and $3/2^-$ and were known upto the level energy at 509 keV and 511 keV, respectively, from the previous work of Sodan et al. [7]. However, the levels at 509 keV, 511 keV and the low lying level 341 keV were tentatively placed in the level scheme. In the present analysis bands 1 and 2 have been extended upto the excitation energies of 2765 and 2826 keV and angular momentum of $25/2^-$ and $27/2^-$, respectively. The tentatively placed 509-keV level of band 1 has been confirmed in the present analysis. All the γ rays of band 1 along with the newly observed transitions are shown in the double gated spectra of Fig. 6.3. The spin and parity for most of the levels of band 1 have been assigned using R_{DCO} and Δ_{PDCO} measurements of the decaying γ rays.

[1]From the 399-keV (E2) gate.
[2]From the 466-keV (E2) gate.
[3]From the 539-keV (E2) gate.
[4]From the 361-keV (E2) gate.
[5]From the 435-keV (E2) gate.
[6]From the 574-keV (E2) gate.
[7]From the 468-keV (E2) gate.
[8]From the 708-keV (E2) gate.
[9]From the 539-keV (E2) gate.

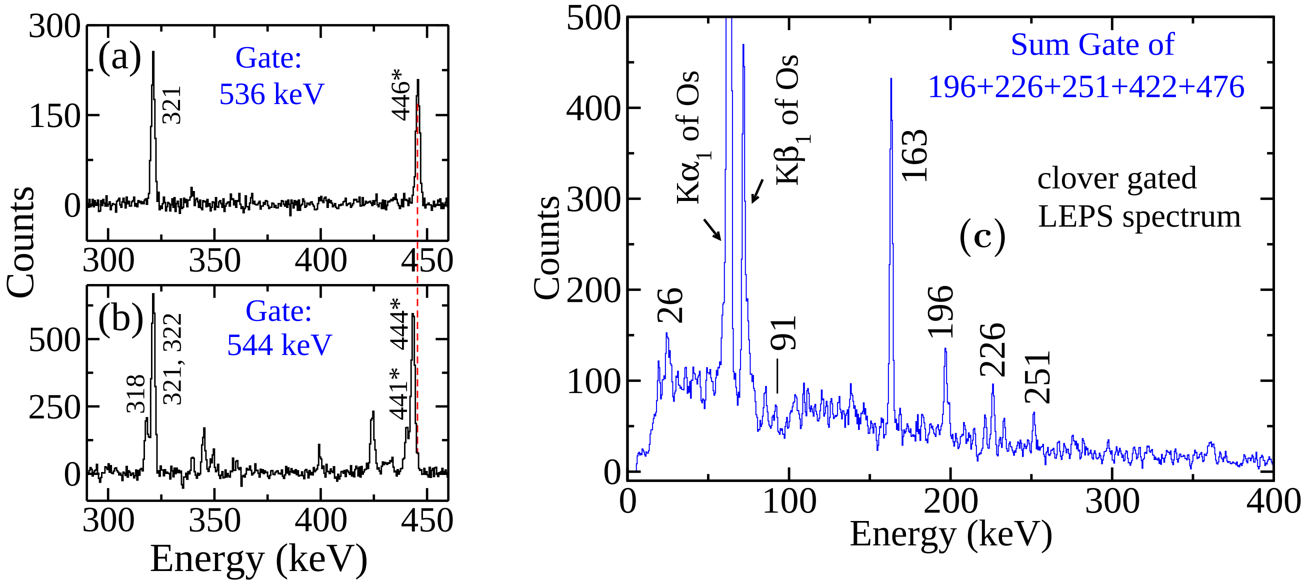

Figure 6.4: Coincidence spectra gated by (a)536-keV and (b) 544-keV showing the closely lying gamma rays of band 2 and 1. (c) Clover gated LEPS spectrum projected from clover vs. LEPS γ-γ matrix. Projection of the sum gate of 196, 226, 251, 422, and 476 keV in LEPS detector shows the low energy 26 keV transition. The new γ-rays are marked by asterisks (*).

Similarly, the tentatively placed level 511 keV in band 2 has been confirmed but the 341 keV level has not been seen in the present analysis. The double gate on the gamma rays of band 2 established the newly observed transitions of band 2 and also the connections between bands 3 and 2 as shown in Fig. 6.3. In the present analysis, the closely spaced tentative levels of 511 and 509 keV could be separated. In Fig. 6.4 the spectra with single gate on 536 and 544 keV are shown. The 444-keV and the 446-keV lines, which decays to 509-keV and 511-keV levels, are clearly seen as separate γ rays. The 441-keV line is also seen in the 544-keV gate but not in the 536-keV gate. Both 321- and 322-keV lines are seen in these two gated spectra, but the 318-keV line is seen only in the 536-keV gate. This again confirms the two seperate levels at 509 keV and 511 keV. Similarly, the other closely spaced levels could be separated out by appropriate gating transitions.

6.2.2 Band 3

The low-lying states in band 3 were known from earlier works and the $7/2^{-}[503]$ configuration of the $7/2^{-}$ band head at 101 keV was proposed by S. G. Malmskog et al.[11]. This configuration

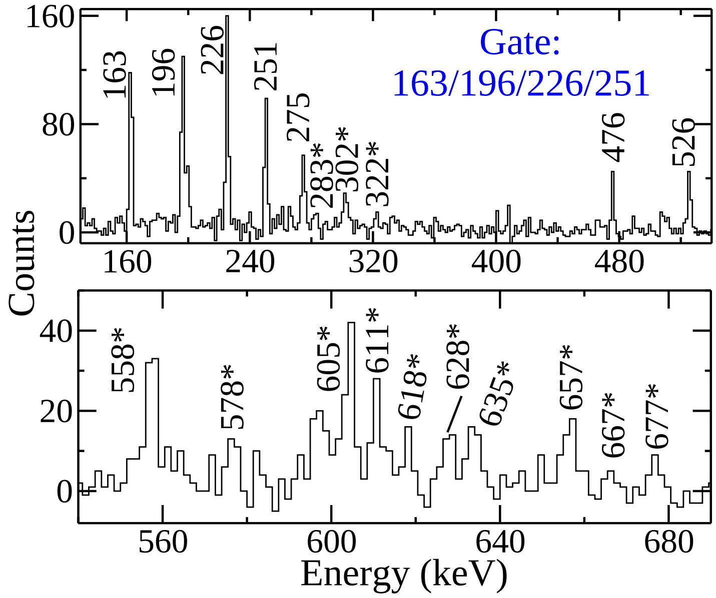

Figure 6.5: Double gated spectra coresponding to gate list of 163, 196, 226, 251 keV of band 3 from γ-γ-γ cube. new γ rays are marked by asterisks (*).

has been adopted in the later works as well [7, 12]. The decay transitions from this level, was however, could not be observed in all earlier works as they are of low energies and highly converted (large electron conversion coefficient, α_T) transitions of energy 26 keV and 91 keV. A good estimate of their total intensity, γ-ray intensity and α_T have been given by Harmatz et al.[13]. It was reported that the total transition intensity of 91-keV is about two orders of magnitude less than the 26-keV one [13]. In the present work, the low-energy, 26-keV γ ray could be observed in the LEPS detector, as shown in Fig.Fig. 6.4(c). This spectrum is a projection from the LEPS vs. clover matrix with sum gates (put on the clovers) on the strong transitions in band 3. The 91-keV line is also seen, albeit very low counts, in this spectrum. The γ-ray branching ratio of the 26-keV, M1 and the 91-keV, E2 transitions has been obtained as 96 : 4 in the present work, which is in good agreement with the values reported by Harmatz et al. (94.5 : 5.5) and the value (95.5 : 4.5) quoted in Ref.[14].

The band 3 of band head spin and parity $7/2^-$ was reported upto 1211 keV level. Even the 1211 keV level was tentatively placed with a tentative gamma ray of energy 526 keV [7]. In the present analysis the band 3 has been extended upto the excitation energy of 3350 keV of angular momenum $31/2\hbar$. The tentatively placed gamma ray of energy 526 keV has been confirmed in the double gated spectra of 163, 196, 226 and 251 keV as shown in Fig. 6.5. All

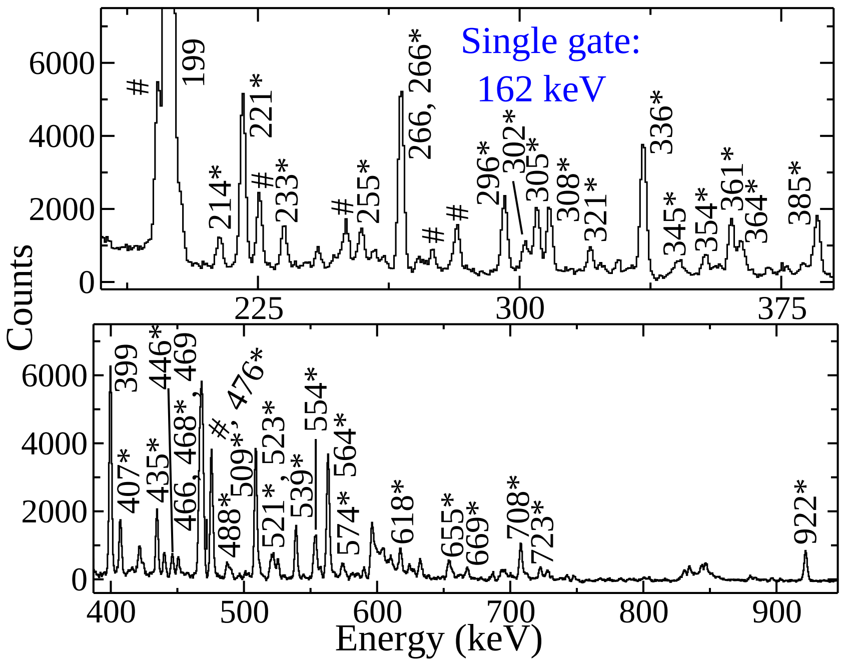

Figure 6.6: Single-gated (162 keV of band 4) spectrum projected from γ-γ matrix. New γ rays are marked by asterisks (*) and the contaminant γ rays are marked by #.

the new transitions of band 3 and the connecting transitions between band 2 and 3, shown in Fig. 6.5, are marked by asterisks (*).

6.2.3 Bands 4, 5, 6, 7 and 8

The single gated spectrum in the gate on an earlier known 162 keV transition shows most of the already known transitions in band 4 and the new gamma rays belonging to the band 5 and 6 as shown in Fig. 6.6. The band 4, based on the $\nu i_{13/2}$ configuration with band head spin and parity at $11/2^{+}$ was known upto the excitation energy at 1084 keV by Sodan et al. [7]. In the present experiment, the band 4 has been extended upto the the excitation energy of 3855 keV (upto first particle alignment). All the new γ rays of band 1 have been confirmed in the sum double-gated spectra shown in Fig. 6.7 with gates put on a few low-lying gammas in the two signature partners. The spin and parity of the new levels of band 4 have been assigned using the DCO ratio and polarisation asymmetry measurement of the newly observed gamma rays of band 4.

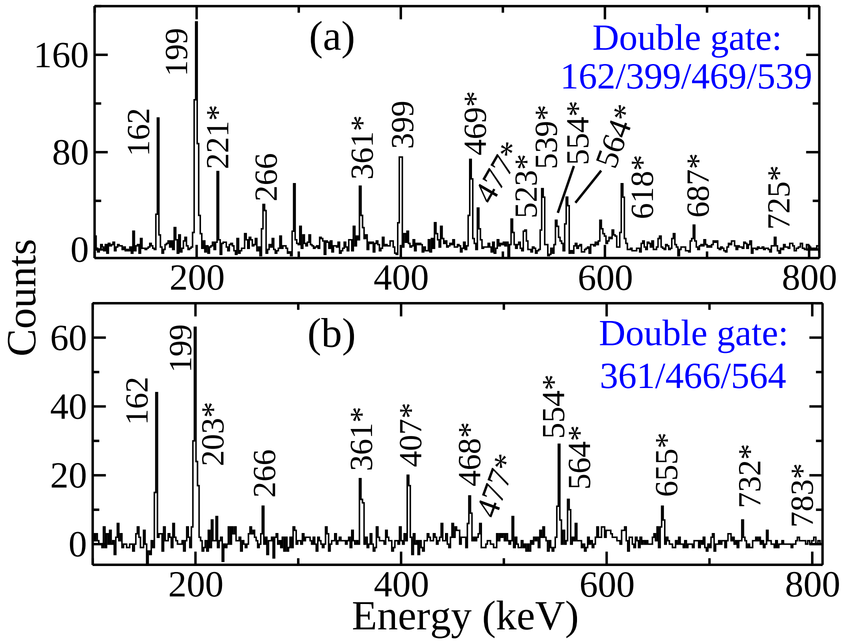

Figure 6.7: Double gated spectra coresponding to gate list of 162, 399, 469, 539 keV and 361, 466, 564 of band 4 from γ-γ-γ cube. New γ rays are marked by asterisks (*).

The band 5 has been newly observed in the present analysis. Most of the new transitions along with the new connecting transitions between band 4 and 5 have been confirmed in the single gated spectrum of 162 keV (Fig. 6.6) and also double gates on already known transitions of positive parity main band (Fig. 6.7). The band 5 has been extended upto the excitation energy of 3327 keV and the new intra and inter-band γ rays of band 5 have been confirmed in the single gate of a new 221 keV transition (Fig. 6.8). The band head spin and parity has been assigned as $15/2^+$ from the DCO ratio and polarisation asymmetry measurements of 638 and 476 keV transitions from 435 keV (pure E2) gated spectrum. The multipolarity of the new cross-over transition 435 keV, has been confirmed from the DCO ratio measurement in a previously known pure E2 (361 keV) gate and the type of 435 keV has been confirmed as the electric from the polarisation asymmetry measurement.

A new band 6 has been observed for the first time in the present analysis, with band head spin and parity $19/2^+$. Most of the inter-band transitions of band 6 and cross-over 574 keV transition have been confirmed in the single gate of 162 keV (Fig. 6.6). The multipolarity of newly observed 574 keV cross-over transition (pure E2) can be obtained using DCO ratio measurement in already known E2 gate at 399 keV and the electric nature has been confirmed form the polarisation asymmetry measurement. The band head spin and parity of band 6

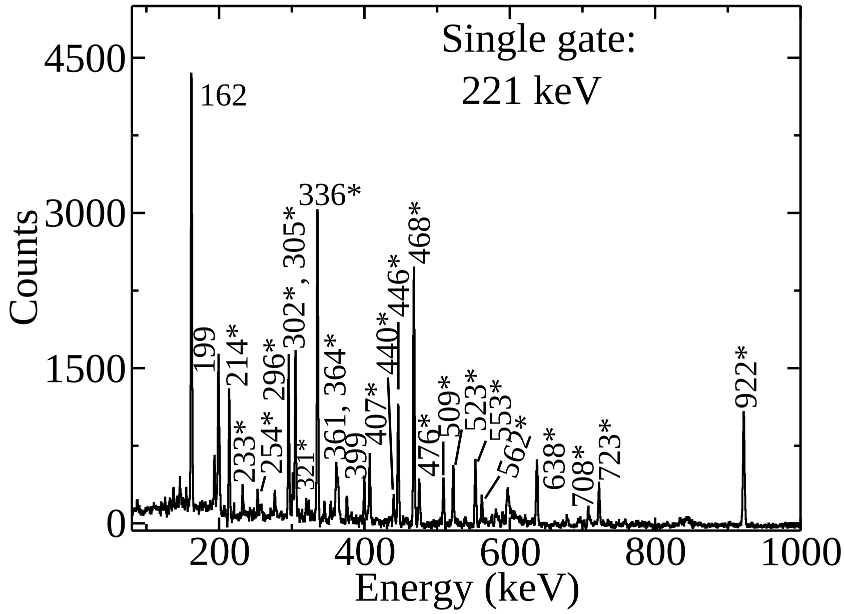

Figure 6.8: Single gate of 221 keV of band 6 from γ-γ matrix. New γ rays are marked by asterisks (*).

have been confirmed from the measurement of multipolarity and nature of the decaying 488 keV transition. This transition can be confirmed as a pure E2 in the DCO gate of 574 keV transition. All the inter and intra-band transitions of band 6 have been shown in the sum-gate of 246 and 308 keV transitions (Fig. 6.9(a)).

The band 7 has been found for the first time in the present analysis at an excitation energy of 2030 keV and band head spin and parity $25/2^+$. This band head spin- parity of this band has been assigned from the DCO and polarisation asymmetry measurement of the 468 keV transition. The E2 nature of the 468 keV transition has been obtained from the 466 keV pure E2 DCO gate and polarisation asymmetry measurement. The new γ rays of band 7 have been shown in the single gate of 221 keV (Fig. 6.8).

Another sequence of gamma rays (band 8) have been found from the present analysis which are in coincidance with each other as shown in Fig. 6.9(b) but the connection between this band structure with any other bands in ^{187}Os has not been observed yet. Therefore, the band head excitation energy and spin-parity is not possible to fix. It has been also checked that this sequence of gamma rays are not present in the neighbouring iostopes which are populated in this reaction.

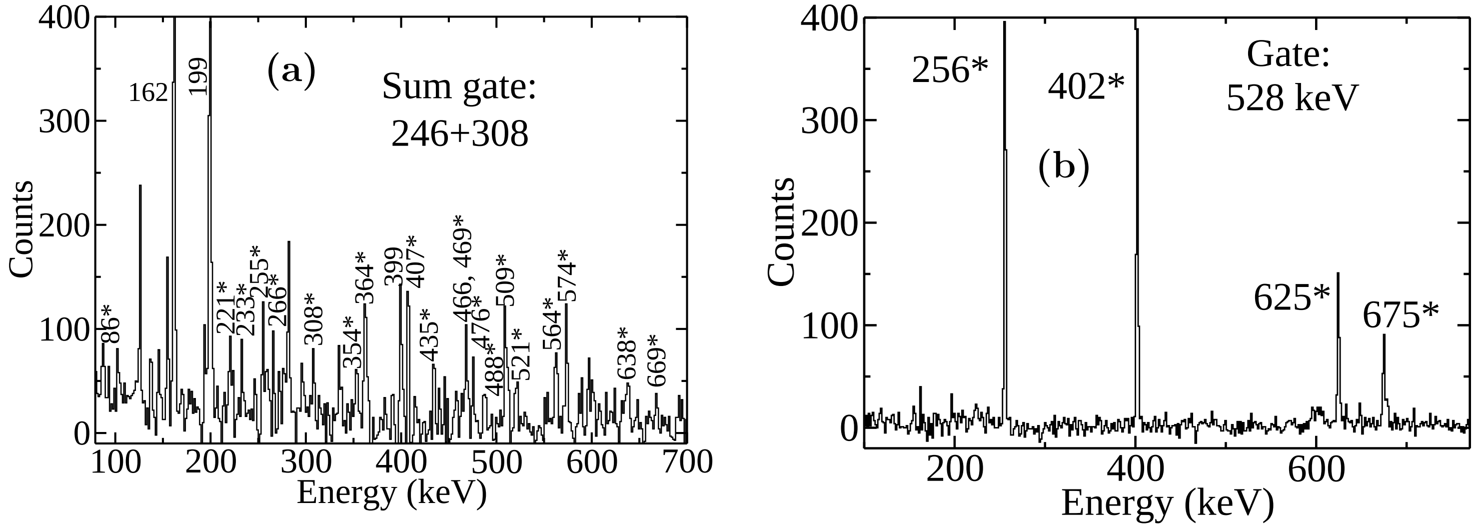

Figure 6.9: (a) Sum gate of 246 and 308 keV of band 6 from γ-γ matrix. (b) Single gate of 528 keV of band 8 from γ-γ-γ cube. New γ rays are marked by asterisks (*).

6.3 Discussions

The rotational bands based on $1/2^-$, $3/2^-$ and $7/2^-$ states of ^{187}Os indicate the occupation of odd-neutron in the single particle orbitals of $2f_{5/2}$, $3p_{3/2}$ and $1h_{9/2}$, respectively. The first excited state $3/2^-$, is an isomeric state [12], corresponding to the $\nu p_{3/2}$ orbital lying close to the neutron Fermi level. The $7/2^-$ state, corresponding to the odd-neutron in Ω=$7/2^-$ Ω component of $\nu h_{9/2}$ orbital, is an isomeric state in the Os isotopes [12]. Various deformed rotational bands in ^{187}Os isotopes could be understood from the coupling of the odd neutron with even-even gamma deformed ^{186}Os core [5].

The aligned angular momenta of the unpaired nucleon along the rotational axis (x) is obtained, in the cranked shell model [15], by substractting the rotational aligned angular momentum of reference configuration from the total aligned angular momentum $I_x(=\sqrt{I(I+1)-K^2})$ of the nucleus. Rotational alignments as a function of rotational frequencies of different bands in ^{187}Os have been done to understand the nature of the bands. In case of odd mass nuclei, the neighbouring even-even nucleus is considered as reference and the Harris parameter of j$_0$=20$\hbar^2 MeV^{-1}$ and j$_1$=94$\hbar^4 MeV^{-3}$ of the reference ^{186}Os can be obtained from the fitting of the ground state rotational band [5], as shown in Fig. 6.10(a).

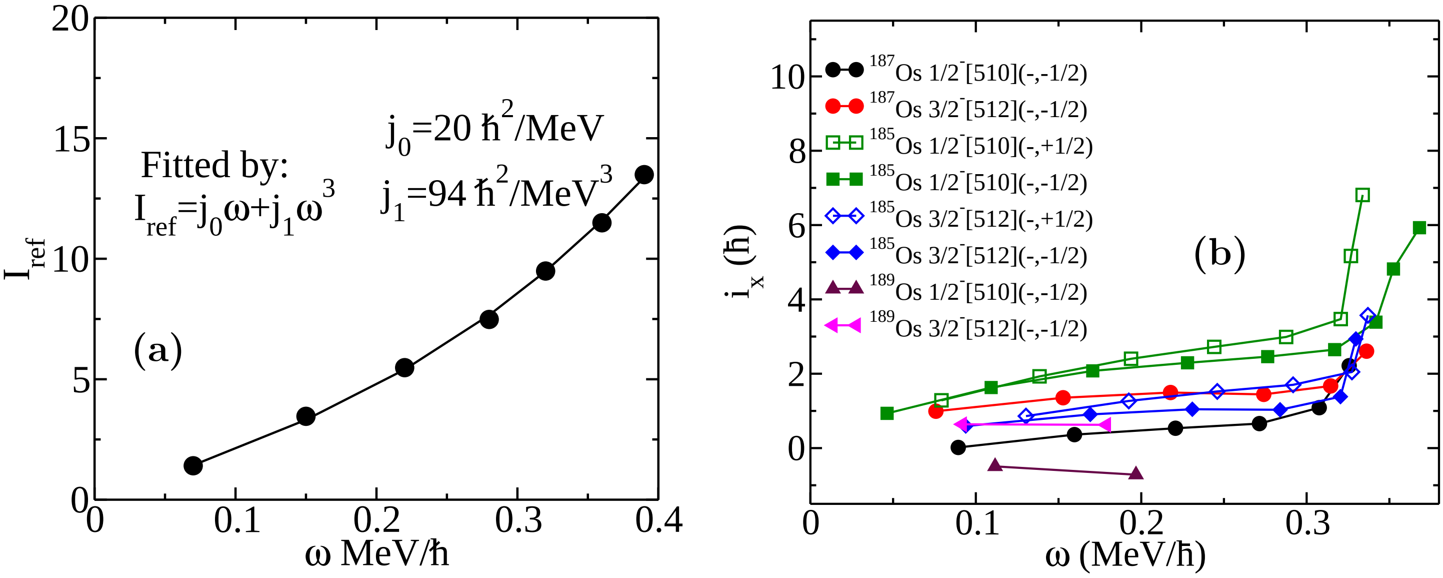

Figure 6.10: (a) Harris parameters (j_0 and j_1) estimated from even-even ^{186}Os ground state rotational band. (b) Aligned angular momentum i_x as a function of rotational frequency (ω) for the twin bands 1 and 2 in ^{185,187,189}Os.

uration of $7/2^-[503]$. The aligned angular momentum (i_x) as a function of rotational frequency (ω) of the bands based on $7/2^-[503]$ has been plotted for ^{183}Os (N=107) [22], ^{185}Os (N=109) [4], and ^{187}Os (N=111) nuclei as shown in Fig. 6.11(a). The band based on $7/2^-[503]$ in ^{185}Os (neutron number N=109) shows delayed crossing at crossing frequency $\hbar\omega$=0.34 MeV as compared to ^{183}Os (N=107) which has a crossing frequency of $\hbar\omega$=0.23 MeV. The delayed crossing in ^{185}Os has been explained by the existence of N=108 deformed shell gap [4]. But the experimental data on the effect of next deformed shell gap at N=110 on an odd neutron nucleus was absent. As shown in Fig. 6.11(a), ^{187}Os (N=111) has a delayed crossing with a crossing frequency $\hbar\omega$=0.31 MeV. Therefore, the crossing frequency of band 3 in ^{187}Os is delayed compared to ^{183}Os but earlier than ^{185}Os. According to Ngijoi-Yogo et al. [8], the delayed crossings have been observed for the isotopes of Hf and W with neutron number 108 and 110 and crossing frequencies $\sim$ 0.4 MeV has been reported. The smaller crossing frequency for the same isotones in Os nuclei may be due to the the presence of gamma deformation. The energy staggering S(I) of a rotational band can be obtained by S(I)= E(I)-[E(I+1)+E(I-1)]/2 which will give better insight about the nuclear structure. Staggering vs. spin($\hbar$) has been plotted in

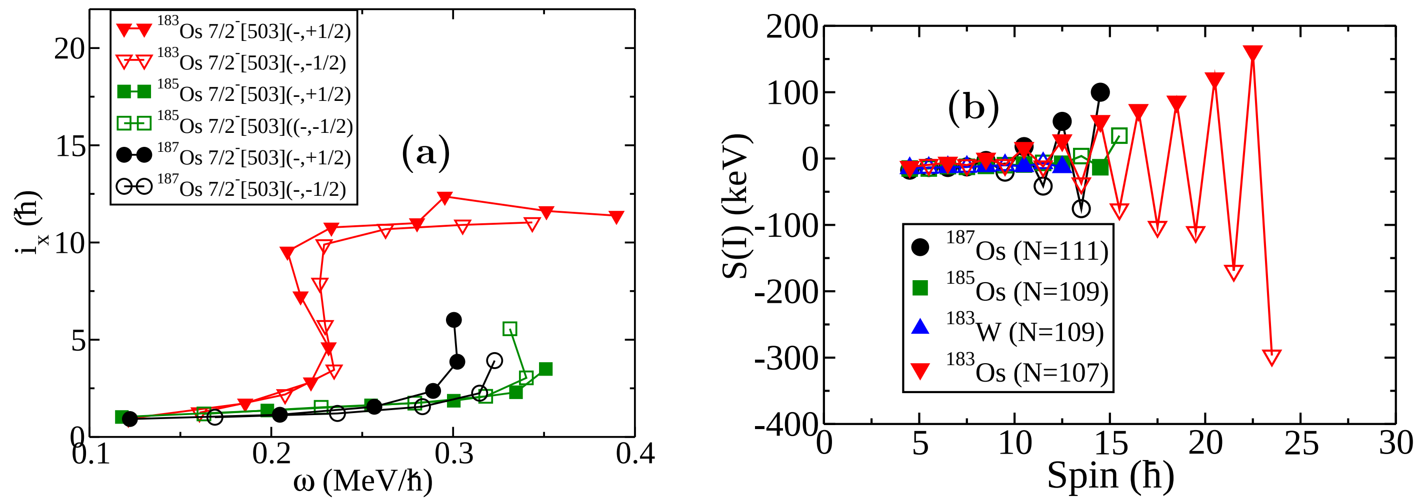

Figure 6.11: (a) Aligned angular momentum i_x as a function of rotational frequency (ω) for the $\nu h_{9/2}$ band in ^{183,185,187}Os. (b) Energy staggering (S(I))) vs. spin ($\hbar$) for the $\nu h_{9/2}$ band in ^{183,185,187}Os and ^{183}W.

Fig. 6.11(b) for different odd-A Os and W isotopes for the same band based on $7/2^-[503]$. All the isotopes show very similar behavior of S(I) with no staggering at lower spin (I). However, at higher spins, they differ for the Os isotopes. ^{183}Os (N = 107) and ^{187}Os (N = 111) have similar (large) staggering after I = 9.5$\hbar$. In case of ^{185}Os (N = 109), the staggering is small and in opposite phase to that of ^{183,187}Os. Data on W isotopes corresponding to the same neutron number are not known at higher spins for comparison. The large signature splitting of band 3 based on high Ω orbital ($\Omega = 7/2$) in ^{187}Os implies the presence of triaxial deformation.

In a triaxial odd-A Os isotope, the odd neutron hole can align along the long axis and generate a stable long-axis rotation of a triaxial core.

The intensity ratios between the ΔI = 1 and ΔI = 2 transitions, can be used to measure the ratio between M1 and E2 transition strengths [B(M1)/B(E2)]. It can be used to get the intrinsic quadruple moments (Q_0) for $11/2^-$ to $21/2^-$ states in band 3 using well known relation of equation 4.1 [23]. In this estimation the g_k value of 0.15 is taken, corresponding to the neutron in $\nu h_{9/2}$ from Ref. [24].

Total Routhian surface calculations (TRS) have also been performed for the configuration of band 3. The TRS plots in the (β_2-γ) plane are shown in Fig. 6.16. A stable triaxial minimum with $\gamma = -100°$ to $-90°$ has been obtained for this configurations and it indicates a stable

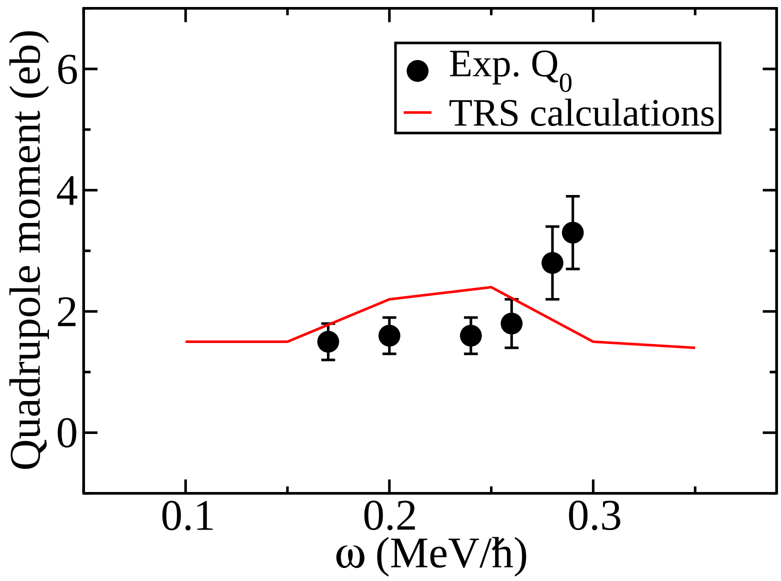

Figure 6.12: Intrinsic quadrupole moments vs rotational frequency (ω) for the $\pi h_{9/2}$ band in ^{187}Os. Experimental valus compared with the results of TRS calculations.

triaxial rotation around long axis (see Fig-2.1). TRS calculations have been performed for different values of rotational frequencies and the (β_2-γ) values corresponding to the minima at each $\hbar\omega$ have been obtained. The theoretical intrinsic quadruple moments can be calculated using these β_2 and γ values from TRS calculations for each $\hbar\omega$ using the equation [25]

$$Q_0 = \frac{6ZA^{2/3}r_\circ^2}{\sqrt{15\pi}}\beta_2(1+0.16\beta_2)\frac{cos(\gamma+30^\circ)}{cos30^\circ} \tag{6.1}$$

. The experimental intrinsic quadruple moments (Q_0) have been plotted with rotational frequencies and compared with the calculated Q_0 as shown in Fig. 6.12. A good agreement of experimental values with the theoratical once confirms the presence of stable long axis rotation in ^{187}Os.

The positive parity main band based on $\nu i_{13/2}$ has also been extended upto the first particle alignment. This band is similar to the $11/2^+[615]$ band observed in the neighbouring isotope ^{185}Os [4]. The aligned angular momentum (i_x) as a function of rotational frequency (ω) of this band has been plotted for ^{187}Os (N=111) nucleus and compared with ^{185}Os (N=109) [4] as shown in Fig. 6.13(a). The energy staggering S(I) of the positive parity rotational band has also been plotted and compared with the positive parity band in the neighbouring odd-A ^{185}Os and has been shown in Fig. 6.13(b). The large energy staggering S(I) with spin in both

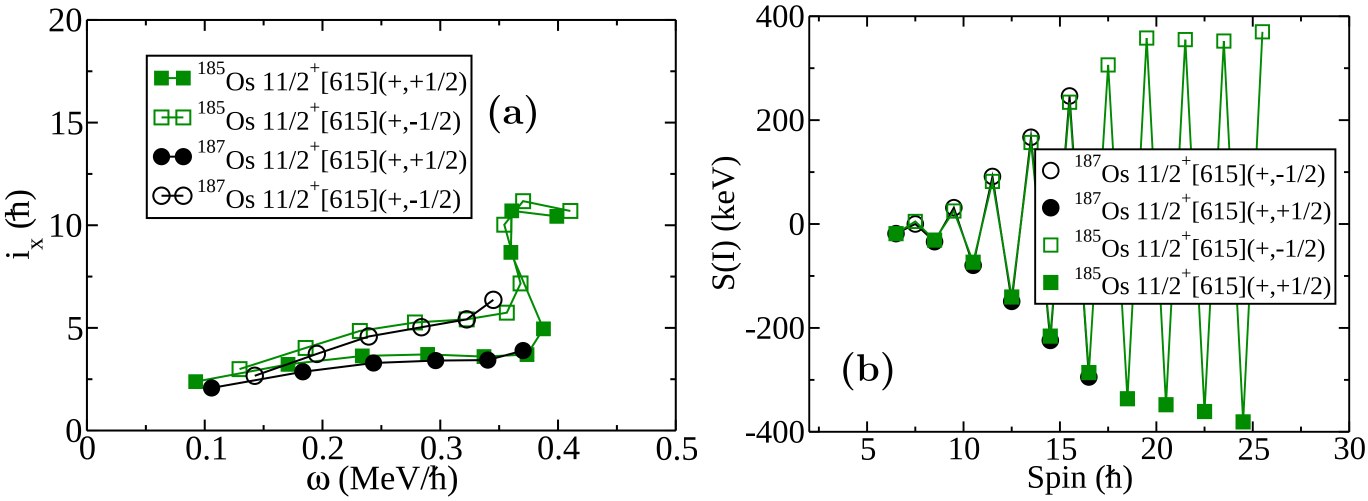

Figure 6.13: (a) Aligned angular momentum i_x as a function of rotational frequency (ω) for the $\nu i_{13/2}$ band in ^{185,187}Os. (b) Energy staggering (S(I)) vs. spin ($\hbar$) for the $\nu i_{13/2}$ band in ^{185,187}Os.

Table 6.3: The systematic comparison of γ and $\gamma\gamma$ band head excitation energies for ^{186,187,188}Os

Nucleus	$K_{1\gamma}$	$E_{1\gamma}$(keV)	$K_{2\gamma}$	$E_{2\gamma}$(keV)	$E_{2\gamma}/E_{1\gamma}$
^{186}Os	2^+	768	4^+	1353	1.76
^{187}Os	$15/2^+$	637	$19/2^+$	1125	1.77
^{188}Os	2^+	633	4^+	1280	2.02

the positive parity bands based on high Ω orbital in ^{185}Os and ^{187}Os can be a menifestation of triaxial nuclear shape.

The band head excitation energies of γ-band and γ-γ band in even-even neighbouring ^{186,188}Os [3, 5] isotopes are mentioned in Table. 6.3. It shows that the band head excitation energy of second 2^+ state of the γ band decreases for heavier Os isotopes. The decrease of band head excitation energy means that the heavier Os isotopes are much more γ deformed as discussed in details at chapter-1. In case of odd-A ^{187}Os, a new γ-band (band 5) and a new γ-γ band (band 6) at the excitation energy of 637 and 1125 keV have been observed with respect to the band head excitation energy of the positive parity main band 4. The generation of γ-band and γ-γ band in ^{187}Os can be represented by a coupling of odd neutron in $11/2^+$[615] orbital with the γ-band and γ-γ band at even-even ^{186}Os. The $11/2^+$ state in positive parity main band

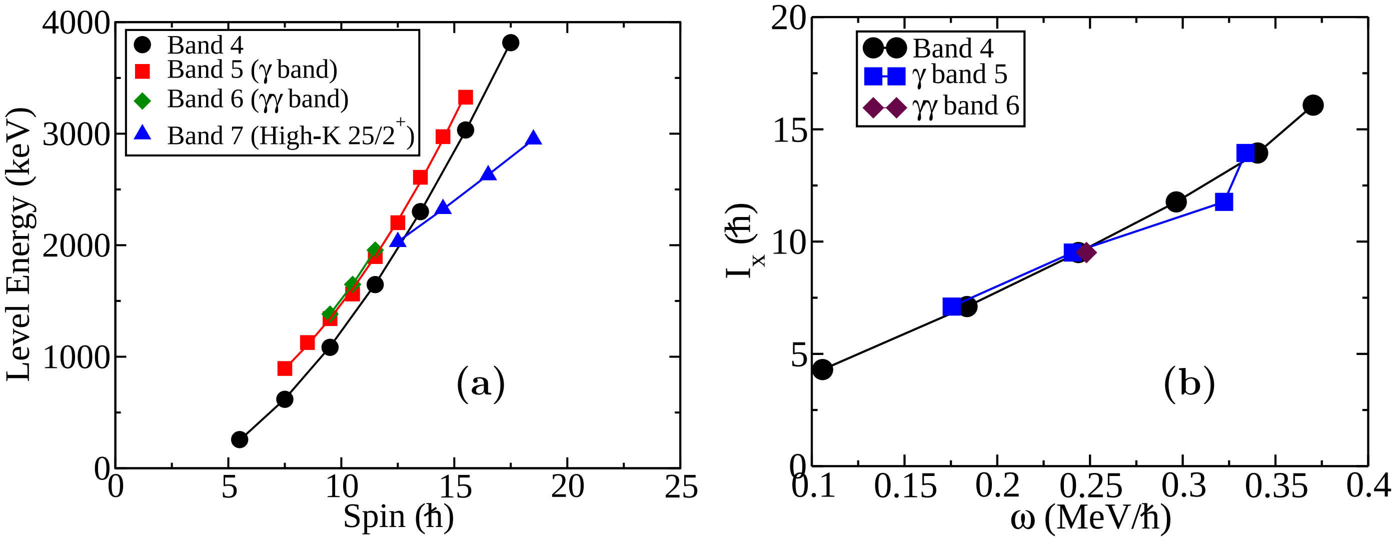

Figure 6.14: (a) Level energy vs. spin ($\hbar$) of the band 4, band 5, band 6 and band 7. (b) Total aligned angular momentum (I_X) vs. rotational frequency (ω)for the band 4, 5, and 6.

in ^{187}Os nucleus couple with the 2^+ and 4^+ state of the γ-band and γ-γ band in ^{186}Os and generate a γ-band and γ-γ band in ^{187}Os. The band head spin and parity of the γ and γ-γ bands are $15/2^+$ and $19/2^+$ respectively as observed in other γ and γ-γ bands in odd A nuclei [26, 27]. The band 5 follows all the signatures of a γ band (disscussed in chapter 1)

- Band 5 is a ΔI = 1 band with regular energy spacing [26].
- The band 5 strongly decays to positive parity main band 4 via M1+E2 and stretched E2 transitions as observed in other γ bands in odd-A nuclei [26, 27].
- The level energy vs angular momentum of positive parity main band, γ-band and γ-γ band have been plotted (Fig. 6.14 (a)) and fitted using second order rotational energy formula of

$$E(I,K) = E_K + A[I(I+1) - K^2] + B[I(I+1) - K^2]^2 \tag{6.2}$$

The inertia parameter A is determined from the fit. The inertia parameter A of positive parity main band, γ-band and γ-γ band are 13.33, 12.28, 10.03 keV respectively. The

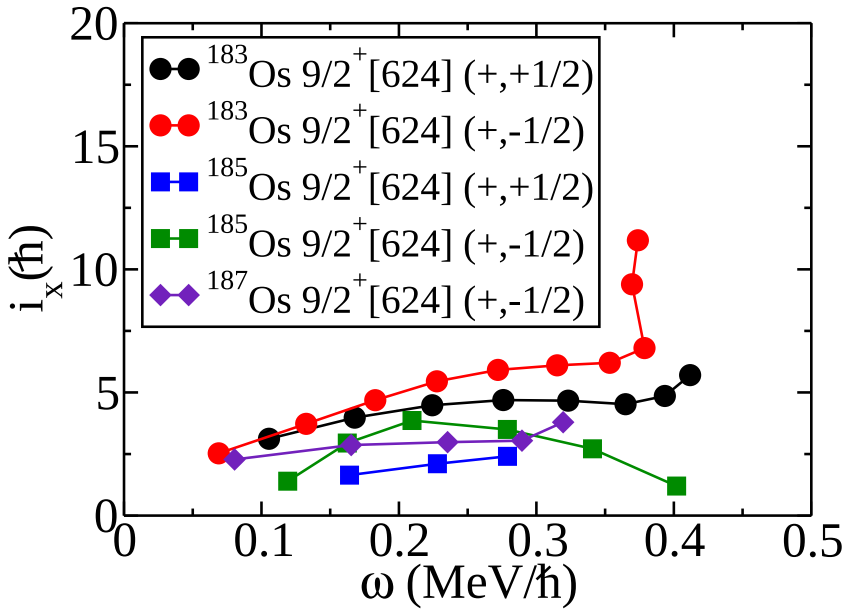

Figure 6.15: Aligned angular momentum i_x as a function of rotational frequency (ω) for the band based on $9/2^+[624]$ configuration in ^{183,185,187}Os.

similar values of inertia parameters of the bands indicate the similar configuration of these two bands.

- Fig. 6.14 (b), shows plots of the Ix (Equation-2.55) vs. rotational frequency for the positive parity main band and γ band. The slopes of the curves are the kinematic moment of inertia. From Fig. 6.14 (b), It can be seen that the slope of the newly observed γ band is similar to the positive parity main band. This is consistent with the expectation of a γ vibrational band.

The non-axial deformation parameter γ can be extracted from the Davydov model [28] using the energy ratio $E_{2_2^+}/E_{2_1^+}$ of the first two 2^+ states for even-even nuclei [25]. In case of ^{187}Os (odd-A), the deformation parameter γ can be extracted using the energy ratio $E_{15/2_2^+}/E_{15/2_1^+}$ of the first two $15/2^+$ states with respect to the band head excitation energy of the positive parity main band using the equation[25]:

$$\frac{E_{15/2_2^+}}{E_{15/2_1^+}} = \frac{1+X}{1-X}, \tag{6.3}$$

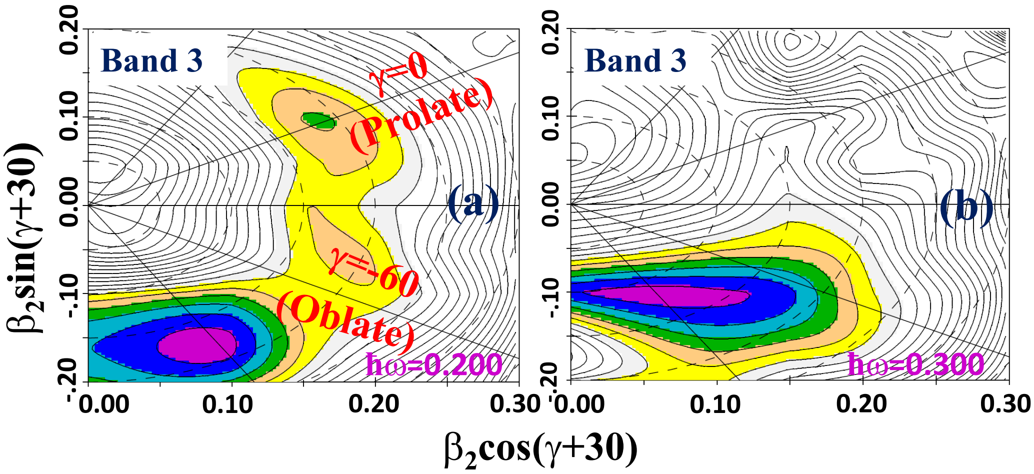

Figure 6.16: 1-qp configuration of $\nu h_{9/2}$ corresponding to the band 3 in ^{187}Os at rotational frquency ($\hbar\omega$) 0.2 (a) and 0.3 (b) MeV

The aligned angular momentum (i_x) as a function of rotational frequency (ω) of the band 8 (band head spin parity $9/2^+$) has been plotted for ^{187}Os (N=111) and compared with the bands based on $9/2^+$[624] configuration in ^{183}Os (N=107) and ^{185}Os (N=109). Similar values of their aligned angular momenta, i_x, as shown in Fig. 6.15, support the configuration assignment of the band 8 as $9/2^+$[624].

6.4 Theoretical Calculations

6.4.1 TRS Calculations

In order to understand the different shapes in ^{187}Os and the effects of the high-j active neutron orbitals (positive and negative) on shapes, the total Routhian surface (TRS) calculations have been performed, as discussed in Chapter 2.5 and 2.6. The formalism of Nazarewicz et al., as depicted in Ref. [32, 33], has been used and the detail technical procedure has been given in Ref. [34] (and references there in). As mentioned before, the deformation of a nucleus for a particular configuration at a particular rotational frequency corresponds to the minimum in the contour plots of the potential energies in β_2 and γ ($\gamma = 0° =$ prolate and $\gamma = -60° =$ oblate) mesh points. The energy minimization on β_4 was done for each value of β_2 and γ. Few TRSs have been calculated for different configurations and at several rotational frequencies

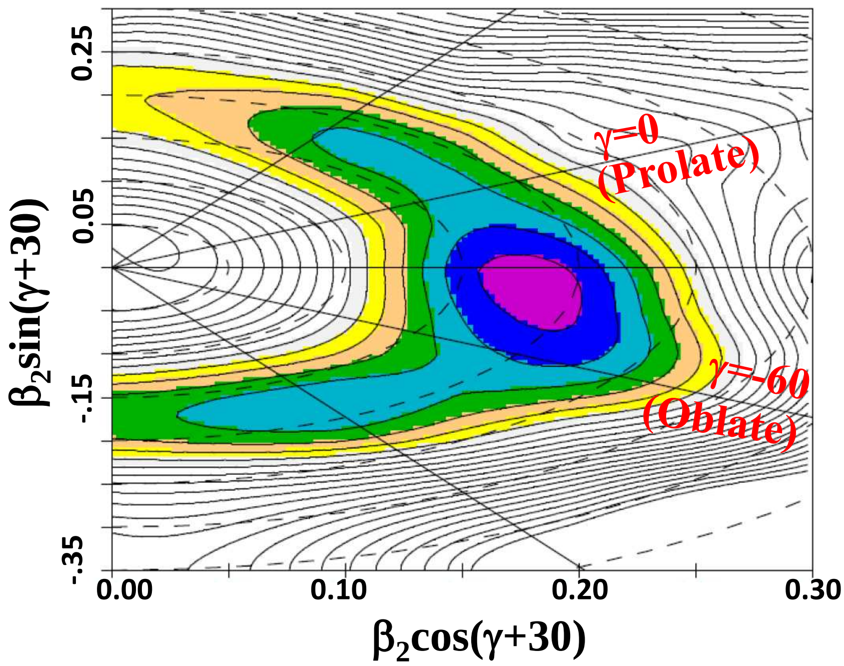

Figure 6.17: 1-qp configuration of $\nu i_{13/2}$ corresponding to the band 4 in ^{187}Os at rotational frquency ($\hbar\omega$) 0.1 MeV

($\hbar\omega$). The TRS calculations, performed for the configuration corresponding to the band 3 in ^{187}Os as shown in Fig. 6.16 for various rotational frequencies ($\hbar\omega$). The Fig. 6.16 show , a stable energy minimum at near-triaxial deformation with $\beta_2 \sim 0.18$ and $\gamma \sim -92°$ and $\beta_2 \sim 0.12$ and $\gamma \sim -90°$ at rotational frequencies $\hbar\omega$= 0.20 and 0.30 MeV, respectively. The triaxial minima at $\gamma \sim -90°$ indicate that the ^{187}Os has rotation axis around the long-axis of the triaxial core.

The TRS calculation was also performed for positive parity band 4 and is shown in Fig. 6.17. A triaxial shape with $\beta_2 \sim 0.18$ and $\gamma \sim -35°$ has been obtained for the positive parity band 4. The triaxial minimum obtained from TRS calculation supported the observation of γ and γ-γ bands couple with positive parity main band.

6.5 Summary

The excited states in ^{187}Os have been studied by γ-ray spectroscopic technique. The reaction ^{186}W(^{4}He,3n)^{187}Os at 36 MeV of beam energy from the K-130 cyclotron at VECC, Kolkata was used to populate the states and the INGA array with 7 Compton-suppressed clover HPGe

Chapter 7

Summary and Future Outlook

7.1 Summary

In the present thesis work, the excited states of ^{197}Tl, ^{183}Au, and ^{187}Os nuclei have been investigated by populating those using the K-130 cyclotron at the Variable Energy Cyclotron Centre (VECC), Kolkata and employing the gamma ray spectroscopy technique. The population of excited states of ^{197}Tl and ^{187}Os have been done using light ion alpha induced fusion evaporation reaction. On the other hand, the excited states of the neutron defficient ^{183}Au have been populated using heavy ion (^{20}Ne) induced fusion evaporation reaction. All the three experiments performed at VECC. The level schemes of all the three nuclei have been modified significantly with the placement of several new γ lines. The spin and parity of the new levels have been assigned from the DCO ratio and polarisation asymmetry measurements of the decaying transitions. Several new band structures have been identified and the experimental data were interpreted using various theoretical model calculations like TRS calculation, PRM calculation and SPAC model calculation. In this work, various manifestations of triaxial nuclear shape have been reported in the nuclei near Z = 82. The triaxial nuclear shape is manifested by following excitations in nuclei

- Double degenerate chiral band

- wobbling band
- γ vibrational band

In ^{197}Tl, chiral bands could not be observed for 3 and 5 quasi particle (qp) configurations although chiral bands were reported earlier for the 3 and 5 qp configurations in the neighboring odd-A isotope ^{195}Tl. Instead magnetic rotational (MR) bands have been observed in ^{197}Tl. The theoretical calculations of Total Routhian Surfaces (TRS) shows that the deformations in ^{197}Tl for the 3 and 5 qp configurations are much smaller than those for the ^{195}Tl. The chiral geometry can only be obtained with a moderate to large core angular momentum along the medium axis of the rigid triaxial shape with high j particle and hole angular momentum along short and long axes of a triaxial core. The aplanar chiral geometry with finite γ deformation can turn to a planar MR geometry for small values of axial deformation parameter β_2. Hence, it is concluded that an evolution of shape towards lower β_2 with the increase in neutron number in Tl isotopes is responsible for the transition from aplanar to planar configuration of the core-particle-hole geometry which is manifested in the change of the band structure from chiral to MR in ^{197}Tl.

Wobbling motion in atomic nuclei is one of most unique manifestation of rigid triaxial nuclear shape. The wobbling motion has been observed in a very few odd-A nuclei in the whole nuclear chart. ^{183}Au, studied in this work, turns out to be a unique nucleus in which multiple transverse wobbling bands have been identified with different behavior of wobbling energy with spin. Both the wobbling bands in this nucleus, based on positive parity $i_{13/2}$ and negative parity $h_{9/2}$ orbitals, have been found to be of transverse wobbling type. However, the wobbling frequency behaves differently in these two bands as a function of spin. This is, so far, the only nucleus in which both the increasing (positive parity band) and decreasing (negative parity band) behaviours of the wobbling frequency with spin could be identified.

Another manifestation of γ deformation is γ vibrational band. The heavier even-even Os isotopes have 1 phonon and 2 phonon gamma vibrational band but the experimental data on heavier odd-A Os isotopes are very scarce. And it is interesting to see the coupling of odd neutron with triaxial even-even Os core. In ^{187}Os, 1 phonon (γ) and 2 phonon (γ-γ) γ

vibrational bands have been observed for the first time. The most-unfavoured long-axis rotation in triaxial nucleus has also been reported in ^{187}Os for the band based on $\nu h_{9/2}$ orbital.

7.2 Study of ^{197}Tl Nucleus

The excited states of ^{197}Tl nucleus have been populated using light-ion induced fusion evaporation reaction ^{197}Au(^{4}He, $4n$)^{197}Tl and the gamma rays were detected using the VENUS array at VECC with 6 Compton Suppressed Clover HPGe detectors. A new level scheme of ^{197}Tl has been proposed with a placement of 28 new γ transitions. New observation on ^{197}Tl are:

- The spin and parity of 1953 keV has been confirmed as $13/2^{+}$ from the Angular distribution and polarization measurement of 957 keV transition and the state identified as intruder $\pi i_{13/2}$ state.
- A new single particle like band structure (band A) has been identified.
- Main Band C based on intruder $\pi h_{9/2}$ orbital has been extended after first particle alignment and shows maximum gain in alignment of $12\hbar$ corresponding to the neutron pair alignment in $i_{13/2}$ orbital.
- A new band B has been identified and the assigned configuration is $\pi i_{13/2} \otimes \nu i^{2}_{13/2}$.
- The band B has been identified as a 3-qp Magnetic rotational band.
- The experimental level energy and $\frac{B(M1)}{B(E2)}$ ratios have been compared with the calculated values from SPAC model calculations which agree well with the data.
- The TRS calculations for band B also suggest weakly deformed core with β_2=0.09.
- The previously observed 3-qp band has been extended to 5-qp structure ($\pi h_{9/2} \otimes \nu i^{-3}_{13/2}(pf)^{-1}$) and it has been identified as a 5-qp Magnetic rotational band.
- Similar to the band B, the level energies of 5-qp band has been compared with calculated values from SPAC model calculations which match well with the data.

- TRS calculation for the 5-qp structure has been performed and it shows potential surface energy minimum at β_2=0.05.
- 3 and 5-qp chiral doublet bands have been obseved in ^{195}Tl compared to 3 and 5-qp MR band in ^{197}Tl.
- Previously identified band E has been modifed using coincidence relation and has been interpreted as a multiplet of 3-qp band D.

7.3 Study of ^{183}Au Nucleus

The high spin states of neutron defficient ^{183}Au have been populated using fusion evaporation reaction of ^{169}Tm(^{20}Ne, 6n)^{183}Au at 146 MeV of beam energy. The gamma rays were detected using the INGA array at VECC which consisted of 8 Compton suppressed clover HPGe detectors and two LEPS detectors at the time of the experiment. A new level scheme of ^{183}Au has been proposed with the placement of 14 new γ transitions. The new observations in ^{183}Au are:

- The linear polarisation (P) and DCO ratio (R_{DCO}) of the connecting transitions between various bands have been measured and compared with the calculated values of P and R_{DCO} and the mixing ratios δ for the transitions have been determined.
- The $\Delta I = 1$ connecting transitions between the negative parity bands 3 and 2 and between the positive parity bands 5 and 4 have been found to be predominantly E2 ($\sim$90%) in nature. Hence, the bands 3 and 5 have been identified as the wobbling partner bands in ^{183}Au. The branching ratios of inter and intra band $E2$ transitions also suggest the wobbling nature of the bands.
- It has been argued from the involved low-Ω orbitals (obtained from the experimental aligned angular momentum) that both the bands are transverse wobbling in nature.

- The experimental wobbling frequency has been found to increase with spin for positive parity transverse wobbling band whereas, it decreases with spin for negative parity transverse wobbling band.

- The contrasting behaviour of the two wobbling bands could be explained from the Frauedorf-Dönau model of transverse wobbling. For the first time, a transverse wobbling band with increasing wobbling frequency as a function of spin has been identified in ^{183}Au.

- The results obtained in this work on the wobbling bands in ^{183}Au changes our thinking to date that a simple increase or decrease of wobbling frequency with angular momentum automatically indicates longitudinal and transverse wobbling, respectively and concept of I_m, which corresponds to the spin at which the wobbling frequency is maximum in a transverse wobbler, has been introduced.

7.4 Study of ^{187}Os Nucleus

The excited states in ^{187}Os isotope were populated using light-ion induced fusion evaporation reaction ^{186}W(^{4}He, 3n)^{187}Os at 36 MeV of beam energy. The gamma rays were detected using INGA array at VECC which consisted of 7 Compton suppressed clover HPGe detectors and one LEPS detector at the time of the experiment. A new level scheme of ^{187}Os has been proposed with the placement of 94 new γ transitions. The new obervations on ^{187}Os are:

- Bands 1 and 2, based on low-Ω Nilsson configuration, have been extended up to first particle alignments. These bands have been identified as the twin bands with pseudo spin partners.

- The level degeneracy between the twin bands get worsened with increasing angular momentum.

- Band 3 based on $\nu h_{9/2}$ configuration has been extended up to first particle alignment and the delay in crossing frequency has been supported by the existence of $N = 110$ deformed shell gap.

- The experimental intrinsic quadrupole moments have been extracted from $\frac{(B(M1)}{B(E2}$) ratios as a function of rotational frequency and compared with the calculated quadrupole moments which were extracted using calculated deformation parameters β_2 and γ obtained from TRS calculations.

- Experimental quadrupole moments are close to calculated quadrupole moments with a triaxial minimum at γ= -90° and the value of γ= -90° suggests unfavoured long-axis rotation of a triaxial nucleus. The triaxial deformation is also supported by the large energy staggering of band 3.

- Alignment of a pair of particles has also been identified in the positive parity band, based on $\nu i_{13/2}$ configuration, by extending its level scheme to higher spins (Band 4). This band also shows large signature splitting similar to ^{185}Os which can be explained by the presence of finite γ-deformation.

- γ (Band 5) and $\gamma\gamma$ (Band 6) vibrational bands have been identified for the first time in ^{187}Os isotope.

7.5 Future Outlook

In this thesis work, various exotic excitations in atomic nuclei due to triaxial nuclear shape have been observed. The experimental results have also been interpreted well using theoretical model calculations. However, this thesis work opens several new aspects which can be addressed in future work. Some of these are mentioned below.

Frauendorf and Meng predicted the occurrences of chiral band structures in both $A \sim 190$ and $A \sim 130$ mass regions. The availability of high-j orbitals for both protons and neutrons along with the triaxial shapes of the nuclei, which are the primary conditions for generating chiral geometry in a nucleus, are equally likely in these two regions. However, the number of observed chiral bands in $A \sim 190$ region are much less than those in the $A \sim 130$ region. In this thesis work, it has been observed that the heavier Tl nuclei with neutron number $N \geq 116$ are unlikely to show chiral bands as the core deformation becomes smaller. Also, the neutron Fermi level moves further away from the high-j $i_{13/2}$ orbital and becomes closer to the low-j orbitals. Both these scenarios are detrimental to forming the chiral geometry. However, in case of lighter Tl nuclei, the deformation of the core increases and the neutron Fermi level lies close to the high-j $i_{13/2}$ orbital also and thereby, increases the possibility of the chiral geometry. The high spin data on the odd-A and odd-odd Tl isotopes around ^{190}Tl are scarce. Therefore, it is indeed important to study the high spin states in these nuclei to look for the chiral bands, because if chiral bands are not observed even in these nuclei, then the primary conditions based on which the occurrences of chiral bands were predicted may have to be modified.

Another manifestation of triaxial deformation, namely the wobbling bands in nuclei, is a new and very interesting phenomenon in nuclear structure physics. Since this is a comparatively new phenomenon, so all the aspects of wobbling bands are not yet fully explored. For example, in the present thesis work, the increasing behaviour of the wobbling frequency with spin have been observed for the first time in a transverse wobbling band in any nucleus and the concept of I_m to classify wobbling motion in odd-A nuclei has been put forward. However, there are several other aspects which need attention in wobbling phenomenon. For example, there is, so far, no or very little is known about the systematic behaviour of the wobbling bands in a chain of proton or neutron numbers. Recently, wobbling band has also been reported in ^{187}Au, which has been found to be of longitudinal wobbling in nature, in contrast to the transverse wobbling in ^{183}Au observed in the present thesis work. So, it would be very interesting to look for the wobbling bands in other Au isotopes, that is in ^{185}Au and in ^{181}Au. Moreover, the wobbling bands, observed so far, are based on the coupling of particle with the triaxial core. Wobbling motion with hole couples with the triaxial core has not yet been observed. This could be another interesting aspect in the study of wobbling motion in nuclei. The multi-phonon wobbling bands are still very rare. In order to establish the model of the wobbling in odd-A nuclei, which has so far been observed only in one nucleus (normal deformed region). It is very important to observe wobbling bands with more than one wobbling phonon in other nuclei as well. Also, the primary interest of the observation of “simple” wobbler in an even-even nucleus still remains a challenge.

In ^{187}Os, both γ band and $\gamma\gamma$ band have been observed in this thesis work. $\gamma\gamma$ vibrational band identified in this nucleus is the first observation in an odd-A nucleus of mass region A $\sim$ 190. In the present study, several band structures have been identified in the odd-A ^{187}Os nucleus representing different configurations of the odd neutron in different orbitals. The coupling of the triaxial core with the coupling of the odd neutron in different configurations have been manifested in different ways, e.g in long-axis rotation and γ bands. It has been found that the excited 2^+ state (2_2^+) comes down in energy with increasing neutron number in even-even Os isotopes. This suggests that the heavier Os isotopes are highly triaxial in shape. Therefore, it would be interesting to investigate the heavier Os isotopes to look for other manifestations of triaxial shapes and the coupling of the odd particle with the highly triaxial core, in odd-A isotopes, for which the experimental data are very scarce. However, the heavier Os isotopes are very difficult to populate and can only be populated using light-ion induced reaction or deep inealstic scattering.

SUMMARY

In this thesis work, the excited states and band structures in three odd-A nuclei with atomic number $Z < 82$ have been experimentally investigated by gamma-ray spectroscopy technique. These include the odd-proton nuclei ^{197}Tl and ^{183}Au and an odd-neutron nucleus ^{187}Os. The neighbouring nuclei (either odd-A, odd-odd or even-even) of the above three nuclei are known to be triaxial in shape. Therefore, the evolution and manifestation of triaxial shapes in these odd-A nuclei have been studied. One of the important findings in these studies is that different manifestations of triaxial nuclear shapes in nuclei, namely, wobbling motion (in ^{183}Au) in nuclei, γ and $\gamma\gamma$ bands and unfavoured "long axis" rotation (in ^{187}Os) in nuclei and transition from an aplanar chiral geometry of the proton-, neutron and core angular momentum vectors to a planar geometry of magnetic rotation (in ^{197}Tl) could be demonstrated with clear observation, identification and characterization. Theoretical calculations of total Routhian surface (TRS), particle rotor model and SPAC (Shears mechanism with Principal Axis Cranking) have been performed to understand the experimental results.

The neutron deficient nuclei with proton number below the $Z = 82$ shell closure are interesting as the proton and neutron single particle levels around the Fermi level have both prolate and oblate driving effects. These, combined with the spherical shape driving effect of the $Z = 82$ core, several interesting band structures including those due to triaxial shape and different symmetries are predicted in the nuclei in the $A \sim 180 - 190$ mass regions.

Fusion evaporation reactions with light-ion (α) and heavy-ion (^{20}Ne) projectiles have been used to populate the excited states in the three nuclei using the reactions:
^{197}Au(α, 4n)^{197}Tl at 50 MeV of beam energy
^{186}W(α, 3n)^{187}Os at 36 MeV of beam energy
^{169}Tm (^{20}Ne, 6n)^{183}Au at 146 MeV of beam energy
The experiments were performed at the Variable Energy Cyclotron Centre (VECC), Kolkata and the beams were delivered from the K-130 cyclotron at VECC. The Indian National Gamma Array (INGA) and VECC Nuclear Spectroscopy (VENUS) array of clover HPGe detectors were used to detect the de-excited γ rays from the residual nuclei. The $\gamma - \gamma$ coincidence relation

(determined from $\gamma-\gamma$ matrix and $\gamma-\gamma-\gamma$ cube) and intensity argument were used to generate the level schemes in the nuclei. The spin and parities of the excited states were obtained from the multipolarity (λ) and type (E and M) of the de-excited γ rays. The λ, type and the mixing ratios (δ) of the γ rays were determined from the combined measurements of DCO (Directional Correlation from Oriented states) ratio and polarization asymmetry ratio.

In this work, a total of 136 new γ rays have been observed and placed in the level schemes of the three nuclei. These new γ rays help to identify several new band structures and to extend the known band structures. Several new aspects and important features those have been found in this thesis work are, (i) an interesting shape evolution from the known aplanar chiral geometry in ^{195}Tl to shears geometry in ^{197}Tl for the 3- and 5-quasiparticle configurations. The the newly observed band crossing in the $h_{9/2}$ band in this nucleus shows, for the first time, a complete alignment of $i_{13/2}$ pair of neutrons in Tl isotopes at neutron number $N = 116$. (ii) observation of two wobbling bands in ^{183}Au nucleus is the first such observation in any atomic nuclei so far and a new concept of an angular momentum I_m has been given in order to distinguish between longitudinal and transverse wobbling bands. (iii) in ^{187}Os nucleus, two distinct γ- and $\gamma\gamma$-vibrational bands, manifestations of triaxial shape, have been identified for the first time in this nucleus. Significant extension of the known $1/2^-[510]$ and $3/2^-[512]$ "twin bands", $11/2^+[615]$, and $7/2^-[503]$ bands have been made. The new result advances our understanding on the structure of this odd-neutron nucleus to the extent that all these bands show different manifestations of triaxial shapes, the unfavoured long-axis rotation, effect of triaxiality on the twin bands and the effect of $N = 110$ deformed shell closure on the band crossing.

The new results obtained in this work not only provide new insight in to the manifestation of triaxial shapes in odd-A nuclei but also opens up new avenues of future research. For example, the investigation of lighter isotopes of Tl, the heavier isotopes of Os and other Au isotopes for possible triaxial shape and their manifestations.

Chapter 1

Introduction

The atomic nucleus is a complex many body quantum system (radius R $\sim 10^{-15}$ m) which could be an ideal playground to observe and test different quantum mechanical laws and symmetries. A nucleus is consisted of protons and neutrons, which are combindly called nucleons. According to the shell model picture, these nucleons lie in different nucleonic orbits, each of which are characterised by certain quantum numbers, e.g total angular momentum, parity, etc. In terms of the nuclear shell model, the angular momentum and parity (I^{π}) of the ground state of an even-even nucleus is 0^{+} because of the pairing interaction of the nucleons. In case of an odd-A nucleus the ground state I^{π} is determined by the angular momentum and parity of the last orbital occupied by the odd nucleon. When energy is imparted to a nuclear system, the constituent nucleon(s) may get excited to another orbital and the I^{π} of the excited state would correspond to the new orbital occupied by the odd nucleon. The excited states of a nucleus which are generated by this process are known as single particle excitations. A nucleus can also have collective mode of excitations in which all or several of the nucleons take part coherently in generating an excited state in the nucleus. The rotational states of a deformed nucleus are the examples of nuclear collective excitation.

The nuclei with proton and/or neutron numbers close to the spherical shell gaps at 2, 8, 20, 28, 50, 82 and 126 (126 is for neutron only) are mostly spherical in nature while the nuclei with nucleon numbers away from these shell closures (mid-shell nuclei) are mostly deformed in nature. The heaviest known doubly magic nucleus is ^{208}Pb with both proton ($Z = 82$) and neutron ($Z = 126$) numbers are magic. The shape of ^{208}Pb is near spherical and the low-lying excited states in its neighboring odd-A nucleus ^{209}Bi ($Z = 83$, $N = 126$) could be well explained by single particle excitations [1]. On the other hand, the nuclei in the rare earth region are deformed nuclei with mostly prolate deformed structures [2]. The excited states in these nuclei are, therefore, generated by collective rotation. The region between the spherical Pb and axially deformed prolate nuclei with proton number Z < 82 are known as transitional region. The experimental investigation of the excited states in such transitional nuclei can provide important information on the evolution of nuclear shape from prolate deformed to spherical. In some nuclei, it has been observed that a change in shape from prolate to oblate takes place through triaxial deformation [3].

The single particle orbitals of the protons and the neutrons play important roles in determining the shape of a nucleus. In consideration of the Nilsson diagram, it can be seen [4] that the low- and high-Ω (Ω = projection of the total angular momentum of a nucleon on the symmetry axis of the nucleus) components of the high-j orbitals have opposite shape driving effects. In the transitional nuclei in mass region $A \sim 190$, the involved single particle orbitals for the neutron deficient Tl (Z = 81) and Bi nuclei are the high-j orbitals $h_{9/2}$ and $i_{13/2}$ for the protons and $i_{13/2}$ for the neutrons. Therefore, the structure of these nuclei will be affected by two opposite effects; while the nuclei will try to be a spherical one due to the proximity of the spherical shell closure at Z = 82, the shape driving effect of the above orbitals would try to drive the shape towards a deformed structure. Because of these, interesting shape evolution in nuclei in this region are expected as a function of excitation energy, angular momentum and particle number. For example, the heavier Tl (Z = 81) and Bi (Z = 83) isotopes are spehrical in nature [5, 6] but the deformed structures are developed for the lighter isotopes. An onset of deformation at neutron number $N = 112$ for Bi isotopes has been reported with the observation of a deformed rotational band in ^{195}Bi. On the other hand, in case of the neutron deficient Tl isotopes in $A \sim 190$ region, it has been observed that the ground and low-lying structures are spherical while at higher excitation energies, the shape changes to a deformed oblate one [7, 8, 9, 10]. Moreover, both prolate and oblate shapes have been reported in a same nucleus in even lighter Tl isotopes, e.g in ^{189}Tl nucleus [11]. In addition to the spherical and axially symmetric deformed shape, triaxial shapes are also expected for the nuclei in the $A \sim 190$ and $A \sim 180$ mass regions. Different nuclear shapes are manifested in the form of different band structures, band properties and excited states in the level scheme of a nucleus, it is, therefore, interesting to study the excited states in the nuclei of these mass regions to understand the effect of the different orbitals and the spherical shell closures in the evolution of nuclear shape and their manifestations.

The quadrupole deformation in a nucleus can be parametrised by the deformation parameters β_2 and γ. The deformation parameter β_2 indicates axial deformation and γ indicates the degree of non-axiality. In case of a spherical nucleus ($\beta_2 \sim 0$), the excited states are dominated by the single particle like excitations with almost no regular sequence of levels, whereas regular band structures, characteristics of a rotational band, are observed in case of a deformed nucleus. The excitation energies of rotational band follows the relation $E \propto I(I+1)$ pattern, where, E and I are the excitation energy and total angular momentum of the nucleus, respectively [12, 13, 14, 15].

One of the important contemporary topics in nuclear structure physics research is to search for stable triaxial shapes and their manifestation in the level structure of a nucleus. This is beacause, a triaxial nucleus can be manisfested in various exotic band structures and different quantum mechanical symmetries can be studied. In this thesis work, some of these exotic excitations which are resulted due to non-axial nuclear shape are mainly investigated.

The rotational band of an odd-A triaxial nucleus gets modified in a way such that the signature splitting ("signature" is a quantum number related to the symmetry of the rotation of a deformed nucleus by π) becomes large even for a strongly coupled band with high-Ω configuration [16]. However, the non-axial or triaxial nuclear shape in atomic nuclei are also manifested in the following excitations:

- **γ vibrational band**
- **Doubly degenerate chiral band**

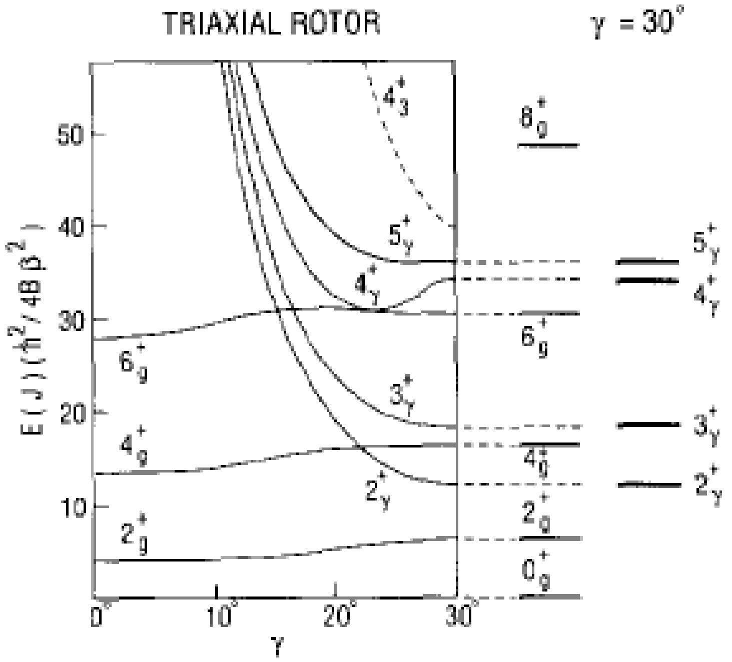

Figure 1.1: Calculated energy levels of a γ band using Davydov model [17, 18].

• **wobbling band**

1.1 γ Vibrational Band

The deformed vibration in atomic nuclei for quadrupole shape can be classified into two types

- β vibration for an axially deformed nucleus
- γ vibration for a non-axial nucleus

The quadrupole phonons carry two units of angular momentum with projections K=0 and K=2. The K=0 vibration, called the β vibration, is along the symmetry axis and preserves the axial symmetry of the nucleus. On the other hand, K = 2 corresponds to γ vibration which represents the fluctuation of nuclear shape from its axial symmetry. When an even-even nucleus has non-axial deformation, a new set of levels of spins 2, 3, 4, 5 ... etc. are generated in addition to the ground state rotational band (0, 2, 4,...etc.). Also, a slight change in the energies of this main ground state rotational band occur compared to the axially symmetric case. The second excited state of spin 2 (2_2^+) comes down in energy as the degree of non-axiality parameter γ increases towards maximum triaxiality of $\gamma = -30°$ [18] (Fig. 1.1). Apart from these single-phonon excitations, It is also possible to get multi-phonon deformed vibration. The possible multi-phonon deformed vibration for quadrupole shapes can have three categories, $\beta\beta$ (K=0) vibration, $\beta\gamma$ (K=2) vibration, and $\gamma\gamma$ (K=0 and K=4) vibration [19]. However, the experimental observation of multi-phonon vibrational bands is very difficult due to their highly non-yrast nature and similar band head excitation energies as that of the 2-qp band.

1.1.1 Experimental Signatures of γ Vibrational Band

The experimental signatures of the γ vibrational bands are the following:

- $\Delta I = 1$ side band with strong decay branch to the ground state band.
- γ vibrational band mostly decay to the main band via $M1+E2$ mixed and E2 transitions.
- Moment of inertia of a γ vibrational band should be very similar to the ground band.

Multiphonon excitations (2-phonon γ band) mainly observed in mass $\sim$ 100 region in even-even ^{104,106,108}Mo [20, 21, 22, 23, 24, 25] and ^{108,112}Ru [26, 27] nuclei. However, the multiphonon 2γ bands have rarely been observed in odd A nuclei. In mass $\sim$ 100 region, 1-γ and 2-γ bands have been reported only in odd-A ^{105}Mo (odd-N) [28] and ^{103}Nb (odd-Z) [29] nuclei. In ^{105}Mo (odd-N), the 1- γ phonon couple with odd neutron in $5/2^-[532]$ orbital of $\nu h_{11/2}$ and generate 1-γ (Δ I =1) band with band head excitation energy 870.5 keV which decay to the ground band via mixed M1 and E2 transitions by destruction of 1-γ phonon. Similarly, 2-phonon γ band at an excitation enrgy 1534.6 keV can be generate by the coupling of 2-phonon γ quanta with odd neutron. The 2-phonon γ band decay to 1-γ phonon γ band via mixed M1 and E2 transitions [29] but the decay to the ground band is forbidden from phonon selection rule [19]. Similarly in odd-Z ^{103}Nb, the 1 and 2 γ phonon couple with odd proton in $5/2^+[422]$ and generate the 1 and 2 γ phonon bands at excitation energy 716.8 keV and 1282.1 keV respectively. In mass

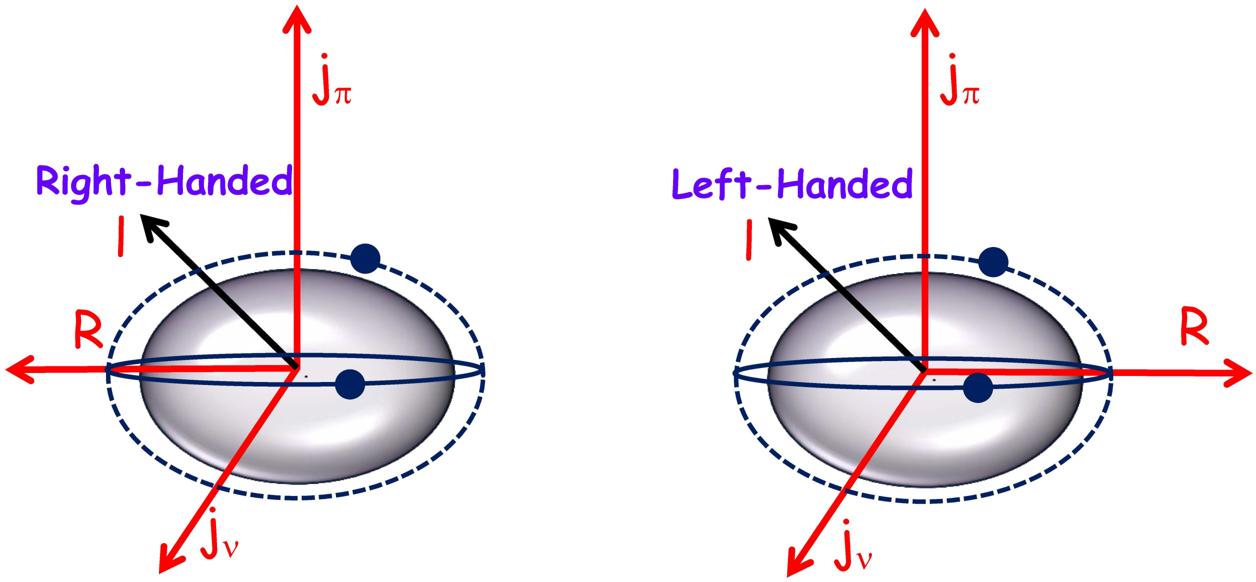

Figure 1.2: Geometrical representation of right-handed and left-handed chiral geometry

$\sim$ 180 region, multiphonon $\gamma\gamma$ vibrational bands are reported in even-even ^{186,188}Os nuclei [30] but, has not been observed in any of the odd-A isotopes in this mass region.

1.2 Chiral Band

The doubly degenerate chiral band was first predicted by Frauendorf and Meng [31] for a nucleus with stable triaxial shape and having a particle-hole configuration. The particle angular momentum, the hole angular momentum and the angular momentum of the triaxial core can be arranged with a right hand - left hand symmetry and form the chiral geometry as shown in Fig. 1.2. A triaxial nucleus has three unequal principal axes: short, long and medium. The unpaired particle aligns along the short axis to maximise the overlap to the core. On the other hand, the hole aligns along the long axis to minimise the overlap to the core and the core angular momentum (R) is perpendicular to both particle and hole angular momenta. The right-handed and the left-handed systems are related with each other by $R_y(\pi))T$ symmetry.

1.2.1 Experimental Signatures of Chiral Band

Following are the signatures of chiral doublet bands:

- Nearly degenerate $\Delta I = 1$ doublet bands of same spin and parity.
- Both the double degenerate bands have very similar properties i.e, very similar values of quasi-particle angular momentum (i_x), moment of inertia ($\mathcal{J}_1$) and electromagnetic properties like B(M1)/B(E2) ratio.
- The electromagnetic transition strength B(M1) and B(E2) as a function of spin should be very similar for the doubly degenerate chiral bands.

Most of the investigations for nuclear chirality were in the A $\sim$ 100 and A $\sim$ 130 regions and very few have been observed in A $\sim$ 190 region. One of the very first chiral bands have been observed in N=75 isotones [32] and later in ^{104}Rh [33], ^{108}Ag [34], ^{135}Nd [35] 2 and 3 qp chiral bands have been reported. Chiral bands in $A \sim 190$ region have been reported for the odd-odd nuclei ^{194}Tl [36] and ^{198}Tl [37]. Recently, multiple chiral doublet bands, based on a 3-qp and 5-qp configurations, have been observed in ^{195}Tl nucleus [38]. The aplaner angular momentum geometry in chiral band can change to planer geometry of a Magnetic Rotational (MR) band for a weakly deformed core. Such shape transitions from chiral to MR band has been observed in mass $\sim$ 130 region (^{134}Cs) with increasing neutron number towards N=82 shell closure.

1.3 Magnetic Rotational Band

In the early 1990s, $\Delta I = 1$ rotational-band like structures have been observed in near spherical nuclei. These bands have large B(M1) values and small B(E2) values, in contrast to the rotational bands of a well deformed nucleus. Such bands were identified as the magnetic rotational (MR) bands which occur in weakly deformed nuclei ($\beta_2 \leq 0.1$) with particle-hole configuration. In this case, the angular momentum vectors of the particles and the holes are

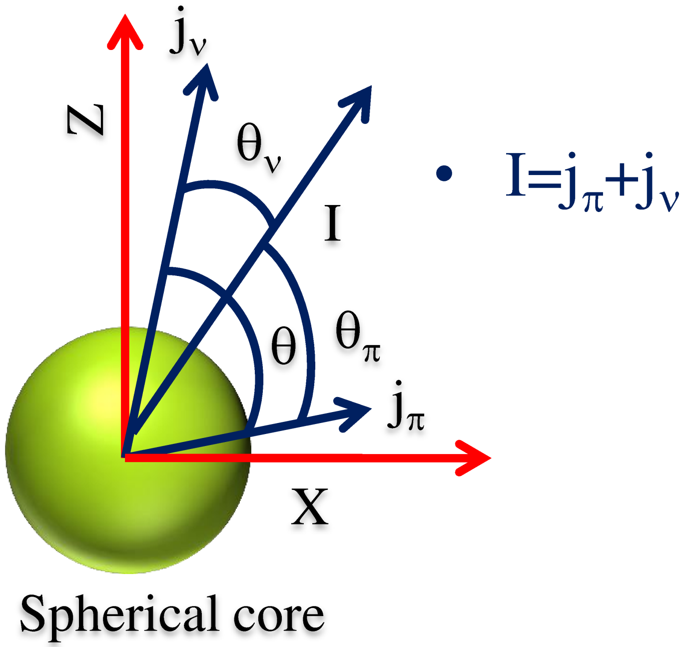

Figure 1.3: Schematic representation of shears mechanism for magnetic rotational band

almost perpendicular to each other. In MR bands, the angular momenta are generated when the particle and hole angular momentum blades align along the total angular momentum axis. The angular momentum generation of an MR band in weakly deformed nuclei in this way is known as shears mechanism [39].

1.3.1 Experimental Signatures of Magnetic Rotational Band

The experimental signatures of the magnetic rotational bands are as follows:

- The level energies in MR band follow $E(I) - E(I_0) = A(I - I_0)^2$, where $E(I_0)$ and I_0 are the bandhead excitation energy and spin, respectively.
- The MR band consists of intraband $\Delta I = 1$ magnetic dipole transitions with weak or no E2 cross-over.
- The dipole transition strengths [B(M1)] are large generally of the order of 1-10 μ_N^2.
- The experimental B(M1) value decreases with spin. Therefore, the $\frac{B(M1)}{B(E2)}$ ratio decreases for a band with fixed B(E2) value.

- The typical value of dynamic moment of inertia ($\mathcal{J}_1$) is small, of the order of 10 - 30 $\hbar^2$MeV^{-1}.

1.3.2 Shears Mechanism

The angular momentum vectors of the particles and holes in Weakly deformed nuclei can be arranged in perpendicular coupling scheme to maximise the overlap of spatial density distribution to the core. The schematic picture of shears mechanism is shown in Fig. 1.3. In this picture, the angle (θ) between the proton particle angular momentum (j_π) and neutron hole angular momentum (j_ν) is called the shears angle. The total angular momentum can be expressed as $\overrightarrow{I} = \overrightarrow{j_\pi} + \overrightarrow{j_\nu}$ and the angle θ between proton and neutron angular momentum blades can be expressed as

$$\cos\theta = \frac{\overrightarrow{j_\pi}.\overrightarrow{j_\nu}}{\mid \overrightarrow{j_\pi} \mid\mid \overrightarrow{j_\nu} \mid} = \frac{[I(I+1) - j_\pi(j_\pi+1) - j_\nu(j_\nu+1)]}{2\sqrt{j_\pi(j_\pi+1)j_\nu(j_\nu+1)}}. \tag{1.1}$$

In case of Pb ($A \sim 190$) region, the proton paricles in high-j $\pi h_{9/2}$ and $\pi i_{13/2}$ and neutron holes in $\nu i_{13/2}$ orbitals are responsible to generate the shears mechanism.

1.4 Wobbling Band

Nuclear wobbling is related with triaxial nuclear shape which was discussed long back by Bohr and Mottelson[40]. The wobbling motion in atomic nuclei is analogous to classical rotation of an asymmtric top. The triaxial nucleus has three unequal moment of inertia along the three principle axes: short, medium, and long. A nucleus with such a shape, tries to rotate around the medium axis, which has maximum moment of inertia, to minimise its rotational energy. But the non-zero values of other two moments of inertia along i.e along the short and the long axes can generate a precession of the medium axis rotation with respect to the body-fixed total angular momentum axis. This is known as "simple" wobbler (Fig. 1.4). The energy levels in

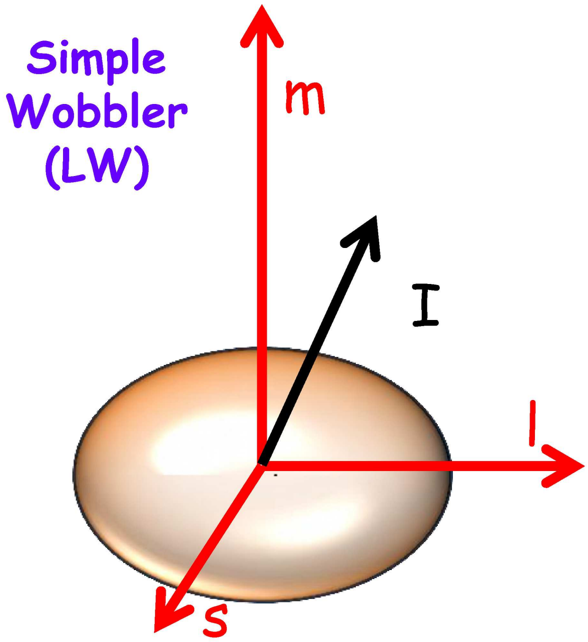

Figure 1.4: Geometrical representation of Simple wobbler in even-even nucleus

wobbling band can be expressed as

$$E = E_{\text{rot}} + (n_w + 1/2)\hbar\omega_{\text{wob}}$$

where, E_{rot} is the rotational energy due to the rotation around the medium axis, n_w is the wobbling quanta and $\hbar\omega_{\text{wob}}$ is the wobbling frequency with wobbling energy $E_{\text{wob}} = \hbar\omega_{\text{wob}}$. However, such "simple" wobbling motion for the even-even nuclei (with zero quasi-particle configuration) has not been observed till date.

But, wobbling motion has been observed in very few odd-A nuclei in the nuclear chart [41, 42, 43, 44, 45, 46, 47, 48, 49, 50]. The wobbling motion in odd-A nuclei can be classified into the following two types based on the coupling of the odd particle with the triaxial core [51]:

I. Transverse wobbling (TW)

II. Longitudinal wobbling (LW)

1.4.1 Experimental Signatures of Wobbling Band

As mentioned before, the wobbling motion is realized in a deformed rotational nucleus. Therefore, the nucleus must possesses a primary rotational band as in a normal deformed nucleus.

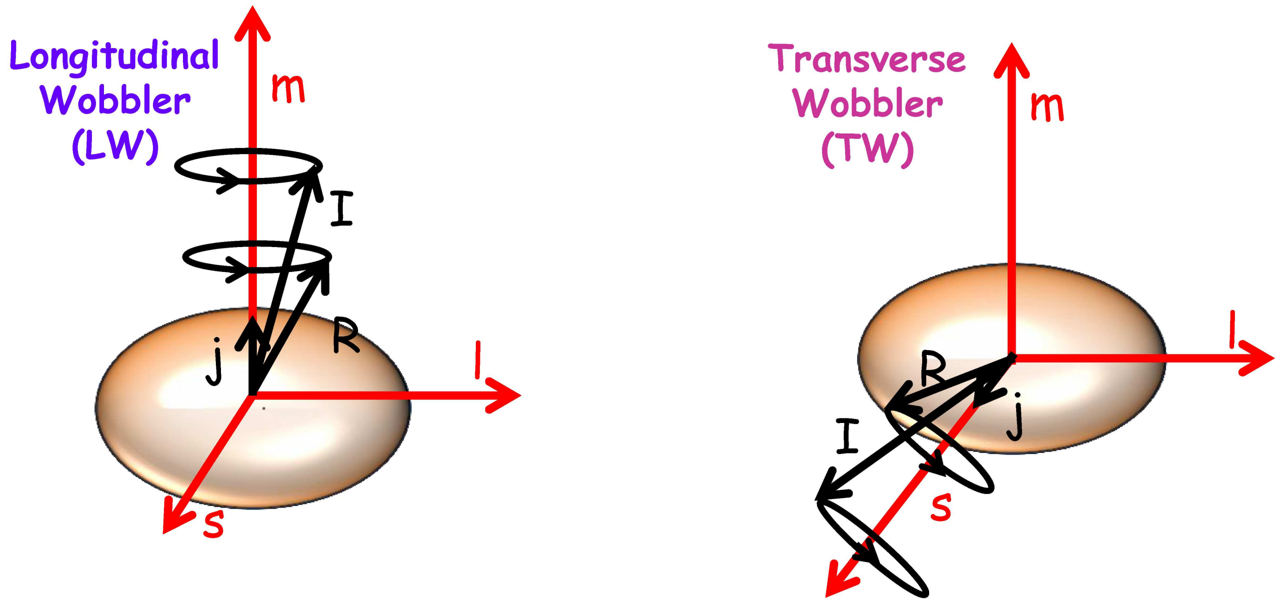

Figure 1.5: Geometrical representation of longitudinal and transverse wobbling motion in odd-A nucleus

The wobbling is manifested as a collective vibration on top of this rotational motion. Following are the specific signatures of wobbling motion in nuclei:

- The wobbling motion is manifested by a series of rotational bands on top of the vibrational states of wobbling quanta n_w.
- These wobbling bands are connected to the primary rotational band via $\Delta I = 1$ E2 transitions.
- The ratio of the strengths of the interband to intraband E2 transitions, i.e $\frac{B(E2)_{out}}{B(E2)_{in}}$ is large.

The two different types of wobbling motions for odd-A nuclei can be distingushied from the coupling of the odd particle with triaxial core. In case of LW, the particle angular momentum aligns along the medium axis while it aligns along the short or long axes for TW motion (Fig. 1.5). The measured wobbling frequency has been found to increase with angular momentum, I for LW, while in case of all the TW identified so far, prior to the present work, the wobbling frequency has been observed to decrease with I. Also, multiple wobbling bands like multiple chiral bands [52] in a triaxial nucleus still not been found in any nuclei in the nuclear chart. The experimental wobbling frequency $E_{\text{wob}} = \hbar\omega_{\text{wob}}$ can be obtained from the energy differences between the $n_w = 1$ wobbling partner band and $n_w = 0$ yrast band using the relation.

$$E_{\text{wob}} = E(I, n_w = 1) - [E(I-1, n_w = 0) + E(I+1, n_w = 0)]/2,$$

where $E(I)$ is the level energy with angular momentum I.

With the aim to observe different manifestations of triaxial shapes and their coupling with the odd-particles, the excited states in three nuclei namely, the odd-proton nuclei ^{197}Tl, and ^{183}Au, and the odd-neutron nucleus ^{187}Os in $A \sim 180 - 190$ mass region and close to the Z = 82 shell closure have been experimentally studied in this thesis work using gamma ray spectroscopy technique. The active proton and neutron orbitals, near the Fermi levels, for these nuclei are primarily the high-j $h_{9/2}$ and $i_{13/2}$ orbitals. Specifically, in case of ^{197}Tl, chiral bands at high excitation energies are reported for the neighboring odd-A ^{195}Tl [38] and odd-odd ^{194}Tl [36] nuclei. Indication of chirality has also been reported for its nearest neighbor ^{198}Tl [37]. However, the multi-quasiparticle high excited states are not well studied in this nucleus [8]. In this study, MR band has been identified for both the 3^- and 5^- quasiparticle configurations in this nucleus in contrast to the chiral bands for the 3^- and 5^- quasiparticle configurations in ^{195}Tl. This shows that the aplanar coupling in ^{195}Tl changes to a planar one in ^{197}Tl which has lower deformation [53]. In case of ^{187}Os and ^{183}Au nuclei in $A \sim 180$ region, the neighboring even-even cores of ^{186}Os and ^{182}Pt have been reported to be triaxial [54, 55]. The motivation of the present study was to investigate the effect of an odd neutron and an odd proton, respectively, on these triaxial cores. It has been observed in the present study that the coupling of the odd neutron and the odd proton with their respective triaxial core has been manifested in different ways in ^{187}Os and ^{183}Au. While, gamma bands have been observed in ^{187}Os, two pairs of wobbling bands, based on two configurations have been identified in ^{183}Au [56]. The details of these studies have been described in the subsequent chapters in this thesis.

The thesis has been arranged in the following way:
In the second and the third chapters, the nuclear models those are used in the present work and the experimental details have been discussed, respectively. The specific details on the experiments and results on the three nuclei ^{197}Tl, ^{187}Os and ^{183}Au have been discussed in the

subsequent three chapters along with the interpretations of the results. Finally, a summary of the present work and outlook, based on this thesis work, have been given in the last chapter.

Bibliography

[1] J. S. Lilley and Nelson Stein, Phys. Rev. Lett. **19** (1967) 709.

[2] E. Ngijoi-yogo et al., Phys. Rev. C **75**, 034305 (2007).

[3] J. Jolie, R. F. Casten, P. von Brentano, and V. Werner, Phys. Rev. Lett. **87** (2001) 162501.

[4] Sven Gösta Nilsson, Dan. Mat. Fys. Medd. **29**, no. 16 (1955).

[5] J. M. Davidson et al., Phys. Rev. C **15**, 635 (1977).

[6] H. Hübel et al., Nucl. Phys. A **294**, 177 (1978).

[7] W. Reviol et al., Nucl. Phys. A **548**, 331 (1992).

[8] H. Pai, et al., Phys. Rev. C **88**, 064302 (2013).

[9] C. B. Li et al., Phys. Rev. C **97**, 034331 (2018).

[10] Soumik Bhattacharya et al., Phys. Rev. C **98**, 044311 (2018).

[11] S. K. Chamoli, et al., Phys. Rev. C **75**, 054323 (2007).

[12] D. Ward et al., Nucl. Phys. A **332**, 433 (1979).

[13] D. Ward et al., Nucl. Phys. A **600**, 88 (1996).

[14] H. Beuscher et al., Z.Phys. **263**, 201 (1973).

[15] A. Johnson et al., Nucl. Phys. A **179**, 753 (1972).

[16] Ikuko Hamamoto Nucl. Phys. **A 520**, 297c-315c (1990).

[17] A.S. Davydov and G.P. Filippov, Nucl. Phys. **8**, 237 (1958).

[18] N. V. Zamfir, et al., Phys. Lett. B **260**, 265 (1991).

[19] R. F. Casten, *Nuclear Structure From A Simple Perspective* (OXFORD UNIVERSITY PRESS, New York 1990).

[20] A. Guessous, et al., Phys. Rev. Lett. **75** (1995) 2280.

[21] A. Guessous, et al., Phys. Rev. C **53** (1996) 1191.

[22] H. Hua, et al., Phys. Rev. C **69** (2004) 014317.

[23] L.M. Yang, et al., Chin. Phys. Lett. **18** (2001) 24.

[24] R.Q. Xu, et al., Chin. Phys. Lett. **19** (2002) 180.

[25] H.B. Ding, et al., Chin. Phys. Lett. **24** (2007) 1517.

[26] X.L. Che, et al., Chin. Phys. Lett. **21** (2004) 1904.

[27] X.L. Che, et al., Chin. Phys. Lett. **23** (2006) 328.

[28] H. B. Ding, et al., Phys. Rev. C **74** 054301 (2006).

[29] Jian-Guo Wang, et al., Phys. Lett. B **675**, 420-425 (2009).

[30] T. Yamazaki et al., Nucl. Phys. A **209**, 153-169 (1973).

[31] S. Frauendorf and J. s, Nucl. Phys. A **617**, 131 (1997).

[32] K. Starosta, et al., Phys. Rev. Lett. **86** (2001) 971.

[33] C. Vaman, et al., Phys. Rev. Lett. **92** (2004) 032501.

[34] J. Sethi et al., Phys. Lett. B **725**, 85 (2013).

[35] S. Zhu, et al., Phys. Rev. Lett. **91** (2003) 132501.

[36] P.L. Masiteng, et al., Phys. Lett. B **719** (2013) 83.

[37] E. A. Lawrie, et al., Phys. Rev. C **78** (2008) 021305(R).

[38] T. Roy et al., Phys. Lett. B **782**, 768-772 (2018).

[39] R. M. Clark and A. O. Macchiavelli, Annu. Rev. Nucl. Part. Sci. **50** 1 (2000).

[40] A. Bohr and B. R. Mottelson, *Nuclear Structure* (Benjamin, New York, 1975), Vol.II.

[41] S. W. Ødegard et al., Phys. Rev. Lett. **86**, 5866 (2001).

[42] D. R. Jensen et al., Phys. Rev. Lett. **89**, 142503 (2002).

[43] P. Bringe et al., Eur. Phys. J. A **24**, 167 (2005).

[44] G. Schönwaßer et al., Phys. Lett. B **552**, 9 (2003).

[45] H. Amro et al., Phys. Lett. B **553**, 197 (2003).

[46] D. J. Hartley et al., Phys. Rev. C **80**, 041304(R) (2009).

[47] J. Timár et al., Phys. Rev. Lett. **122**, 062501 (2019).

[48] S. Biswas et al., Eur. Phys. J. A **55**, 159(2019).

[49] J. T. Matta et al., Phys. Rev. Lett. **114**, 082501 (2015).

[50] N. Sensharma et al., Phys. Rev. Lett. **124**, 052501 (2020)

[51] S. Frauendorf and F. Dönau, Phys. Rev. C **89**, 014322 (2014).

[52] C.M. Petrache, et al., Phys. Rev. C **97** (2018) 041304(R).

[53] S. Nandi et al., Phys. Rev. C **99** (2019) 054312

[54] C. Wheldon et al., Nucl. Phys. A **652**, 103-131 (1991).

[55] D. G. Popescu et al.,Phys. Rev. C **55**, 1175 (1997).

[56] S. Nandi et al., Phys. Rev. Lett. **125**, 132501 (2020).

Chapter 2

Nuclear Models

Atomic nuclei are complex many mody system consist of protons and neutrons which are bound together by the sort range strong force. In order to explain different nuclear properties, different nuclear models are used. The experimentally observed data are interpreted using these models. For such interpretation, various parameters which are relevant to a particular model need to be extracted from the experimental data. The main focus of this thesis work is to study the nuclear structure properties of different nuclei as a function of angular momentum. The structures of the nuclei in the $A \sim 180 - 190$ region change as a function of angular momentum and excitation energy. Correspondingly, different modes of excitations are expected in these nuclei. Nuclear excitions may be classified into two primary types, namely single particle excitation and collective excitation. The single particle excitations are mostly described in the shell model picture which is considered as the backbone of nuclear structure physics. The shell model was originally developed for the spherical nuclei [1] which was extended for deformed nuclei as Nilsson model [2]. The collective excitations are mostly two types, vibration and rotation. The concept of collective excition was first discused by A. Bohr and B. Motelsson [3] using collective model. The collectivity in a nucleus arises due to the collective coherent motion of all the nucleons of a nucleus. The collective vibration can occur in either spherical or deformed nuclei, but the rotation is the characteristics of a deformed nucleus only. Therefore, in order to describe both shell model and collective model, it is necessary to describe and parametrize the nuclear deformation.

2.1 Nuclear Deformation Parameters

In order to describe the dynamical shape and surface oscillations of a nucleus, its radius parameter in three dimension R(θ, ϕ) is expanded as:

$$R(\theta, \phi) = R_0 \left[1 + \sum_{\lambda=0}^{\infty} \sum_{\mu=-\lambda}^{\lambda} \alpha^*_{\lambda\mu} Y_{\lambda\mu}(\theta, \phi) \right] \tag{2.1}$$

where R_0 is the radius of the sphere of the same volume and $Y_{\lambda\mu}(\theta, \phi)$ are the spherical harmonic functions. $\alpha^*_{\lambda\mu}$ are the parameters which describe the orientation of atomic nuclei and different shapes. λ is the multipolarity corresponding to the different modes of shape vibrations and μ is the projection of λ. As $R(\theta, \phi)$ is invariant under reflection and rotation of the coordinate system, the following property has to be satisfied

$$Y^*_{\lambda\mu} = (-1)^{\mu} Y_{\lambda-\mu} \tag{2.2}$$

From eq.(2.2), we get

$$\alpha^*_{\lambda\mu} = (-1)^{\mu} \alpha_{\lambda-\mu} \tag{2.3}$$

The λ=2 mode indicates the quadrupole deformation which is most common in nuclear structure. In the quadrupole deformation (λ=2) five parameters of $\alpha_{2\mu}$ describe the nuclear shape completely. Out of these five, three were used as Euler angles to determine the orientation of three principal axes and rest of the two are real independent parameters a_{20} and $a_{22} = a_{2-2}$ which represent the shape of a nucleus. These two parameters can be expressed in terms of the so-called Hill-Wheeler [4] coordinates β_2 and γ as

$$a_{20} = \beta_2 \cos\gamma \tag{2.4}$$

$$a_{22} = \frac{1}{\sqrt{2}} \beta_2 \sin\gamma \tag{2.5}$$

Table 2.1: Different rotation axis of a triaxial nucleus with deformation parameter γ

Rotation axis	Deformation parameter γ
Medium axis	$0^\circ > \gamma > -60^\circ$
Short axis	$0^\circ < \gamma < +60^\circ$
Long axis	$-60^\circ > \gamma > -120^\circ$

From eq^n's (2.4) and (2.5), we get

$$\sum_\mu \mid \alpha_{2\mu} \mid^2 = a_{20}^2 + 2a_{22}^2 = \beta_2^2 \tag{2.6}$$

$$R(\theta,\phi) = R_0\left[1 + \beta_2\sqrt{\frac{5}{16\pi}}(\cos\gamma(3\cos^2\theta - 1) \quad + \sqrt{3}\sin\gamma\cos^2\theta\cos 2\phi)\right] \tag{2.7}$$

The parameters β_2 and γ represent the degree of axial deformation and axial asymmetry, respectively. The increments of the three semi-axes along the $x-$, $y-$ and $z-$axes in the body-fixed frame are given by

$$\delta R_x = R(\frac{\pi}{2},0) - R_0 = R_0\frac{5}{4\pi}\beta_2\cos(\gamma - \frac{2\pi}{3}) \tag{2.8}$$

$$\delta R_y = R(\frac{\pi}{2},\frac{\pi}{2}) - R_0 = R_0\frac{5}{4\pi}\beta_2\cos(\gamma + \frac{2\pi}{3}) \tag{2.9}$$

$$\delta R_z = R(0,0)) - R_0 = R_0\frac{5}{4\pi}\beta_2\cos\gamma \tag{2.10}$$

Different nuclear shapes can be described in a $\beta_2 - \gamma$ plane using Lund convention [5]. For example, $\gamma = 0^\circ$ and -60° represent collective prolate and oblate shapes, respectively. On the other hand, the even multiple of 60° represents noncollective prolate and odd multiple of 60° represents noncollective oblate shapes. Otherwise, any other value of γ indicate axially asymmetric shapes. The different nuclear shapes in the $\beta_2 - \gamma$ plane in the Lund convention are shown in Fig. 2.1. The asymmetric nuclear shape has three unequal moments of inertia with respect to the three unequal axes (medium, short, long). Different values of the deformation parameter γ represent different rotation axis of a triaxial nucleus. The range of values applicable for medium axis, short axis and long axis rotations are tabulated in Table 2.1.

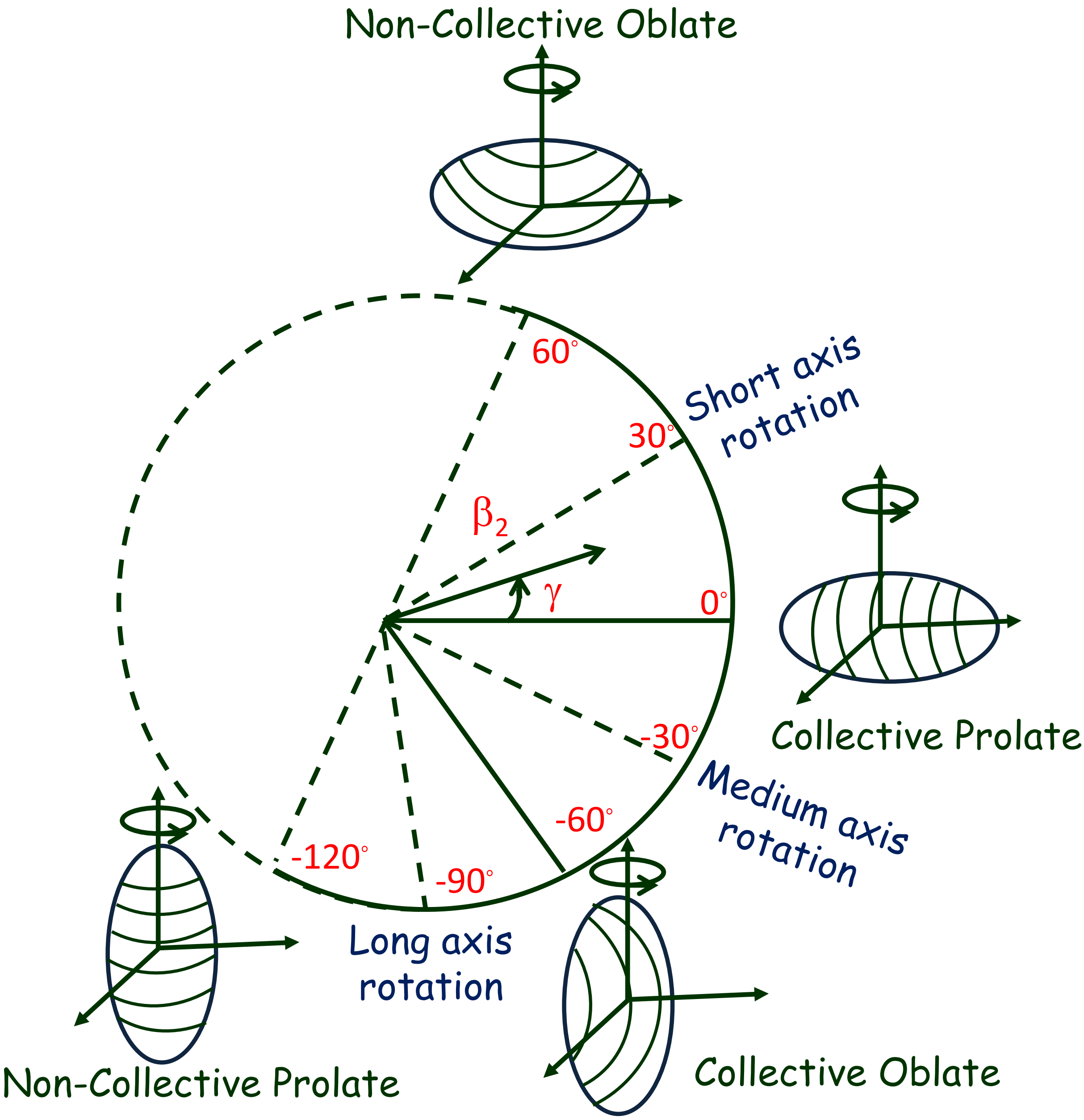

Figure 2.1: Different nuclear shapes in (β_2-γ) plane using Lund convention[5].

2.2 Shell Model

The nuclear shell model was first introduced by Maria Mayer and Jenssens [1] in order to explain the extra stability in atomic nuclei at the nucleon numbers 2, 8, 20, 28, 50, 82 and 126. These are called the "magic numbers". In shell model, the nucleons are considered as independently moving particles in an average nuclear potential created by all the nucleons which constitute the nucleus. The average nuclear potential can be written as:

$$V(r_i) = \left\langle \sum_j v(r_{ij}) \right\rangle \tag{2.11}$$

where, $v(r_{ij})$ is the short range interaction between ith and jth nucleon. The total Hamiltonian can be written as:

$$H = \sum_i T_i + \sum_{i>j} v(r_{ij}) = \sum_i \left[T_i + V(r_i) \right] + \sum_{i>j} \left[v(r_{ij}) - V(r_i) \right] \tag{2.12}$$

where $V_{res} = \sum_{ij} \left[v(r_{ij}) - V(r_i) \right]$ is the residual interaction between nucleons. For the sake of simplicity, the residual interaction part between the nucleons can be neglected. The average nuclear potential can be expressed by various phenomenological potentials. The spherical harmonic oscillator potential is the simplest one to solve which nicely explain various nuclear phenonmena. It is given by

$$V(r) = \frac{1}{2} m\omega^2 r^2 \tag{2.13}$$

the energy levels can be represented as

$$\epsilon_N = \left(N + \frac{3}{2} \right) \hbar\omega_0 \tag{2.14}$$

with

$$N = 2(n-1) + l, \text{ where } n = 1, 2, 3, .. \text{ and } l = 0, 1, 2, ... \tag{2.15}$$

Where, $N = 2(n-1) + l$ is the oscillator quantum number, n is the radial quantum number, l is the orbital quantum number and ω is the oscillator frequency. Each nuclear level has $\frac{1}{2}(N+1)(N+2)$-fold degeneracy (Fig. 2.2). But, the spherical harmonic oscillator potential can not explain the emperical magic numbers. It can be explained by introducing l^2 and $l.s$

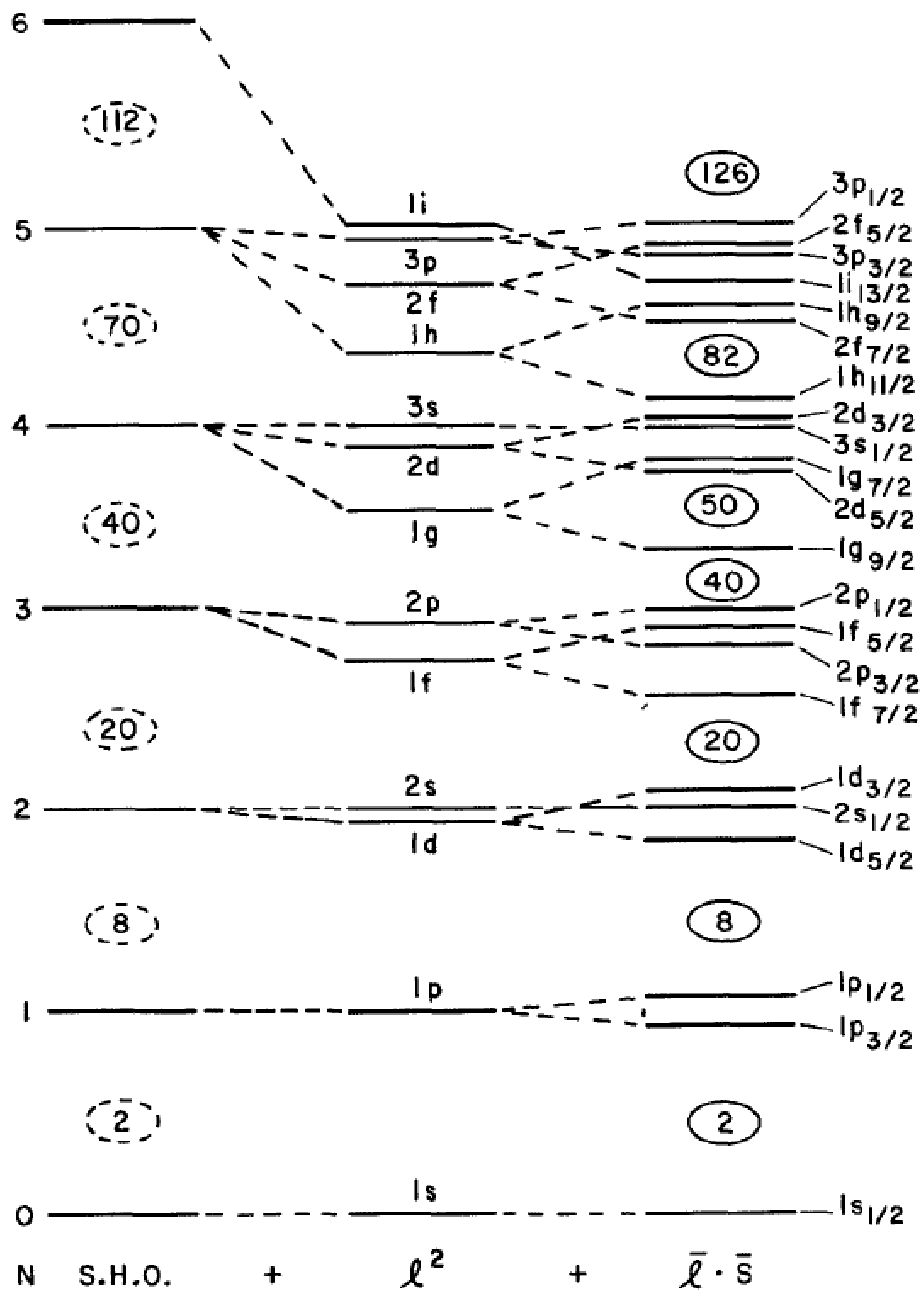

Figure 2.2: Spherical shell model diagram of single particle states with spin orbit term reproducing magic numbers 2, 8, 20, 28, 50, 82, 126 [6].

coupling term in the total Hamiltonian by Maria Mayer for which she got Nobel prize in 1963. The potential can also be visualised as a Woods-Saxon potential which is written as:

$$V(r) = -\frac{V_0}{1 + exp[(r - R)/a]} \tag{2.16}$$

where $R \approx r_0 A^{1/3}$ with $r_0 \approx 1.2$ fm is nuclear radius, $V_0 \approx 50$ MeV is the depth of the potential and a ≈ 0.5 fm is the skin thickness parameter. This model successfully explains the excited states in spherical and near spherical nuclei.

2.3 Nilsson Model

In deformed nuclei, the mass distribution can be represented by an ellipsoid and the average potential should be ellipsoidal. In this model, anisotropic harmonic oscillator potential is considered as the average potential:

$$V = \frac{1}{2} m \left(\omega_x^2 x^2 + \omega_y^2 y^2 + \omega_z^2 z^2 \right) \tag{2.17}$$

where ω_x, ω_y and ω_z are the three oscillator frequencies which are inversely proportonal to the ellipsoid half axes a_x, a_y, a_z, respectively.

$$\omega_i = \dot{\omega}_0 \frac{R_0}{a_i}, (i = x, y, z) \tag{2.18}$$

The volume conservation can be satisfied by the relation:

$$\omega_x \omega_y \omega_z = \text{constant} = \dot{\omega}_0^3 \tag{2.19}$$

where $\dot{\omega}_0$ is the oscillator frequency for the spherical potential. The energy eigen values of the eigen states of anisotropic harmonic oscillator potential can be represented in terms of quantum numbers n_x, n_y, n_z as

$$\epsilon_0(n_x, n_y, n_z) = (n_x + \frac{1}{2})\hbar\omega_x + (n_y + \frac{1}{2})\hbar\omega_y + (n_z + \frac{1}{2})\hbar\omega_z \tag{2.20}$$

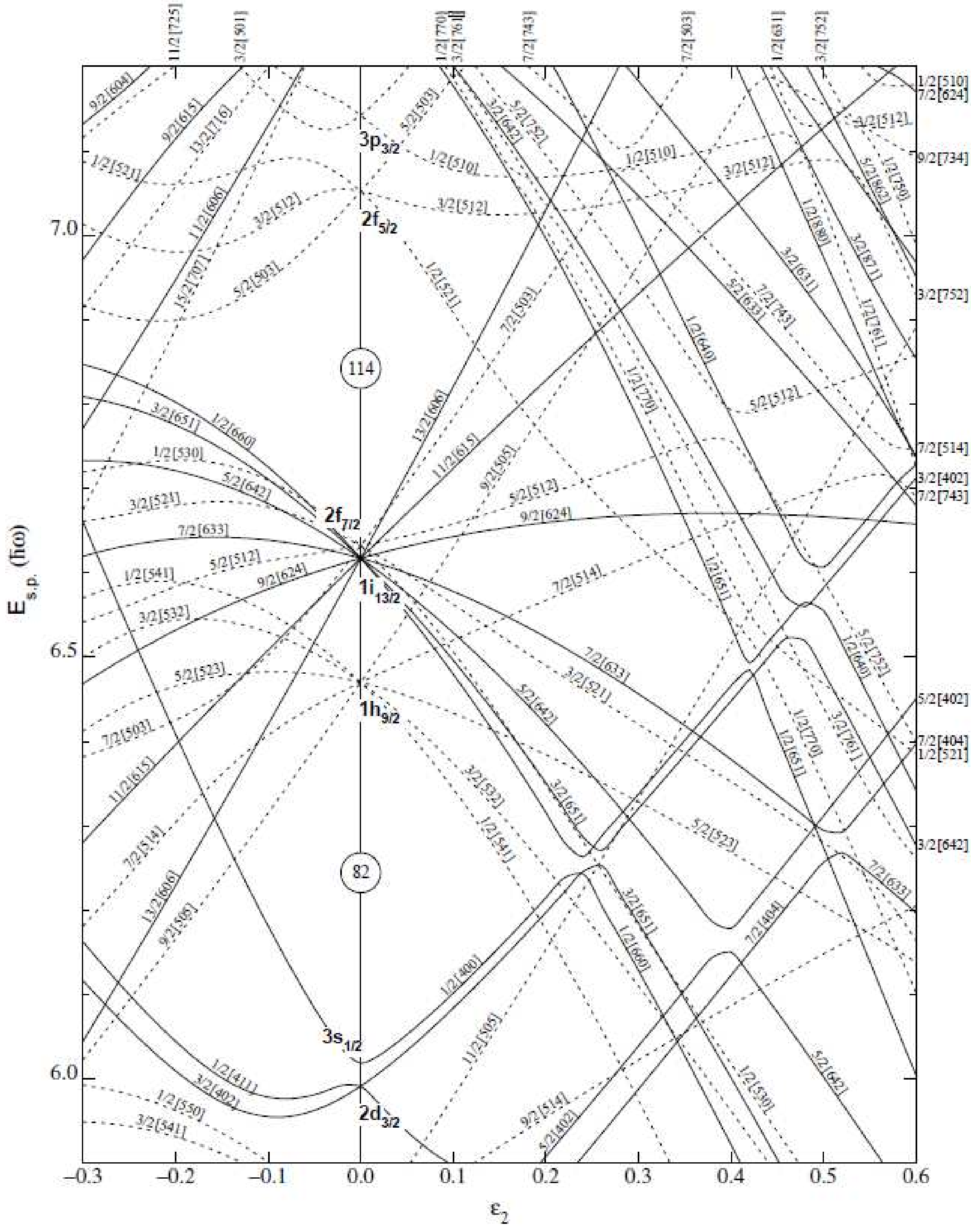

Figure 2.3: Nilsson diagram for proton (Z $\sim$ 82) single particle energy states as a function of axial deformation parameter ϵ_2 (ϵ_2=δ). Solid and dashed lines represent positive and negative parity orbitals, respectively [7].

In axially deformed nuclei with z-axis as a symmetry axis of the nucleus, the oscillator frequencies can be written as

$$\omega_x = \omega_y = \omega_\perp = \omega_0(\delta)\sqrt{1+\frac{2}{3}\delta} \tag{2.21}$$

$$\omega_z = \omega_0(\delta)\sqrt{1-\frac{4}{3}\delta} \tag{2.22}$$

$$\omega_\perp^2\omega_z = \dot{\omega}_0^3 \tag{2.23}$$

Where, δ is the distortion parameter, and $\omega_\perp$ and ω_z represent the oscillator frequencies along the perpendicular and parallel directions to the symmetry axis, respectively. The oscilator frequency $\omega_0(\delta)$ is given by

$$\omega_0(\delta) = \dot{\omega}_0\left(1+\frac{2}{3}\delta^2\right) \tag{2.24}$$

And the distortion parameter δ is related to the axial deformation parameter β_2 as

$$\delta \approx \frac{3}{2}\sqrt{\frac{5}{4\pi}}\beta_2 \approx 0.95\beta_2 \tag{2.25}$$

The eigenstates of the axially deformed Hamiltonian are characterized by the quantum numbers $n_\perp = n_x + n_y$, n_z and the eigenvalues are given by

$$\epsilon(n_\perp n_z) = (n_\perp + 1)\hbar\omega_\perp + (n_z + \frac{1}{2})\hbar\omega_z \tag{2.26}$$

It is convenient to use cylindrical coordinates. The eigen states can be represented by the quantum numbers n_z, n_ρ, m_l, where, m_l is the projection of orbital angular momentum on to the symmetry axis. The principal quantum number N can be written in cylindrical coordinate system as

$$N = n_z + 2n_\rho + m_l = n_x + n_y + n_z = 2(n-1) + l \tag{2.27}$$

Therefore, the energy eigen value for an axially deformed nuclei can be expressed in cylindrical coordinate system and the eigenvalues are given by

$$\epsilon(n_z, n_\rho, m_l) = (2n_\rho + m_l + 1)\hbar\omega_\perp + (n_z + \frac{1}{2})\hbar\omega_z \simeq (N + \frac{3}{2}) + \delta(\frac{N}{3} - n_z)\hbar\dot{\omega}_0 \tag{2.28}$$

Each level in Nilsson model can be specified by the quantum numbers (Fig. 2.3)

$$\Omega^\pi[Nn_zm_l] \tag{2.29}$$

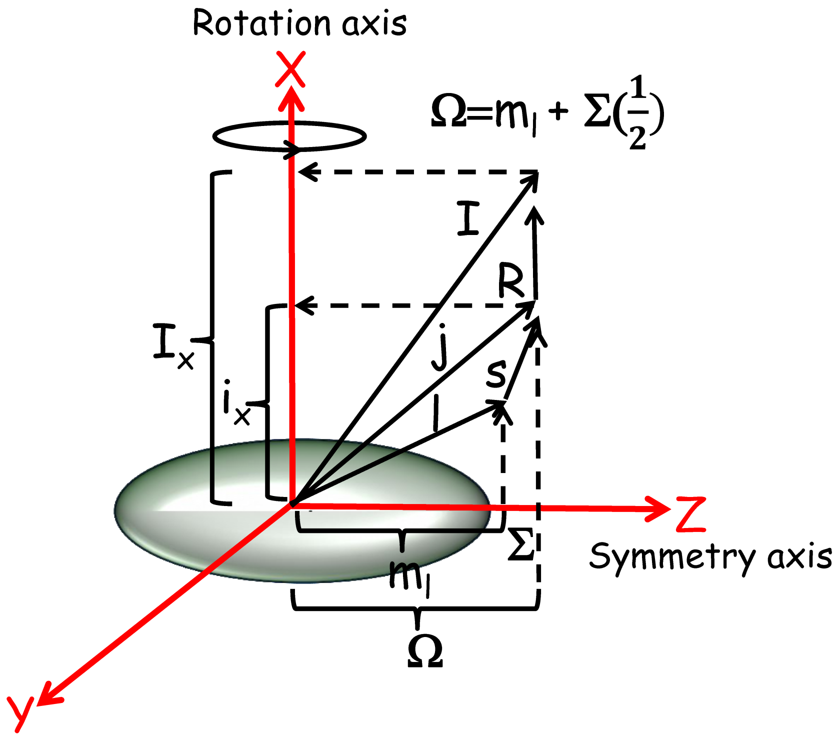

Figure 2.4: Asymptotic quantum numbers m_l, Σ, Ω for the Nilsson model are shown

where N is the principal quantum number, Ω is projection of single-particle angular momentum on the symmetry axis (z), m_l is projection of the orbital angular momentum on the symmetry axis and n_z is number of oscillator quanta along the symmetry axis (Fig. 2.4. The z-projection of the total angular momentum of the particle satisfies

$$\Omega = (m_l \pm \frac{1}{2}), \tag{2.30}$$

where, $\pm\frac{1}{2}$ are the projections of the spin angular momentum. These quantum numbers are known as asymptotic quantum numbers. The z-projection of total angular momentum of the particle (Ω) and the parity π are the only two good quantum numbers for a nucleus with large deformation. One of the features in Nilsson model is that the 2j+1 fold degeneracy of the shell model states are lifted and each level splits into (2j+1)/2 number of states. Each level has only two fold degeneracy $\pm\Omega$.

Example: For $1\pi i_{13/2}$ state split into 7 levels of $\Omega = \frac{1}{2}, \frac{3}{2}, ...\frac{13}{2}$. The orbital and principal quantum numbers for the $i_{13/2}$ orbital are $l = 6$ and $N = 6$, respectively. Now, for $\Omega = \frac{1}{2}$,

$$m_l = 0(\Omega = (m_l \pm \frac{1}{2}))$$
$$n_z = 6 \text{ from } eq^n \text{ [2.27]}$$
$$\text{parity}(\pi) = +ve((-1)^l or (-1)^N)$$

Therefore, the Nilsson quantum numbers for $\Omega = \frac{1}{2}$ can be written as $\frac{1}{2}^+[660]$. Similarly, for $\Omega = \frac{3}{2}$,

$$m_l = 1$$
$$n_z = 5$$
$$\pi = +ve$$

and the Nilsson quantum numbers are $\frac{3}{2}^+[651]$. Similarly the Nilsson asymptotic quantum numbers for the other components of $i_{13/2}$ orbital can be obtained.

2.4 Cranking Model

The Nilsson model describes the dependence of the single-particle states on the amount of deformation of a deformed nucleus. In Cranked shell model, the influence of rotation on single particle levels has been discussed. Conventionally, x axis is considered as the rotation axis of a nucleus which is perpendicular to the symmetry axis (z) at a fixed rotational frequency ω. This model was discussed by Inglis [8, 9] in a semiclassical way. The model is very successful in describing the rotational band structures of the rotating nuclei. The Hamiltonian of a rotating nucleus can be expressed as

$$H^\omega = \sum_{i=1}^{A} h_i^\omega = \sum_{i=1}^{A} \left[h_i^0 - \omega j_{ix}\right] \tag{2.31}$$

where, $h_i^\omega = h_i^0 - \omega j_{ix}$ is the single particle Hamiltonian in the rotating frame, h_i^0 is the single particle Hamiltonian in the laboratory frame and j_{ix} is the projection of the angular momentum of the i^{th} particle on to the rotation (x) axis. ωj_{ix} is analogous to Coriolis and centrifugal forces in the rotating frame. Therefore, the single particle energy in the laboratory frame is given by,

$$e_i = \langle i^\omega \mid h_i^0 \mid i^\omega \rangle = e_i^\omega + \omega \langle i^\omega \mid j_{ix} \mid i^\omega \rangle \tag{2.32}$$

Where, e_i^ω is the single particle Routhian i.e energy in the rotating frame of reference. Therefore, the total energy of the nucleus in the laboratory frame can be written as:

$$E = \sum_{i=1}^{A} e_i = \sum_{i=1}^{A} [e_i^\omega + \omega \langle i^\omega \mid j_{ix} \mid i^\omega \rangle] \tag{2.33}$$

And the total projection of the nuclear angular momentum on the rotation axis is obtained by:

$$I_x = \sum_{i=1}^{A} \langle i^\omega \mid j_{ix} \mid i^\omega \rangle \tag{2.34}$$

The contribution of particle angular momentum along rotational axis (i_x) can be obtained from the slope of the single particle Routhian (e_i^ω) as:

$$i_x = -\frac{de_i^\omega}{d\omega} = -\langle i^\omega \mid j_{ix} \mid i^\omega \rangle \tag{2.35}$$

which can be compared with the experimental aligned angular momenta. The coriolis term -ωI_x (I_x represents the total angular momenta of the nucleus along x-axis) breaks the time-reversal symmetry and the Hamiltonian is invariant under the operation of parity (π) and a rotation of 180° about the x axis. The eigen value of rotation operator ($\mathcal{R}_x \Psi = e^{-i\pi I_x}$) is given by

$$\mathcal{R}_x \Psi = e^{-i\pi I_x} \Psi = r\Psi \tag{2.36}$$

where,$r = e^{-i\pi\alpha}$ is the eigen value and α is the signature quantum number [3]. The signature quantum number α is related with the total angular momentum I by the relation I= α mod 2. Therefore, a nucleus with π-rotational symmetry would have two sets of states i.e two bands corresponding to two values of α. In case of even-A nucleus

$$I = 0, 2, 4, ... \text{ for } \alpha = 0, r = +1$$

$$I = 1, 3, 5, ... \text{ for } \alpha = 1, r = -1$$

and for odd-A nucleus

$$I = 1/2, 5/2, 9/2, ... \text{ for } \alpha = 1/2, r = -i$$
$$I = 3/2, 7/2, 11/2, ... \text{ for } \alpha = -1/2, r = +i$$

2.5 Strutinsky Shell Correction

The total energy of a nucleus can be determined from both liquid drop model (LDM) as well as shell model approaches. However, though the bulk properties are well explained in LDM the shell model approach is necessary to explain the microscopic properties. Hence, a combined method for the determination of total energy of a nucleus would be essential. V.M. Strtinsky provided a prescription which combines the both approaches [10, 11]. The Strutinsky shell correction considers smoothly varying nuclear binding energy from the LDM and the fluctuation comes from the nuclear shell model. The combined effect of both can explain the oscillatory behavior of the experimetal binding energy as a function of mass number. Therefore, the total energy E of a nucleus can be calculated by adding the smooth part E_{LDM} from the liquid drop model with the oscillatory part E_{osc} from the shell model as [12]

$$E = E_{LDM} + E_{osc} \tag{2.37}$$

In nuclear shell model, the total binding energy of a nucleus can be written as a combination of smoothly varying part $\tilde{E}_{sh}$ and an oscillatory part E_{osc} as:

$$E_{sh} = \sum_{i=1}^{A} \epsilon_i = E_{osc} + \tilde{E}_{sh} \tag{2.38}$$

where, ϵ_i is the single particle energy of i^{th} nucleonic level. The E_{sh} can be calculated using the single particle nucleonic level density function $g(\epsilon)$. The number of single particle levels in an energy interval between ϵ to $\epsilon + d\epsilon$ is $g(\epsilon)d\epsilon$. The level density function $g(\epsilon)$ can be represented as

$$g(\epsilon) = \sum_i \delta(\epsilon - \epsilon_i) \tag{2.39}$$

And the total number of nucleon (A) in the nucleus can be calculated by the following relation

$$A = \int_{-\infty}^{\lambda} g(\epsilon)d\epsilon \tag{2.40}$$

where, λ is the Fermi energy. Now, the total shell model energy for a nucleus of mass number A can be calculated as

$$E_{sh} = \int_{-\infty}^{\lambda} \epsilon g(\epsilon)d\epsilon \tag{2.41}$$

The smooth part of the shell model energy ($\tilde{E}_{sh}$) can be written in terms of smooth part of $g(\epsilon)$ which is $\tilde{g}(\epsilon)$. Now the smooth part of shell model energy is

$$\tilde{E}_{sh} = \int_{-\infty}^{\tilde{\lambda}} \epsilon \tilde{g}(\epsilon)d\epsilon \tag{2.42}$$

Therefore, the total energy of a nucleus is given by

$$E = E_{LDM} + E_{osc} = E_{LDM} + (E_{sh} - \tilde{E}_{sh}) \tag{2.43}$$

2.6 Total Routhian Surface (TRS) Calculations

The Total Routhian Surface (TRS) calculations give quantitative idea about the shape of an atomic nucleus for a particular configuration. TRS calculations have been performed for ^{197}Tl and ^{187}Os nuclei in the present thesis work. The TRS code, developed by Nazarewicz et al. [13, 14], has been used for such calculations. In this code, the single-particle energies have been calculated using the following deformed Woods-Saxon potential

$$V(\vec{r}, \hat{\beta}) = \frac{V_0}{1 + exp[dist_{\Sigma}(\vec{r}, \hat{\beta})/a]} \tag{2.44}$$

where $dist_{\Sigma}(\vec{r}, \hat{\beta})$ is the distance of a point $\vec{r}$ from the nuclear surface and $\hat{\beta}$ denotes the set of all deformation parameters. The total Routhian energy $E^{\omega}(Z, N; \hat{\beta})$ of a nucleus can be written as

$$E^{\omega}(Z, N; \hat{\beta}) = E^{\omega}_{LD}(Z, N; \hat{\beta}) + E^{\omega}_{shell}(Z, N; \hat{\beta}) + E^{\omega}_{pair}(Z, N; \hat{\beta}) \tag{2.45}$$

where $E^{\omega}_{LD}(Z,N;\hat{\beta})$ is the smooth part of the energy obtained from the LDM, $E^{\omega}_{shell}(Z,N;\hat{\beta})$ is the fluctuation term from the shell model calculated using Strutinsky shell correction approach and $E^{\omega}_{pair}(Z,N;\hat{\beta})$ is the pairing energy term calculated from the cranking Hartee-Fock-Bogoliubov approach. In this calculation, the total nuclear energy is calculated in the rotating frame in (β_2,γ,β_4) deformation mesh points for different values of the rotational frequencies $\hbar\omega$ as discussed in Ref. [15, 16]. For each values of β_2 and γ, the energy is minimised with respect to the β_4 deformation and the energy contours are plotted in the (β_2,γ) plane for each value of $\hbar\omega$. The values of β_2 and γ corresponding to the minimum of the contours are considered to determine the calculated shape of the nucleus. Different sets of β_2 and γ values for the minimum of the TRS calculations for different rotational frequencies of a nucleus provide the evolution of nuclear shape as a function of rotational frequency and thereby, as a function of excitation energy and angular momentum. The TRS calculations can be extended for different configurations of a nucleus to calculate the shape of a nucleus for different quasi-particle configurations.

2.7 Shears Mechanism with the Principal Axis Cranking for Magnetic Rotational Band

The magnetic rotational (MR) bands are generated for weakly deformed near spherical or spherical nuclei with particle-hole configurations based on high-j orbitals. In magnetic rotation, the particle and hole angular momenta dominate over the weakly deformed core rotation. However, it has been observed in recent studies that there is also a significant contribution from the angular momentum of the weakly deformed core to the total angular momentum of a nucleus in its MR band. The core contribution can be introduced in the shears mechanism using a geometrical model called Shears mechanism with the Principal Axis Cranking (SPAC) which can succesfully explain intrinsic properties of the MR bands. In SPAC model the particle $(\overrightarrow{j_2})$ and hole $(\overrightarrow{j_1})$ angular momenta couple to generate shears angular momentum $\overrightarrow{j_{sh}}$ (Fig. 2.5). The total angular momentum (I) of a nucleus can be generated by the coupling of the core

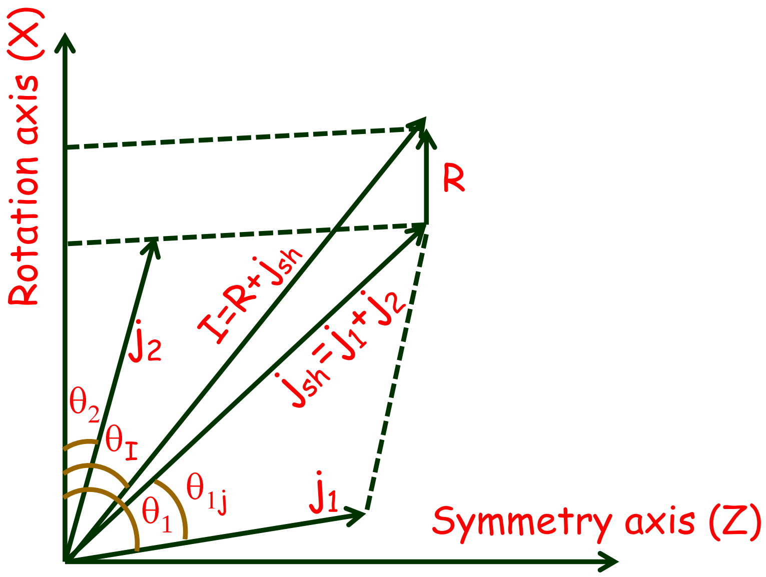

Figure 2.5: Schematic diagram of the shears mechanism in the principal axis cranking picture

angular momentum ($\overrightarrow{R}$) with the shears angular momentum ($\overrightarrow{j_{sh}}$)[17, 18, 19]. The level energy of an MR band of spin I can be expressed as

$$E(I) = E(core) + E(shears) + constant.$$

Where,

$$E(core) = \frac{R^2\,(\mathrm{I},\,\theta_1,\,\theta_2)}{2J(I)}$$

is the contribution to the total energy E(I) from core rotation, and

$$E(shears) = v_2 P_2(cos(\theta_1 - \theta_2))$$

is the shears energy due to the interaction between the shear blades $\overrightarrow{j_1}$ and $\overrightarrow{j_2}$. The particle and hole angular momenta $\overrightarrow{j_2}$ and $\overrightarrow{j_1}$ make angle θ_2 and θ_1 with respect to the rotational axis $\hat{x}$. The reduced transition probabilities of dipole ($B(M1)$) and quadrupole ($B(E2)$) transitions, with the classical approximation for Clebsch-Gordon coefficients, can be written as [18, 19, 20, 21, 22],

$$B(M1) = \frac{3}{8\pi}[j_1 g_1^* sin(\theta_1 - \theta_I) - j_2 g_2^* sin(\theta_I - \theta_2)]^2$$

$$\text{and } B(E2) = \frac{15}{128\pi}[Q_{eff}sin^2\theta_{1j} + Q_{coll}cos^2\theta_I]^2,$$

respectively, where, $g_1^* = g_1 - g_R$, $g_2^* = g_2 - g_R$ and $g_R = \frac{Z}{A}$ are the g-factors; Q_{eff} and Q_{coll} are the quasi-particle and collective quadrupole moments, respectively; and

$$\theta_I = (\theta_1 - \theta_2) \tag{2.46}$$

is the angle between the total angular momentum vector (I) with respect to the rotational axis ($\hat{x}$). The energy minimisation can be found with respect to θ_1 and θ_2 for each state of angular momentum I as

$$\frac{\partial^2 E(I, \theta_1, \theta_2)}{\partial\theta_1 \partial\theta_2} = 0.$$

The experimental energy (E_γ), spin (I), rotational frequency (ω) and $\frac{B(M1)}{B(E2)}$ values of MR bands for weakly deformed nuclei in ^{197}Tl have been well reproduced in the framework of the SPAC model.

2.8 Particle-Rotor Model

The particle rotor model has been very successful in explaining various properties of the rotational bands of a deformed rotor with a single or multiple particles. This model requires a set of single-particle orbits in a deformed Nilsson potential. The total wave function is composed of a correlated motion of nucleons in this intrinsic field and the collective rotational motion of the rotor. The total energy Hamiltonian of Particle-rotor Model (PRM) can be written as [3, 12]

$$H_{PRM} = H_{coll} + H_{intr} \tag{2.47}$$

where, H_{coll} and H_{intr} are the collective and the intrinsic parts, respectively.

$$H_{coll} = \sum_k \frac{R_k^2}{2\mathcal{J}_k} = \sum_k \frac{(I_k - j_k)^2}{2\mathcal{J}_k} (k = 1, 2, 3) \tag{2.48}$$

Where, $k = 1, 2, 3$ denotes the principal axes in the body-fixed frame. The collective rotor and the total nuclear angular momentum can be represented by R_k and I_k, respectively and the angular momentum due to the valence particle is denoted by j_k. Moreover, the parameters $\mathcal{J}_k$ are the three principal moments of inertia. H_{intr} can be expressed as an intrinsic Hamiltonian which describes the motion of the single nucleon in a Nilsson orbital.

$$H_{intr} = \pm\frac{1}{2}C[\cos(j_3^2 - \frac{j(j+1)}{3}) + \frac{\sin\gamma}{2\sqrt{3}}(j_+^2 + j_-^2)] \tag{2.49}$$

where, $\pm$ refers to the particle and hole nature of valance nucleon. The parameter γ is the triaxial deformation parameter and the coefficient C is proportional to the axial (quardupole) deformation parameter β_2 [23]. The PRM Hamiltonian is generally solved by diagonalization in the strong-coupling basis to calculate the energy spectra of the yrast and other side band e.g wobbling bands in a triaxial nucleus. The quadrupole deformation parameters (β_2 and γ) for a particular configuration were obtained from energy minimization and have been used in the PRM calculations.

2.9 Comparison of Experimental Results with the Theoretical Calculations

In order to compare the experimental results with the theoretical calculations, one has to determine different parameters related to the corresponding theoretical model from the experimental observables. The primary experimental observables in gamma ray spectroscopy are the energy and intensity of the gamma rays. From these observables and their correlations, a level scheme is generated with energy of the excited states and their spin and parity are also assigned. For deformed nuclei rotational bands are obtained. The energy of the excited states in the rotational bands follow the relation:

$$E(I) = \frac{\hbar^2}{2\mathcal{J}}I(I+1) \tag{2.50}$$

where, $\mathcal{J}$ is the static moment of inertia of the nucleus and I is the spin or angular momentum of the excited state. In case of a rotational band of an axially symmetric quadrupole deformed nucleus, the $E2$ transitions between the states $I \to I-2$ are generally enhanced. Different parameters corresponding to a deformed rotor can be determined from the rotational bands in analogy with classical rotor formula as follows: The kinematic moment of inertia ($j^{(1)}$) and dynamic moment of inertia ($j^{(2)}$) of a rotating nuclei can be defined as

$$j^{(1)} = \frac{I}{\omega} \tag{2.51}$$

and

$$j^{(2)} = \frac{dI}{d\omega} \tag{2.52a}$$

$$\approx \frac{4\hbar}{\Delta E_\gamma} \quad \text{for the ground state band of even-even nuclei} \tag{2.52b}$$

In case of dynamic moment of inertia, it only depends on the difference in energy of transitions between two consecutive decays and has no dependence on the absolute spin of the levels. Therefore, it is a very useful quantity in cases where the decay out of a band is not observed and the spin of the states is not well established. The variation of the dynamic moment of inertia with rotational frequency can give important information about the structural changes that are taking place within a rotational band. The comparision of experimental observables like excitation energies, spins and transition probabilities with theoretical calculation in rotating frame is not possible. And the experimental excitation energies and experimental angular momentum I need a transformation to the intrinsic rotating frame of the nucleus. The total experimental Routhian in the rotating frame can be expressed as

$$E^{'}(\omega) = E(\omega) - \hbar\omega I_x(I). \tag{2.53}$$

Where, the rotational frequency ω for a gamma transition between two levels $I-1$ to $I+1$ can be expressed as

$$\omega(I) = \frac{dE(I)}{dI_x} = \frac{E(I+1) - E(I-1)}{I_x(I+1) - I_x(I-1)} \tag{2.54}$$

where, I_x is the projection of total angular momentum I on to the rotation axis of a nucleus. On the other hand, the projection along the symmetry axis is denoted by K. The angular momentum (I_x) along the rotational axis can be obtained from the relation:

$$I_x = \sqrt{I(I+1) - K^2}, \tag{2.55}$$

The quasi-particle energy Routhian and aligned angular momentum along rotation axis can be obtained by substracting a reference from their absolute values as

$$e^{'}(\omega) = E^{'}(\omega) - E_{ref}(\omega) \tag{2.56}$$

and

$$i(\omega) = I_x(\omega) - I_{ref}(\omega), \tag{2.57}$$

The aligned angular momentum and energy Routhian for the reference can be calculated using the relation

$$I_{ref}(\omega) = (\mathcal{J}_0 + \omega^2 \mathcal{J}_1)\omega \tag{2.58}$$

and

$$E_{ref}(\omega) = -\frac{1}{2}\omega^2 \mathcal{J}_0 - \frac{1}{4}\omega^4 \mathcal{J}_1 + \frac{\hbar^2}{8\mathcal{J}_0}, \tag{2.59}$$

Where, $\mathcal{J}_0$ and $\mathcal{J}_1$ are the Harris parameters.

Bibliography

[1] Maria Goeppert Mayer Science **145** 999-1006, (1964)

[2] Sven Gösta Nilsson, Dan. Mat. Fys. Medd. **29**, no. 16 (1955).

[3] A. Bohr and B. R. Mottelson, *Nuclear Structure* (Benjamin, New York, 1975), Vol.II.

[4] D. L. Hill and J. A. Wheeler, Phys. Rev. **89**, 1102 (1953).

[5] G. Andersson et al., Nucl. Phys. **A 268**, 205 (1976).

[6] R. F. Casten, *Nuclear Structure From A Simple Perspective* (OXFORD UNIVERSITY PRESS, New York 1990).

[7] R. B. Firestone, et al., Table of Isotopes (John Wiley and Sons, Inc., New York (1999)).

[8] D.R.Inglis, Phys. Rev. **96**, 1059 (1954).

[9] D.R.Inglis, Phys. Rev. **103**, 1786 (1956).

[10] V. M. Strutinski Nucl. Phys. A **95**, 420 (1967).

[11] V. M. Strutinski Nucl. Phys. A **122**, 1 (1968).

[12] P. Ring and P. Schuck, *The Nuclear Many Body Problem* (Springer Verlag, Berlin, 1980).

[13] W. Nazarewicz et al., Nucl. Phys. A 435, 397 (1985).

[14] W. Nazarewicz et al., Nucl. Phys. A 512, 61 (1990).

[15] G. Mukherjee, H. C. Jain, R. Palit, P. K. Joshi, S. D. Paul, and S. Nagraj, Phys. Rev. C 64, 034316 (2001).

[16] G. Mukherjee et al., Nucl. Phys. A 829, 137 (2009).

[17] A.O. Macchiavelli *et al.*, Phys. Lett. **B 450**, 1 (1999).

[18] E. O. Podsvirova, *et al.*, Eur. Phys. J. **A 21**, 1 - 6 (2004).

[19] A. A. Pasternak, *et al.*, Eur. Phys. J. **A 23**, 191 - 196 (2005).

[20] A. A. Pasternak, *et al.*, Eur. Phys. J. **A 37**, 279 - 286 (2008).

[21] S. Rajbanshi *et al.*, Phys. Rev. C **90**, 024318 (2014).

[22] S. Rajbanshi *et al.*, Phys. Rev. C **89**, 014315 (2014).

[23] S. Y. Wang, B. Qi, and S. Q. Zhang, Chin. Phys. Lett. **26**, 052102 (2009).

Chapter 3

Experimental Techniques and Data Analysis

In the present thesis work, the gamma-ray spectroscopy technique has been used to study the structure of nuclei at medium to high angular momentum and excitation energies. The experimental techniques for such study involves mainly two aspects, namely, the production of the nucleus of interest at that angular momentum and excitation energy and secondly, the detection of the gamma rays emitted from the excited states of the nucleus of interest. Both of these aspects will be discussed in this Chapter along with the details of the data analysis.

In order to study the properties of the nuclei at medium to high angular momentum and excitation energies, such states will have to be populated by nuclear reaction mechanism. Among the several nuclear reaction mechanisms, the fusion evaporation reaction is one of the most useful one to populate the high spin states in nuclei. In this thesis work, both the heavy-ion and the light-ion induced fusion evaporation reactions have been used to populate the excited states.

3.1 Fusion Evaporation Reaction

Fusion-evaporation reaction is the most common method to populate the excited states in nuclei as it has several advantages than the other reaction mechanisms. Firstly, a wide variety of nuclei can be populated in such reactions by varying the target, projectile and the projectile energy. Secondly, the nuclei will be produced with a large amount of angular momentum. Moreover, the nuclei from near the stability line to the ones lie at the far from the stability line could be produced with relatively large cross-section in the fusion-evaporation reaction. One of the disadvantages in the fusion-evaporation reaction with stable beam-target combination is that the nuclei are mostly produced in the neutron deficient side of the stability line.

In the fusion-evaporation reaction the projectile nucleus, with kinetic energy greater than the Coulomb energy between the target and the projectile nuclei, collides with target nucleus and fuse together to form a compound nucleus (CN). This compound nucleus is produced at large angular momentum and with high excitation energy (depending on the target-projectile combination and the projectile energy). The excitation energy is, usually, much higher than the particle separation energy and hence, in the first stage of its decay, particles (neutron, proton, alpha, etc.) are evaporated from the compound nucleus followed by the emission of continuous statistical gamma rays, which are mainly E1 transitions, until the excitation energy of the compound nucleus comes down to around the yrast line. Most of the time, the evaporated particles are the neutrons and the charged particle emission is hindered due to the Coulomb barrier. Until this point, the CN, though loses a large amount of excitation energy, it loses only a small amount of angular momentum. Thus the residual nucleus still has a substantial amount of angular momentum. At this point the residual nucleus cools down to the ground state by emitting discrete gamma rays through states which lie at or around the yrast line. These discrete gamma rays carry the information about the structure of the residual nucleus.The yrast line is the loci of the states which have lowest excitation energy for a given angular momentum. If the residual nuclei are deformed rotating nuclei, then the emitted γ-rays are mainly of $E2$ type. A schematic diagram of the formation and decay mechanisms of the compound nucleus has been shown in Fig. 3.1 and 3.2.

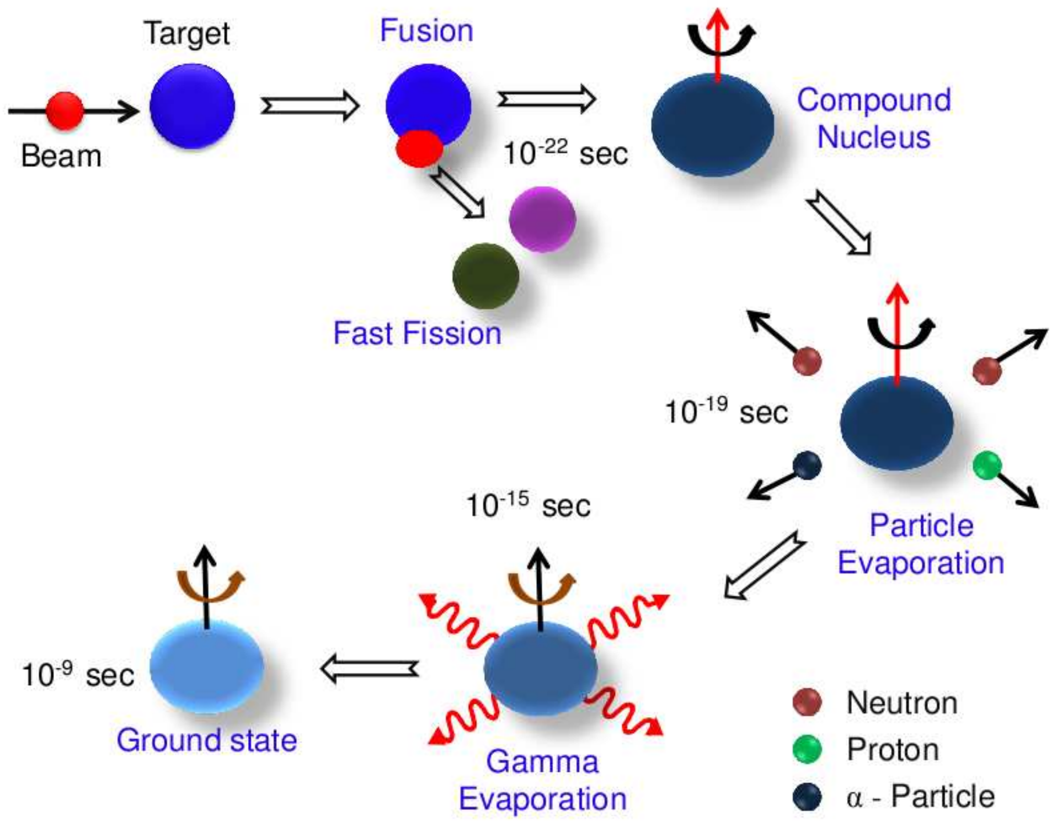

Figure 3.1: Schematic diagram of fusion evaporation reaction. This figure is taken from Ref. [1].

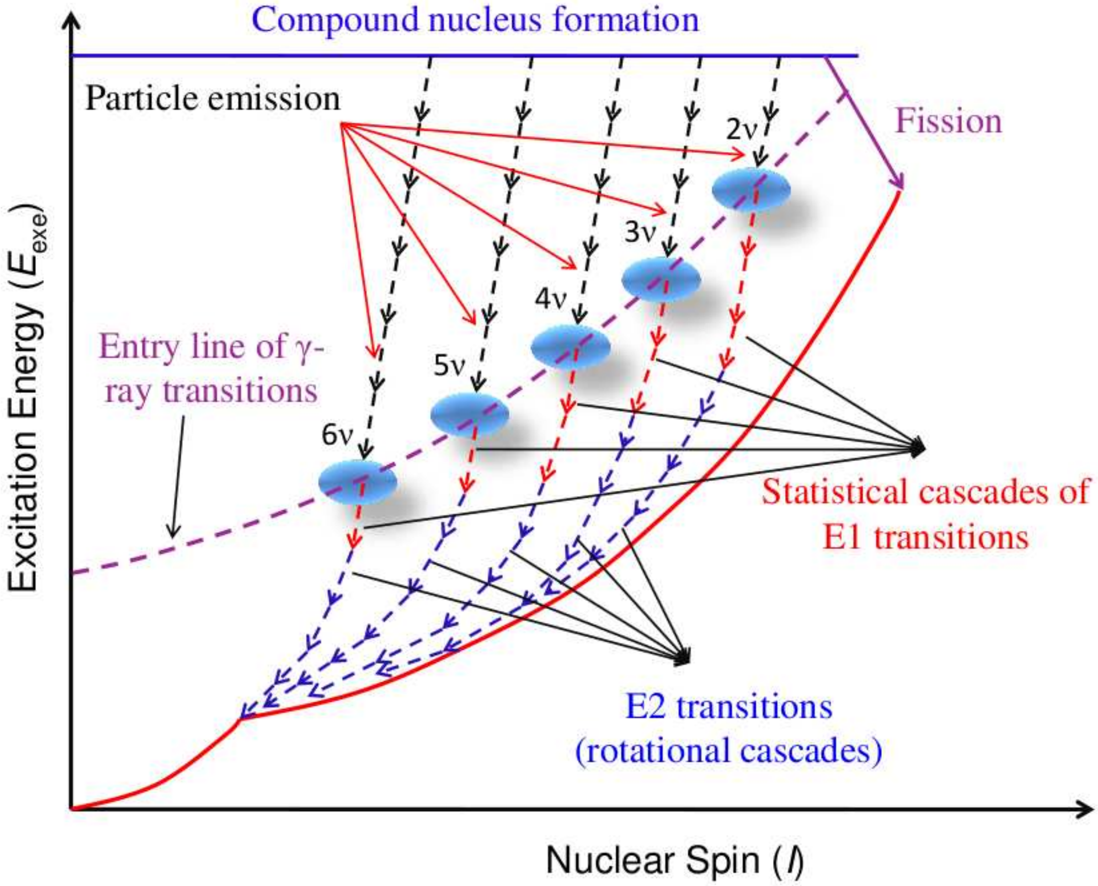

Figure 3.2: Excitation energy as a function of nuclear spin is shown. This figure is taken from Ref. [1].

In this reaction, the kinetic energy (E_{CM}) of the collision between projectile and target nuclei in the centre of mass frame is converted in to the excitation energy (E_x) of the compound nucleus. The excitation energy of the compound nucleus can be expressed by

$$E_x = Q + E_{CM} \tag{3.1}$$

where Q is the Q-value for the formation of the compound nucleus and E_{CM} is the kinetic energy of the collision in the centre of mass frame. Q and E_{CM} can be calculated by the following relation:

$$Q = M_T + M_P - M_{CN} \tag{3.2}$$

$$E_{CM} = \frac{M_T}{M_T + M_P} E_B \tag{3.3}$$

where M_T, M_P and M_{CN} are the masses of target, projectile and compound nucleus, respectively. E_B is the beam energy in the laboratory frame. The maximum angular momentum (l_{max}) transferred to the compound nucleus in fusion-evaporation reaction can be achieved when the projectile and the target nuclei just touch each other. This is given by the following expression:

$$l_{max} = \sqrt{\frac{2\mu R^2}{\hbar^2}(E_{CM} - V_C)} \tag{3.4}$$

where $\mu = \frac{M_P M_T}{M_P + M_T}$ is the reduced mass for the projectile and the target nuclei. R is the centre-to-centre distance of the projectile and the target nuclei and is given by [2]

$$R = 1.36(A_P^{\frac{1}{3}} + A_T^{\frac{1}{3}}) + 0.5 \tag{3.5}$$

Unit of R is fm. A_P and A_T are the mass numbers of the projectile and the target nuclei, respectively. V_C is the Coulomb barrier energy (in MeV) between the projectile and the target nuclei and is given by

$$V_C = 1.44 \frac{Z_P Z_T}{R} \tag{3.6}$$

It is seen from eq. (3.4) that the maximum angular momentum (l_{max}) transferred to the compound nucleus depends on reduced mass of the projectile-target combination and the beam energy in CM frame with respect to the Coulomb barrier energy (V_C).

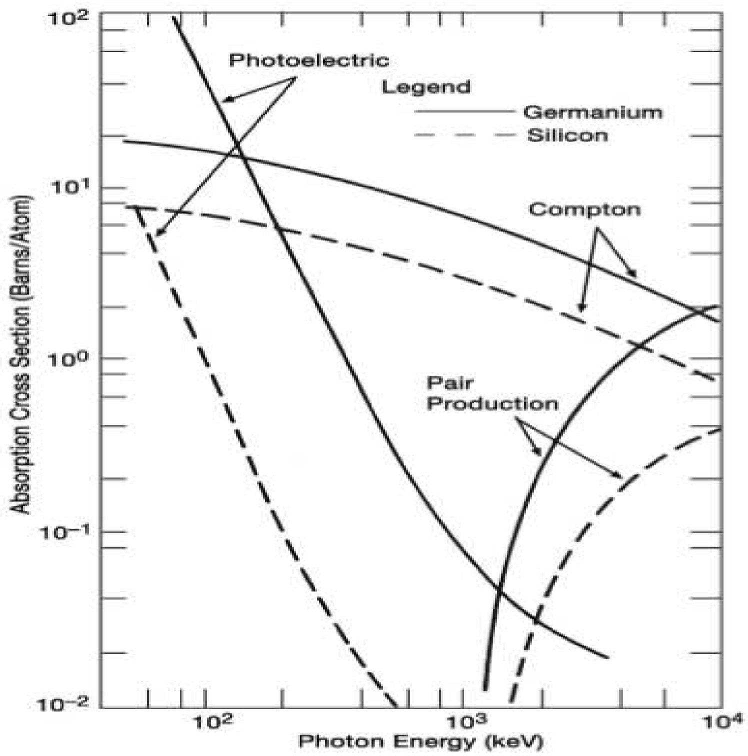

Figure 3.3: Cross section for each of the three types of γ-ray interactions in Ge (Z = 32) and Si (Z = 14) as a function of γ energy. This figure is taken from Ref. [3].

3.2 γ Ray Detection

In a fusion-evaporation reaction, the compound nucleus, in an excited state below the particle separation threshold, decays predominantly through the emission of γ rays until it reaches to the ground state. In this way, the compound nucleus and/or residual nucleus decay through mainly γ rays before reaching to the ground state. The gamma rays interact with material by three major processes, photoelectric effect, Compton scattering and pair production. In all the three interaction mechanisms gamma ray deposits its energy either completely or partially and the electrons inside the material takes this energy. In a detector medium these energetic electrons ultimately generate an electric pulse which is proportional to the energy deposited by the gamma ray.

Figure 3.4: Clover HPGe (left) and LEPS HPGe (right) detector at Laboratory.

3.2.1 Photoelectric Effect

The most desirable interaction to obtain the full energy of gamma transition is the photoelectric effect. In the photoelectric effect, the γ-ray photons interact with the bound atomic electrons and transfer full energy to the electrons. Due to the absorption of energy the bound electron emits with kinetic energy E_e, such that,

$$E_e = E_\gamma - E_b \tag{3.7}$$

Where E_γ is the γ-ray energy and E_b is the electron binding energy. The dependence of the photoelectric cross section with the energy of the incident γ ray is shown in Fig. 3.3 [3]. The photoelctric effect cross-section decreases with the increase of the γ-ray energy. Along with the energy dependence, the photoelctric cross-section also depends on the atomic number (Z) of the interacting material which can be calculated using born aproxiamtion for non-relativistic case. It can be shown that the dependence of the photoelectric effect cross-section (σ_{photo}) on Z follows the equation

$$\sigma_{photo} \propto Z^n,$$

where n varies from 4 to 5 over the γ-ray energy region of interest.

3.2.2 Compton Scattering

The Compton scattering is the scattering of photons by the free electrons. Although, the electrons inside the matter are bound but for the large incident gamma energies (compared to the electron binding energies) being considered here, the electrons binding energy can be neglected and they can be considered as free electrons. In the Compton scattering, the energy of the γ-ray transfers only a portion of its energy to the electron and the amount of energy transferred varies from zero to a maximum value which is less than the incident γ-ray energy. Considerng the conservation of energy and momentum, the energy of the scattered photon can be expressed as:

$$E'_\gamma = \frac{E_\gamma}{1 + (\frac{E_\gamma}{m_e c^2})(1 - cos\theta)} \tag{3.8}$$

where θ is the scattering angle, E_γ is the incident γ-ray energy and $m_e c^2$ (0.511 MeV) is the rest mass energy of the recoil electron. Therefore, the kinetic energy of the recoil electron can be written as:

$$\begin{aligned} E_e &= E_\gamma - E'_\gamma \\ &= E_\gamma \frac{(\frac{E_\gamma}{m_e c^2})(1 - cos\theta)}{1 + (\frac{E_\gamma}{m_e c^2})(1 - cos\theta)} \end{aligned} \tag{3.9}$$

As θ can take any value from $0°$ to $180°$, the recoil electrons will have a energy distribution for a particular energy of the incident γ ray. The maximum energy transfers to the electron can occur at the scattering angle $\theta = 180°$ which is called the Compton edge. Because of the partial energy diposition of a γ ray in this process, the energy loss due to Compton effect mostly contributes to the Compton background in the total γ-ray spectrum.

3.2.3 Pair Production

In the pair production process, when a γ ray of energy greater than twice the rest-mass energy of an electron ($2m_e c^2 = 1.022$ MeV) enters the detector medium, it creates an electron-positron pair. The cross-section of this interaction increases with the increase of the energy of the γ ray and and hence, this process dominates only at higher energies (E_γ>5 MeV). In this process, a γ-ray photon is converted into an electron-positron pair which need 1.022 MeV of energy for their creation and rest of the energy contributes to the kinetic energy of the pair. The pair production cross section depends approximately on the square of the atomic number of the medium. The created positron annihilates after slowing down in the medium and creates two annihilation γ-ray photons as secondary products of the process. These two annihilation γ rays may or may not get absorbed within the detector medeium. “Single escape” and ”double escape” peaks can be seen in a gamma ray spectrum (when high enrgy gamma rays are detected in a detector) depending on whether one of the two annihilation gammas or both of them escape out of the detector medium, respectively. The variation of the interaction cross sections for the photoelectric effect, Compton scattering and pair production as a function of incident gamma ray energy has been shown in Fig. 3.3.

3.3 High-Purity Germanium (HPGe) Detectors

The solid state (semiconductor) dectectors are known to be very good in energy resolution with moderate detection efficiency. The energy resolution of a dectector is inversely proportional to the number of electron-hole pair created by the amount of energy deposited in the detector medium. In the γ-ray spectroscopy studies, High Purity Germanium (HPGe) semiconductor detectors are widely used for experimental nuclear structure studies. The energy required to create an electron-hole (e-h) pair in Ge semiconductor is as small as about 3 eV. Therefore, a large number of e-h pairs can be created from the energy deposited by the incident gamma ray photon in a semiconductor HPGe detector medium. However, because of the low band-gap, sufficient amount of leakage current is also developed even at room temperature. The leakage current can be minimised by reducing the temperature of the HPGe crystal to 77K by using liquid nitrogen (LN2) and thereby minimizing the thermal excitation. Germanium semicondutor is preferred over Silicon semiconductor as gamma ray detectors as Geranium has higher atomic number (Z = 32) than Silicon (Z = 14). Therefore, the photoelectric cross-section for gamma rays are much higher in Germanium than Silicon.

The detectors are operated in reverse bias mode by creating a fully depleted region. The width of the depletion layer for a semiconductor can be expressed as [4]

$$d = \sqrt{\frac{2\epsilon V}{eN}} \tag{3.10}$$

where, V is the reverse bias voltage, N is the impurity concentration of the semiconductor material, ϵ is the dielectric constant and e is the electronic charge. Therefore, to get a desired large depletion depth, the impurity concentration in Ge crystals must be very low. This is achieved by making the Ge crystal with high purity ($\leq 2 \times 10^{-4}$ ppb) and hence, the name "High Purity Ge" (HPGe) detector.

In making the HPGe detectors the high purity Ge crystal is connected (by a cooling finger) with a Dewar to store LN2. There are several variants of HPGe detectors depending on the size and number of the crystals connected with a LN2 cryostat (Dewar). In "single crystal" HPGe detector, one crystal is attached with a LN2 Dewar. However, in "clover" configuration, four HPGe crystals of same (or very similar) sizes and shapes are connected with a single Dewar. Sometimes, a large Dewar is also connected to a crystal. These are specific purpose with less portability and for use in horizontal plane. Normally the detectors with Dewar sizes of 3 litres capacity are used in the HPGe detector arrays. In order to detect the low-energy gamma rays or X-rays, LEPS (Low Energy Photon Spectrometer) detectors are favoured. These are HPGe detectors in planar configuration and are much thinner compared to the clover detectors. In this thesis work, two types of HPGe detectors have been used, clover and LEPS. The clover and LEPS dectector have very similar crystal arrangement but the LEPS has a very thin berilium window at the front side of the detector compare to thick aluminium casing in clover detector.

3.3.1 Clover Detector

Clover detector [5] is a composite HPGe detector which is composed of four separate n-type coaxial HPGe crystals mounted on a common cryostat. The typical diameter of each crystal is 50mm dia × 70mm length. The crystals are tapered in the front face, which enables a close

Figure 3.5: VENUS setup at VECC.

packing (Ge-Ge distance of about 0.2 mm). The detector is housed inside an aluminium vacuum chamber. A picture of a Clover detector is shown in Fig. 3.4. Due to the thick aluminium cover in front of the crystals the detection efficiency for low energy γ rays (E_γ<100 keV) is reduced. The clover detectors, used in the present thesis work, were equipped with Anti-Compton shields (ACS) consisted of Bismuth Germanate ($Bi_4Ge_3O_{12}$) scintillation detectors (BGO). The ACS detects the Compton scattered γ rays which escape from the HPGe crystals after depositing a partial energy to the HPGe detector. The energy signals of such γ rays are vetoed out and are not registered as they contribute to the Compton background. This way, the Compton background is minimized. In a clover HPGe detector full energies of some of these Compton scattered events could be recovered by the process called addback. In this addback process, the energy deposited by a γ ray in the neighboring crystals of a clover detector, following a Compton scattering event, are added up in the offline analysis. Therefore, the partial energy deposition in two (or more) crystals of a clover detector detector are added up to give full energy peak, which would otherwise contribute to the Compton background. In this way, a double advantage of an increase of full energy peak as well as a decrease of Compton background is achieved. The “addback factor” can be expressed as the ratio of the total count of a peak in a clover detector after doing “addback” (addition of photo peaks of four crystals and additional count in the photo peak due to “addback”) to the sum of the photoelectric counts of the four individual crystals of the clover.

$$\text{Addback factor} = \frac{\text{Addback counts of the clover detector}}{\text{Sum of photoelectric counts of the 4 crystals}}$$

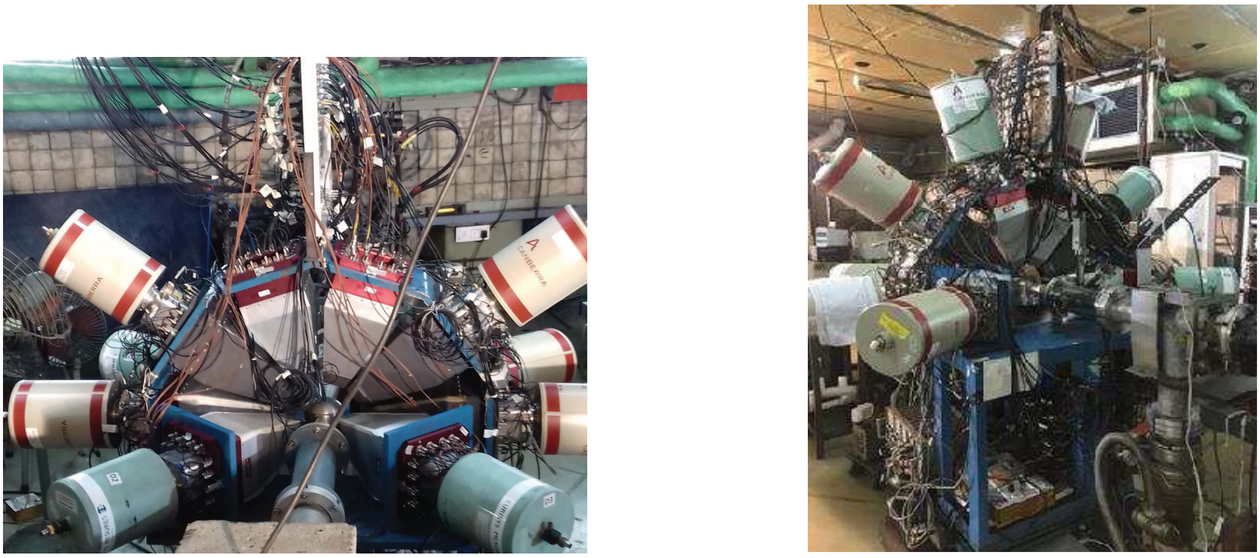

Figure 3.6: INGA setup at VECC (Phase I (left) and II (right)).

This addback factor is close to unity for low energy γ rays because of the large photo electric cross-section for such γ rays. But it increases with energy as the photo electric cross section decreases (but Compton scattering cross section almost remains same) and attains a maximum value ~ 1.5 at about 1.4 MeV γ ray.

3.3.2 Low Energy Photon Spectrometer (LEPS)

Low Energy Photon Spectrometer (LEPS) is a planer HPGe detector (Fig. 3.4) which is specially designed for the detection of low energy transitions with higher efficiency compared to the clover detector. The LEPS detector used in this work has a planar HPGe crsytal which has four electronically separated segments and a very thin Berilium window at the entry face. The thin Berilium window compared to the thick aluminium cover for clover detector allows the low energy γ transitions to enter the detector medium with much less attenuation. However, due to its small size, the effciency of the LEPS detector is very poor for high energy ($>\sim$ 400 keV) γ rays.

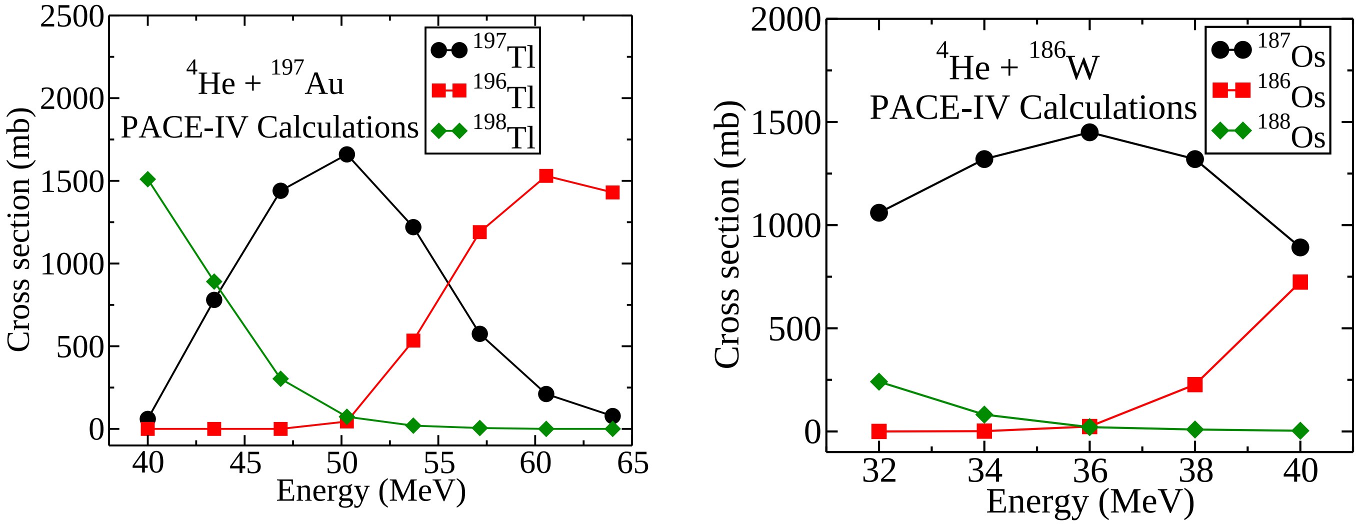

Figure 3.7: The excitation function of ^{4}He+^{197}Au (left) and ^{4}He+^{186}W (right) reactions as calculated from PACE-IV.

3.4 Experimental Setups and Performed Experiments

In this thesis work, the γ ray spectroscopic studies have been performed using the VECC array for NUclear Spectroscopy (VENUS) and Indian National Gamma Array (INGA) at Variable Energy Cyclotron Centre, kolkata. The detail discussions about the experimental setups have been discussed below:

3.4.1 VECC array for NUclear Spectroscopy (VENUS)

VECC array for NUclear Spectroscopy (VENUS) [6] at VECC is an array of Clover HPGe detectors, which consisted of 6 Compton-suppressed Clover detectors (at the time of the experiment) and arranged in four different angles (θ) in the median plane (ϕ=0° and 180°). Two detectors each were placed at θ = 150° and 90° angles with respect to the beam direction and the other two were placed at 45° and 55° angles (shown in Fig. 3.5). VME-based data acqusition system was used for VENUS with conventional electronics at the time of the experiment performed in the present thesis work. The data were collected in the list-mode format which were further analysed in the offline.

3.4.2 Indian National Gamma Array (INGA)

The experiments related to the present thesis work were performed using both the phase (I) and the phase (II) of the Indian National Gamma Array (INGA) [7] campaigns at VECC. INGA is a national research facility with Clover and LEPS detectors (as shown in Fig. 3.6). The INGA phase (I) facility at VECC consisted of 7 Compton-suppressed Clover detectors and 1 LEPS detector. Four of those detectors were at 90° (at different ϕ angles), two of them were at 125° and one detector was at 40° with respect to the incident beam direction and the LEPS detector was placed at 40°.

In INGA phase II, there were 8 clovers and 2 leps detectors. Five of the clover detectors were at 90° (at different ϕ angles), two were at 125° and one was at 40° with respect to the beam direction. The two LEPS detectors were placed at 40° and 90°. The INGA setup was setup in channel 3 of the K-130 cyclotron cave at VECC. Experiments for the thesis work were performed using both light (^{4}He) and heavy (^{20}Ne) ions. The maximum number of detectors in 90° was useful to collect good statistics data for the gamma ray polarization measurement. The clover and the LEPS detectors were at a distance of about 26 cm from the target position. The present INGA array at VECC can accomodate 12 clover detectors. PIXIE-16 digitizer based digital data acquisition system devoloped by UGC-DAE-CSR Kolkata centre [8] was used to record the data.

3.4.3 Experiment 1 (^{197}Tl)

The light-ion induced fusion evaporation reaction ^{197}Au(^{4}He, $4n$)^{197}Tl was used to populate the excited states in ^{197}Tl. The α beam of 50-MeV energy was delivered from the K-130 cyclotron at Variable Energy Cyclotron Centre, Kolkata (VECC). The excitation functions, calculated from the PACE-IV code, is shown in Fig. 3.7. It shows that the population cross section of ^{197}Tl is $\sim$ 94% of the total reaction cross section at the beam energy 50 MeV. Therefore, the excited states of the residual nucleus of interest, i.e ^{197}Tl were cleanly populated in the reaction. A self-supporting target (thickness 5 mg/cm^2) was mounted on a target ladder at an angle of

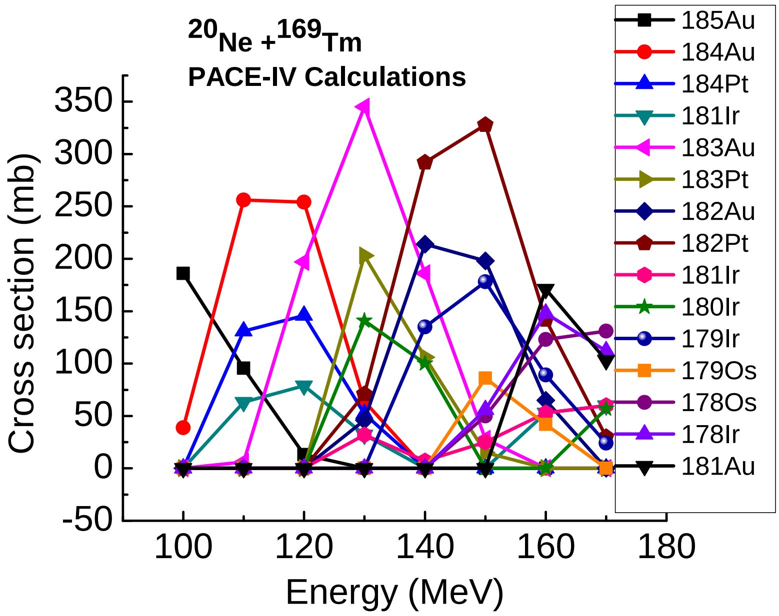

Figure 3.8: The excitation function of ^{20}Ne+^{169}Tm reaction as calculated from PACE-IV.

about 55° with respect to the beam direction. The gamma rays were detected using the VENUS setup [6, 9] as described above. The energy and efficiency calibration of all the detectors were done using the known radioactive sources of ^{133}Ba and ^{152}Eu. The γ-γ coincidence data were recorded using VME based data aqusition system in the list-mode format. The time-difference data between the master gate and the RF signal of cyclotron was also recorded in a time to amplitude converter (TAC) module. Also, experimental data in singles mode were taken for the intensity and angular distribution measurements of the γ rays.

3.4.4 Experiment 2 (^{183}Au)

The heavy-ion induced fusion evaporation reaction ^{169}Tm(^{20}Ne, $6n$)^{183}Au at 146 MeV has been used to populate the excited states of the neutron deficient nucleus ^{183}Au. The beam was delivered from the K-130 cyclotron at VECC. A self supporting target of thickness ~23 mg/cm^2 has been used for this experiment. The excitation function, as calculated from the PACE-IV code, is shown in Fig. 3.8. It shows that several nuclei have been populated in this reaction and the population cross section of ^{183}Au is maximum at the beam energy 130 MeV which can be achived in the middle of the target by the incident beam energy of 146 MeV. In this experiment INGA phase II setup with eight Compton-suppressed clover and two LEPS detectors were used

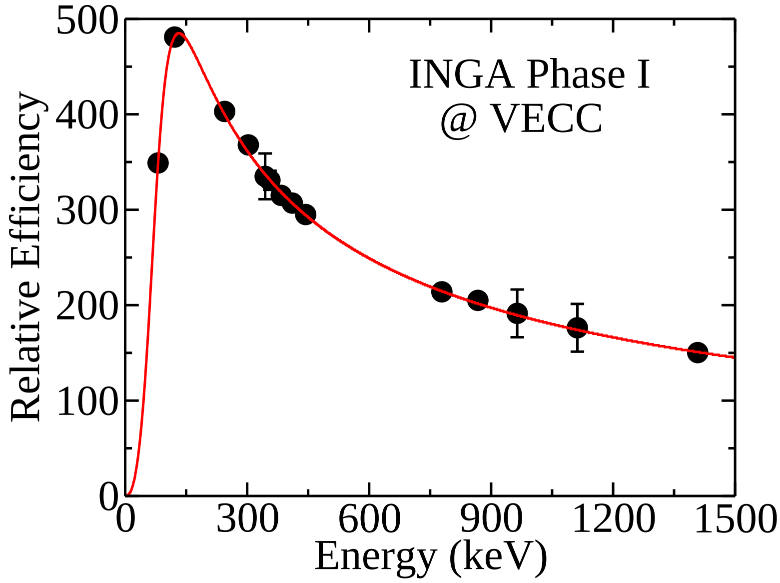

Figure 3.9: Relative efficiency of INGA phase I array at VECC.

to detect the gamma rays. The energy and efficiency calibration of all the detectors have been done using known radioactive source of ^{133}Ba and ^{152}Eu. The γ-γ coincidence data were recorded in two- and higher-fold coincidence mode with time stamp in a fast (250 MHz) digital data acquisition system based on Pixie-16 modules of XIA [8].

3.4.5 Experiment 3 (^{187}Os)

The excited states in heavier Os isotopes can only be populated using light-ion induced reaction or deep inealstic scattering. In the present study, the excited states of ^{187}Os were populated by the alpha-induced fusion evaporation reaction ^{186}W(^{4}He, 3n)^{187}Os at 36 MeV of beam energy delivered from the K-130 cyclotron at VECC. The excitation function, calculated from the PACE-IV code, is shown in Fig. 3.7. It shows that the population cross section of ^{187}Os is $\sim$ 96% of the total reaction cross section at the beam energy of 36 MeV. A stack of 3 ^{186}W foils, each of 300μg/cm^2 thick on 20μg/cm^2 ^{12}C backing, was used as target which was placed at an angle $\sim$ 55° with respect to the beam direction. The γ rays were detected using the INGA phase I setup [7] with seven Compton-suppressed clover HPGe detectors and one LEPS detetctor. The energy and efficiency calibrations of clover detectors were done using radioactive ^{133}Ba and ^{152}Eu sources. Two and higher fold data were recorded using PIXIE-16 digitizer based system devoloped by UGC-DAE-CSR Kolkata centre [8] with the requirement

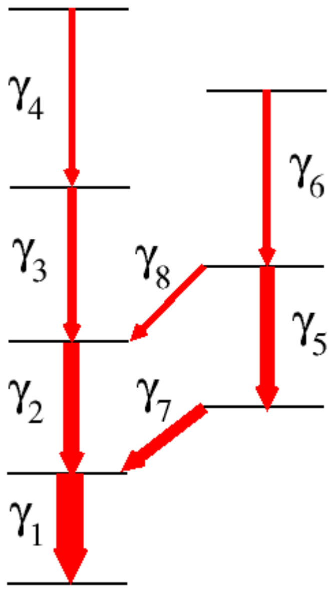

Figure 3.10: Example of level scheme for γ-ray coincidence demonstration.

of γ-γ coincidence master trigger. Some of the data files were recorded in singles mode for the intensity measurement of the γ rays.

3.5 Data Analysis Technique

The raw data files were sorted and analysed using Linux Advanced MulitParameter System (LAMPS) [10], IUCPIX [8], RADWARE [11] and INGASORT [12] analysis packages. The data from each crystal of clover detectors were calibrated and gain matched and addback data were generated on event-by-event basis. These addback data were used to generate several γ-γ matrices and a three dimensional γ-γ-γ cube for further analysis. Similarly, the data from the LEPS detectors were used to generate a LEPS vs. Clover asymmetric matrix for further analysis. The level schemes of the nuclei of interest have been constructed using the coincidence relation of the γ rays and their intensity arguments. The spin and parity of a nuclear level have been assigned from the multipolarity (λ) and type (E/M) of the γ ray decaying from that level. The measurements of directional correlation from the oriented states (DCO) ratio [13], angular distribution and the polarization asymmetry ratio (along with the linear polarizatioom,

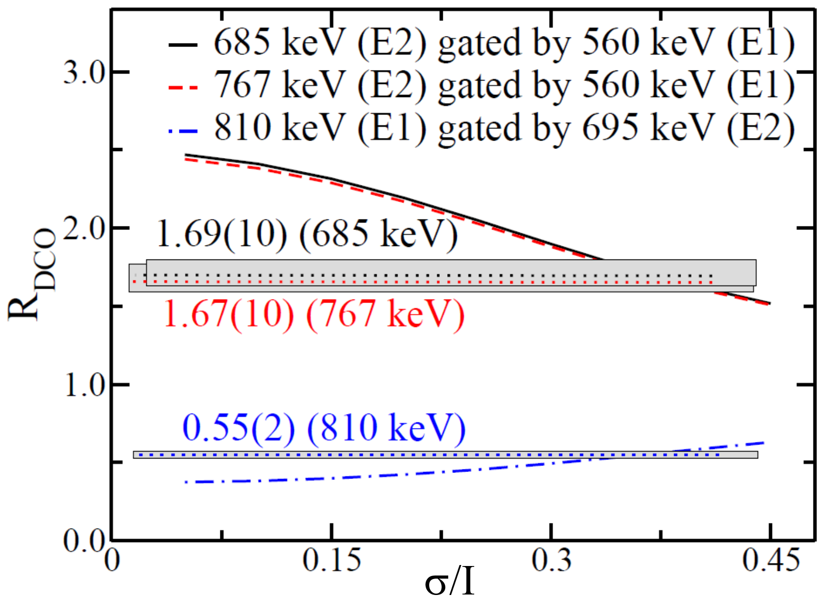

Figure 3.11: Theoretical (solid, dashed and dashed-dot lines) and measured (dotted lines with shaded regions encompass the uncertainties) R_{DCO} values for different values of σ/I for the three stretched γ rays. The σ/I values for the present experiment were determined from the crossing point of the theoretical lines and the experimental ones.

P) were used to determine the λ and E/M of the γ rays. The detail discussions on different data analysis techniques are discussed below.

3.5.1 Calibration and Efficiency

The energy calibration represents the relation between the channel number, as recorded by the data acquisition, and the corresponding energy of the γ-ray peak in the spectrum. This can be determined using the known γ-ray energies from the radioactive sources. The energies and channel numbers of the known γ-lines can be fitted using the following polynomial.

$$E_\gamma = \sum_{i=1}^{n} (a_0 + a_i x^i) \tag{3.11}$$

where the coefficients a_0 and a_i are known as the calibration constants and n represents the order of the polynomial. The energy of an unknown photopeak can be obtained from the corresponding channel number using the calibration constants. In the present thesis work, ^{152}Eu and ^{133}Ba radioactive sources have been used for to determine the calibration constants

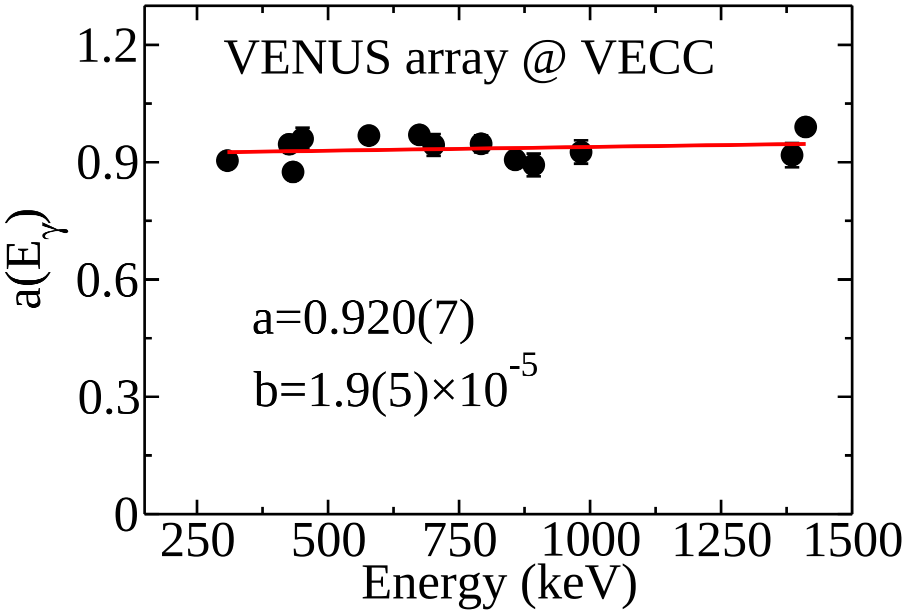

Figure 3.12: Asymmetric correction factor $a(E_\gamma)$ for the detectors at 90° (VENUS). solid line is the linear fit of the experimental data points. The values of coefficients, a and b, are also given.

from second order polynomial using the following equation:

$$E_\gamma = a_0 + a_1 x + a_2 x^2 \tag{3.12}$$

where E_γ and x are the energy and channel number, respectively, corresponding to the incident γ ray while a_0, a_1 and a_2 are the calibration parameters. The values of these parameters have been obtained from the fitting of the known-energy source data.

In order to determine the intensity of a gamma ray, one needs to know the efficiency of the detection system. In γ-ray spectroscopic study, the relative intensities of the γ rays are essential to build the level scheme and also to determine the branching ratios. The efficiency of the γ rays is energy dependent and therefore, the relative efficiencies of the γ rays as a function of the γ-ray energy need to be determined. The relative efficiency curves as a function of γ-ray energy of INGA and VENUS array has been obtained using ^{152}Eu source. Similarly, the relative efficiency of the LEPS detector has been obtained using the known low energy γ rays from ^{133}Ba source. The experimental data were fitted with the following equation, using the "effit" program of the RADWARE package [11].

$$\ln(\epsilon) = \{(A + Bx + Cx^2)^{-G} + (D + Ey + Fy^2)^{-G}\}^{-1/G} \tag{3.13}$$

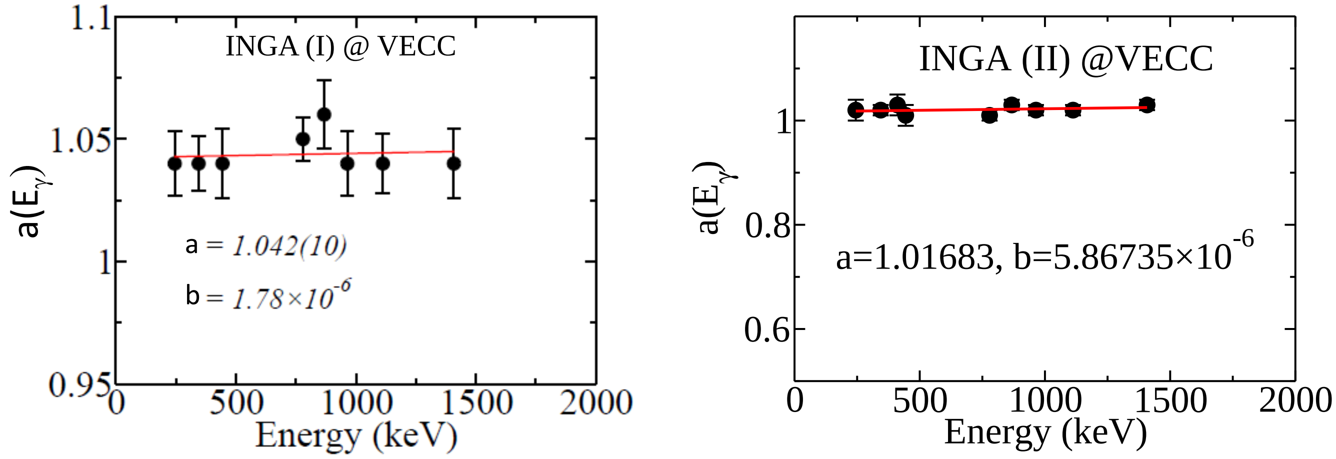

Figure 3.13: Asymmetric correction factor $a(E_\gamma)$ for the detectors at 90° (INGA I (left) and INGA II (right)). solid line is the linear fit of the experimental data points. The values of coefficients, a and b, are also given.

where ϵ is the efficiency, $x = \ln(\frac{E_\gamma}{100})$, $y = \ln(\frac{E_\gamma}{1000})$ and E_γ is the γ-ray energy in keV. A, B, C, D, E, F and G are the fitting parameters. A typical relative efficiency curve, obtained from the present work, is shown in Fig.3.9.

3.5.2 γ Ray Coincidence Relation and Intensity Arguments

The level scheme of a nucleus is a pictorial representation of its excited states. Construction of the level scheme is the primary building block to understand the structure of a nucleus. As mentioned above one of the methods to construct a level scheme is the coincidence relation between the γ rays. This can be performed by analysing the gated spectra projected from a $\gamma - \gamma$ matrix and/or a $\gamma - \gamma - \gamma$ cube. The concept of coincidence and parallel γ rays are important for this analysis. As an example, to construct the level scheme as shown in Fig. 3.10, if one puts a "single-gate" on the γ-ray energy γ_2 in the $\gamma - \gamma$ coincidence matrix, then the gated spectrum will show the peaks at γ_1, γ_3, γ_4, γ_6 and γ_8 energies as these γ rays are in "coincidence" with γ_2. But the γ rays γ_7 and γ_5 will not appear in that spectrum as these two γ rays are not in coincidence with γ_2. Therefore, the γ_2 is "parallel" with γ_7 and γ_5. Similarly, if one puts a "double-gate" on the γ-ray energies γ_7 and γ_5 in the $\gamma - \gamma - \gamma$ coincidence cube, then the gated spectrum will contain only the γ_1 and γ_6 peaks which are in coincidence with both

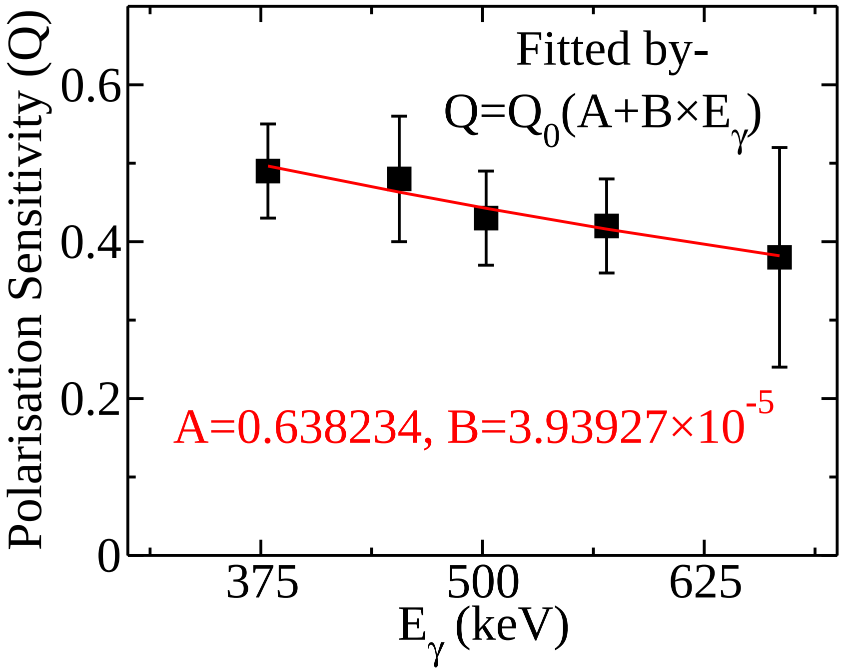

Figure 3.14: Polarization Sensitivity of INGA (phase II) array at VECC

the gating γ rays γ_7 and γ_5. Therefore, by putting "double-gate" on a $\gamma-\gamma-\gamma$ cube, one can uniquely identify a band. However, the number of counts in a "double-gated" spectrum is much less than a "single-gated" spectrum. In this way by analysing various single- and double-gated coincidence spectra, the level scheme of a nucleus can be established. In the fusion evaporation reaction, the CN is produced at high excitation energy and high angular momentum and since the residual nucleus (which is the nucleus of interest) retains much of its angular momentum, but loses a large amount of excitation energy because of particle evaporation, the entry point remains close to the yrast line and its decay follows mostly the yrast line. Moreover, the produced CN and, hence, the residual nucleus has a large distribution in angular momentum. Therefore, the intensity of the γ rays increases with the decrease of angular momentum and hence, with the excitation energy of the residual nucleus. This implies that the low-lying γ rays will have larger intensities. So, in order to maintain the proper ordering of the γ rays in the level scheme, the intensity balance are checked at each energy level such that the feed-in intensity of a level is lower (or may be similar but not larger) than the feed-out intensity.

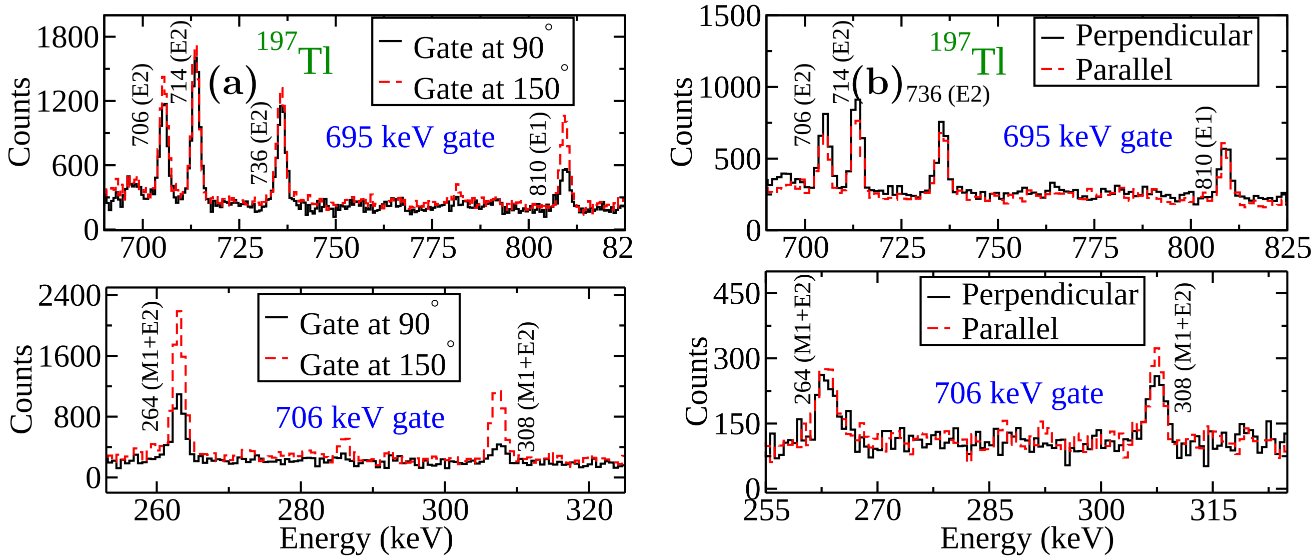

Figure 3.15: Typical gated spectra of DCO ratio (a) and polarization asymmetry (b) measurements in ^{197}Tl.

3.5.3 Angular Distribution of γ-ray Transition

In a heavy-ion fusion evaporation reaction the linear momentum of the projectile brings the orbital angular momentum in to the compound nucleus and, hence, the residual nucleus (the nucleus of interest) is aligned in a particular (perpendicular) direction. Now, the γ-rays emitted from such aligned states follow angular distributions depending on their multipolarities [14, 15]. Therefore, by measuring the angular distribution of the γ-rays, their multipolarities can be determined, and hence, the angular momentum (spin) of the initial nuclear state, from which the γ ray is being emitted, if the spin of the final state is known. In case of complete alignment of the nuclear excited states, the angular distribution of γ-rays is expressed as [16, 17]:

$$W(\theta) = \sum_{k=0}^{\lambda} a_k^{max} P_k(\cos\theta) \quad \text{where k = 0, 2, 4,...} \tag{3.14}$$

where $P_k(\cos\theta)$ are the Legendre polynomials and a_k^{max} are the angular coefficients for the completely aligned nuclear state. In the actual cases, the nuclear oriented states are partially aligned. Therefore, the angular coefficients are expressed as

$$a_k(I_iL_1L_2I_f) = \alpha_k(I_i)a_k^{max}(I_iL_1L_2I_f) \tag{3.15}$$

Where $\alpha_k(I_i) = \frac{\rho_k(I_i)}{B_k(I_i)}$ are the attenuation coefficient of alignment. $\rho_k(I)$ is the degree of alignment of $I-$spin state and is expressed as,

$$\rho_k(I) = \sqrt{2I+1}\sum_m (-1)^{I-m}(ImI-m|k0)P_m(I) \tag{3.16}$$

P_m is the mth substate population parameter and is expressed as,

$$P_m(I) = \frac{exp(-\frac{m^2}{2\sigma^2})}{\sum_{m'=-I}^{I} exp(-\frac{m'^2}{2\sigma^2})} \tag{3.17}$$

where σ is the measure of the alignment of the nuclear m-substates and is usually expressed in terms of σ/I. Only when the condition $P_m(I) = P_{-m}(I)$ is satisfied, the nuclear state is considered aligned. $\sigma/I \sim 0$ corresponds to complete alignment. As the degree of alignment decreases, the value of σ/I increases. The value of σ/I for heavy ion induced fusion evaporation reaction is considered as ∼0.3. In the present thesis work, the light ion induced (^{4}He) fusion evaporation reaction was also used along with the heavy-ion (^{20}Ne) induced fusion evaporation reaction to populate the excited states of residual nuclei.

The value of σ/I is expected to be wider in the α-induced reactions and estimated in this work by comparing the experimental and calculated values of the DCO ratios (discussed in the next section) of some of the stretched transitions with known multipolarities. These are shown in Fig. 3.11.

The DCO ratio (R_{DCO}) values for these transitions have been calculated using the ADRAP code [18] for different values of σ/I. This gives similar values of σ/I for the three transitions, namely, σ/I = 0.38(4), 0.37(4), 0.37(2) corresponding to 685-keV (E2), 766-keV (E2) and 810-keV (E1) transitions, respectively (see Fig. 3.11). So, a weighted average value of σ/I = 0.37(3) has been adopted for the α-induced reactions used in this study.

3.5.4 Directional Correlation from the Oriented (DCO) states ratio (R_{DCO})

The multipolarities of the γ rays, in this work, have been assigned primarily from the measurement of directional correlation from oriented states (DCO) ratio [13]. This technique specially used to get rid of the contaminations in the singles spectrum, coming from the nearly similar energy gamma transitions from different states of the same or other nuclei. This technique is also useful for the limited number of angles covered by an array. For DCO ratio (R_{DCO})

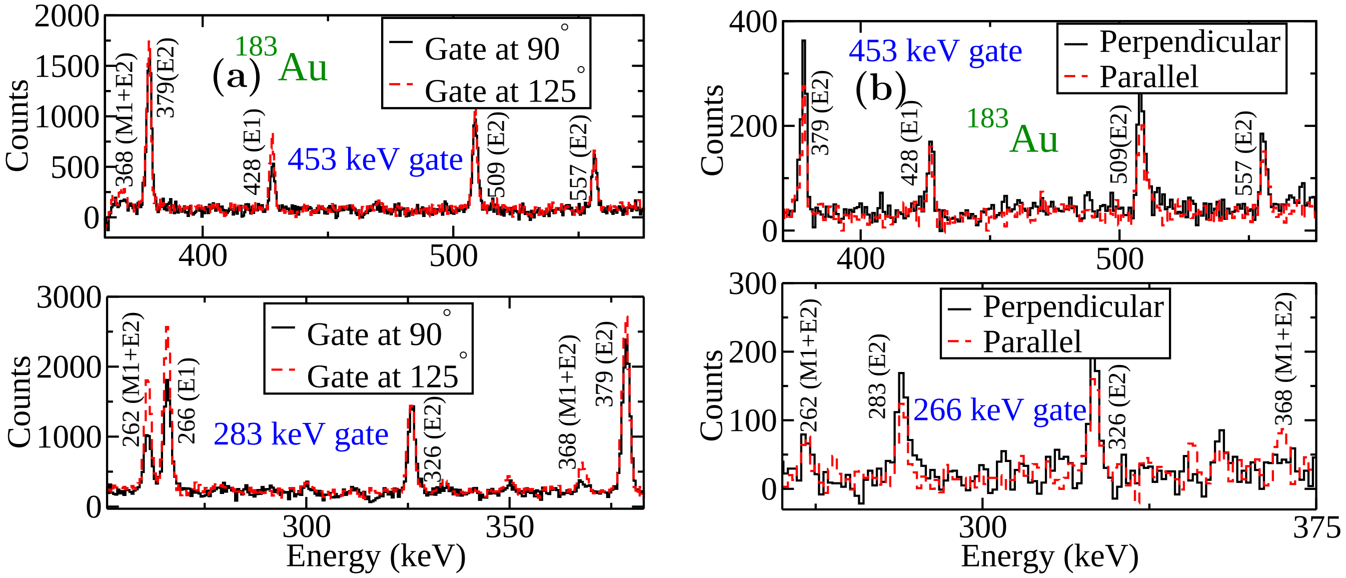

Figure 3.16: Typical gated spectra of DCO ratio (a) and polarization asymmetry (b) measurements in ^{183}Au.

measurement, an angle-dependent asymmetric $\gamma-\gamma$ matrix (DCO matrix) was formed using the coincidence data from the 150° (θ_1) detectors and the 90° (θ_2) detectors in the VENUS array setup and for the INGA array, θ_1 and θ_2 were 125° and 90°, respectively. The R$_{DCO}$ of a γ ray (γ_1) is obtained from the ratio of its intensities (I_γ) gated by a transition (γ_2) with known multipolarity at the above two angles from the DCO matrix. This ratio is obtained from the experimental data using the following relation:

$$R_{DCO} = \frac{I_{\gamma_1} \text{ at } \theta_1, \text{ gated by } \gamma_2 \text{ at } \theta_2}{I_{\gamma_1} \text{ at } \theta_2, \text{ gated by } \gamma_2 \text{ at } \theta_1} \tag{3.18}$$

In the present geometry of VENUS and INGA arrays, theoretical value of DCO ratio of a γ transition gated by the same multipolarity transition is unity whereas, DCO ratio of a pure dipole transition gated by a stretched quadrupole transition is $\sim$ 0.5 and that of stretched quadrupole transition gated by pure dipole transition is $\sim$ 2. Representative gated spectra for DCO ratio measurements in ^{197}Tl, ^{183}Au and ^{187}Os nuclei have been shown in Fig. 3.15, 3.16 and 3.17.

3.5.5 Linear Polarization (P) and Polarization Asymmetry (Δ_{PDCO})

The geometrical advantage of a clover detector has been used as a polarimeter to measure the polarization asymmetry (Δ_{PDCO}) of a γ ray. Out of the four crystals of a clover, any one them

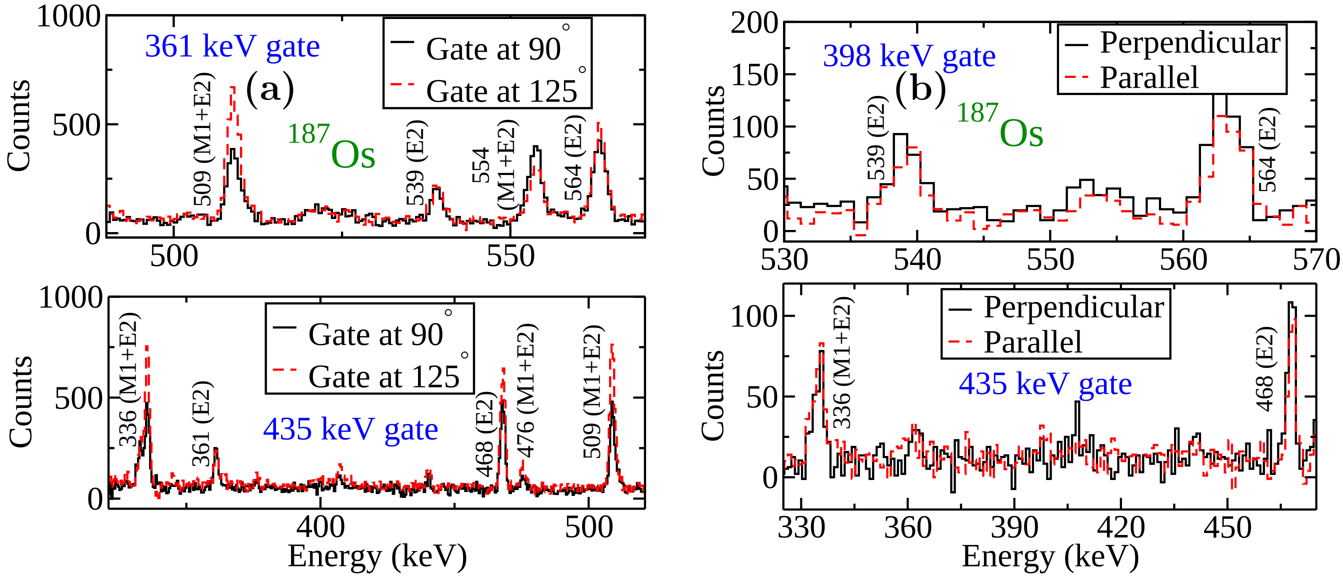

Figure 3.17: Typical gated spectra of DCO ratio (a) and polarization asymmetry (b) measurements in ^{187}Os.

acts as a scatterer and the two adjacent crystals act as analyzers for the Compton scatter of a γ ray inside the detector. The type (E/M) of a transitions can be obtained from the polarization asymmetry measurement [19, 20]. The polarization asymmetry (Δ_{PDCO}) is defined as

$$\Delta_{PDCO} = \frac{a(E_\gamma)N_\perp - N_\parallel}{a(E_\gamma)N_\perp + N_\parallel} \tag{3.19}$$

where, $N_\perp$ and $N_\parallel$ are the perpendicular and parallel scattered counts of a γ-ray transition in the 90° detectors with respect to the reaction plane. $a(E_\gamma)$ is a geometrical correction factor for the array. To measure $N_\perp$ and $N_\parallel$, two asymmetric matrices of $N_\perp$ vs. all detectors and $N_\parallel$ vs. all detectors were generated. The asymmetric response of the clover segments was corrected by the factor $a(E_\gamma)$ $(=\frac{N_\parallel}{N_\perp})$ which needs to be determined for an unpolarized radioactive source. In the VENUS experment, we have used the decay radiations (during beam-off period) from the target foil to estimate the exact value of $a(E_\gamma)$ in order to avoid any uncertainty due to the positioning of external sources. The values of $a(E_\gamma)$ are shown in Fig. 3.12 along with the fit using the equation, $a(E_\gamma) = a + bE_\gamma$. The fitting gives the values of the coefficients as, $a = 0.920(7)$ and $b = 1.9(5) \times 10^{-5}$. Positive and negative values of the polarization asymmetry Δ_{PDCO} indicate electric (E) and magnetic (M) types of the transitions, respectively. But, in the experiment 2 and 3, ^{152}Eu radioactive source has been used to obtain $a(E_\gamma)$ as shown in Fig. 3.13 due to the lack of enough radioactive decay gamma rays. Typical gated spectra for polarization asymmetry measurements in ^{197}Tl, ^{183}Au and ^{187}Os nuclei are shown in Fig. 3.15, 3.16 and 3.17. The linear polarization (P) can be obtained from the measured polarization

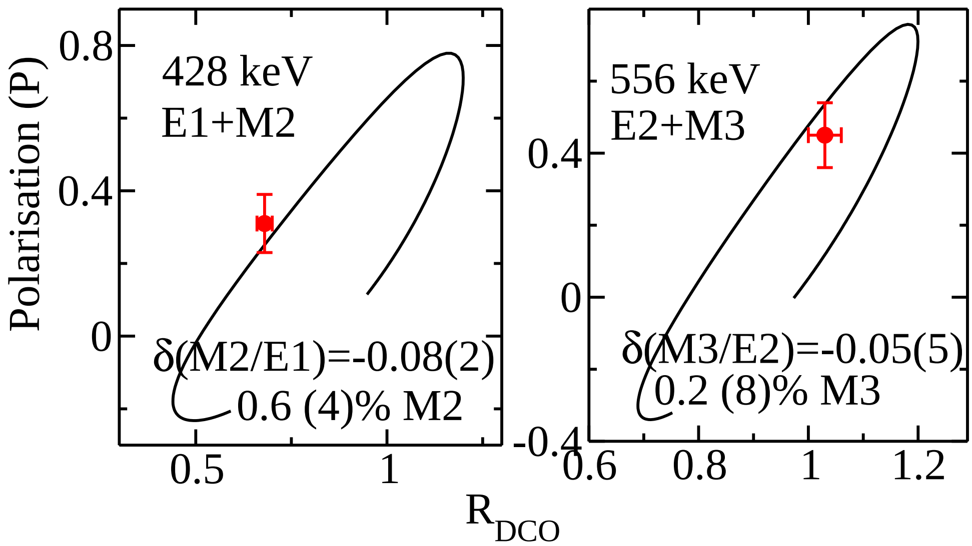

Figure 3.18: The experimental (symbol) and calculated (solid line) values of R_{DCO} and P of two of the transitions in ^{183}Au. The 557 keV is a known $E2$ transition decaying from $37/2^{+}$ to $33/2^{+}$ in band (4) and 428 keV is a known $E1$ transition from $13/2^{+}$ to $11/2^{-}$ between band (4) and band (1). These transitions show very small mixing ratios (δ) as they should be.

asymmetry (Δ_{PDCO}) as:

$$P = \frac{\Delta_{PDCO}}{Q} \tag{3.20}$$

Where, Q is the polarization sensitivity. It depends on the incident γ-ray energy and the geometry of the polarimeter. The polarization sensitivity can be expressed as:

$$Q(E_\gamma) = (A + BE_\gamma)Q_0(E_\gamma) \tag{3.21}$$

with

$$Q_0(E_\gamma) = \frac{\alpha + 1}{\alpha^2 + \alpha + 1} \tag{3.22}$$

where $\alpha = E_\gamma/m_ec^2$, E_γ is the incident γ-ray energy and m_ec^2 is the electron rest mass energy. The parameters A and B, and $Q(E_\gamma)$ can be experimentally determined using γ-rays with known polarizations. The polarization sensitivity (Q) has been obtained for the INGA array (experiment 2) using the known stratched E2 transitions as shown in Fig. 3.14.

The mixing ratio δ can be obtaind for a mixed transition from the simultaneous measurement of DCO ratio and polarization (P) measurement. The experimental linear polarization (P) and

R_{DCO} ratios have been compared with the calculated P and R_{DCO} values for different δ values to get the experimental mixing ratio δ. The measured mixing ratio δ is close to 0 for pure transition. The mixing ratio measurement technique has been varified for already known pure E2 (557 keV) and E1 (428 keV) transitions in ^{183}Au nucleus and it give very small mixing ratios close to zero which is expected for pure transitions as shown in Fig. 3.18. This similar technique has been applied for other unknown transitions to determine mixing ratio δ.

Bibliography

[1] Subhendu Rajbanshi's Thesis (Generation of Angular momentum for Weakly Deformed Nuclei in Mass $\sim$ 140 Region).

[2] H. Ejiri and M.J.A. de Voigt, Gamma-ray and Electron Spectroscopy in Nuclear Physics, Clarendon Press, Oxford (1989)

[3] Experiments in Nuclear Science, High-Resolution Gamma-Ray Spectroscopy published by EG and G ORTEC.

[4] G.F. Knoll, Radiation Detection and Measurement.

[5] G. Duchene, F.A. Beck, P.J. Twin, G. de France, D. Curien, L. Han, C.W. Beausang, M.

[6] S. Bhattacharya et al., DAE-BRNS Symp. Nucl. Phys. **61**, 98 (2016).

[7] S. Bhattacharya et al., DAE-BRNS Symp. Nucl. Phys. **63**, 1156 (2018).

[8] S. Das et al., Nucl. Instrum. Meth. Phys. Res. **A 893**, 138 (2018).

[9] Soumik Bhattacharya et al., Phys. Rev. C **98**, 044311 (2018).

[10] http://www.tifr.res.in/pell/lamps.html

[11] D. C. Radford, Nucl. Instrum. Methods Phys. Res.**A 361**, 297 (1995).

[12] R. K. Bhowmik INGASORT mannual (private communication).

[13] A. Krämer-Flecken et al., Nucl. Instrum. Methods Phys. Res.**A 275**, 333 (1989).

[14] F.A. Beck, Ann. Phys. (Paris) 1, **503** (1966).

[15] P.J. Twin, in: W.D. Hamilton, The Electromagnetic Interaction in Nuclear Spectroscopy (North-Holland Pub. Co-Amsterdam, 1975), p. 701.

[16] T. Yamazaki, Nucl. Data, Section **A, Vol.3** (1967).

[17] E. Der Mateosian and A.W. Sunyar, Atomic Data and Nuclear Data Tables 13, 391-406(1974).

[18] Md. A. Asgar and G. Mukherjee, Proc. DAE Symp. on Nucl Phys. **62**, 104 (2017).

[19] K. Starosta et al., Nucl. Instrum. Meth. Phys. Res. **A 423**, 16 (1999).

[20] Ch. Droste et al., Nucl. Instrum. Meth. Phys. Res. **A 378**, 518 (1996).

Chapter 4

Band Structures in ^{197}Tl

4.1 Introduction

The Tl nuclei ($Z = 81$) lie just below the $Z = 82$ spherical proton shell closure with the proton Fermi level around the $3s_{1/2}$ orbital and, hence, the ground state spin-parity of the odd-A Tl isotopes is $1/2^+$ [1, 2, 3] corresponding to the occupation of the odd proton in the $3s_{1/2}$ orbital. However, the low-(high-)Ω components of the high-j $h_{9/2}$ and $i_{13/2}$ orbitals, situated above the $Z = 82$ shell gap, come down in energy with prolate (oblate) deformation and intrudes into the region of the proton Fermi level of Tl nuclei. As a consequence, deformed rotational bands are observed at higher excitation energies in the neutron-deficient odd-A Tl isotopes which are based on the above high-j intruder orbitals [4, 5, 6, 7, 8, 9, 10, 11, 12, 13, 14, 15, 16, 17]. The excitation energy of the band heads for $h_{9/2}$ and $i_{13/2}$ bands increases, and hence indicates that the deformation decreases, as the neutron number increases towards $N = 126$ spherical shell closure [13]. However, the effect of the odd valence high-j proton in breaking the spherical symmetry in Tl nuclei has been reported in heavier odd-A Tl nuclei up to even ^{203}Tl [16] i.e. up to neutron number as close as $N = 122$ to the spherical shell closure at $N = 126$. The spherical symmetry is restored at moderate excitation in Tl nuclei only for neutron number $N = 124$ and no $9/2^-$ state, corresponding to the intruder $h_{9/2}$ orbital, has been found in ^{205}Tl ($N = 124$) [18].

On the other hand, for Tl nuclei in mass $A \sim 190$ region, neutorn hole excitations are possible in the high-j, shape-driving $i_{13/2}$ orbital around neutron number $N = 114$. The band crossings phenomenon in the odd-A Tl nuclei in $A \sim 190$ region is therefore, related to the alignment of a pair of neutrons in the $\nu i_{13/2}$ orbital with a large gain in aligned angular momentum. Moreover, the particle-hole coupling with proton and neutron, respectively, is possible with both of them are at high-j orbitals. Such particle-hole coupling gives rise to magnetic rotational (MR) bands (when the deformation of the core is small) and chiral bands (when the core has triaxial deformation) at moderate to high spins. Such MR and chiral doublet bands have been reported in a few odd-odd and odd-A Tl nuclei up to neutron number $N = 117$ at their 2-, 3- and 5-quasiparticle configurations [19, 20, 21, 22, 23]. However, no MR or chiral bands are reported in ^{199,200}Tl which might indicate that the neutron number below $N = 118$ puts a boundary in Tl nuclei for the observation of such interesting exotic band structures which emerge from the particle-hole excitaions in high-j orbitals. This boundary may correspond to the energetically unfavoured excitations of neutron holes to the $\nu i_{13/2}$ orbital at or above this neutron number. Therefore, ^{197}Tl, with neutron number $N = 116$, is an interesting nucleus to investigate its moderate to high spin states if such exotic modes are excited. It is worth mentioning that the occurrence of nearly degenerate bands due to chiral symmetry breaking in a triaxial nucleus with proton(s) and neutron(s) in the high-j particle and hole angular momentum states, were predicted in the nuclei in both the $A \sim 130$ and $A \sim 195$ regions [24, 25]. Doubly degenerate bands in an odd-A nucleus in $A \sim 190$ region were first observed in ^{195}Tl [22], the nearest lighter odd-A neighbor of ^{197}Tl. In this nucleus, evidence for two pairs of doubly degenerate bands were observed. Therefore, the first experimental signatures of multiple chiral doublet (MχD) bands, first predicted by J. Meng et al. [26], in $A \sim 190$ region have been reported in this nucleus which signifies triaxial shape co-existence in ^{195}Tl. Still the observed chiral doublet bands in this region are very few in number compared to that in the $A \sim 130$ region.

A logical extension, therefore, would be to look for such doubly degenerate bands in the neighboring nuclei in this mass region. In ^{197}Tl, the neutron Fermi level would lies around the $\nu i_{13/2}$ orbital and in between that of ^{195}Tl and ^{198}Tl, for both of which doubly degenerate bands have been reported. The high spin states in ^{197}Tl nucleus are known mostly from the ^{4}He and ^{3}He

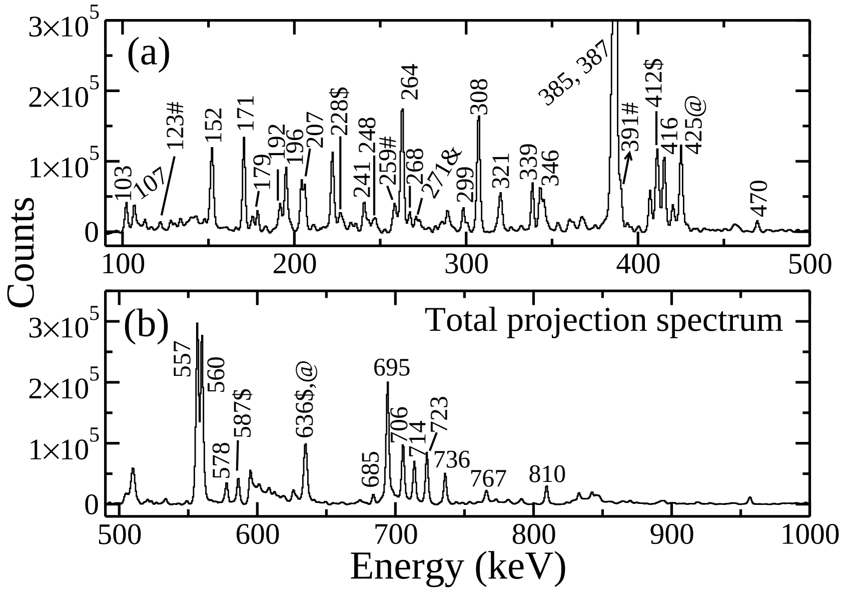

Figure 4.1: The total projection spectrum from the $\gamma - \gamma$ matrix for the lower (a) and the higher (b) energy parts. The known γ-ray peaks from different nuclei are shown. The peaks with no symbol are the known peaks in ^{197}Tl while the symbols correspond to #: ^{198}Tl, &: ^{196}Tl, $: ^{198}Hg, and @: ^{196}Hg.

induced fusion evaporation reactions [12, 13, 27] with the help of a very limited number of Ge detectors. In these studies, two rotational bands, based on an 1-quasiparticle (qp) and a 3-qp configurations were reported. However, no band crossing phenomenon has been observed in any of these bands. So, the effect of the alignment of a pair of neutrons in these rotational-like bands could not be studied. It may be noted that the doubly degenerate bands in ^{195}Tl were observed after neutron alignments in the $i_{13/2}$ orbital. Apart from the $i_{13/2}$, the negative parity $f_{5/2}$, $p_{3/2}$ and $p_{1/2}$ neutron orbitals are also available near the Fermi level for the nuclei with neutron number $N > 114$. Therefore, it is important to study the higher spin states in ^{197}Tl beyond the neutron alignments in order to understand the type of band structures generated due to the neutron alignments in the positive and in the negative parity orbitals.

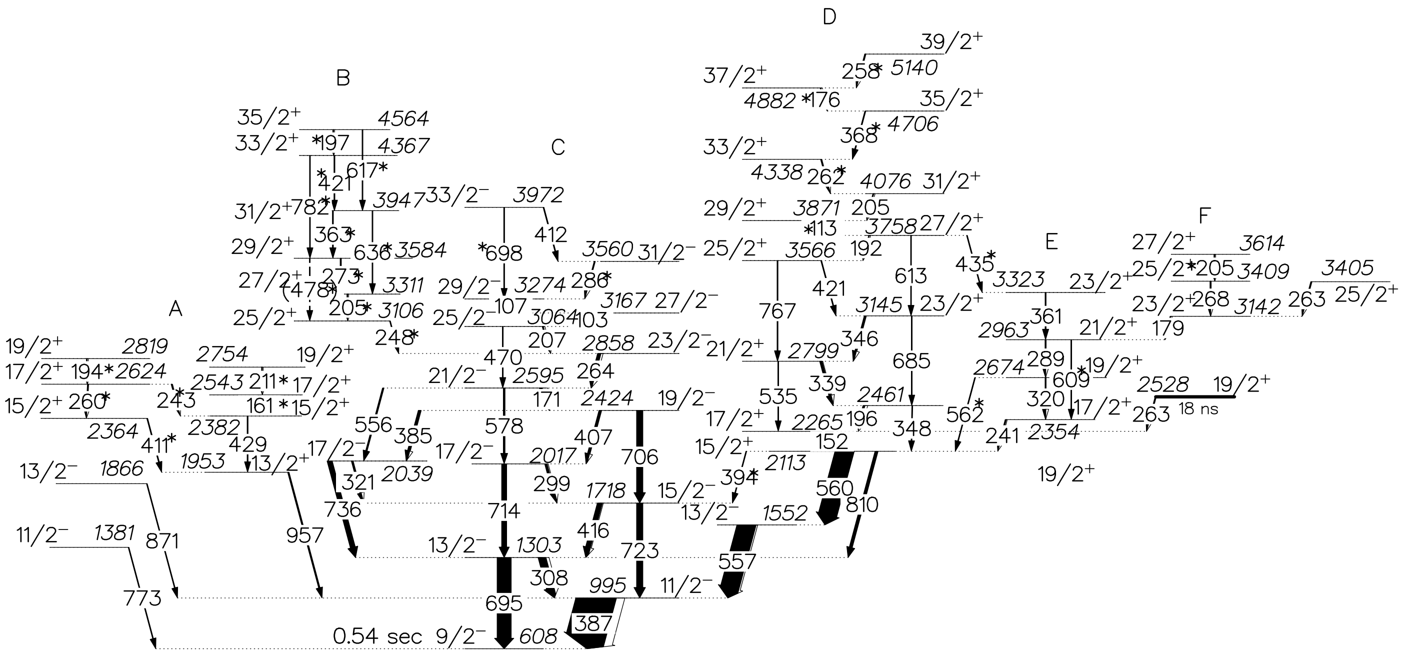

Figure 4.2: Proposed level scheme of ^{197}Tl from the present work. Levels above the 0.54-sec isomer at 608 keV are shown. The new γ transitions are marked by asterisks (*)

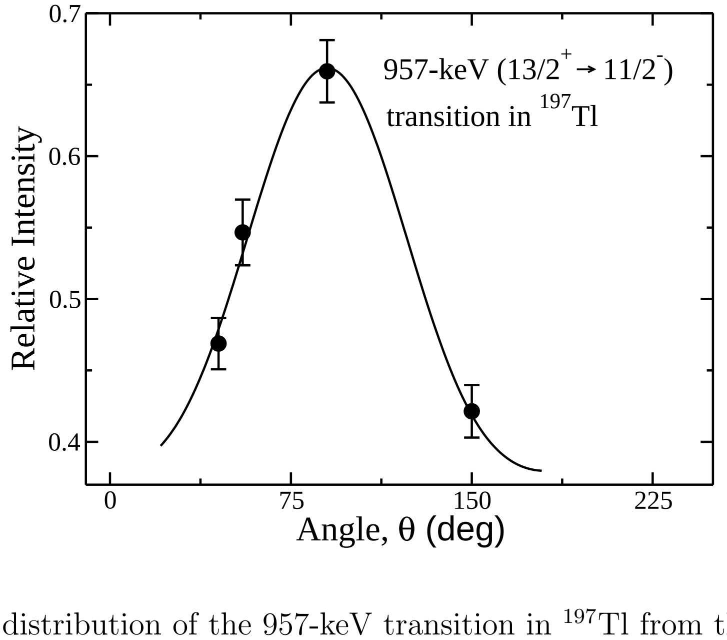

Figure 4.3: Angular distribution of the 957-keV transition in ^{197}Tl from the singles-data. The solid line is the fitted curve for a dipole transition.

4.2 Experimental Results

A total spectrum projected from the γ-γ symmetric matrix has been shown in Fig. 4.1. It contains mostly the known peaks of ^{197}Tl nucleus. A few stronger peaks from other neighboring nuclei, which were also populated in the reaction, are also marked in the spectrum.

A new and improved level scheme of ^{197}Tl has been obtained in the present work and is shown in Fig. 4.2. The level scheme has been extended upto the excitation energy of 5.14 MeV and angular momentum of 19.5 $\hbar$ with the placement of 28 new γ transitions which have been placed for the first time. The level scheme, shown in Fig. 4.2, is based on the $9/2^-$ isomer ($\pi h_{9/2}$ configuration) with half life of $T_{1/2}$ = 0.54(1) sec at 608 keV of excitation energy [28]. The experimental results of γ-ray transition energies (E_γ), level energies (E_i), spins and parities of the initial (I_i^π) levels, R_{DCO} and Δ_{PDCO} values along with the adopted multipolarities of the γ-rays have been tabulated in Table 4.1. Different gated spectra were used for the determination of the relative intensities of the γ rays and all the intensities quoted in Table 4.1 are after proper normalization. The intensities of the nearly-degenerate γ rays could be separately determined using various single gated spectra.

Table 4.1: List of γ rays belonging to ^{197}Tl with their energies (E_γ) and intensities (I_γ). The placement of these γ rays in the level scheme are denoted by the energy (E_i) and spin-parity (I_i^π) of the decaying state. The measured values of R_{DCO} and Δ_{PDCO} along with the adopted multipolarities are also given.

$E_\gamma(keV)$	$E_i(keV)$[9]	I_i^π	I_γ	R_{DCO}	Δ_{PDCO}	Multipolarity
102.5(2)	3166.9(6)	$27/2^-$	1.22(5)	0.65(6)[1]		M1+E2
107.1(2)	3273.9(7)	$29/2^-$	1.05(5)	0.46(6)[1]		M1+E2
113.4(3)	3871.4(7)	$29/2^+$	0.63(3)	0.61(5)[6]		M1+E2
152.3(2)	2264.9(4)	$17/2^+$	5.02(9)	1.04(2)[5]		M1+E2
161.1(4)	2542.7(7)	$17/2^+$	0.16(1)	1.05(13)[4]		M1+E2

Table 4.1: Continued....

$E_\gamma(keV)$	$E_i(keV)$[9]	I_i^π	I_γ	R_{DCO}	Δ_{PDCO}	Multipolarity
170.9(1)	2594.8(3)	$21/2^-$	7.04(11)	0.53(2)[1]		M1+E2
176.2(5)	4881.8(11)	$37/2^+$	0.65(3)	0.51(4)[6]		M1+E2
178.9(3)	3141.6(5)	$23/2^+$	1.31(5)	0.64(5)[8]		M1+E2
192.1(4)	3758.1(5)	$27/2^+$	1.36(5)	1.00(7)[5]		M1+E2
194.2(4)	2818.5(10)	$19/2^+$	0.075(1)	1.06(12)[4]		M1+E2
195.5(2)	2460.5(4)	$19/2^+$	5.02(9)	0.90(2)[5]	-0.05(2)	M1+E2
197.1(3)	4563.9(8)	$35/2^+$	0.11(1)			(M1+E2)
204.5(3)	4075.9(8)	$31/2^+$	2.51(8)	0.58(6)[6]	-0.30(12)	M1(+E2)
204.7(2)	3310.9(7)	$27/2^+$	0.63(2)	0.50(7)[5]	-0.13(8)	M1(+E2)
204.7(3)	3614.1(7)	$27/2^+$	0.25(1)	0.51(6)[8]		M1+E2
206.6(5)	3064.4(6)	$25/2^-$	3.14(9)	0.64(4)[2]	-0.23(5)	M1(+E2)
210.9(3)	2753.6(8)	$19/2^+$	0.11(1)	0.96(10)[4]		M1+E2
241.1(2)	2353.9(4)	$17/2^+$	2.99(7)	1.01(5)[5]	-0.28(8)	M1(+E2)
242.8(6)	2624.4(9)	$17/2^+$	0.18(1)	1.06(16)[4]		M1+E2
247.9(3)	3106.2(6)	$25/2^+$	0.95(4)	0.47(5)[2]	0.16(9)	E1
258.3(6)	5140.1(12)	$39/2^+$	0.30(2)	0.51(6)[6]		M1+E2
260.1(4)	2624.4(9)	$17/2^+$	0.05(2)			(M1+E2)
262.2(3)	4338.1(8)	$33/2^+$	2.42(8)	0.53(5)[6]	-0.22(7)	M1(+E2)
263.6(4)	2858.4(5)	$23/2^-$	8.60(20)	0.44(2)[1]	-0.14(5)	M1(+E2)
262.9(3)	3404.5(6)	$25/2^+$	0.61(2)	0.43(6)[8]	-0.22(8)	M1(+E2)
263.1[10]	2528.0(2)	$19/2^+$	0.17(6)			M1+E2
267.8(3)	3409.4(6)	$25/2^+$	0.79(4)	0.89(7)[5]	-0.1(1)	M1+E2
273.1(3)	3584.1(7)	$29/2^+$	0.68(2)	0.50(5)[2]	-0.14(8)	M1(+E2)
286.2(3)	3560.2(7)	$31/2^-$	0.91(7)	0.55(5)[2]	-0.33(12)	M1(+E2)
288.9(4)	2962.7(4)	$21/2^+$	2.33(6)	0.91(5)[5]	-0.12(5)	M1(+E2)
298.9(2)	2016.9(3)	$17/2^-$	6.05(9)	0.38(5)[1]	-0.11(4)	M1+E2
307.6(3)	1302.6(2)	$13/2^-$	19.53(3)	0.31(1)[2]	-0.10(4)	M1+E2

Table 4.1: Continued....

$E_\gamma(keV)$	$E_i(keV)$[9]	I_i^π	I_γ	R_{DCO}	Δ_{PDCO}	Multipolarity
319.8(1)	2673.7(4)	$19/2^+$	2.56(8)	0.91(4)[5]	-0.09(4)	M1(+E2)
320.5(2)	2038.8(3)	$17/2^-$	3.41(8)	0.39(5)[1]	-0.03(10)	M1+E2
338.9(2)	2799.4(4)	$21/2^+$	5.73(11)	0.46(2)[6]	-0.04(5)	M1+E2
345.8(3)	3145.2(4)	$23/2^+$	3.15(9)	1.00(6)[5]	-0.15(17)	M1+E2
348.1(2)	2460.5(4)	$19/2^+$	0.72(2)	1.02(7)[6]		E2
360.9(3)	3323.5(5)	$23/2^+$	0.95(4)	1.18(6)[8]	-0.09(8)	M1+E2
362.8(3)	3946.8(8)	$31/2^+$	0.54(3)	0.45(5)[2]		M1+E2
367.5(6)	4705.6(9)	$35/2^+$	0.95(1)	0.49(6)[6]	-0.11(5)	M1(+E2)
385.2(2)	2423.9(3)	$19/2^-$	6.08(34)	0.56(1)[1]	-0.03(3)	M1+E2
387.2(3)	995.1(2)	$11/2^-$	100.0(1)	0.33(4)[2]	-0.05(1)	M1+E2
394.4(2)	2112.5(3)	$15/2^+$	0.90(5)	0.93(14)[6]		E1
407.0(2)	2423.9(3)	$19/2^-$	5.70(11)	0.26(2)[1]	-0.19(4)	M1(+E2)
412.3(4)	3972.4(7)	$33/2^-$	0.36(3)	0.46(3)[2]		M1+E2
411.2(6)	2363.8(7)	$15/2^+$	0.61(3)	0.72(4)[4]		M1+E2
415.5(6)	1718.1(2)	$15/2^-$	12.67(16)	0.25(1)[1]	-0.08(4)	M1+E2
420.9(3)	3566.1(5)	$25/2^+$	1.97(8)	0.38(2)[7]		M1+E2
420.7(2)	4367.3(8)	$33/2^+$	0.34(1)	0.58(5)[2]		M1+E2
429.1(3)	2381.6(7)	$15/2^+$	0.66(3)	0.76(3)[4]	-0.05(5)	M1+E2
434.7(4)	3758.1(5)	$27/2^+$	0.48(3)	1.41(20)[5]		E2
469.6(5)	3064.4(6)	$25/2^-$	1.51(5)	0.98(8)[1]	0.07(7)	E2
478.0 (2)	3584.2(7)	$29/2^+$	0.05(1)			
534.5(2)	2799.4(4)	$21/2^+$	1.72(4)	0.87(11)[6]	0.02(1)	E2
555.7(2)	2594.8(3)	$21/2^-$	3.73(11)	1.09(6)[1]	0.11(4)	E2
556.9(8)	1552.3(4)	$13/2^-$	47.31(3)	0.23(1)[7]	0.05(3)	M1+E2
560.1(1)	2112.5(3)	$15/2^+$	47.13(6)	0.53(2)[7]	0.15(3)	E1
562.3(4)	2673.7(4)	$19/2^+$	1.43(5)	1.89(20)[5]	0.15(5)	E2
578.1(4)	2594.8(3)	$21/2^-$	4.19(11)	0.92(5)[1]	0.09(4)	E2

Table 4.1: Continued....

$E_\gamma(keV)$	$E_i(keV)$[9]	I_i^π	I_γ	R_{DCO}	Δ_{PDCO}	Multipolarity
608.8(2)	2962.7(4)	$21/2^+$	1.25(7)	1.73(28)[5]	0.2(1)	E2
612.8(7)	3758.1(5)	$27/2^+$	1.40(5)	1.89(22)[5]	0.1(1)	E2
616.5(4)	4563.9(8)	$35/2^+$	0.18(1)	0.92(22)[3]		E2
635.9(6)	3946.8(8)	$31/2^+$	0.09(1)	0.86(14)[3]		E2
684.7(4)	3145.2(4)	$23/2^+$	1.36(7)	1.69(10)[5]	0.2(1)	E2
694.6(3)	1302.6(2)	$13/2^-$	35.30(8)	1.09(3)[2]	0.12(4)	E2
698.4(4)	3972.4(7)	$33/2^-$	2.08(20)	1.0(2)[1]	0.22(11)	E2
705.8(2)	2423.9(3)	$19/2^-$	15.77(23)	1.09(3)[1]	0.12(3)	E2
714.4(4)	2016.9(3)	$17/2^-$	12.54(22)	1.04(2)[1]	0.08(2)	E2
723.0(1)	1718.1(2)	$15/2^-$	15.77(3)	1.04(2)[3]	0.07(2)	E2
736.2(2)	2038.8(3)	$17/2^-$	12.67(16)	1.00(2)[1]	0.12(6)	E2
766.6(6)	3566.1(5)	$25/2^+$	2.28(9)	1.67(10)[5]	0.2(1)	E2
773.1(3)	1381.1(3)	$11/2^-$	0.44 (2)			
782.3(6)	4367.3(8)	$33/2^+$	0.14(1)	1.05(14)[3]		E2
809.8(3)	2112.5(3)	$15/2^+$	7.60(16)	0.55(2)[1]	0.09(3)	E1
871.2(5)	1866.3(6)	$13/2^-$	0.63(4)		-0.27(18)	M1+E2
957.4(6)	1952.5(7)	$13/2^+$	8.58(10)		0.13(4)	E1

The spin and parity of the level at 1953 keV was assigned as $13/2^+$ in the previous work [13]. This assignment was based on the proposed dipole nature of the 957-keV γ ray based on the measured R_{DCO} value. However, the R_{DCO} value of this transition was extracted gated by

[1]From the 695-keV (E2) gate.
[2]From the 737-keV (E2) gate.
[3]From the 706-keV (E2) gate.
[4]From the 957-keV (E1) gate.
[5]From the 560-keV (E1) gate.
[6]From the 767-keV (E2) gate.
[7]From the 685-keV (E2) gate.
[8]From the 609-keV (E2) gate.
[9]least square fit using the GTOL code of ENSDF [29]

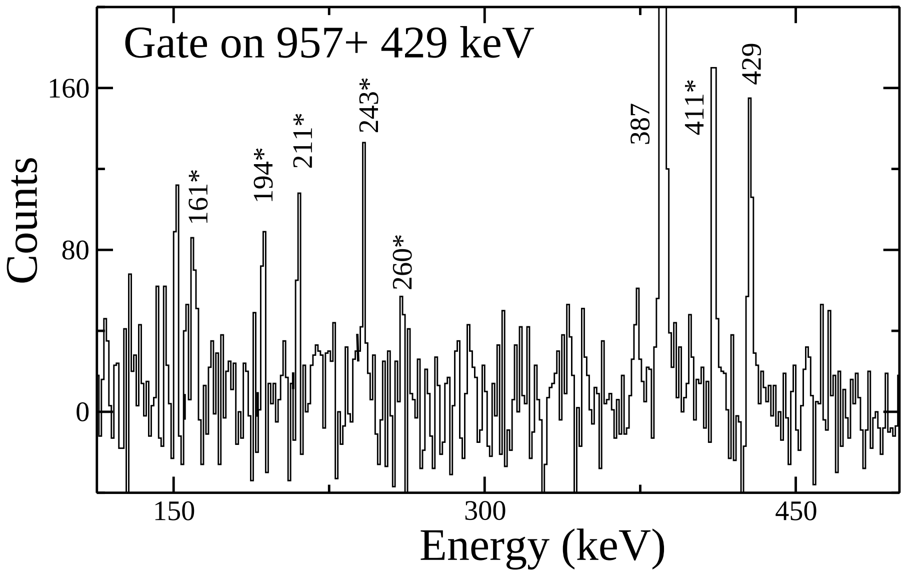

Figure 4.4: Sum-gated spectrum with gates on 957-keV and 429-keV transitions corresponding to the band-like structure A in ^{197}Tl; new γ rays are marked by asterisks (*).

a mixed ($M1 + E2$) transition (387 keV) and hence, the dipole assignment of the 957-keV γ ray was tentative. But the nature of the transition was confirmed as an Electric (E) from the Δ_{PDCO} value in the previous measurement [13]. The information about the multipolarity of the transition can be obtained from the angular distribution measurement, which could not be performed in the earlier work due to the lack of detectors at different angles. In the present work, the angular distribution measurement has been performed using the clover detectors at four different angles in the VENUS setup [30]. Data for the angular distribution measurement were taken in singles mode. The result of angular distribution measurement has been ploted in Fig. 4.3. It confirms the dipole nature of the transition. The electric (E) nature of this γ has also been confirmed in the present work from the Δ_{PDCO} measurement. Therefore, the spin and parity assignment of $13/2^+$ state has been confirmed form the $E1$ nature of the 957-keV γ-ray.

The 429-keV γ-ray, on top of the $13/2^+$ state and decaying from the 2382-keV level, was known earlier [13] but without any spin-parity assignment. In the present work, several new γ-ray transitions on top of 1953-keV and 2382-keV levels have been observed. These new γ-rays formed a single-particle like structure A. All the new γ rays are confirmed in the sum-gated spectrum with gates on 957- and 429-keV γ-rays as shown in Fig. 4.4. The R_{DCO} values of the new transitions have been obtained in the gate of pure E1 transition of 957-keV.

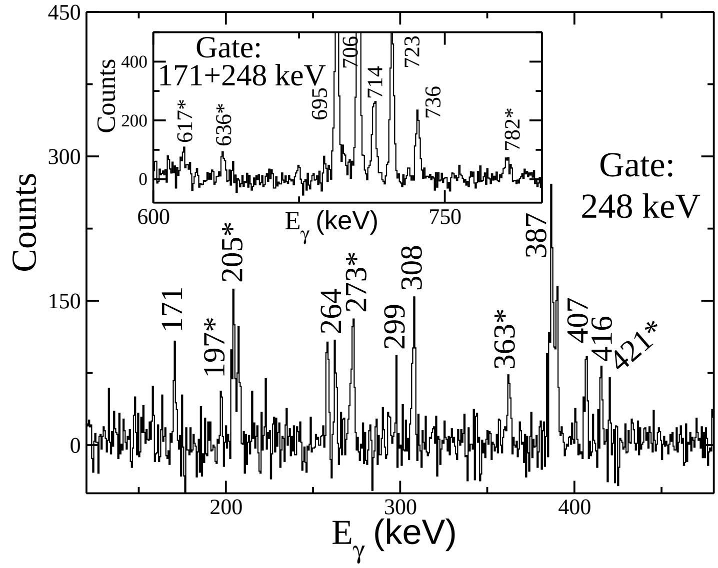

Figure 4.5: A spectrum gated by 248-keV transition showing the γ rays in band B. The higher energy γ-lines in band B are shown in the sum gated (171+248 keV) spectrum in the inset. The new γ-rays are marked by asterisks (*).

A new band B has been observed in the present work which deacays to the main rotational band C. All the new transitions of band B has been confirmed in the single gate of the 248-keV connecting transition (Fig. 4.5). The week E2 cross-over transitions of band B have been confirmed in the sum gate of 171- and 248-keV transitions. The connecting transition 248-keV has been observed in the sum-gated spectrum of Fig. 4.6 along with the other transitions of band C. The placement of the 248-keV γ-ray has been made from the fact that the 470-keV γ ray decaying from the 3064-keV, $25/2^-$ level and the ones above it in band C are not observed in the 248-keV gated spectrum of Fig. 4.5. But the 171- and 264-keV γ-rays and the ones below it are observed in that spectrum. The band-head spin and parity of band B has been assigned by the R_{DCO} and polarization asymmetry measurements of the 248 keV connecting transition and the nature of the transitions has been found to be a pure $E1$ type. Therefore, the spin-parity (I^π) of the band head of the band B at 3106-keV has been assigned as $I^\pi = 25/2^+$.

In case of the band C, most of the transitons were previously known and have been verifed in the present work. All the gamma rays belonging to band C are shown in Fig. 4.6. In one of the earlier works by Lieder et al., [12], a 412-keV γ ray was placed on top of the 3274-keV level. The placement of this transition has been changed in the present analysis. A new 286-keV,

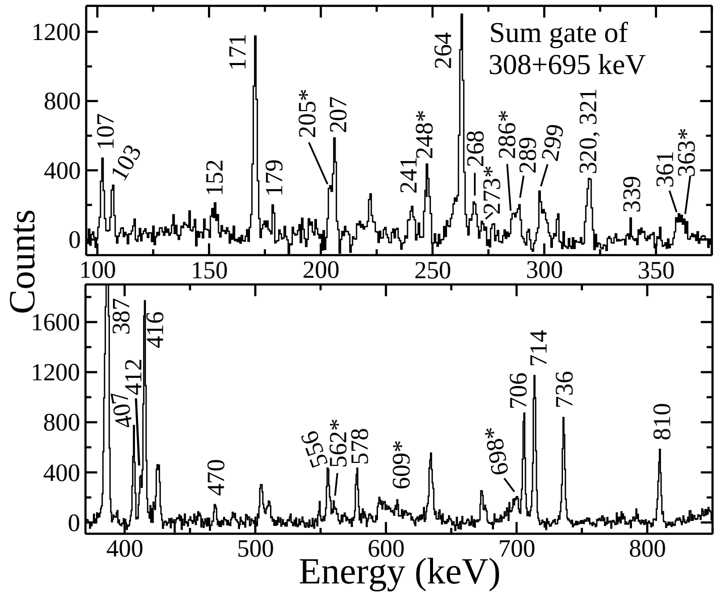

Figure 4.6: Sum gated spectrum with gates on 695-keV and 308-keV transitions corresponding to band C in ^{197}Tl; new γ rays are marked by asterisks (*).

and a cross-over 698-keV transition have been identified and placed in this band for the first time from this work. The R$_{DCO}$ values of 286 and 412-keV transitions indicate predominantly dipole in nature and the cross-over 698 keV is a quadrupole one.

Most of the transitions of the band structures D, E and F are confirmed in the single gate of 560 keV as shown in Fig. 4.7(a). The transitions in the lower part of the band D were known earlier [13]. This band has been extended in the present work beyond the first paticle alignment and up to $39/2^+\hbar$ of angular momentum with the observation of several new transitions above the $27/2^+$ state. The new γ transitions of band D have been confirmed in the sum gates on 767-keV and 339-keV transitions as shown in Fig. 4.7(b). The measured R$_{DCO}$ and the Δ_{PDCO} values of the 557-, 560- and the 810-keV transitions are consistent with the positive parity assignment for this band. It is interesting to note that no cross-over $E2$ transition has been observed above $J^\pi = 27/2^+$ in this band.

In the earlier work [13], a new band ($B3$) was observed at the band-head excitation energy of 2376 keV with six transitions of energy 179, 241, 267, 289, 320 and 361 keV. This band decays to the lower levels by a 262-keV transition. However, due to insufficient statistics coincidence relation among these transitions could not be checked in the ealier work and the placements of the transitions were somewhat tentative. In the present work, coincidence relation between

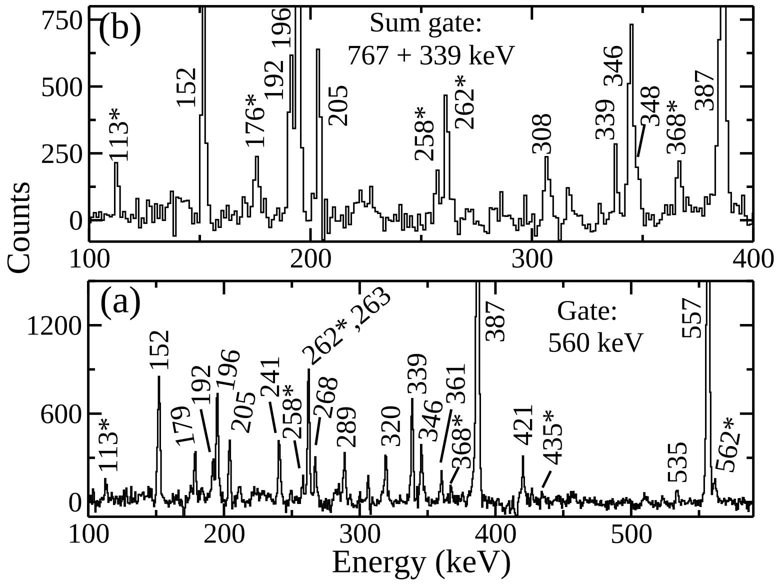

Figure 4.7: (a) Coincidence spectrum gated by 560-keV γ ray and (b) sum coincidence spectrum gated by 767-keV and 339-keV γ rays showing the transitions in the sequences D and E. The new γ-rays are marked by asterisks (*).

the transitions have been checked due to better statistics and it has been observed that the placements of the γ rays need to be modified. These sequences are built above a 2354-keV level which is connected to the known lower-lying levels by a 241-keV transition. Fig. 4.8 shows the coincidence relation for the transitions in the sequences E and F. The spectrum in Fig. 4.8(a) is gated by the 241-keV transition which shows all the γ-rays in the E and F bands. Moreover, the intensity of the 241-keV transition is the largest among the transitions in the two sequences as can be seen from the spectrum in Fig. 4.7(a). Therefore, the 241-keV transition is placed at the bottom of the two sequences E and F.

The 263-keV γ ray is not observed in the 268-keV gated spectrum [see Fig. 4.8(b)] whereas, it is observed to be in coincidence with both 241-keV and 179-keV transitions (see Fig. 4.8(a) and Fig. 4.8(c), respectively). Therefore, there must be a 263-keV transition which is in coincidence with both 241- and 179-keV transitions but in parallel with the 268-keV one. A new level at 3405 keV, in parallel to the sequence F, has been placed (see Fig.4.2) that decays to the 3142 keV level by a 263-keV γ ray which satisfies the above coincidence conditions. There is another transition of exactly similar energy in the level scheme of ^{197}Tl which decays from an 18-ns isomer at 2528 keV ($19/2^{-}$). The peak at 263-keV has been found to have a larger intensity in the spectrum gated 560-keV transition (Fig.4.7(a) in which both the 263-keV transitions will

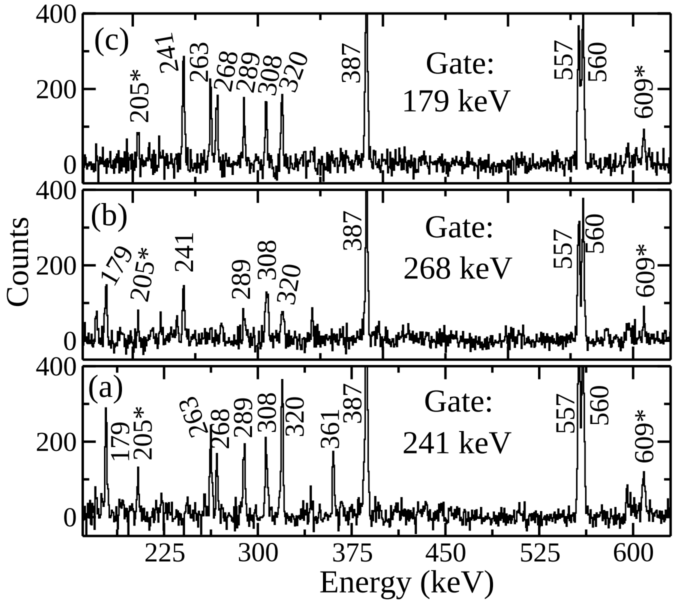

Figure 4.8: Coincidence spectra gated by 241-keV (a), 268-keV (b) and 179-keV (c) transitions showing the γ-lines placed in sequence E and F in the level scheme. New γ rays are marked by asterisks (*).

contribute to the peak. Also, the ratios of intensities of 263 keV and 268 keV peaks observed in Fig. 4.8(a) and (c) (in which only the newly placed 263-keV transition at higher excitation energy will only contribute to the peak) are found to be much smaller compared to that observed in Fig.4.7(a)). This supports the multiple placement of the 263-keV transition. However, it is interesting to note that no transitions above the newly placed $25/2^+$, 3405-keV state could be identified although the intensity of the 263-keV peak corresponding to the decay of this state is relatively large. This might indicate the presence of a long-lived high-spin isomer in ^{197}Tl.

The 361-keV transition is observed in 241-keV gate but it is not present in the spectra gated by 268-keV or 179-keV transitions. Therefore, the 179-keV, 268-keV and the newly observed 205-keV transitions are placed to form the sequence F, parallel to the 361-keV transition. A new 609-keV cross-over transition has also been observed in the sequence E but no other such cross-over transition is observed in these two sequences.

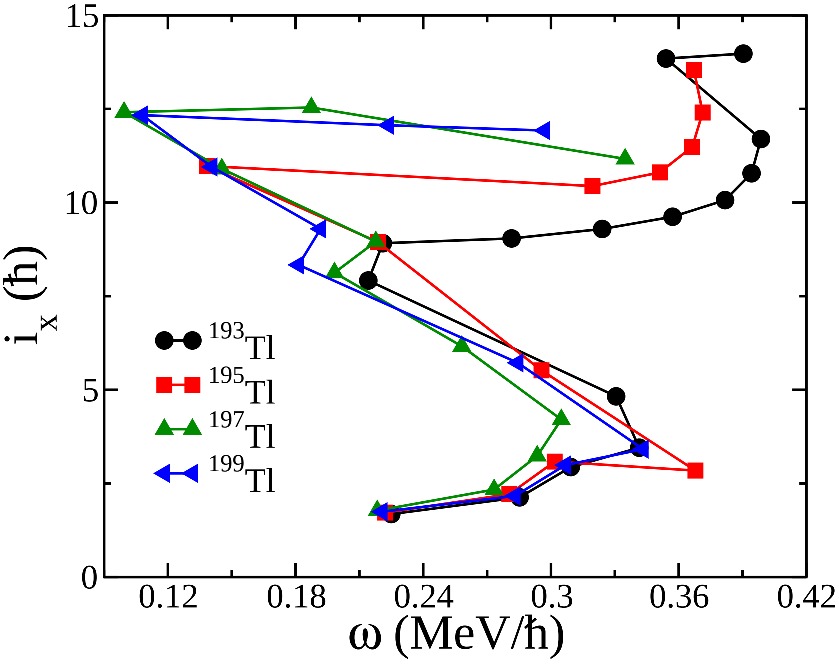

Figure 4.9: Aligned angular momentum i_x as a function of rotational frequency (ω) for the $\pi h_{9/2}$ band in ^{193,195,197,199}Tl. The Harris reference parameters are chosen to be j_0=$8\hbar^2 MeV^{-1}$ and j_1=$40\hbar^4 MeV^{-3}$.

4.3 Discussions

As mentioned before, the ground state spin-parity of odd-A Tl isotopes are $I^\pi = 1/2^+$ corresponding to the occupation of the odd-proton in the $3s_{1/2}$ orbital below the $Z = 82$ shell closure. The first excited state with $I^\pi = 3/2^+$ is obtained by the excitation of the odd proton to the $2d_{3/2}$ orbital. The second excited state in the odd-A Tl isotopes is $9/2^-$, corresponding to the occupation of the intruder $\pi h_{9/2}$ orbital by the odd proton. It is an isomeric state in all the odd-A Tl isotopes. Rotational band based on this configuration has been observed up to ^{201}Tl [17] and indication of a band-like structure has been observed in ^{203}Tl [16]. This indicates that the shape driving effect of the $\pi h_{9/2}$ orbital still competes with the spherical shell closures even up to the neutron number $N = 122$. The observation of these rotatonal bands has been interpreted as the coupling of the intruder $\pi h_{9/2}$ orbital with the deformed core of neighboring even-even Hg.

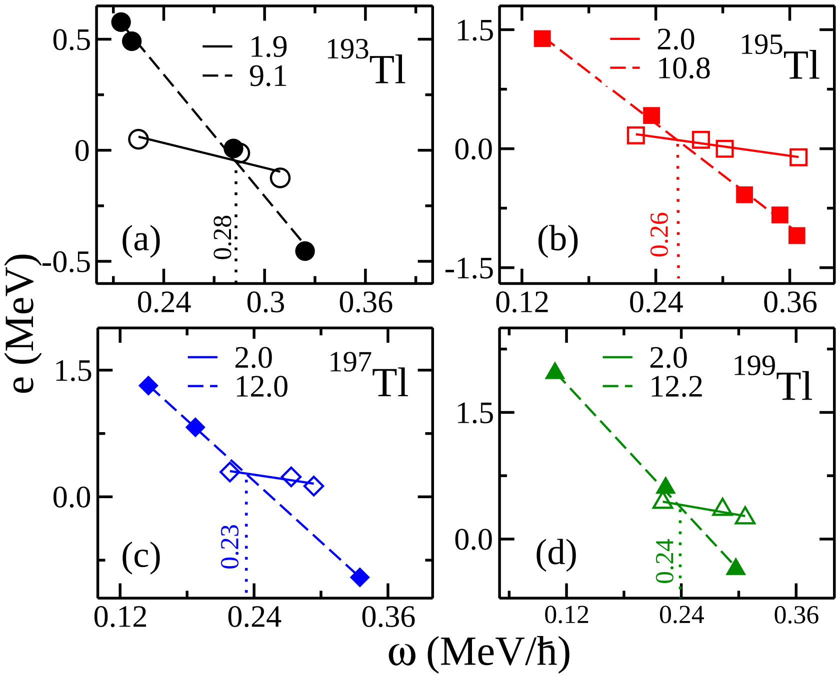

Figure 4.10: Experimental Routhians (e) as a function of rotational frequency (ω) for the πh$_{9/2}$ band in ^{193}Tl (a) ,^{195}Tl (b), ^{197}Tl (c) and ^{199}Tl (d). The open and filled symbols correspond to the experimental data before and after the band crossing. The solid (dashed) lines are the linear fit to the data points before (after) the band crossing. The dotted lines denote the crossing point with the associated number is the crossing frequency, ω_c. The values of the slopes of the two linear fits are also given for each isotope.

The band C in ^{197}Tl is based on the aforementioned intruder $\pi h_{9/2}$ orbital and it has been extended in the present work beyond its spin region where band crossing takes place. The band crossing of this band can be explained as the alignment of a pair of $i_{13/2}$ neutrons. The newly observed band crossing phenonmena of ^{197}Tl has been compared with the other neighbouring odd-A Tl isotopes. The aligned angular momentum (i$_x$) as a function of rotational frequency (ω) for the $\pi h_{9/2}$ band in ^{197}Tl along with its other neighbouring isotopes are plotted in Fig. 4.9. Similar behavior is observed in all these isotopes which indicates a common phenomenon of the alignment of two neutrons in $i_{13/2}$ orbital for the Tl isotopes. From the similarities of band crossing frequency and gain in alignment the configuration of band C in ^{197}Tl after the band crossing has been assigned as $\pi h_{9/2} \otimes \nu i^2_{13/2}$. However, there are certain differences in the gain

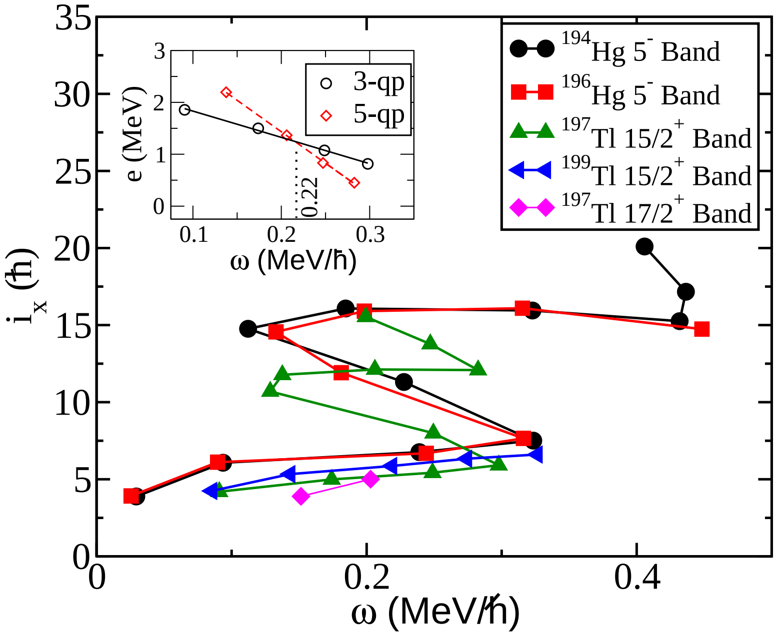

Figure 4.11: Aligned angular momentum i_x as a function of rotational frequency (ω) for the bands D and E, based on the $15/2^+$ and $17/2^+$ states, respectively, in ^{197}Tl. Same quantities for the 3-qp band in the neighboring isotope ^{199}Tl and for the 5^- bands in ^{194,196}Hg are also shown. (inset) the experimental routhian (e) vs. rotational frequency for the band D in ^{197}Tl. The solid and the dashed lines are the linear fits to the 3-qp and the 5-qp parts of the band D. The crossing frequency is indicated by the dotted line.

in alignment for the different odd-A Tl isotopes. In order to get a better quantitative values of the crossing frequency and the alignment gain, the experimental energy Routhians (e) are plotted as a function of rotational frequency (ω) in Fig. 4.10. In this plot, the intersections between the two energy Routhians, corresponding to before and after the particle alignment, defines the crossing frequency. In order to plot the two Routhians, the two regions were easily identified and separated from Fig. 4.9.

The slopes of the Routhians give the aligned angular momentum (i_x) which can be obtained by a linear fit of the data points in Fig. 4.10. The initial gain in alignment for all the isotopes remain constant at a value of $i_x \sim 2\hbar$ which has been otained using linear fitting of the energy Routhians before particle alignment (Fig. 4.10). Similarly, the values of i_x for the Tl isotopes after the alignments have also been obtained from the fitted slope of the 3-qp Routhians, i.e,

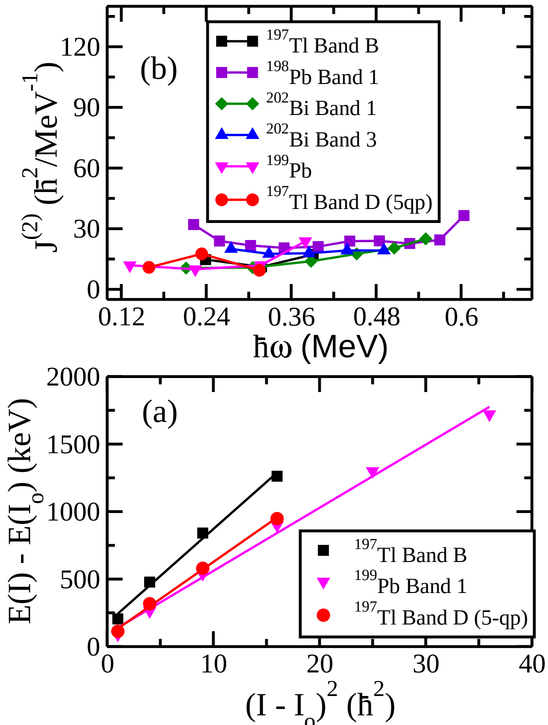

Figure 4.12: (a) Level energy E(I) with respect to the band head energy ($E_\circ$) as a function of the square of spin difference and (b) dynamic moment of inertia ($J^{(2)}$) as a function of rotational frequency ($\hbar\omega$) for the band B in ^{197}Tl and some other MR bands in the neighboring nuclei. The solid lines in (a) are the linear fits to the respective data points (symbol). Data for ^{199}Pb, ^{198}Pb and ^{202}Bi are taken from Ref. [31] [32] and [33], respectively.

the Routhian after the particle alignments, and has been compared with the other neighbouring Tl isotopes. The i_x values have been found to increase from $\sim 9\hbar$ in N = 112 isotope ^{193}Tl to $\sim 12\hbar$ in N = 116 isotope ^{197}Tl which remains constant thereafter for N = 118 isotope ^{199}Tl. On the other hand, crossing frequency, ω_c, has been observed to decrease with the increase in neutron number until ^{197}Tl and remains almost same in ^{199}Tl. This can be understood from the fact that as the neutron number increases, the neutron Fermi level moves from higher- Ω to lower-Ω orbitals (corresponding to small to large values of j_x, respectively, where j_x is the projection of particle angular momentum on to the rotation axis) in the Nilsson diagram for oblate deformation and, as a result, the required Coriolis force ($\omega_c j_x$) can be achieved to align a pair of neutrons at a lower ω_c. It may be noted that the maximum gain in alignment can be obtained as $12\hbar$ from the alignment of a pair of neutrons in $i_{13/2}$ orbital, which seems to be the value for neutron number $N \geq 116$ in Tl isotopes and below which the $i_{13/2}$ neutrons are only partially aligned.

The levels in the sequence A in Fig. 4.2 are mostly non-collective and single particle like excitations in nature. This sequence is built on top the $13/2^+$ state which was identified as the $\pi i_{13/2}$ character in Ref. [14] and has been confirmed in the present work. Therefore, the states on top of this $13/2^+$ state can be originated from the coupling of $\pi i_{13/2}$ proton with the non-collective 2^+, 3^+ and 4^+ states known in the neighboring even-even ^{196}Hg [34], which have most likely configuration of two neutrons in the negative parity $f_{5/2}$ and $p_{3/2}$ orbitals. Such non-collective states in ^{197}Tl have been populated in this work because of the choice of the light-ion (α) induced fusion evaporation reaction as the method to populate this nucleus.

The new band B having band head energy $\sim 3.1MeV$ and $I^\pi = 25/2^+$ has been identified for the first time in ^{197}Tl in the present work. The relatively high excitation energy of this band indicates that it has a 3-qp configuration. This band decays to the negative parity main band which has the configuration of $\pi h_{9/2} \otimes \nu i^2_{13/2}$. Therefore, considering these facts and also considering its positive parity, the possible configuration of the band B is assigned as $\pi i_{13/2} \otimes \nu i^2_{13/2}$. The experimental transition strengths, B(M1)/B(E2), have been determined for the states in this band from the intensities of the $\Delta I = 1$ ($I_\gamma(\Delta I = 1)$) and $\Delta I = 2$ ($I_\gamma(\Delta I = 2)$) transitions using the following equation [35]

$$\frac{B(M1)}{B(E2)} = 0.697 \frac{E_2^5}{E_1^3} \frac{1}{1+\delta^2} \frac{I_\gamma(\Delta I = 1)}{I_\gamma(\Delta I = 2)} \tag{4.1}$$

Where, E_1 and E_2 are the dipole and quadrupole transition energies in MeV, δ is the γ ray mixing ratio of $\Delta I = 1$ dipole transition. The experimental $\frac{B(M1)}{B(E2)}$ ratios compared wih calculated $\frac{B(M1)}{B(E2)}$ ratios to estimate the g-factors (g_k) for the $29/2^+$, $31/2^+$ and the $33/2^+$ states of this band B. The calculated $\frac{B(M1)}{B(E2)}$ extracted using the following equations

$$B(M1) = \frac{3}{4\pi} \mu_N^2 (g_K - g_R)^2 K^2 \frac{(I-K)(I+K)}{I(2I+1)} \tag{4.2}$$

$$B(E2) = \frac{5}{16\pi} Q_\circ^2 \frac{3(I-K)(I-K-1)(I+K)(I+K-1)}{(2I-2)(2I-1)I(2I+1)} \tag{4.3}$$

Where, g_k and g_R ($\sim \frac{Z}{A}$) are the g-factors, I is the initial spin of the branching state, K is the projection of I on to the symmetry axis, and $Q_\circ$ is the intrinsic quadrupole moment. This gives experimental values of $g_k = 0.57(4)$ to $0.60(4)$ for the three states. In these estimations, the quadrupole moment $Q_\circ = 3.0$ eb, corresponding to a deformation of $\beta_2 \sim 0.1$, was used.

These experimental values of g_k have excellent agreement with the calculated value of $g_k = 0.58$ corresponding to the $\pi i_{13/2} \otimes \nu i^2_{13/2}$ configuration. Hence, it provides a strong support to the assigned configuration of the band B. In the neighbouring ^{195}Tl, the high-spin part of the negative parity $h_{9/2}$ band i.e, the 3-qp part (after the band crossing) has a $\Delta I = 1$ partner band [22], but no such partner band has been observed in ^{197}Tl in the present work. However, the excitation energy (3138 keV) of the partner band in ^{195}Tl [36] is very similar to the band B in ^{197}Tl.

The 3-qp band D of ^{197}Tl has an excitaton energy which is very similar to the 5^- band of the even-even core ^{196}Hg [37]. The configuration of 5^- band in even-even ^{196}Hg has been assigned as $\nu i^{-1}_{13/2} \otimes (pf)^{-1}$, where (pf) denotes the negative parity orbitals, $3p_{3/2}$ and $2f_{5/2}$ which are situated around the Fermi level for neutron number $N = 116$ [38]. A rotational band based on the 5^- state at the excitation energy of 1757 keV has been observed in ^{196}Hg with both the even and odd spin members. The 3-qp band, D, of ^{197}Tl having band head spin parity, $I^\pi = 15/2^+$ at an excitation energy of 2113 keV suggest a coupling of $\pi h_{9/2}$ isomeric state (608 keV) in ^{197}Tl with the 5^- configuration in even-even ^{196}Hg. Similar 3-qp band structure has been also observed in the neighbouring isotope ^{199}Tl [14]. The aligned angular momentum (i_x) vs. rotational frequency ($\hbar\omega$) for this band has been plotted for ^{197}Tl (Fig. 4.11) and compared with the other neighbouring nuclei. The initial gain in alignment of the odd-A ^{197,199}Tl nuclei are very similar to that of the 5^- band in even-even ^{194}Hg [39] and ^{196}Hg [37]. This implies a very little contribution of odd-proton ($\pi h_{9/2}$) in the initial alignment of band D, which is as expected for the involvement of the $\Omega = 9/2$ component of the $\pi h_{9/2}$ orbital for the oblate deformation. The band D has been extended from 3-qp structure to 5-qp band structure due to a paritcle alignment. This 5-qp structure, built at the excitation energy of 3566 keV (see Fig. 4.2), has been extended upto 5140 keV and $I^\pi = 39/2^+$. The similar crossing in even-even core of Hg has been interpreted as due to the alignment of an additional pair of neutrons in the low-Ω components of the $\nu i_{13/2}$ orbital located near the Fermi level for oblate deformation [37]. The aligned angular momentum (i_x) in Fig. 4.11 and crossing frequency ($\hbar\omega = 0.22$ MeV) of band D are very similar to the 5^- band in ^{196}Hg [37]. Therefore, a configuration of $\pi h_{9/2} \otimes \nu i^{-3}_{13/2}(pf)^{-1}$ is proposed for this 5-qp band in ^{197}Tl.

On the other hand, a doubly degenerate 5-qp negative parity band was observed in ^{195}Tl [22] at an excitation energy of $\sim$ 4 MeV with the same neutron configuration as in the 5-qp band in ^{197}Tl but the proton is in $i_{13/2}$ orbital. The total Routhian surface (TRS) calculations suggested a stable triaxial shape in ^{195}Tl [22] and this band in ^{195}Tl was interpreted as the 5-qp chiral band. However, such 5-qp partner band has not been observed in ^{197}Tl. The 5-qp band in ^{197}Tl is different from the 3-qp part of band D. The band B and the 5-qp part of band D (i.e after particle alignment) have the particle and hole arrangements in high j orbitals with proton acts as particle and neutrons as hole. This type of particle-hole geometry is suitable for the generation of angular momentum using shears mechanisum for weakly deformed system and such bands are known as Magnetic rotatinal bands (MR bands) [40, 41].

Such MR bands have been observed in several isotopes of Pb, Tl and Bi nuclei in the A$\sim$ 190 mass region [19, 31, 42]. In such a band, the plot of the level energies (with respect to the band head energy) as a function of $(I - I_\circ)^2$, where I and I$_\circ$ are the level spin and the band head spin, respectively forms a straight line due to the $I(I + 1)$ nature of the level energies. Such plots are shown Fig. 4.12(a) for the bands B and D in ^{197}Tl and compared with an already established MR band in ^{199}Pb [31]. The straight-line behaviour is quite evident from this plot. The dynamic moment of inertia, J$^{(2)}$ are also plotted for the band B and the 5-qp part of band D in Fig. 4.12(b) and are compared with the already established MR bands in this region. Again, the J$^{(2)}$ values for bands B and D in ^{197}Tl have been found to be greater than or $\sim$ 10 $\hbar^2 MeV^{-1}$ as expected for an MR band and compare well with the neighbouring known MR bands. The experimental B(M1)/B(E2) ratios have also been extracted from the intensities of the γ rays of the $\Delta I = 2$ and $\Delta I = 1$ transitions. B(M1)/B(E2)= 6.3(5), 8.4(22), and 10.4(19) have been determined for the $33/2^+$, $31/2^+$, and $29/2^+$ states in band B. Considering an almost same deformation throughout the band B (fixed B(E2)) these values clearly show a decreasing trend of the B(M1) values with the increasing spin which is a clear evidence of the MR nature of the band B. Although the lifetimes of the states for this band could not be measured in the present experiment, but all other conditions clearly suggest the MR nature of this band in ^{197}Tl.

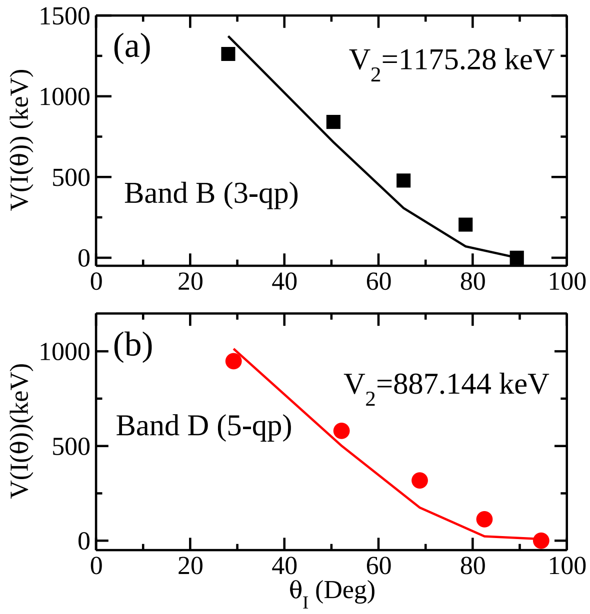

Figure 4.13: Plot of V(I(θ)) as a function of shears angle θ for the band B (a) and the band D (b) in ^{197}Tl. The solid lines are the fits to the data points from which the effective interaction V_2 between the proton and neutron angular momentum vectors has been obtained.

The present results of the 3-qp and 5-qp bands in ^{197}Tl, discussed above, imply an interesting shape transtion in odd-A Tl isotopes at higher excitation energy. Two doubly degenerate bands of chiral nature were obseved in the $N = 114$ isotope ^{195}Tl, Where as, MR bands are observed in case of ^{197}Tl with neutron number $N = 116$. Therefore, the increase in neutron number in Tl isotopes modifies the aplanar configuration, corresponding to chiral band, of the three angular momentum vectors of proton, neutron, and core in ^{195}Tl to a planar one in ^{197}Tl. Similar transition from an aplanar to a planar configuration was also observed in Cs isotopes in $A \sim 130$ mass region [43].

The band E has been modifed compared to that proposed in [13] and a new level structure F has been observed in this study. Very similar excitation energy of the bands D and E suggests a 3-qp nature of the band E. This band E decays to the $15/2^+$ state of the band D. The band E may be interpreted as a multiplet of band D of configuration $\pi h_{9/2} \otimes \nu i_{13/2}(fp)$. Similar values of their aligned angular momenta, i_x, as shown in Fig. 4.11, support this configuration assignment of band E. Level structure similar to that in band E has also been observed in the next heavier odd-A isotope ^{199}Tl [14]. The MR band B and the 5-qp part of band D were further investigated in the framework of a semiclassical model of magnetic rotation [44] to extract the particle-hole interaction strength. In this semiclassical model, the proton blade (j_π) and the

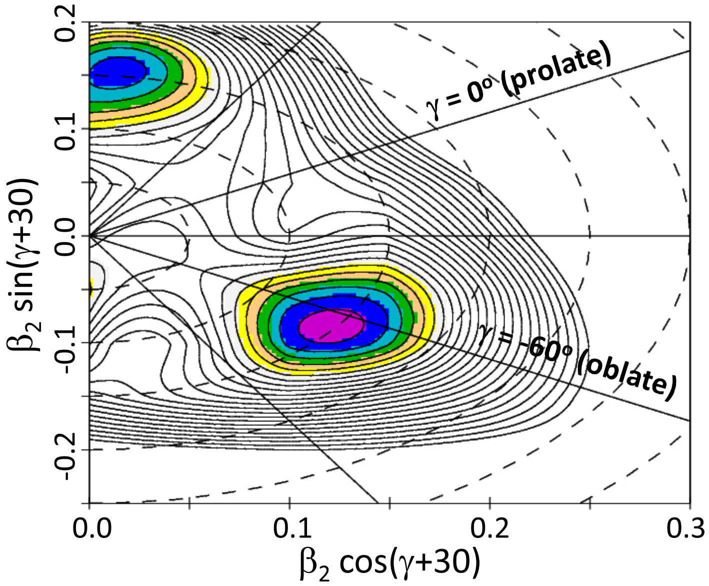

Figure 4.14: The total Routhian surfaces calculated for ^{197}Tl for the configuration of $\pi h_{9/2} \otimes \nu i^{-2}_{13/2}$, that is after the band crossing in band C. The contours are 250 keV apart.

neutron blade (j_ν) are coupled together to produce the total angular momentum (I). The angle between the proton and the neutron angular momentum blades is called the shears angle and it can be represented in a semiclassical way with the formula [44]:

$$\cos\theta_I = \frac{I(I+1) - j_\pi(j_\pi+1) - j_\nu(j_\nu+1)}{2\sqrt{j_\pi(j_\pi+1)j_\nu(j_\nu+1)}} \tag{4.4}$$

Where, I is the total angular momentum of a state. Considering the values of j_π and j_ν as $5.5\hbar$ and $11\hbar$, respectively, for the proposed 3-qp configuration $\pi i_{13/2} \otimes \nu i^{-2}_{13/2}$ for the band B, the band head spins of $12.5\hbar$ is well reproduced. similarly, for the 5-qp part of the band D, $j_\pi = 4.5$ and $j_\nu = 13$ are considered and the band head spin of $13.5\hbar$ is well reproduced by assuming perpendicular coupling between j_π and j_ν. The maximum angular momentum that can be generated by the complete alignment of the proton and the neutron angular momentum blades along the total angular momentum axis would be $16.5\hbar$ and $17.5\hbar$ for the 3-qp and 5-qp bands, respectively. The levels above $I^\pi = 33/2^+$ and $37/2^+$ in the 3- and 5-qp bands, respectively, show irregular level spacings which indicates the initiation of another band crossing for both the bands. Thus, the maximum possible spins which can be generated in these two bands by shears mechanism are also well reproduced.

According to the prescription of Macchiavelli et al. [44] in the case of shears mechanism, the neutron and proton angular momenta are coupled to spin I and interact via a term of the form

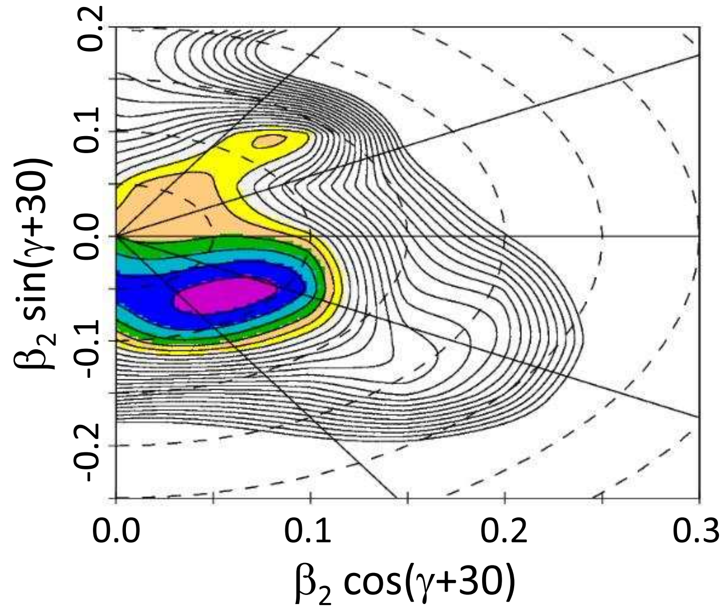

Figure 4.15: 3-qp configuration of $\pi i_{13/2} \otimes \nu i^{-2}_{13/2}$ corresponding to the band B in ^{197}Tl.

$V_2P_2(\cos\theta)$. The energy along the band is given only by the change in potential energy due to the angular momentum coupling, and accordingly, the excitation energies of the states in the MR bands, with respect to the band head energy, can be written as

$$V(I(\theta)) = E_I - E_b = (3/2)V_2\cos^2(\theta_I), \tag{4.5}$$

where E_I and E_b are the level energies corresponding to the angular momentum I and the band head energy, respectively; θ_I is the shears angle related to the angular momentum I, and V_2 is the total interaction strength between the proton and the neutorn blades. The experimental $V(I(\theta))$ and θ_I have been extracted and are plotted in Fig. 4.13 for the two MR bands in ^{197}Tl. The experimental data points are fitted by using Eqn.(4.5) to extract the value of the interaction strength V_2. The fitted values of V_2 are also shown in the Fig. 4.13. We have obtained V_2 = 1175 keV for the 3-qp MR band and V_2 = 887 keV for the 5-qp MR band. These lead to the interaction strength per particle-hole pair as V_2^{ph} = 587.5 keV and 221.8 keV, respectively, for the 3-qp and 5-qp bands. The value of V_2^{ph} for the 3-qp band is similar to the values reported in the Pb region [45], but it is some what less for the 5-qp band. It is to be noted that the 5-qp configuration also includes low-j negative parity orbitals, hence, it seems that not all of the neutron holes are taking part in the shears mechanism and the interaction strength may not be equally divided among all the particle-hole pairs.

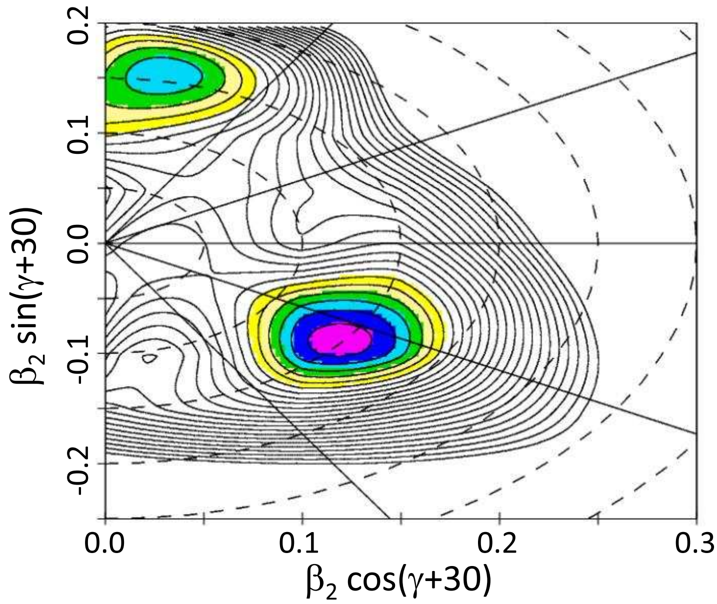

Figure 4.16: 3-qp configuration of $\pi h_{9/2} \otimes \nu i^{-1}_{13/2}(fp)^{-1}$ corresponding to the lower part of band D in ^{197}Tl.

4.4 Theoretical Calculations

4.4.1 TRS Calculations

In order to understand the different shapes in ^{197}Tl and the effects of the high-j active proton and neutron orbitals on shapes, the total Routhian surface (TRS) calculations have been performed, as discussed in Chapter 2.5 and 2.6. The formalism of Nazarewicz et al., as depicted in Ref. [46, 47], has been used and the detail technical procedure has been given in Ref. [48] (and references there in). As mentioned before, the deformation of a nucleus for a particular configuration at a particular rotational frequency corresponds to the minimum in the contour plots of the potential energies in β_2 and γ ($\gamma = 0°$ = prolate and $\gamma = -60°$ = oblate) mesh points. The energy minimization on β_4 was done for each value of β_2 and γ. Several TRSs have been calculated for different configurations and at several rotational frequencies ($\hbar\omega$). The TRS calculation for the 1-qp, $\pi h_{9/2}$ and $\pi i_{13/2}$, configurations in ^{197}Tl were earlier calculated in Ref. [13] using the same procedure. It showed oblate shapes for the $\pi h_{9/2}$ configuration and nearly spherical shape for the $\pi i_{13/2}$ configuration.

The TRS calculations, performed for the configuration corresponding to the band C in ^{197}Tl after the band crossing, is shown in Fig. 4.14. It shows energy minimum at near-oblate defor-

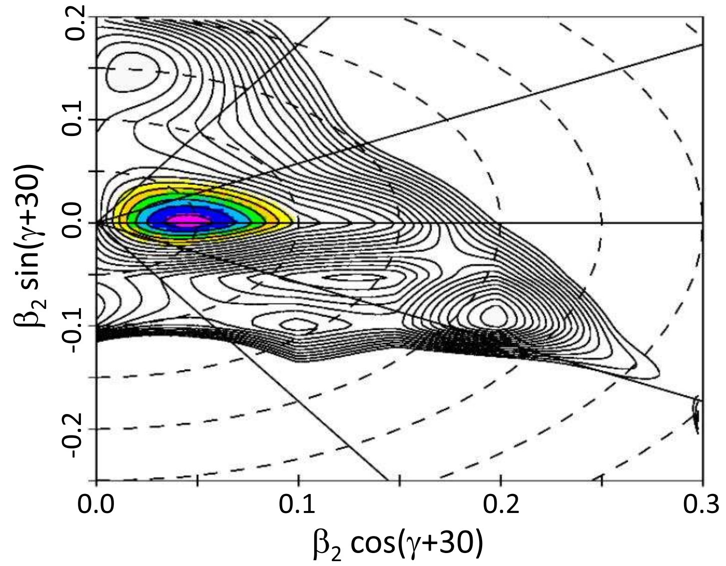

Figure 4.17: 5-qp configuration of $\pi h_{9/2} \otimes \nu i_{13/2}^{-3}(fp)^{-1}$ corresponding to the upper part of the band D in ^{197}Tl.

mation with $\beta_2 \sim 0.15$ and $\gamma \sim -62°$ which is similar to the 1-qp $\pi h_{9/2}$ configuration. The TRS plot for the 3-qp band B of configuration $\pi i_{13/2} \otimes \nu i_{13/2}^{-2}$ in ^{197}Tl are shown in Fig. 4.15. The minimum of the TRS for this configuration indicates a near-spherical shape with $\beta_2 \sim 0.08$ and $\gamma \sim -72°$. Similar near spherical shape was obtained for the 1-qp $\pi i_{13/2}$ configuration in ^{197}Tl as well [13].

The TRS calculations were also performed for the 3-qp and 5-qp part of the band D and are shown in Fig. 4.16 and 4.17, respectively. An oblate shape with $\beta_2 \sim 0.14$ and $\gamma \sim -66°$ has been obtained for the 3-qp part of band D. On the other hand, the calculations for the configuration $\pi h_{9/2} \otimes \nu i_{13/2}^{-3}(fp)^{-1}$, corresponding to the upper part of band D (5-qp), shows a near-spherical minimum at a very low deformation with $\beta_2 \sim 0.05$ and $\gamma \sim -30°$. The near-spherical shape for the band B and the 5-qp part of the band D, obtained from the TRS calculations, are consistent with the observed MR nature of these bands. In the TRS plot for the 3-qp configuration of band D (Fig. 4.16), a secondary minimum appears at about 400 keV above the first primary minimum. The observation of the band E (Fig. 4.2) at about the similar excitation energy relative to the band D provides an impression that the band E may correspond to this second minimum.

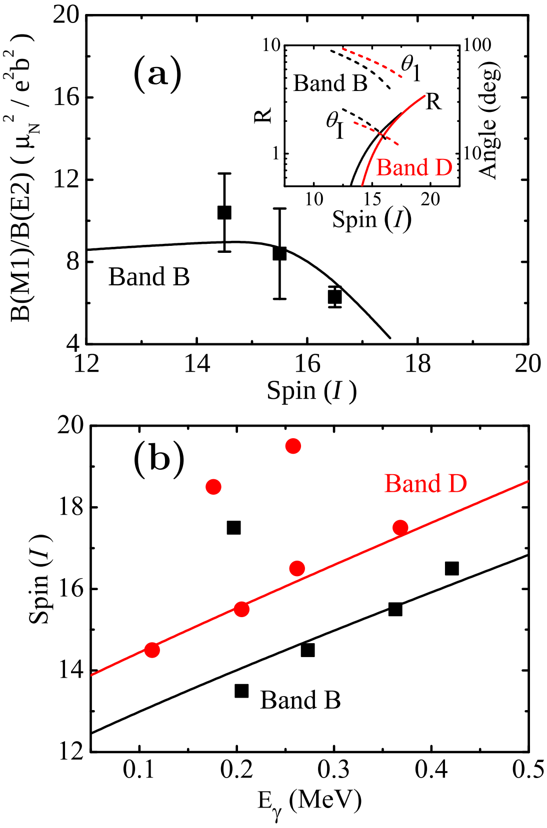

Figure 4.18: Comparison of the experimental results for the dipole bands B (represented by the black filled squares) and the upper part of D (represented by the red filled solid circles) in ^{197}Tl with the SPAC model (solid black and red lines for the bands B and upper part of D, respectively). The $B(M1)/B(E2)$ transition strengths against spin (I) have been depicted in (a) and the variation of spin (I) with the level energy difference (E_γ) is shown in (b). The variation of R and θ_1 with spin (I) are shown in the inset of (a).

4.4.2 SPAC Calculations

As discussed in Chapter 2.7, the Shears mechanism with the Principal Axis Cranking (SPAC) model [49, 50, 51, 52, 53] has been successfully applied to explain the MR bands. This model can be used as a powerful tool to extract the intrinsic character, quasiparticle configurations, and contribution of (deformed) core rotation in shears sequences. The SPAC model calculation has been performed to understand the shears mechanisms in the 3-qp and 5-qp (ΔI=1) dipole bands in^{197}Tl identified as a MR bands on top of the $25/2^+$ and the $27/2^+$ states, respectively.

In the SPAC model, the total angular momentum of a state (I) can be generated by the coupling of shears angular momentum ($\overrightarrow{j_{sh}}$) with the weakly deformed collective core angular momentum vector $\overrightarrow{R}$. The shears angular momentum ($\overrightarrow{j_{sh}}$) can be visualised as a coupling of particle and hole angular momentum. The total energy of an excited state $E(I)$ can be expressed as,

$$E(I) = E(core) + E(shears) + constant.$$

Here,

$$E(core) = \frac{R^2\,(I, \theta_1, \theta_2)}{2J(I)}$$

is the energy due to rotation of the core and

$$E(shears) = V_2 P_2(cos(\theta_1 - \theta_2))$$

is the quasiparticle energy due to the interaction between the shear angular momenta $\overrightarrow{j_1}$ and $\overrightarrow{j_2}$. Here, θ_1 and θ_2 are the angles of $\overrightarrow{j_1}$ and $\overrightarrow{j_2}$ with respect to the rotational axis directed towards $\overrightarrow{R}$, respectively. In the SPAC, the θ_1 and θ_2 can be found from the energy minimization condition for each value of I.

$$\frac{\partial^2 E(I, \theta_1, \theta_2)}{\partial\theta_1 \partial\theta_2} = 0.$$

The two dimensional energy minimisation can be changed to one dimension by fixing the direction of $\overrightarrow{j_2}$ along rotational axis. Only θ_1 was extracted from the energy minimisation of the excited state of angular momentum I. In the subsequent procedure, the level energy difference (E_γ) and the transition strengths, $B(M1)$ and $B(E2)$, of the state of interest are calculated for this minimized values of θ_1 [50, 53].

The energy has been minimized for the dipole bands assuming the respective configurations and normal initial alignments. The calculations have been performed assuming unstretched condition of the angular momenta with j_1 = 5.5$\hbar$, j_2 = 10$\hbar$, V_2 = 0.90-MeV, g_1 = -0.15 and g_2 = +1.11 for band B and j_1 = 4.5$\hbar$, j_2 = 12$\hbar$, and V_2 = +0.85-MeV for the upper part of D [49, 53]. The quasiparticle and collective quadrupole moments for the band B have been adopted as Q_{eff} = 3.5 eb and Q_{coll} = 1.5 eb, respectively, to reproduce the experimental $B(M1)/B(E2)$

values. Under these assumptions the energy levels and the spin (I) values for the dipole bands were well reproduced. The experimental ratio of the $B(M1)/B(E2)$ values vs. spin (I) of the states and the I vs. the level energy difference (E_γ) are plotted in Fig. 4.18 (a) and (b) along with the calculated values from the SPAC model. For initial normal alignment, the spin dependence of θ_1, θ_I and R are also shown in the inset of Fig. 4.18(a).

The experimental values have been found to be reproduced well for both the bands, assuming that the particle pair is initially not fully stretched. The successful interpretation of the experimental results in the framework of the SPAC model indicates that the dipole band B and the upper part of the band D in ^{197}Tl have been generated by the shears mechanism.

4.5 Summary

The excited states in ^{197}Tl have been studied by γ-ray spectroscopic technique. The reaction ^{197}Au(^{4}He,4n)^{197}Tl at 50 MeV of beam energy from the K-130 cyclotron at VECC, Kolkata was used to populate the states and the VENUS array with 6 Compton-suppressed clover HPGe detectors were used to detect the γ-rays. An improved level scheme of ^{197}Tl with the placement of 28 new γ-ray transitions has been proposed. The analysis was based on the $\gamma-\gamma$ coincidence relation, DCO ratio and polarization asymmetry ratio measurements. The new level scheme also includes several new band structures. The known oblate bands based on the 1-qp $\pi h_{9/2}$ and the 3-qp $\pi h_{9/2} \otimes \nu i^{-1}_{13/2}(fp)^{-1}$ configurations have been extended to observe the $i_{13/2}$ neutron alignments. Two new band structures based on a 3-qp (band B) and a 5-qp (band D, upper part) configurations have been identified for the first time in this work which were interpreted as the MR bands. The level ordering and the placement of the γ-ray transitions of a previously reported band structure, based on the $17/2^+$ state have been rearranged with the placement of a few additional γ-rays (bands E and F).

Theoretical calculations have been performed in the frame work of the cranking model using the Woods-Saxon potential and BCS pairing. The total Routhian surfaces for the different configurations of the observed band structures in ^{197}Tl have been calculated within this model.

The calculations predict that the 1-qp $\pi h_{9/2}$ band retains its oblate deformation even after the neutron alignment. However, the calculations suggest a change in shape from an oblate one for the 3-qp band with $\pi h_{9/2} \otimes \nu i_{13/2}^{-1}(fp)^{-1}$ configuration to a near spherical one at higher spin after the neutron alignment that is for the $\pi h_{9/2} \otimes \nu i_{13/2}^{-3}(fp)^{-1}$ configuration. The near-spherical shape is consistent with the observation of the MR band for this 5-qp configuration. Similar near-spherical shape is obtained in the TRS calculations for the other MR band in this nucleus with 3-qp configuration of $\pi i_{13/2} \otimes \nu i_{13/2}^{-2}$. The SPAC model calculations reproduced the experimental observables well and supports the shears mechanism involved in the generation of angular momentum in the bands B and the upper part of D.

It is interesting that no evidence of chiral doublet bands has been observed in ^{197}Tl in the present work, unlike the two pairs of doublet band structures reported in ^{195}Tl for 3-qp and 5-qp configurations. Instead, MR bands have been observed for the 3-qp and 5-qp configurations in ^{197}Tl. It may also be noted that neither MR nor chiral bands have been observed in the heavier isotope from ^{199}Tl onwards. It gives an indication that perhaps the neutron number $N \sim 116$ forms a boundary for the observation of the MR and chiral bands in odd-A Tl isotopes. The importance of $N \sim 116$ may be attributed to the fact that the neutron Fermi level goes beyond the high-j $i_{13/2}$ orbital above this neutron number. More experimental and theoretical studies are, therefore, warranted in order to fully understand the behaviour of the Tl and the other neighboring nuclei as their neutron Fermi level approaches $N = 126$.

The experimental data and results from this chapter have been published in Ref. [54].

Bibliography

[1] R. M. Diamond et al., Nucl. Phys. **A 45**, 632 (1963).

[2] V. T. Gritsyna et al., Nucl. Phys. **A 61**, 129 (1965).

[3] J. O. Newton et al., Nucl. Phys. **A 148**, 593 (1970).

[4] W. Reviol et al., Phys. Rev. **C 61**, 044310 (2000).

[5] P. M. Raddon et al., Phys. Rev. **C 70**, 064308 (2004).

[6] G. J. Lane et al., Phys. Lett. **B 324**, 14 (1994).

[7] G. J. Lane et al., Nucl. Phys. **A 586**, 316 (1995).

[8] M.-G. Porquet, et al., Phys. Rev. **C 44**, 2445 (1991).

[9] S. K. Chamoli, et al., Phys. Rev. **C 75**, 054323 (2007).

[10] W. Reviol et al., Phys. Scr. **T 56**, 167 (1995).

[11] W. Reviol et al., Nucl. Phys. **A 548**, 331 (1992).

[12] R. M. Lieder et al., Nucl. Phys. **A 299**, 255 (1978).

[13] H. Pai, et al., Phys. Rev. **C 88**, 064302 (2013).

[14] C. B. Li et al., Phys. Rev. **C 97**, 034331 (2018).

[15] Soumik Bhattacharya et al., Phys. Rev. **C 98**, 044311 (2018).

[16] M. G. Slocombe et al., Nucl. Phys. **A 275**, 166 (1977).

[17] S. Dasgupta et al., Phys. Rev. **C 88**, 044328 (2013).

[18] J. Wrzesiński et al., Eur. Phys. J. **A 20**, 57 (2004).

[19] H. Pai, et al., Phys. Rev. **C 85**, 064313 (2012).

[20] P.L. Masiteng, et al., Phys. Lett. **B 719**, 83 (2013).

[21] P.L. Masiteng, et al., Eur. Phys. J. **A 52**, 28 (2016).

[22] T. Roy, et al., Phys. Lett. **B 782**, 768 (2018).

[23] E.A. Lawrie, et al., Phys. Rev. **C 78**, 021305(R) (2008).

[24] S. Frauendorf and J. Meng, Nucl. Phys. **A 617**, 131 (1997).

[25] S. Frauendorf, Rev. Mod. Phys. **73**, 463 (2001).

[26] J. Meng, J. Peng, S.Q. Zhang, S.-G. Zhou, Phys. Rev. **C 73**, 037303 (2006).

[27] D. Venos et al., Nucl. Phys. **A 280**, 125 (1977).

[28] Huang Xiaolong, Zhou Chunmei Nucl. Data Sheets **104**, 283 (2005).

[29] https://www-nds.iaea.org/public/ensdf_pgm/.

[30] S. Bhattacharya et al., DAE-BRNS Symp. Nucl. Phys. **61**, 98 (2016).

[31] G. Baldsiefen et al., Nucl. Phys. **A 574**, 521 (1994).

[32] A. Görgen et al., Nucl. Phys. **A 683**, 108 (2001).

[33] R. M. Clark et al., J. Phys. G: Nucl. Part. Phys. **19** (1993) L57.

[34] Huang Xiaolong Nucl. Data Sheets **108**, 1093 (2007).

[35] P.H. Regan et al, Nucl. Phys. **A 586**, 351 (1995).

[36] T. Roy, thesis, Homi Bhabha National Institute, Variable Energy Cyclotron Centre, India (2017).

[37] D.Mehta et al., Z. Phys. **A 339** 317 (1991).

[38] H. Helpi et al., Phys. Rev. **C 28**, 1382 (1983).

[39] H. H*ü*bel et al., Nucl. Phys. **A 453**, 316 (1986).

[40] R.M. Clark and A.O. Macchiavelli, Ann. Rev. Nucl. Part. Sci. **50**, 1 (2000).

[41] A.K. Jain et al., Pramana, **75**, 51 (2010).

[42] H. Pai, et al., Phys. Rev. **C 90**, 064314 (2014).

[43] H. Pai, et al., Phys. Rev. **C 84**, 041301(R) (2011).

[44] A. O. Macchiavelli et al., Phys. Rev. **C 57**, R1073 (1998).

[45] A. O. Macchiavelli et al., Phys. Rev. **C 58**, R621 (1998).

[46] W. Nazarewicz et al., Nucl. Phys. **A 435**, 397 (1985).

[47] W. Nazarewicz et al., Nucl. Phys. **A 512**, 61 (1990).

[48] G. Mukherjee et al., Nucl. Phys. **A 829**, 137 (2009).

[49] A. A. Pasternak, *et al.*, Eur. Phys. J. **A 23**, 191 - 196 (2005).

[50] E. O. Podsvirova, *et al.*, Eur. Phys. J. **A 21**, 1 - 6 (2004).

[51] A. A. Pasternak, *et al.*, Eur. Phys. J. **A 37**, 279 - 286 (2008).

[52] S. Rajbanshi *et al.*, Phys. Rev. C **90**, 024318 (2014).

[53] S. Rajbanshi *et al.*, Phys. Rev. C **89**, 014315 (2014).

[54] S. Nandi *et al.*, Phys. Rev. C **99**, 054312 (2019).

Chapter 5

Wobbling Bands in ^{183}Au

5.1 Introduction

The wobbling motion of a nucleus can be realized for the yrast rotation of an even-even axially asymmetric nucleus i.e in a triaxial rotor; this was long ago disscused by Bohr and Mottelson [1]. The axially asymmetric (triaxial) nuclear shape arises due to the unequal mass distributions along its three principal axes, short (s), medium (m), and large (l). In case of a triaxial shape, change of mass distribution from its axially symmetric shape is maximum along the m axis which gives rise to the largest moment of inertia along this axis. Therefore, a triaxial deformed nucleus always try to rotate around its medium axis to minimise the rotational energy but, the presence of non-zero values of the moment of inertia along s and l axes give a finite rotation around those axes which generates a precession of the medium axis rotation about the space-fixed angular momentum axis, similar to the rotation of an axially asymmetric top in classical mechanics [2]. The energy values of this wobbling motion is given by [1]:

$$E = E_{\mathrm{rot}} + (n_w + 1/2)\hbar\omega_{\mathrm{wob}}$$

where, E_{rot} is the rotational energy due to the rotation along the medium axis, n_w is the wobbling quanta and $\hbar\omega_{\mathrm{wob}}$ is the wobbling frequency with wobbling energy $E_{\mathrm{wob}} = \hbar\omega_{\mathrm{wob}}$. Therefore, the wobbling motion is manifested in nuclear excitation by a series of rotational bands on top of the vibrational states corresponding to each of the wobbling quanta n_w. This rare excitation mode in its zero quasiparticle (vacuum) configuration in even-even triaxial nuclei was predicted by Bohr and and Mottelson [1] but has not been observed so far. However, nuclear wobbling motion has been observed in odd-A nuclei, although only in a few nuclei [3, 4, 5, 6, 7, 8, 9, 10, 11, 12, 13]. According to Frauendorf and Dönau, the wobbling motion in an odd-A nucleus can be classified in to two categories, Longitudinal Wobbling (LW) and Transverse Wobbling (TW) depending on how the odd-particle (or odd-hole) is aligned with the triaxial core [14]. The odd particle/hole, in the bottom/top of a deformed j shell, aligns along the s/l axis, respectively and gives rise to Transverse wobbling motion. Whereas, if the odd particle is in the middile of the deformed j shell, it aligns along the medium axis and generates Longitudinal wobbling motion. The wobbling motion in the odd-particle system was extensively discussed by Frauendorf and Dönau [14] with an emphasis on TW motion in the framework of a quasiparticle triaxial rotor (QTR) model. Frauendorf and Dönau also derived the analytical expression for $\hbar\omega_{\text{wob}}$ using the assumption of "Frozen Alignment" and harmonic oscillation (HFA). It was shown that the wobbling energy E_{wob} increases with spin (I) for LW motion which has been recently observed in ^{133}La [10] and ^{187}Au [12]. However, the variation of wobbling energy with spin for TW motion depends on the three moment of inertia values ($\mathcal{J}_m$, $\mathcal{J}_s$, $\mathcal{J}_l$) and the coupling of the odd nucleon with the triaxial core. The wobling frequency in TW motion generally decreases with spin [3, 4, 5, 6, 7, 8, 9, 11]. But, in the special case when the moment of inertia along the medium axis, $\mathcal{J}_m$, is slightly larger than $\mathcal{J}_s$ and both are much larger than $\mathcal{J}_l$, the value of E_{wob} increases with the increase of I for the smaller values of I and then decreases with I [14]. Since the special case mentioned above has not been realised in any of the observed TW bands so far, so it has been generally belived that the increasing and decreasing nature of the wobbling frequency with angular momentum (I) can be considered as an observable to distinguish LW motion from TW motion. The crucial signature for the wobbling motion is the $\Delta I = 1$ collectively enhanced $E2$ transitions between the excited $n_w = 1$ wobbling band and $n_w = 0$ main yrast band [14, 12]. On the other hand, the signature partner (SP) band decay to the main band via $\Delta I = 1$, $M1$ type [12] transitions.

So that, the nature of the connecting transitions will differentiate the wobbling band from the signature partner band.

5.2 Experimental Results

The level scheme of ^{183}Au as obtained from the present measurement is shown in Fig. 5.1. The level scheme has been built from the coincidence and intensity relations of the detected γ-rays, as discussed in "Experimental Techniques and Data Analysis" chapter. Total symmetric and angle dependent asymmetric γ-γ coincidence matrices were generated from the raw data for analysis. A γ-γ-γ cube and two polarization matrices were also generated and analysed. The total γ-γ matrix contained a total of 1.5×10^9 γ-γ coincidence events. The previously known level scheme of ^{183}Au [15, 16] has been modified with the placement of 14 new gamma transitions. The experimental results of γ-ray transition energies (E_γ), level energies (E_i), spins and parities of the initial (I_i^π) levels, final (I_f^π) levels, I_γ, R_{DCO} and Δ_{PDCO} values along with the adopted multipolarities of the γ-rays have been tabulated in Table 5.1. Most of the transitions of band 2 and 3 were already known from the previous work and are confirmed in this experiment. A summed double-gated spectrum, projected from the γ-γ-γ cube has been shown in Fig. 5.2. Gates were put on the transitions in Band 2 of ^{183}Au. The higher energy γ rays, which are low intensities, are shown in the sum gated spectrum (projected from the γ-γ matrix) of inset (a1) in Fig. 5.2. In the present analysis two new connecting transitions between the bands 3 and 2 have been observed as shown in the inset (a2) of Fig. 5.2 obtained by gating on 220-keV transition of band 2. The band 2 has been extended upto the excitation energy of 6242 keV from the placement of new 745 keV transition which can be seen in the spectrum shown in the inset (a1) of Fig. 5.2. Band 3 is also extended upto the excitation energy of 5912 keV with the placement of 676 and 779 keV newly observed transitions.

All the known gamma rays of band 4 has been verified and extended upto the excitation energy of 7848 keV with the placement of a new 746 keV γ ray as shown in Fig. 5.3. The previously known signature partner band 5 has also been extended upto the 4465-keV level and two new

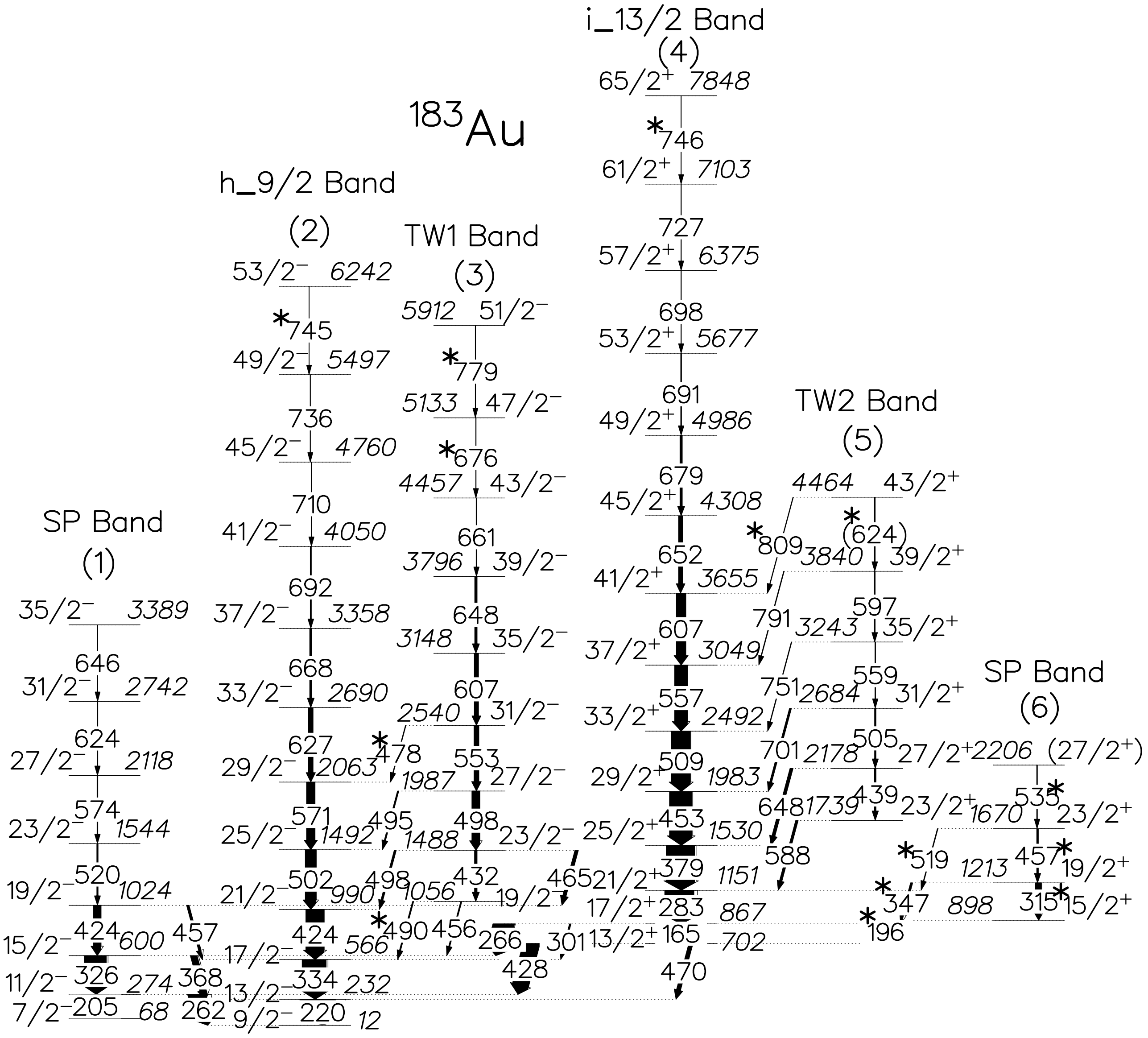

Figure 5.1: New level scheme of ^{183}Au from the present work. Line widths are proportional to their intensities. The level energies are obtained by fitting the γ-ray energies using the code *GTOL* [17]. The new transitions in the level scheme are marked by asterisks.

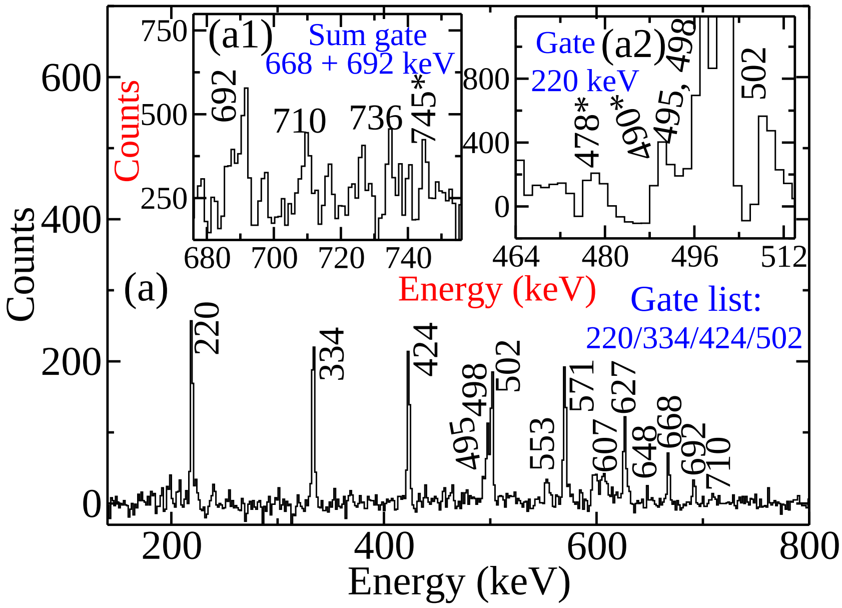

Figure 5.2: Summed double-gated γ-ray spectra projected from the γ-γ-γ cube and the γ-γ matrix. In (a) the gates were put in the cube on all the 6 pair combinations from the gatelist of 220, 334, 424, 502 keV γ rays in band (2) of ^{183}Au. The higher energy γ rays at the top of this band are shown in the sum gated (668- and 692-keV) spectrum projected from the matrix (a1). The connecting transitions between the band (3) and the band (2) are shown in the spectrum gated by 220-keV (a2).

gamma rays of energy 624 and 809 keV, decaying form that level, have been identified in the present work. In the present analysis, a new band 6 has been identified and extended up to the excitation energy of 2206 keV. The gamma rays belong to this band have been confirmed in the sum gate of 196 and 428 keV as shown in Fig. 5.4.

As mentioned before, the nature of the connecting transitions between the main and the side bands are crucial in identifying the wobbling or signature partner band. Between the wobbling partner bands, the connecting transitions are predominantly $E2$ in nature, that is their M1+E2 mixing ratios are large; whereas, in case of signature partner bands, the mixing ratios of the connecting transitions should be small. Simultaneous measurements of linear polarisation (P) and DCO ratio (R_{DCO}) were performed in the present work for the determination of mixing ratio (δ) of a mixed M1+E2 transition. For this, the measured linear polarisation (P) and R_{DCO} values were compared with the ones calculated for different mixing ratio (δ). The measured mixing ratio δ is close to 0 for pure transitions, which has been obtained for a pure $E1$ and a pure $E2$ transition as shown in Fig. 3.18 in Chapter 3. The negative parity band 2 and the

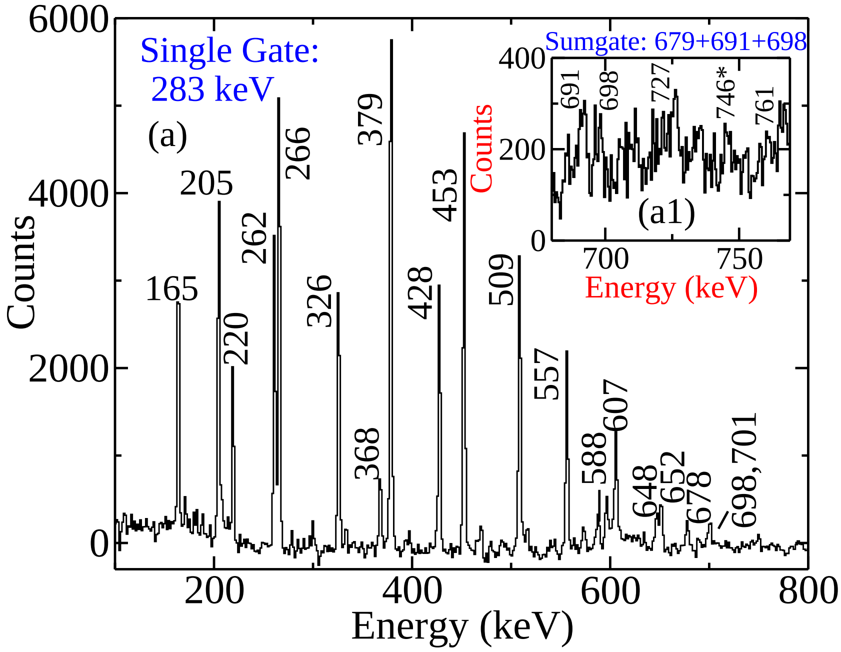

Figure 5.3: Single gated γ-ray spectra projected from the γ-γ-γ cube and the summed gated spectra from γ-γ matrix. In (a) the single gate was put in 283 keV transition in the cube from band (4) of ^{183}Au. The higher energy γ rays at the top of this band are shown in the sum gated (679, 691 and 698-keV) spectrum projected from the matrix (a1).

positive parity band 4 have two E2 rotational side bands each of which decay to the yrast main band by $\Delta I = 1$ M1+E2 transitions. The measured values of P and R$_{DCO}$ has been compared with the calculated ones for these connecting transitions and are shown in Fig. 5.5. The low values of δ for the conecting transitions between band 1 and band 2 suggest that the transitions are mostly $M1$ in nature. Therefore, the assignment of band 1 as the signature partner of the negative parity yrast band is justified.

Similarly, the polarization and R$_{DCO}$ measurements were done for the 490, 495,and 498 keV connecting transitions between band 3 and band 2. It may be noted that there are two 498 keV transitions and the 495 keV transition is parallel to both of them. Therefore, the 495-keV transition can easily be seperated by putting a gate on 502 keV (E2). In case of 498 keV transiton, it is difficult to seperate the in-band 498-keV transition of band 3 from the inter-band connecting 498 keV one. So, we have measured the P and R$_{DCO}$ of the connecting 498 keV transition in the following way: the 334-keV (E2) gate includes both the 498-keV transitions whereas, a gate on the 465-keV (E2) transition, (connecting transition from $23/2^-$ in band 3 to $19/2^-$ in band 1) contanis only the contribution of the in-band 498 keV transition. Therefore, a spectrum, obtained by subtracting the 465-keV gate to the 334-keV gate was used to determine

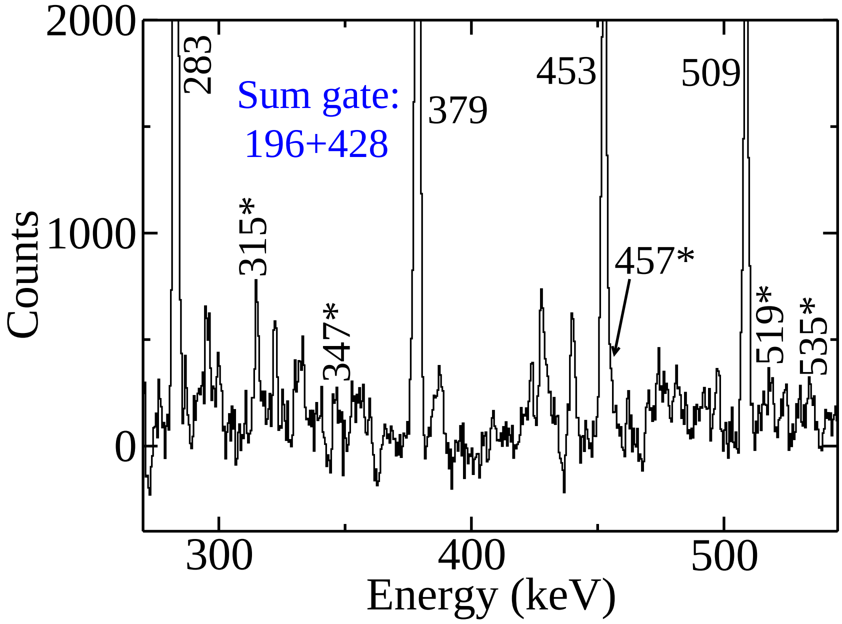

Figure 5.4: Summed single-gated γ-ray spectra projected from γ-γ matrix. All the new gamma rays of band 6 are shown in the sum gated (196 and 428-keV) spectrum projected from the matrix.

the R$_{DCO}$ and P of the connecting 498-keV γ-ray. The R_{DCO} value of the 498-keV in-band transition gated by 465-keV γ ray comes out to be 1.01(4), as it should be as both of them are stretched quadrupole transitions. It may be noted that this procedure could be adopted because both the 334-keV and the 465-keV gating transitions are of same (E2) type.

It can be seen from Fig. 5.5 that the values of δ are quite large for all the connecting transitions from band 3 to the main band 2 (in contrast to the connecting transitions between band 1 and band 2). Similarly, the δ values of the connecting transitions between the bands 5 and 4 are large whereas, the δ values for the connecting transitions from band 6 to band 4 are small. The large values of δ indicate that the transitions from band 3 to band 2 and also from band 5 to band 4 are predominantly $E2$ ($\sim$ 90%) in nature. Hence, the bands 3 and 5 may be considered as the wobbling partner bands of band 2 and band 4, respectively. On the other hand, the bands 1 and 6 are the signature partner bands of band 2 and band 4, respectively.

The branching ratios, $B(E2)_{\text{out}}/B(E2)_{\text{in}}$ and $B(M1)_{\text{out}}/B(E2)_{\text{in}}$ are also extracted from the measured intensities and the δ values of the corresponding transitions as suggested in [18]. These are shown in Fig. 5.6 for both the negative and the positive parity configurations. Larger values

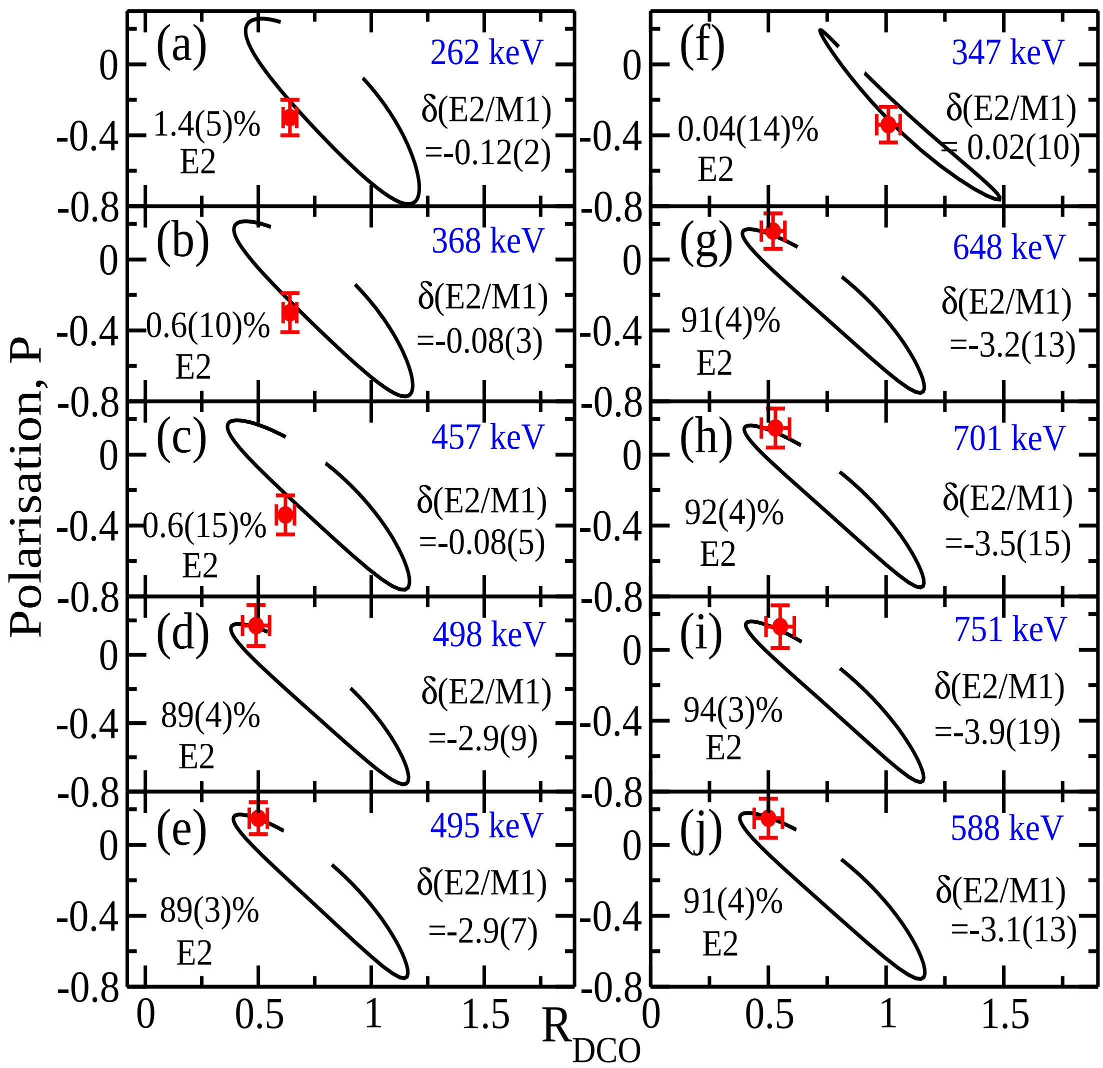

Figure 5.5: Experimental (symbol) and calculated (solid line) values (for different mixing ratios δ) of DCO ratios (R_{DCO}) and linear polarization (P) of the connecting transitions that decay to the negative parity band (2) (a − e) and to the positive parity band (4) (f − j).

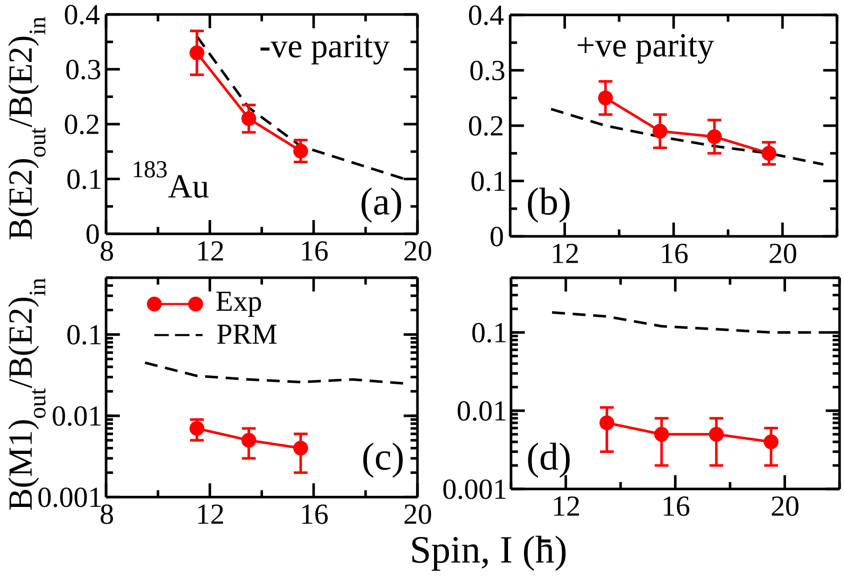

Figure 5.6: Measured values of the ratio of transition probabilities, $B(E2)_{\mathrm{out}}/B(E2)_{\mathrm{in}}$ and $B(M1)_{\mathrm{out}}/B(E2)_{\mathrm{in}}$, determined from the γ-ray intensities, as a function of angular momentum I for the negative parity (a and c) and the positive parity (b and d) bands in ^{183}Au. The theoretical values calculated from PRM are also shown.

of $B(E2)_{\mathrm{out}}/B(E2)_{\mathrm{in}}$ and smaller values of $B(M1)_{\mathrm{out}}/B(E2)_{\mathrm{in}}$ have been obtained for both the configurations, which suggest that the bands 3 and 5 are of wobbling nature [18].

Table 5.1: Energy (E_γ) and intensity (I_γ) of the γ rays, the spin and parity of the initial (I_i^π) and the final (I_f^π) states and the energy of the initial state (E_i) (GTOL fit) of ^{183}Au. The measured values of R_{DCO} and Δ_{PDCO} of the γ rays are also tabulated.

$E_\gamma(keV)$	$E_i(keV)$	$I_i^\pi \rightarrow I_f^\pi$	I_γ [1]	R_{DCO}	Δ_{PDCO}	Multipolarity
12.4 [2]	12.4	$9/2^- \rightarrow 5/2^-$	-	-	-	(E2)
164.6	866.9	$17/2^+ \rightarrow 13/2^+$	27.3(8)	1.03(3) [3]	-	E2
195.9	898.1	$15/2^+ \rightarrow 13/2^+$	12.5(14)	0.58(4) [4]	-	M1+E2
205.3	274.0	$11/2^- \rightarrow 7/2^-$	57.8(1)	1.04(2) [3]	-	E2
219.7	232.1	$13/2^- \rightarrow 9/2^-$	100.0(1)	0.99(3) [3]	-	E2
261.6	274.0	$11/2^- \rightarrow 9/2^-$	42.5(1)	0.64(3) [5]	-0.17(5)	M1+E2
266.4	866.9	$17/2^+ \rightarrow 15/2^-$	59.0(2)	0.55(2) [5]	0.24(3)	E1

Table 5.1: Continued....

$E_\gamma(keV)$	$E_i(keV)$	$I_i^\pi \rightarrow I_f^\pi$	I_γ [1]	R_{DCO}	Δ_{PDCO}	Multipolarity
283.5	1150.6	$21/2^+ \rightarrow 17/2^+$	82.1(1)	1.07(2) [5]	0.11(3)	E2
300.5	866.9	$17/2^+ \rightarrow 17/2^-$	4.3(1)	0.94(7) [3]	-0.02(4)	E1
315.4	1213.4	$19/2^+ \rightarrow 15/2^+$	16.3(14)	1.43(11) [6]	0.25(6)	E2
326.4	600.5	$15/2^- \rightarrow 11/2^-$	61.9(1)	0.97(2) [3]	0.14(2)	E2
334.2	566.4	$17/2^- \rightarrow 13/2^-$	67.5(4)	1.04(2) [4]	0.28(5)	E2
346.6	1213.4	$19/2^+ \rightarrow 17/2^+$	4.9(2)	1.01(5) [6]	-0.17(5)	M1+E2
368.5	600.5	$15/2^- \rightarrow 13/2^-$	18.5(3)	0.64(3) [3]	-0.15(5)	M1+E2
379.2	1529.8	$25/2^+ \rightarrow 21/2^+$	79.7(9)	0.94(2) [3]	0.25(2)	E2
423.4	1023.9	$19/2^- \rightarrow 15/2^-$	21.1(6)	0.91(5) [7]	0.25(3)	E2
423.8	990.3	$21/2^- \rightarrow 17/2^-$	49.8(3)	0.96(2) [8]	0.19(2)	E2
428.3	702.3	$13/2^+ \rightarrow 11/2^-$	45.8(4)	0.68(2) [3]	0.15(4)	E1
432.2	1488.5	$23/2^- \rightarrow 19/2^-$	7.0(5)	0.98(5) [4]	0.26(5)	E2
439.2	2178.4	$27/2^+ \rightarrow 23/2^+$	4.3(4)	0.98(7) [3]	0.13(4)	E2
453.1	1982.8	$29/2^+ \rightarrow 25/2^+$	63.5(8)	0.95(2) [3]	0.13(2)	E2
456.1	1056.5	$19/2^- \rightarrow 15/2^-$	4.0(2)	0.95(12) [9]	0.14(8)	E2
456.8	1670.1	$23/2^+ \rightarrow 19/2^+$	4.5(3)	1.40(17) [6]	0.16(8)	E2
457.4	1023.9	$19/2^- \rightarrow 17/2^-$	6.3(3)	0.62(4) [4]	-0.16(5)	M1+E2
464.5	1488.5	$23/2^- \rightarrow 19/2^-$	9.2(8)	0.96(7) [9]	0.20(6)	E2
470.3	702.3	$13/2^+ \rightarrow 13/2^-$	11.5(2)	1.10(6) [3]	-0.19(6)	E1
477.9	2540.5	$31/2^- \rightarrow 29/2^-$	1.1(1)	0.52(8) [10]	-	M1+E2
490.3	1056.5	$19/2^- \rightarrow 17/2^-$	3.13(9)	0.49(5) [4]	-	M1+E2
494.7	1986.9	$27/2^- \rightarrow 25/2^-$	3.5(1)	0.50(4) [4]	0.07(4)	M1+E2
497.8	1488.5	$23/2^- \rightarrow 21/2^-$	5.2(5)	0.49(6) [11]	0.08(5)	M1+E2
498.1	1986.9	$27/2^- \rightarrow 23/2^-$	14.8(15)	0.95(5) [12]	0.25(3)	E2
502.2	1492.2	$25/2^- \rightarrow 21/2^-$	30.2(3)	1.04(3) [8]	0.16(2)	E2
505.4	2683.9	$31/2^+ \rightarrow 27/2^+$	4.9(5)	1.01(12) [3]	0.27(8)	E2
509.2	2492.1	$33/2^+ \rightarrow 29/2^+$	53.4(7)	0.88(2) [3]	0.22(2)	E2

Table 5.1: Continued....

$E_\gamma(keV)$	$E_i(keV)$	$I_i^\pi \rightarrow I_f^\pi$	I_γ [1]	R_{DCO}	Δ_{PDCO}	Multipolarity
519.3	1670.1	$23/2^+ \rightarrow 21/2^+$	1.8(1)	0.70(5) [3]	-	M1+E2
520.3	1544.2	$23/2^- \rightarrow 19/2^-$	3.6(7)	1.06(9) [9]	0.20(5)	E2
535.6	2205.7	$(27/2^+) \rightarrow 23/2^+$	< 0.6	-	-	(E2)
553.5	2540.5	$31/2^- \rightarrow 27/2^-$	13.5(1)	1.08(8) [12]	0.17(8)	E2
556.9	3049.1	$37/2^+ \rightarrow 33/2^+$	35.8(6)	1.03(2) [3]	0.19(4)	E2
559.7	3243.5	$35/2^+ \rightarrow 31/2^+$	2.0(3)	1.03(12) [3]	-	E2
570.7	2062.8	$29/2^- \rightarrow 25/2^-$	23.7(2)	0.97(3) [8]	0.26(3)	E2
573.7	2117.9	$27/2^- \rightarrow 23/2^-$	2.2(4)	0.95(9) [9]	0.23(7)	E2
588.6	1739.2	$23/2^+ \rightarrow 21/2^+$	6.6(1)	0.50(6) [3]	0.06(4)	M1+E2
597.0	3840.3	$39/2^+ \rightarrow 35/2^+$	2.6(1)	0.83(6) [3]	0.21(8)	E2
606.5	3655.5	$41/2^+ \rightarrow 37/2^+$	26.2(5)	1.00(3) [3]	0.23(4)	E2
607.2	3147.7	$35/2^- \rightarrow 31/2^-$	11.7(13)	0.94(10) [12]	0.20(7)	E2
623.7	4464.1	$43/2^+ \rightarrow 39/2^+$	< 0.6	-	-	(E2)
624.5	2742.4	$31/2^- \rightarrow 27/2^-$	2.1(4)	0.87(12) [9]	-	E2
627.1	2689.9	$33/2^- \rightarrow 29/2^-$	12.8(2)	0.94(5) [8]	0.22(4)	E2
646.3	3388.7	$35/2^- \rightarrow 31/2^-$	0.84(16)	-	-	(E2)
648.3	3796.0	$39/2^- \rightarrow 35/2^-$	6.6(8)	1.05(14) [12]	0.23(8)	E2
648.5	2178.4	$27/2^+ \rightarrow 25/2^+$	8.2(3)	0.52(5) [3]	0.06(4)	M1+E2
652.3	4307.8	$45/2^+ \rightarrow 41/2^+$	11.3(2)	1.02(6) [5]	0.16(4)	E2
661.4	4457.4	$43/2^- \rightarrow 39/2^-$	1.8(4)	1.12(14) [12]	-	E2
667.8	3357.7	$37/2^- \rightarrow 33/2^-$	5.9(1)	0.94(8) [8]	0.28(6)	E2
675.5	5132.9	$47/2^- \rightarrow 43/2^-$	1.1(4)	1.04(12) [12]	-	E2
678.5	4986.3	$49/2^+ \rightarrow 45/2^+$	6.5(2)	1.03(8) [5]	0.26(8)	E2
690.8	5677.1	$53/2^+ \rightarrow 49/2^+$	2.4(1)	1.10(13) [5]	0.24(8)	E2
692.1	4049.8	$41/2^- \rightarrow 37/2^-$	3.1(1)	0.99(9) [8]	0.17(8)	E2
698.3	6375.5	$57/2^+ \rightarrow 53/2^+$	1.2(1)	0.93(11) [13]	-	E2
701.3	2683.9	$31/2^+ \rightarrow 29/2^+$	5.2(4)	0.53(6) [14]	0.06(4)	M1+E2

Table 5.1: Continued....

$E_\gamma(keV)$	$E_i(keV)$	$I_i^\pi \rightarrow I_f^\pi$	I_γ [1]	R_{DCO}	Δ_{PDCO}	Multipolarity
710.4	4760.2	$45/2^-\rightarrow41/2^-$	1.5(1)	0.98(9) [8]	0.17(11)	E2
727.2	7102.7	$61/2^+\rightarrow57/2^+$	1.2(1)	0.93(13) [13]	-	E2
736.4	5496.6	$49/2^-\rightarrow45/2^-$	1.0(1)	0.99(18) [8]	-	E2
745.5	6242.1	$53/2^-\rightarrow49/2^-$	0.60(3)	-	-	(E2)
745.7	7848.4	$65/2^+\rightarrow61/2^+$	0.8(1)	1.03(14) [13]	-	E2
751.3	3243.5	$35/2^+\rightarrow33/2^+$	1.7(1)	0.55(6) [14]	0.05(4)	M1+E2
779.1	5912.0	$51/2^-\rightarrow47/2^-$	0.7(4)	1.04(15) [12]	-	E2
791.0	3840.3	$39/2^+\rightarrow37/2^+$	1.7(2)	0.53(9) [14]	-	M1+E2
808.7	4464.1	$43/2^+\rightarrow41/2^+$	1.4(1)	0.50(10) [14]	-	M1+E2

5.3 Discussions

In ^{183}Au (Z = 79), the proton Fermi level lies just below the Z = 82 shell closure. However, Ω components of the high-j proton orbitals $\pi h_{9/2}$ and $\pi i_{13/2}$ come down in energy with deformation and intrudes in to the region of the proton fermi level in Au isotopes. Rotational bands have, accordingly, been observed in different Au isotopes based on the above configurations

[1]Relative γ-ray intensities are estimated from prompt spectra and normalized to 100 for the total intensity of 220-keV γ-rays.

[2]Adopted from [19];

[3]From 283 keV (E2) gate;

[4]From 220 keV (E2) gate;

[5]From 379 keV (E2) gate;

[6]From 428 keV (E1) gate;

[7]From 326 keV (E2) gate;

[8]From 334 keV (E2) gate;

[9]From 205 keV (E2) gate;

[10]From 571 keV (E2) gate;

[11]From 465 keV (E2) gate substracted from 334 keV (E2) gate;

[12]From 465 keV (E2) gate;

[13]From 557 keV (E2) gate;

[14]From 453 keV (E2) gate;

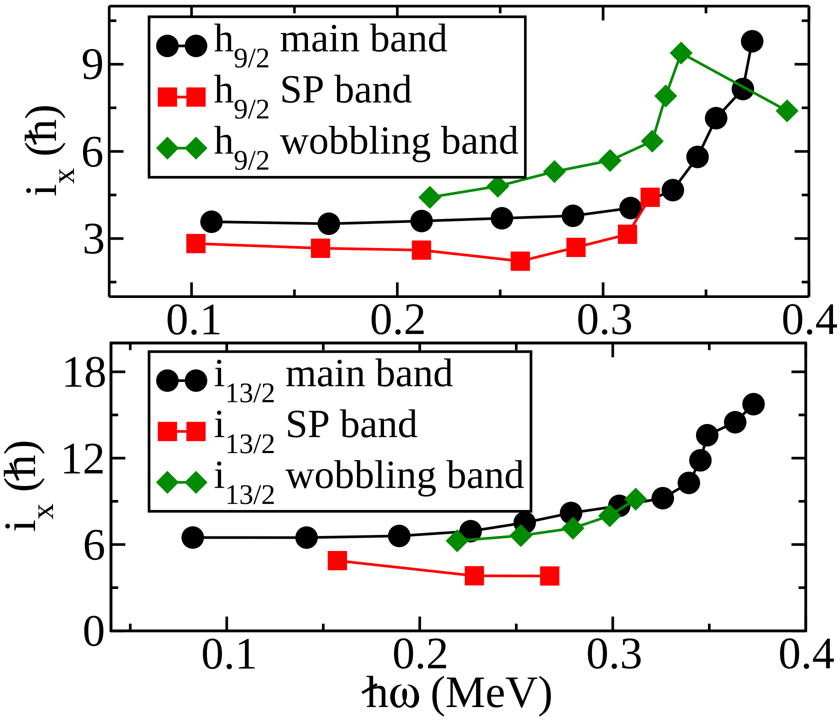

Figure 5.7: Aligned angular momentum i_x as a function of rotational frequency (ω) for the $\pi h_{9/2}$ and $\pi i_{13/2}$ band in ^{183}Au. The Harris reference parameters j_0=29.4 $\hbar^2 MeV^{-1}$ and j_1=121 $\hbar^4 MeV^{-3}$, from Ref. [16] have been used.

[15, 16, 20, 21]. The configurations of negative and positive parity bands in ^{183}Au were already known as $\pi h_{9/2}$ and $\pi i_{13/2}$, respectively [15, 16]. The invlovement of the Ω components for these high-j configurations can be obtained from the quasiparticle aligned angular momentum i_x of the observed rotational bands. The plot of i_x as a function of rotational frequency ($\hbar\omega$) is shown in Fig. 5.7. It can be seen that in case of the positive parity main band, $i_x \approx 6.5\hbar$ at the begining of the band. This indicates the involvement of the fully aligned $\Omega = 1/2$, $i_{13/2}$ configuration for this positive parity band. In case of the negative parity band, the estimated value of i_x ($\approx 3.5\hbar$) is somewhat less than the fully aligned value ($= 4.5\hbar$) corresponding to $\Omega = 1/2$ and, suggesting small mixing with other Ω orbitals, but nevertheless, still the low-Ω components are involved in generating the negative parity band. The involvement of low-Ω component indicates that the odd-particle is aligned along the short axis of a prolate-like triaxial nucleus. Therefore, the geometrical arrangement of odd particle and the core is similar to a Transverse Wobbler as shown in Fig. 1.5 in Chapter 1. So, both the wobbling bands in ^{183}Au are suggested as Transverse wobbling (TW) bands.

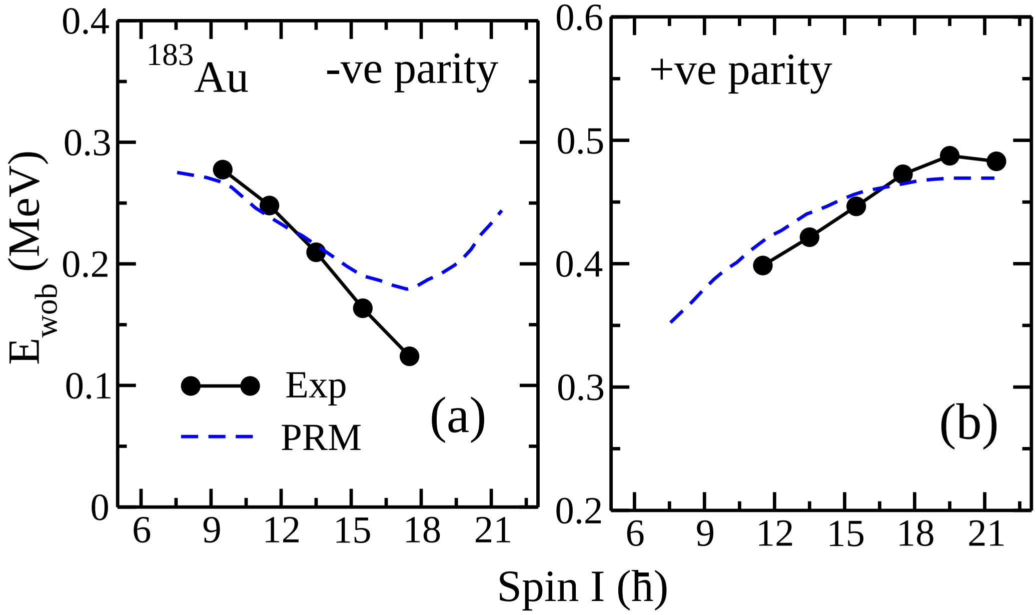

Figure 5.8: Experimental wobbling energy $E_{\rm wob}$ as a function of angular momentum I for the negative parity (a) and the positive parity (b) bands in ^{183}Au. The theoretically calculated values are also shown. The error bars on experimental values are within the size of the data points.

It was shown in Ref. [14] that the variation of the wobbling energy with spin (I) depends on the type (LW or TW) of wobbling motion. Experimentally, the wobbling energy $E_{\rm wob} = \hbar\omega_{\rm wob}$ can be obtained from the energy differences between the $n_w = 1$ wobbling partner band and $n_w = 0$ yrast band using the relation [9, 10, 11, 12]:

$$E_{\rm wob} = E(I, n_w = 1) - [E(I-1, n_w = 0) + E(I+1, n_w = 0)]/2,$$

where $E(I)$ is the level energy with angular momentum I. The experimental values of $E_{\rm wob}$ for both the wobbling bands have been obtained in the present work and the wobbling frequency are plotted with spin (I) as shown in Fig. 5.8. It has been observed that the wobbling frequency decreases with spin for the negative parity wobbling band whereas, it increases for the positive parity wobbling band. The general understanding suggest that the increase (decrease) of wobbling frequency with spin I is the manifestation of LW (TW). However, the the low-Ω, $i_{13/2}$ configuration for the positive parity band is in contradiction to the LW geometry of the coupling of the odd quasiparticle. Therefore, more in depth analysis is needed to understand the nature of these two bands. It is worth pointing out that Frauendorf and Dönau showed that it is possible, in case of TW, that the wobbling frequency increases with the increase of spin for initial lower values of spin for a special condition on the ratio of moments of inertia

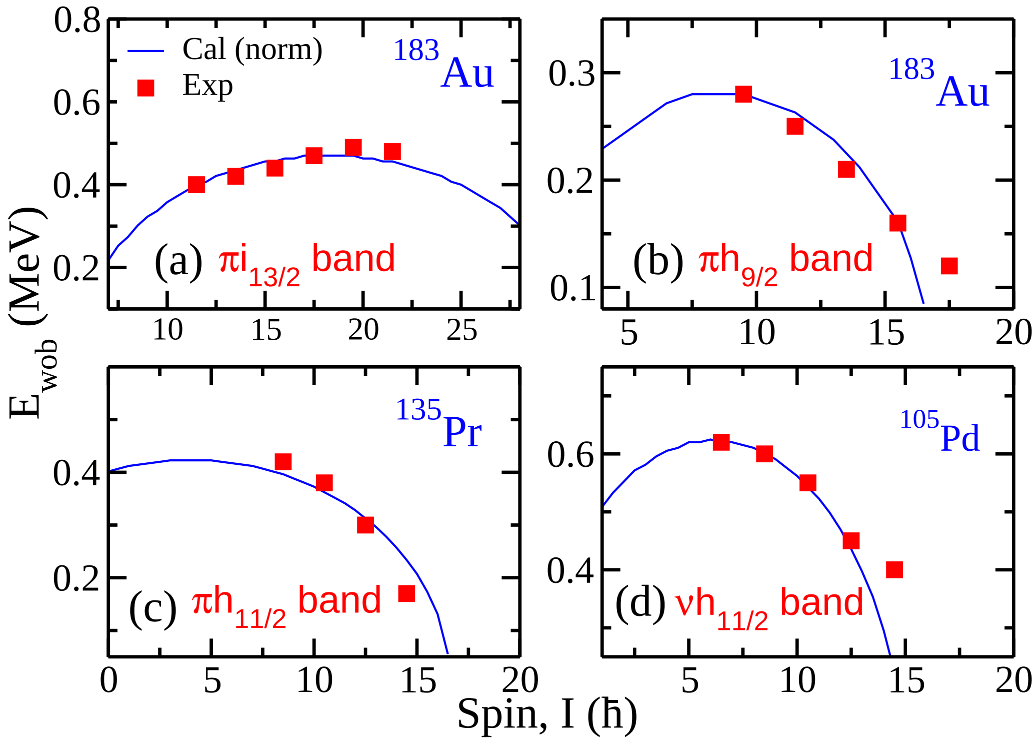

Figure 5.9: Experimental and calculated values (see text for details) of wobbling energies as a function of angular momentum (I) for the (a) positive ($i_{13/2}$) and (b) negative ($h_{9/2}$) parity wobbling bands in ^{183}Au. For comparison, the same for the normal deformed TW bands in ^{135}Pr (c) and ^{105}Pd (d) are also shown. Data for the later two nuclei are obtained from Ref.[11] and [9], respectively.

along short, long and medium axes [14]. However, that feature has not been observed in any of the wobbling bands observed so far, prior to this work and it is likely that the wobbling band based on $\pi i_{13/2}$ orbital observed in ^{183}Au in this work, is that special mode of TW as predicted in Ref.[14].

5.4 Theoretical Calculations and Conclusions

In order to understand the observation of multiple wobbling bands in ^{183}Au, theoretical calculations have been performed in the frame work of particle rotor model (PRM) [14, 22, 23, 24, 25]. The input deformation parameters of $\beta_2 = 0.30$ and $\gamma = 20.0°$ have been obtained for the negative parity band while for the the positive parity band the β_2 and γ values are 0.29 and 21.4°, respectively as obtained from CDFT calculations [26]. The dependence of the defor-

Table 5.2: The moments of inertia along medium ($\mathcal{J}_m$), short ($\mathcal{J}_s$) and long ($\mathcal{J}_l$) axes obtained for the wobbling bands in ^{183}Au, ^{135}Pr and ^{105}Pd. The values for the later two nuclei are taken from Ref. [14] and [9], respectively. The estimated values of I_m based on HFA approximation are also given.

	^{183}Au	^{183}Au	^{135}Pr	^{105}Pd
	$\pi i_{13/2}$ band	$\pi h_{9/2}$ band	$\pi h_{11/2}$ band	$\nu h_{11/2}$ band
$\mathcal{J}_m$	50.00	36.85	21.0	9.24
$\mathcal{J}_s$	37.52	25.70	13.0	5.87
$\mathcal{J}_l$	2.38	5.45	4.0	1.99
$\mathcal{J}_m/\mathcal{J}_s$	1.33	1.43	1.61	1.57
I_m ($\hbar$)	16.5	7.5	5.5	6.5

mation parameters on the angular momentum also been checked and it change only within 0.01 for β and 1° for γ from the bandhead to the highest spin for both the negative and positive parity band. It justifies the stability of triaxial shape for both the wobbling bands. The three moment of inertia for the negative and positive parity bands have been extracted by fitting the experimental energy spectra and the values are $\mathcal{J}_{m,s,l} = 36.85, 25.70, 5.45$ $\hbar^2$/MeV and $\mathcal{J}_{m,s,l} = 50.00, 37.52, 2.38$ $\hbar^2$/MeV, respectively. In both calculations, the pairing gap $\Delta = 12/\sqrt{A} = 0.89$ MeV is adopted. It should be noted that the calculations can reproduce the experimental $B(E2)$ values [27], which justifies the correct prediction of the deformation parameters by CDFT. The experimental values are compared with the calculations as shown in Fig. 5.8. The wobbling energies for both the positive and the negative parity wobbling bands have been well reproduced by the calculations. Also the experimental $B(E2)_{\text{out}}/B(E2)_{\text{in}}$ values whcih are highly sensitive to the nuclear triaxiality, agree well with the calculated ones (Fig. 5.6). It also justifies the correct inputs of triaxiality by CDFT calculation. The over estimation of the $B(M1)_{\text{out}}/B(E2)_{\text{in}}$ values is attributed to the absence of scissors mode in the calculations [28]. The large values of $B(E2)_{\text{out}}/B(E2)_{\text{in}}$ and small values of $B(M1)_{\text{out}}/B(E2)_{\text{in}}$ obtained in the calculations, further support the wobbling interpretation for both the bands.

The values of the three moments of inertia obtained for the two wobbling bands in ^{183}Au are compared with those in other TW wobbling bands in Table 5.2. The ratio of $\mathcal{J}_m/\mathcal{J}_s$ are the smallest for the positive parity $\pi i_{13/2}$ band which, therefore, can be an ideal candidate for the observation of the, hitherto unobserved, initial part of a TW band in which E_{wob} increases with I until a certain value I_m after which, it starts to decrease. The value of I_m must be sufficiently large compared to the band head spin of the wobbling band to be able to observe the initial increasing part of the wobbling energy with I. The larger I_m value can be obtained by the combined effects of larger values of the quasi particle angular momentum j, and how close is the value of $\mathcal{J}_m$ / $\mathcal{J}_s$ to unity, as discussed in Ref. [14] in the frame work of the harmonic wobbling model with frozen orbital approximation (HFA). The I_m values estimated from the HFA model in ^{183}Au have been compared, in Table 5.2, with the TW bands reported in the two other normal deformed nuclei, ^{105}Pd [9] and ^{135}Pr [11]. The TW bands in ^{105}Pd and ^{135}Pr have the configurations of $\nu h_{11/2}$ and $\pi h_{11/2}$, respectively. The value of I_m is the largest for the $\pi i_{13/2}$ band in ^{183}Au among these nuclei and is much more than the initial spin of its wobbling band. Therefore, E_{wob} for this band would fall in the increasing part of the predicted TW band. This is further established from Fig. 5.9 in which E_{wob} is calculated from the HFA model using the fitted moments of inertia values $\mathcal{J}_{m,s,l}$ from Table 5.2 are plotted as a function of spin along with the measured E_{wob}. The calculated values are suitably normalised for comparison. Excellent agreement between experiment and theory has been achieved for all the cases. It can be seen that the data points corresponding to the $\pi i_{13/2}$ band in ^{183}Au match with the increasing part while for the others they fall nicely on the decreasing part of the curves for which the values of I_m are lower than the lowest spin of the observed wobbling bands. Therefore, both the TW bands with different behaviour of their wobbling frequency with spin could be understood. This is for the first time that the increasing part of the wobbling frequency with spin of a transverse wobbling band could be experimentally observed.

5.5 Summary

In summary, It is the first experimental observation of muliple TW bands based on a positive ($i_{13/2}$) and a negative ($h_{9/2}$) parity configuration in the nuclear chart. ^{183}Au is, so far, the only nucleus in which both increasing and decreasing parts of the $E_{\rm wob}$ transverse wobbling have been observed. Different behaviours of wobbling frequency for the same kind of wobbling excitations (TW) would modify the general understanding on wobbling excitation and the way to distinguish TW from LW. It may also be pointed out that similar to the multiple chiral doublet (MχD) bands [29], the observation of the presence of multiple TW bands is also an evidence of triaxial shape coexistence in ^{183}Au. Though the triaxial shape coexistence has been experimentally confirmed in several nuclei through MχD bands (see for example [30, 31] and references there in), but its realization through the observation of multiple wobbling bands has been observed for the first time in this work.

The experimental data and results from this chapter have been published in Ref. [32].

Bibliography

[1] A. Bohr and B. R. Mottelson, *Nuclear Structure* (Benjamin, New York, 1975), Vol.II.

[2] L. D. Landau and E. M. Lifshitz, *Course of Theoretical Physics*, Mechanics, Vol. 1 (Pergamon Press, London, 1960)

[3] S. W. Ødegard et al., Phys. Rev. Lett. **86**, 5866 (2001).

[4] D. R. Jensen et al., Phys. Rev. Lett. **89**, 142503 (2002).

[5] P. Bringe et al., Eur. Phys. J. **A 24**, 167 (2005).

[6] G. Schönwaßer et al., Phys. Lett. **B 552**, 9 (2003).

[7] H. Amro et al., Phys. Lett. **B 553**, 197 (2003).

[8] D. J. Hartley et al., Phys. Rev. **C 80**, 041304(R) (2009).

[9] J. Timár et al., Phys. Rev. Lett. **122**, 062501 (2019).

[10] S. Biswas et al., Eur. Phys. J. **A 55**, 159(2019).

[11] J. T. Matta et al., Phys. Rev. Lett. **114**, 082501 (2015).

[12] N. Sensharma et al., Phys. Rev. Lett. **124**, 052501 (2020)

[13] N. Sensharma et al., Phys. Lett. **B 792**, 170 (2019).

[14] S. Frauendorf and F. Dönau, Phys. Rev. **C 89**, 014322 (2014).

[15] W.F. Mueller et al., Phys. Rev. **C 59**, 2009 (1999).

[16] L. T. Song et al., Phys. Rev. **C 71**, 017302 (2005).

[17] https://www-nds.iaea.org/public/ensdf_pgm/

[18] S. C. Pancholi, *Exotic Nuclear Excitations* (Springer Tracts in Modern Physics), Vol 242

[19] Coral M. Baglin Nucl. Data Sheets **134**, 149, (2016).

[20] A. J. Larabee et al., Phys. Lett. **B 169**, 21 (1986).

[21] C. Bourgeois et al., Z. Phys. **A 333**, 5 (1989).

[22] I. Hamamoto, Phys. Rev. C **65**, 044305 (2002).

[23] W. X. Shi and Q. B. Chen, Chin. Phys. C **39**, 054105 (2015).

[24] E. Streck, Q. B. Chen, N. Kaiser, and U.-G. Meißner, Phys. Rev. C **98**, 044314 (2018).

[25] Q. B. Chen, S. Frauendorf, and C. M. Petrache, Phys. Rev. C **100**, 061301(R) (2019).

[26] Q.B. Chen, Private Communication.

[27] P. Joshi et al., Phys. Rev. **C 66**, 044306 (2002).

[28] S. Frauendorf and F. Dönau, Phys. Rev. C **92**, 064306 (2015).

[29] J. Meng, J. Pengi, S.Q. Zhang, S-G. Zhou, Phys. Rev. **C 73**, 037303 (2006).

[30] A.D. Ayangekaa et al., Phys. Rev. Lett. **110**, 172504 (2013).

[31] T. Roy et al., Phys. Lett. **B 782**, 768 (2018).

[32] S. Nandi et al., Phys. Rev. Lett. **125**, 132501 (2020)

Chapter 6

Different Modes of Excitations in ^{187}Os

6.1 Introduction

Osmium nuclei lie between the axially deformed prolate rare earth [1] and spherical Pb nuclei [2]. Many of the even even Os isotopes are known to be γ-soft and odd-A Os isotopes show rotational bands based on different multi-quasi-particle configurations. As mentioned before γ deformations in nuclei are manifested in gamma band, anomalous signature splitting, doubly degenerate band structure, wobbling motion, K mixing etc. In even even Os isotopes, the presence of gamma band implies the existence of finite gamma deformations in nuclear structure. The decrease in excitation energy of the second 2^+ state of the γ bands in the Os isotopes with the increase in neutron number indicates that the nuclei become more gamma deformed with increasing neutron number. The excitation energies of the second 2^+ state of γ band in ^{184,186,188}Os isotopes are 945, 768, 633 keV, respectively, and in ^{186,188}Os, $\gamma\gamma$ bands were also observed at excitation energies of 1353, 1278 keV, respectively [3]. So the heavier Os nuclei are the ideal laboratories to study the effects of gamma deformation on the nuclear level structure. But the experimental data on heavier odd A Os isotopes are very scarce mostly because of the limited ways of populating the excited states in heavier Os isotopes. They can only be populated by using light ion induced reaction or deep-inelastic scattering. The level scheme in Os isotopes, upto neutron number 109 (^{185}Os) [4] are well extended but beyond that the data are very scarce, mainly for odd A isotopes. Therefore, we have performed an experiment to study ^{187}Os (N=111), to understand the effect of one unpaired neutron on the γ deformed ^{186}Os core [5]. The neutron fermi level in heavier Os isotopes lie in the upper half of $\nu h_{9/2}$ and $\nu i_{13/2}$ orbitals. The unpaired neutron hole in odd-A heavier Os isotopes can align the particle angular momentum along the long axis of triaxial core and manifested most unfavoured long-axis rotation of triaxial shape nucleus. Recently, ^{193}Tl (Z=81, N=112) shows long-axis rotation based on neutron hole in $\mathrm{i}_{13/2}$ [6]. This is one of such exotic excitation has not yet been observed in any heavier odd-A Os isotopes. The ^{187}Os [7] can be a ideal nucleus to search for a long-axis rotation having odd hole in $\mathrm{h}_{9/2}$ or $\mathrm{i}_{13/2}$ orbitals. The existence of N=108 and 110 deformed shell gaps has already been seen in the axially deformed even-even Hf and W isotopes [8]. The delayed particle crossing in the even-even isotopes with neutron number 108 and 110 can be explained by the existence of deformed shell gap. But, the effect of deformed shell gap 110 on odd A nuclei has not been well investigated. The ^{187}Os with neutron number 111, will be ideal case for the study of N=110 deformed shell gap for odd-A system. The neutron Fermi levels for odd-A heavier Os isotopes lie close to $1/2^-[510]$ and $3/2^-[512]$ orbitals. These two single particle orbitals lie very close to each other and the band based on these orbitals are very similar in nature and are called twin bands. The twin bands based on these configurations have been observed in ^{187}Os but are limited to the excitation energy at 511 keV (tentative level) only and these bands were interpreted in terms of pseudo Nilsson quantum numbers [9, 10].

Therefore, it may be noted that although the possibility of some interesting high spin phenonmena in ^{187}Os, there is no data in that. The alignment phenonmena are not known in this nucleus, with an aim to study the high spin states and band structure based on different configurations. The high spin states in ^{187}Os have been investigated in this thesis work.

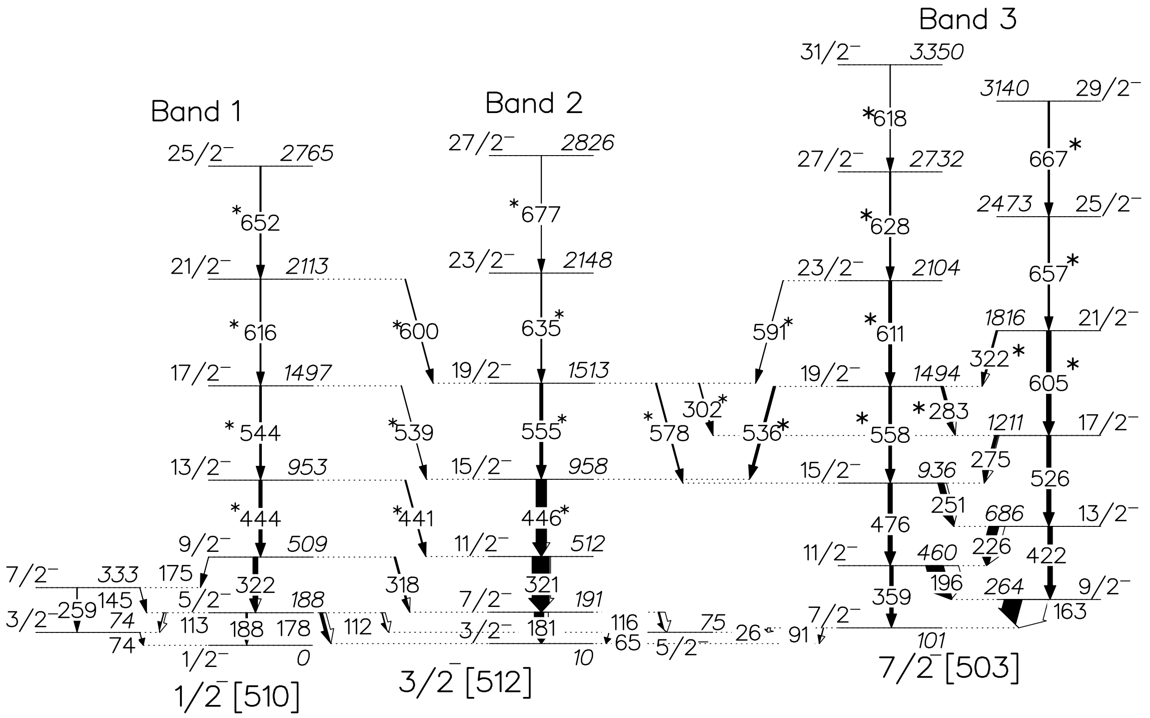

Figure 6.1: Negative parity states of level scheme of ^{187}Os, proposed from the present work. The width of the transitions are proportional to their intensity and new γ transitions are marked by asterisks(*)

Table 6.1: List of γ rays belonging to negative parity bands of ^{187}Os with their energies (E_γ) and intensities (I_γ). The placement of these γ rays in the level scheme are denoted by the energy (E_i) and spin-parity (I_i^π) of the decaying state. The measured values of R_{DCO} and Δ_{PDCO} along with the adopted multipolarities are also given.

E_γ (keV)	E_i (keV)	I_i^π	I_γ^a	R_{DCO}	Δ_{PDCO}	Multipolarity
25.9(2)	101	7/2⁻	38(12)[1]			(M1+E2)
65.31(2)	75	5/2⁻				(M1+E2)
74.3(2)	74	3/2⁻				(M1+E2)
91.1(2)	101	7/2⁻	1.6(11)[1]			(E2)
112.4(2)	188	5/2⁻	3.9(1)			(M1+E2)
113.3(2)	188	5/2⁻	2.9(3)			(M1+E2)
115.8(2)	191	7/2⁻	8.17(3)	0.49(6)[2]		M1+(E2)

Table 6.1: Continued....

E_γ (keV)	E_i (keV)	I_i^π	I_γ^a	R_{DCO}	Δ_{PDCO}	Multipolarity
145.3(2)	333	$7/2^-$	0.46(6)			(M1+E2)
162.9(2)	264	$9/2^-$	100.0(18)	0.62(3)[3]	-0.06(4)	M1+E2
175.4(2)	509	$9/2^-$	0.57(8)			(M1+E2)
177.8(2)	188	$5/2^-$	16.8(2)	0.76(4)[4]		M1+(E2)
181.0(2)	191	$7/2^-$	54.7(2)	0.93(3)[2]	0.13(10)	E2
187.7(2)	188	$5/2^-$	6.5(2)	0.99(7)[4]		E2
196.4(2)	460	$11/2^-$	99.9(16)	0.58(3)[5]	-0.07(5)	M1+E2
225.6(2)	686	$13/2^-$	57.0(16)	0.48(2)[6]	-0.14(9)	M1+E2
250.6(2)	936	$15/2^-$	34.1(8)	0.52(3)[3]	-0.11(8)	M1+E2
259.1(2)	333	$7/2^-$	3.11(4)			(E2)
275.2(2)	1211	$17/2^-$	19.1(10)	0.59(4)[5]	-0.06(2)	M1+E2
282.6(2)	1494	$19/2^-$	4.0(2)	0.60(6)[5]		M1+(E2)
302.2(2)	1513	$19/2^-$	3.9(1)	0.62(9)[5]		M1+(E2)
318.1(2)	509	$9/2^-$	7.7(10)	0.67(7)[7]	-0.17(14)	M1+E2
321.3(2)	512	$11/2^-$	100(1)	0.95(2)[2]	0.13(5)	E2
321.6(2)	509	$9/2^-$	26.0(5)	1.01(3)[8]	0.17(11)	E2
321.9(2)	1816	$21/2^-$	8.2(13)	0.53(7)[5]		M1+(E2)
359.3(2)	460	$11/2^-$	18.8(5)	1.03(7)[5]	0.11(8)	E2
421.9(2)	686	$13/2^-$	26.8(5)	0.92(5)[6]	0.09(8)	E2
440.8(2)	953	$13/2^-$	6.4(2)	0.69(2)[9]	-0.15(12)	M1+E2
443.5(2)	953	$13/2^-$	18.0(15)	0.93(9)[8]	0.18(14)	E2
445.8(2)	958	$15/2^-$	58.6(8)	1.07(4)[9]	0.10(5)	E2
476.3(2)	936	$15/2^-$	24.5(8)	1.03(7)[10]	0.09(4)	E2
525.8(2)	1211	$17/2^-$	24.2(4)	1.07(5)[3]	0.12(7)	E2
536.1(2)	1494	$19/2^-$	14.0(6)	1.04(9)[10]	0.17(13)	E2
539.4(2)	1497	$17/2^-$	2.1(1)	0.70(10)[2]	-0.11(5)	M1+E2
544.4(2)	1497	$17/2^-$	10.0(3)	1.04(12)[8]	0.17(13)	E2

Table 6.1: Continued....

E_γ (keV)	E_i (keV)	I_i^π	I_γ^a	R_{DCO}	Δ_{PDCO}	Multipolarity
555.4(2)	1513	$19/2^-$	17.4(4)	0.99(7)[9]	0.14(8)	E2
557.7(2)	1494	$19/2^-$	16.2(4)	0.98(10)[3]	0.12(7)	E2
577.7(2)	1513	$19/2^-$	6.9(3)	1.04(14)[5]	0.13(11)	E2
591.3(2)	2104	$23/2^-$	1.9(2)			(E2)
599.5(2)	2113	$21/2^{(-)}$	4.1(4)	0.57(13)[2]		M1+(E2)
604.5(2)	1816	$21/2^-$	26.3(5)	1.02(7)[3]	0.09(6)	E2
610.5(2)	2104	$23/2^-$	17.3(4)	1.00(10)[3]	0.16(11)	E2
616.0(2)	2113	$21/2^{(-)}$	<5.72	1.10(13)[4]		(E2)
618.0(2)	3350	$31/2^-$	2.6(2)	1.02(12)[11]	0.11(10)	E2
627.9(2)	2732	$27/2^-$	7.6(3)	1.03(16)[5]	0.22(12)	E2
635.0(2)	2148	$23/2^-$	5.2(2)	1.04(10)[5]	0.14(12)	E2
652.0(2)	2765	$25/2^{(-)}$	<6.72(11)	1.02(13)[4]		(E2)
657.1(2)	2473	$25/2^-$	8.8(2)	0.98(4)[3]	0.19(13)	E2
667.1(2)	3140	$29/2^-$	8.7(2)	0.91(14)[6]	0.19(16)	E2
677.2(2)	2826	$27/2^{(-)}$	1.6(1)	1.07(21)[5]		E2

[1] From LEPS data, not normalized to clovers

[2] From the 446-keV (E2) gate.
[3] From the 422-keV (E2) gate.
[4] From the 322-keV (E2) gate.
[5] From the 476-keV (E2) gate.
[6] From the 526-keV (E2) gate.
[7] From the 444-keV (E2) gate.
[8] From the 188-keV (E2) gate.
[9] From the 181-keV (E2) gate.
[10] From the 610-keV (E2) gate.
[11] From the 628-keV (E2) gate.

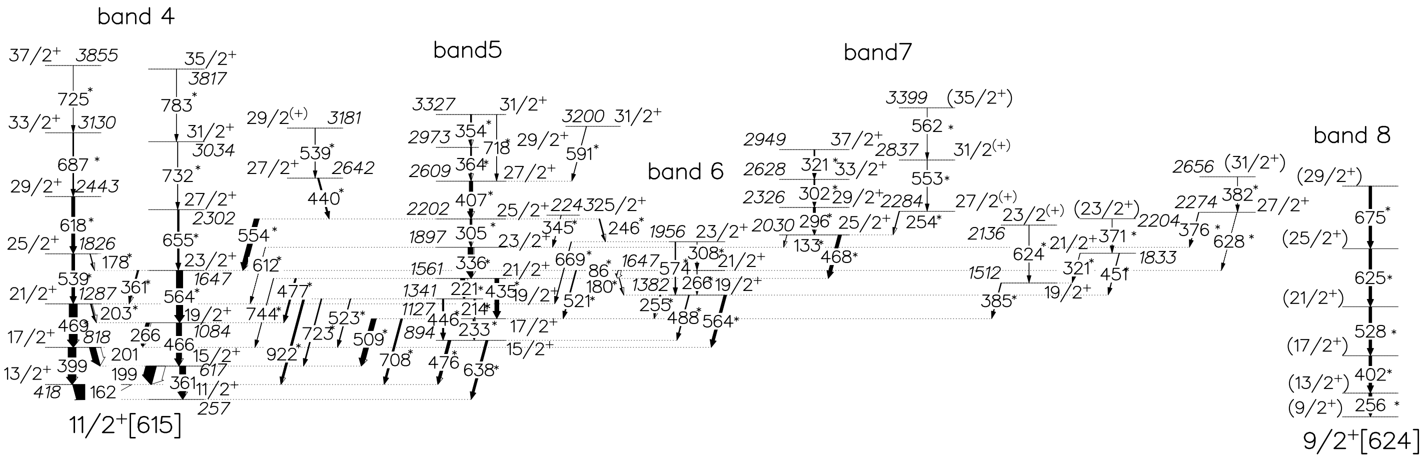

Figure 6.2: Positive parity states of level scheme of ^{187}Os, proposed from the present work. The width of the transitions are proportional to their intensity and new γ transitions are marked by asterisks(*)

6.2 Experimental Results

The proposed negative and positive parity parts of the level scheme of ^{187}Os, as obtained using coincidence relation and intensity argument is shown in Fig. 6.1 and 6.2. The experimental γ-ray transition energies (E_γ), the level energies (E_i), the spins and parities of the initial (I_i^π) levels, the R_{DCO} and Δ_{PDCO} values along with the adopted multipolarities of the γ-rays belong to the negative and positive parity parts have been tabulated in Table. 6.1 and Table. 6.2. A total of 94 new γ ray transitions have been identified for the first time and are placed in the level scheme. These are marked by asterisks (*) in the level schemes. All the bands have been extended upto first pair alignment.

The relative intensities of the γ rays were measured from different single and double-gated spectra to remove contamination from similar γ ray energies of other bands in ^{187}Os as well as γ rays coming from the other nuclei produced in this reaction. All the intensities quoted in the above table are after proper normalization.

Table 6.2: List of γ rays belonging to positive parity bands of ^{187}Os with their energies (E_γ) and intensities (I_γ). The placement of these γ rays in the level scheme are denoted by the energy (E_i) and spin-parity (I_i^π) of the decaying state. The measured values of R_{DCO} and Δ_{PDCO} along with the adopted multipolarities are also given.

E_γ (keV)	E_i (keV)	I_i^π	I_γ^a	R_{DCO}	Δ_{PDCO}	Multipolarity
86.4(2)	1647.3	$21/2^+$	1.22(1)			(M1+E2)
132.8(2)	2029.9	$25/2^+$	0.21(1)			(M1+E2)
162.4(2)	418.4	$13/2^+$	100.0(9)	0.41(1)[1]		M1+E2
178.5(2)	1825.6	$25/2^+$	1.09(4)	0.44(6)[1]		M1+E2
179.9(2)	1561.4	$21/2^+$	0.96(7)			(M1+E2)
199.1(2)	617.4	$15/2^+$	37.6(3)	0.49(1)[2]		M1+E2
200.8(2)	817.7	$17/2^+$	21.9(6)	0.68(2)[3]		M1+E2
203.0(2)	1286.5	$21/2^+$	4.11(13)	0.47(5)[1]	-0.25(16)	M1+E2
214.1(2)	1340.5	$19/2^+$	4.23(4)	0.61(7)[4]	-0.13(11)	M1+E2
220.9(2)	1561.4	$21/2^+$	15.92(2)	0.73(4)[4]	-0.06(4)	M1+E2
232.7(2)	1126.5	$17/2^+$	5.80(1)	0.59(3)[5]	-0.15(10)	M1+E2
246.4(2)	2202.1	$25/2^+$	2.6(1)	0.72(8)[6]		M1+E2
253.9(2)	2283.8	$27/2^{(+)}$	1.71(4)	0.84(11)[7]		M1+E2
254.8(2)	1381.6	$19/2^+$	3.66(9)	0.54(5)[8]	-0.14(10)	M1+E2
265.9(2)	1647.3	$21/2^+$	1.29(4)	0.67(11)[8]	-0.07(5)	M1+E2
266.3(2)	1083.9	$19/2^+$	13.2(3)	0.48(1)[1]	-0.11(6)	M1+E2
296.3(2)	2326.2	$29/2^+$	7.6(5)	0.90(10)[8]	0.24(13)	E2
301.8(2)	2628.0	$33/2^+$	4.0(4)	0.95(5)[7]	0.17(10)	E2
305.3(2)	2202.1	$25/2^+$	6.01(7)	0.75(10)[1]	-0.18(10)	M1+E2
308.5(2)	1955.5	$23/2^+$	1.06(5)	0.69(10)[8]		M1+E2

Table 6.2: Continued....

E_γ (keV)	E_i (keV)	I_i^π	I_γ^a	R_{DCO}	Δ_{PDCO}	Multipolarity
320.8(2)	1832.6	$21/2^+$	0.90(14)			(M1+E2)
321.1(2)	2949.1	$37/2^+$	3.5(4)	$1.00(9)^{7}$	0.23(11)	E2
335.7(2)	1897.4	$23/2^+$	18.3(7)	$0.66(5)^{1}$	-0.14(10)	M1+E2
345.4(2)	2242.8	$25/2^+$	1.27(2)	$0.51(7)^{5}$	-0.17(11)	M1+E2
353.6(2)	3327.0	$31/2^+$	3.70(2)	$0.67(11)^{5}$	-0.23(11)	M1+E2
360.9(2)	1647.0	$23/2^+$	4.74(19)	$0.52(4)^{1}$	-0.13(8)	M1+E2
361.0(2)	617.4	$15/2^+$	21.3(2)	$0.88(6)^{9}$	0.09(8)	E2
363.8(2)	2973.3	$29/2^+$	3.89(4)	$0.52(6)^{5}$	-0.14(9)	M1+E2
371.3(2)	2203.9	$(23/2^+)$	0.80(2)			(M1+E2)
376.5(2)	2274.4	$27/2^+$	1.88(3)	$0.91(12)^{5}$	0.15(12)	E2
381.8(2)	2656.2	$(31/2^+)$	0.55(2)			(E2)
385.4(2)	1511.9	$19/2^+$	2.5(2)	$0.50(4)^{8}$	-0.20(9)	M1+E2
399.0(2)	817.7	$17/2^+$	27.7(2)	$0.99(4)^{9}$	0.22(5)	E2
407.3(2)	2609.4	$27/2^+$	11.6(2)	$0.65(9)^{5}$	-0.09(7)	M1+E2
434.9(2)	1561.4	$21/2^+$	14.5(2)	$0.93(6)^{4}$	0.26(9)	E2
440.3(2)	2642.4	$27/2^+$	5.1(2)	$0.63(6)^{5}$	-0.17(10)	M1+E2
446.5(2)	1340.5	$19/2^+$	5.5(1)	$0.83(9)^{7}$	0.15(9)	E2
451.0(2)	1832.6	$21/2^+$	2.17(2)	$0.54(15)^{8}$	-0.14(11)	M1+E2
466.5(2)	1083.9	$19/2^+$	18.9(9)	$1.0(2)^{9}$	0.12(7)	E2
468.2(2)	2029.9	$25/2^+$	11.8(5)	$1.01(11)^{2}$	0.13(11)	E2
468.9(2)	1286.5	$21/2^+$	29.0(5)	$1.00(4)^{1}$	0.09(3)	E2
475.7(2)	893.8	$15/2^+$	9.8(1)	$0.53(5)^{5}$	-0.09(6)	M1+E2
476.9(2)	1561.4	$21/2^+$	5.5(8)	$0.62(6)^{1}$	-0.16(11)	M1+E2
488.3(2)	1381.6	$19/2^+$	3.35(9)	$1.03(10)^{6}$	0.24(12)	E2
508.9(2)	1126.5	$17/2^+$	13.7(10)	$0.58(2)^{5}$	-0.11(7)	M1+E2
520.6(2)	1647.3	$21/2^+$	3.8(1)	$0.98(8)^{8}$	0.22(12)	E2
523.0(2)	1340.5	$19/2^+$	2.6(2)	$0.62(11)^{4}$	-0.14(12)	M1+E2

Table 6.2: Continued....

E_γ (keV)	E_i (keV)	I_i^π	I_γ^a	R_{DCO}	Δ_{PDCO}	Multipolarity
538.7(2)	3181.1	$29/2^{(+)}$	0.65(3)	0.62(8)[5]		M1+E2
539.0(2)	1825.6	$25/2^+$	10.8(3)	1.00(4)[1]	0.11(4)	E2
553.1(2)	2836.9	$31/2^{(+)}$	1.15(8)	0.91(10)[7]		E2
554.3(2)	2202.1	$25/2^+$	17.0(2)	0.79(5)[1]	-0.19(11)	M1+E2
562.2(2)	3399.1	$(35/2^+)$	0.44(6)			(E2)
563.5(2)	1647.0	$23/2^+$	23.1(2)	0.92(2)[2]	0.08(4)	E2
563.7(2)	1381.6	$19/2^+$	9.7(2)	0.42(3)[6]	-0.12(8)	M1+E2
573.9(2)	1955.5	$23/2^+$	3.0(1)	1.02(11)[1]	0.22(13)	E2
590.6(2)	3200.0	$31/2^+$	1.49(3)	1.08(15)[5]	0.19(8)	E2
611.8(2)	1897.4	$23/2^+$	0.19(2)			(M1+E2)
617.6(2)	2443.2	$29/2^+$	12.0(2)	1.05(8)[1]	0.19(5)	E2
624.5(2)	2136.4	$23/2^{(+)}$	1.30(3)	0.96(15)[8]		E2
627.6(2)	2274.4	$27/2^+$	0.27(2)			(M1+E2)
637.7(2)	893.8	$15/2^+$	8.5(1)	0.93(6)[5]	0.22(10)	E2
654.6(2)	2301.9	$27/2^+$	6.0(1)	0.95(5)[2]	0.15(6)	E2
668.7(2)	1955.5	$23/2^+$	2.14(5)	0.69(11)[8]		M1+E2
686.6(2)	3129.8	$33/2^+$	3.7(1)	1.00(11)[1]	0.19(9)	E2
708.0(2)	1126.5	$17/2^+$	7.1(1)	0.91(4)[5]	0.18(10)	E2
717.8(2)	3327.0	$31/2^+$	0.82(1)	0.92(19)[5]		E2
722.9(2)	1340.5	$19/2^+$	3.55(2)	0.94(11)[4]	0.24(9)	E2
725.1(2)	3854.9	$37/2^+$	0.58(4)	1.10(14)[1]		E2
732.2(2)	3034.1	$31/2^+$	1.5(1)	1.02(17)[2]	0.29(17)	E2
743.8(2)	1561.4	$21/2^+$	1.4(2)	1.04(14)[1]		E2
783.3(2)	3817.4	$35/2^+$	0.50(6)	0.90(16)[2]		E2
922.0(2)	1340.5	$19/2^+$	7.2(1)	0.99(7)[7]	-0.05(3)	M3+E4

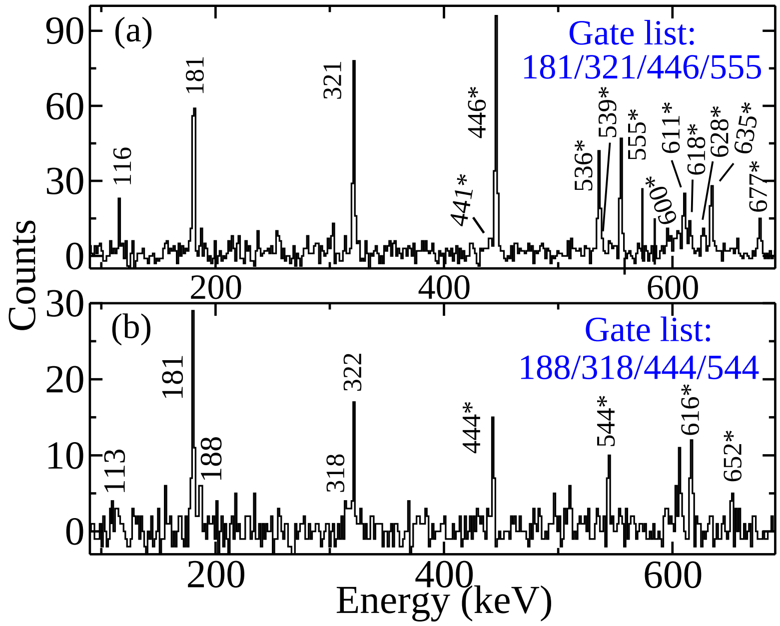

Figure 6.3: Double gated spectra of gatelist of (a) 181, 321, 446, 555 keV and (b) 188, 318, 444, 544 keV transitions in band 2 and 1, respectively. Newly observed transitions are marked by (*).

6.2.1 Bands 1 and 2

The spin and parity of the band heads of bands 1 and 2 were assigned as $1/2^-$ and $3/2^-$ and were known upto the level energy at 509 keV and 511 keV, respectively, from the previous work of Sodan et al. [7]. However, the levels at 509 keV, 511 keV and the low lying level 341 keV were tentatively placed in the level scheme. In the present analysis bands 1 and 2 have been extended upto the excitation energies of 2765 and 2826 keV and angular momentum of $25/2^-$ and $27/2^-$, respectively. The tentatively placed 509-keV level of band 1 has been confirmed in the present analysis. All the γ rays of band 1 along with the newly observed transitions are shown in the double gated spectra of Fig. 6.3. The spin and parity for most of the levels of band 1 have been assigned using R_{DCO} and Δ_{PDCO} measurements of the decaying γ rays.

[1]From the 399-keV (E2) gate.
[2]From the 466-keV (E2) gate.
[3]From the 539-keV (E2) gate.
[4]From the 361-keV (E2) gate.
[5]From the 435-keV (E2) gate.
[6]From the 574-keV (E2) gate.
[7]From the 468-keV (E2) gate.
[8]From the 708-keV (E2) gate.
[9]From the 539-keV (E2) gate.

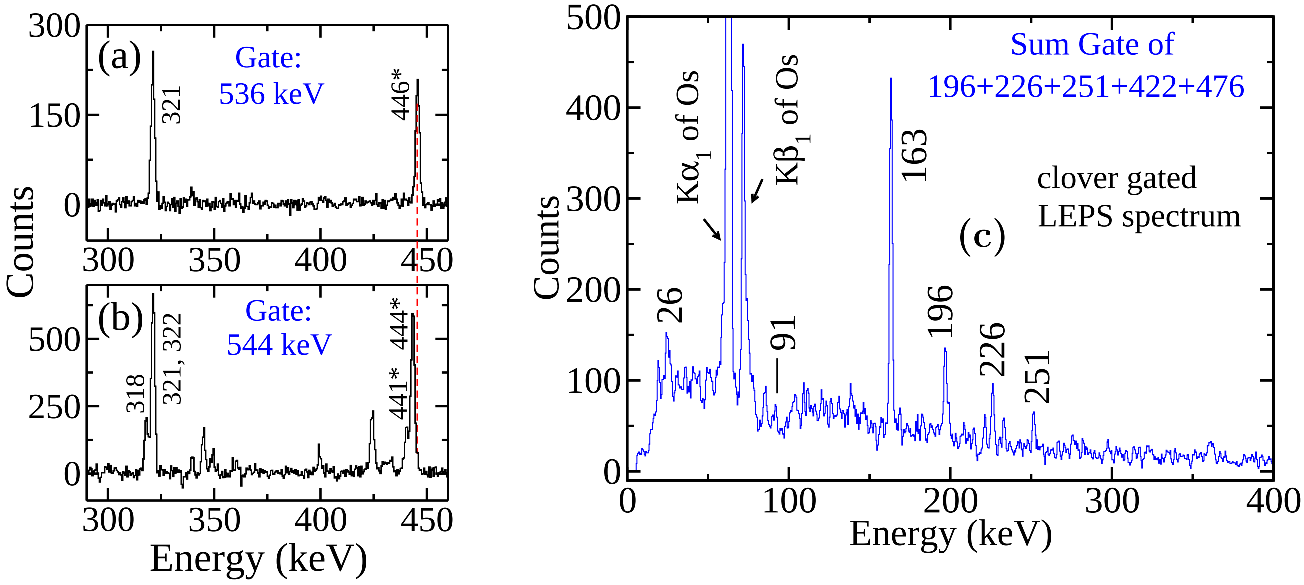

Figure 6.4: Coincidence spectra gated by (a)536-keV and (b) 544-keV showing the closely lying gamma rays of band 2 and 1. (c) Clover gated LEPS spectrum projected from clover vs. LEPS γ-γ matrix. Projection of the sum gate of 196, 226, 251, 422, and 476 keV in LEPS detector shows the low energy 26 keV transition. The new γ-rays are marked by asterisks (*).

Similarly, the tentatively placed level 511 keV in band 2 has been confirmed but the 341 keV level has not been seen in the present analysis. The double gate on the gamma rays of band 2 established the newly observed transitions of band 2 and also the connections between bands 3 and 2 as shown in Fig. 6.3. In the present analysis, the closely spaced tentative levels of 511 and 509 keV could be separated. In Fig. 6.4 the spectra with single gate on 536 and 544 keV are shown. The 444-keV and the 446-keV lines, which decays to 509-keV and 511-keV levels, are clearly seen as separate γ rays. The 441-keV line is also seen in the 544-keV gate but not in the 536-keV gate. Both 321- and 322-keV lines are seen in these two gated spectra, but the 318-keV line is seen only in the 536-keV gate. This again confirms the two seperate levels at 509 keV and 511 keV. Similarly, the other closely spaced levels could be separated out by appropriate gating transitions.

6.2.2 Band 3

The low-lying states in band 3 were known from earlier works and the $7/2^-[503]$ configuration of the $7/2^-$ band head at 101 keV was proposed by S. G. Malmskog et al.[11]. This configuration

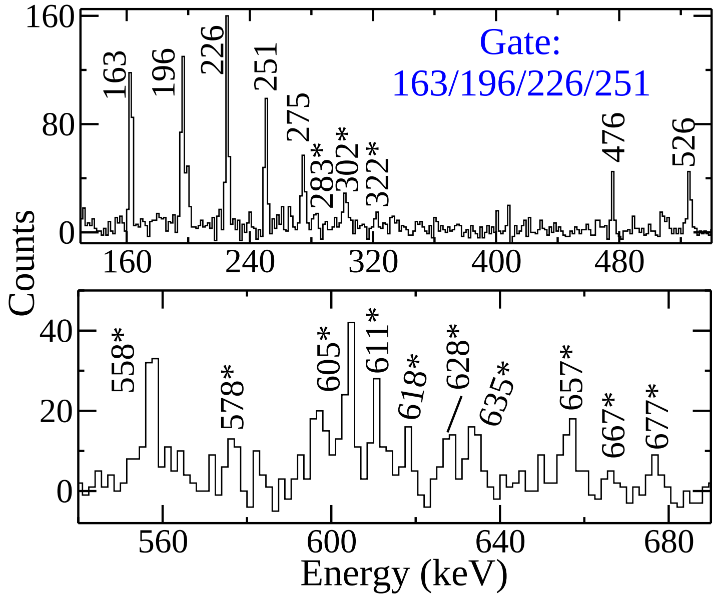

Figure 6.5: Double gated spectra coresponding to gate list of 163, 196, 226, 251 keV of band 3 from γ-γ-γ cube. new γ rays are marked by asterisks (*).

has been adopted in the later works as well [7, 12]. The decay transitions from this level, was however, could not be observed in all earlier works as they are of low energies and highly converted (large electron conversion coefficient, α_T) transitions of energy 26 keV and 91 keV. A good estimate of their total intensity, γ-ray intensity and α_T have been given by Harmatz et al.[13]. It was reported that the total transition intensity of 91-keV is about two orders of magnitude less than the 26-keV one [13]. In the present work, the low-energy, 26-keV γ ray could be observed in the LEPS detector, as shown in Fig.Fig. 6.4(c). This spectrum is a projection from the LEPS vs. clover matrix with sum gates (put on the clovers) on the strong transitions in band 3. The 91-keV line is also seen, albeit very low counts, in this spectrum. The γ-ray branching ratio of the 26-keV, M1 and the 91-keV, E2 transitions has been obtained as 96 : 4 in the present work, which is in good agreement with the values reported by Harmatz et al. (94.5 : 5.5) and the value (95.5 : 4.5) quoted in Ref.[14].

The band 3 of band head spin and parity $7/2^-$ was reported upto 1211 keV level. Even the 1211 keV level was tentatively placed with a tentative gamma ray of energy 526 keV [7]. In the present analysis the band 3 has been extended upto the excitation energy of 3350 keV of angular momenum $31/2\hbar$. The tentatively placed gamma ray of energy 526 keV has been confirmed in the double gated spectra of 163, 196, 226 and 251 keV as shown in Fig. 6.5. All

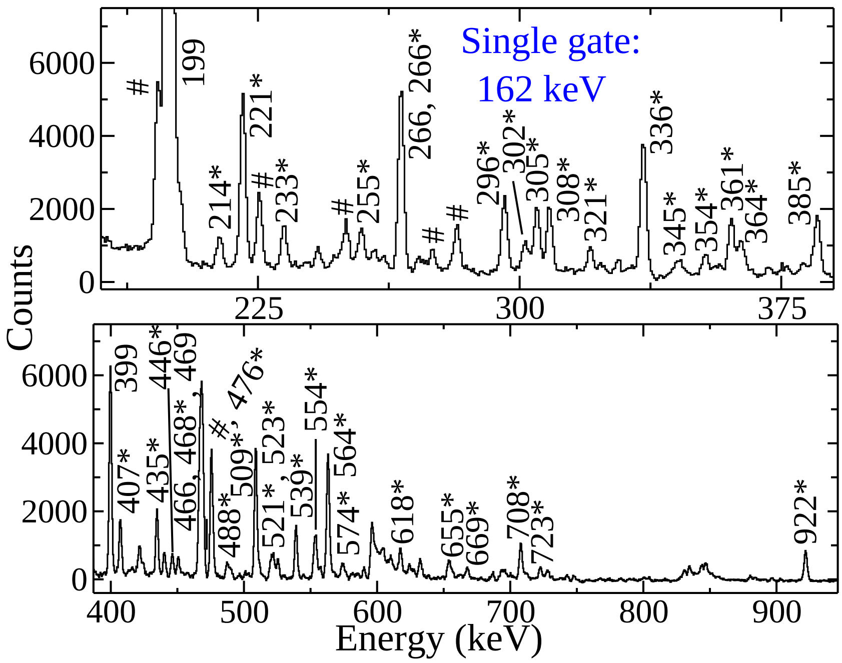

Figure 6.6: Single-gated (162 keV of band 4) spectrum projected from γ-γ matrix. New γ rays are marked by asterisks (*) and the contaminant γ rays are marked by #.

the new transitions of band 3 and the connecting transitions between band 2 and 3, shown in Fig. 6.5, are marked by asterisks (*).

6.2.3 Bands 4, 5, 6, 7 and 8

The single gated spectrum in the gate on an earlier known 162 keV transition shows most of the already known transitions in band 4 and the new gamma rays belonging to the band 5 and 6 as shown in Fig. 6.6. The band 4, based on the $\nu i_{13/2}$ configuration with band head spin and parity at $11/2^+$ was known upto the excitation energy at 1084 keV by Sodan et al. [7]. In the present experiment, the band 4 has been extended upto the the excitation energy of 3855 keV (upto first particle alignment). All the new γ rays of band 1 have been confirmed in the sum double-gated spectra shown in Fig. 6.7 with gates put on a few low-lying gammas in the two signature partners. The spin and parity of the new levels of band 4 have been assigned using the DCO ratio and polarisation asymmetry measurement of the newly observed gamma rays of band 4.

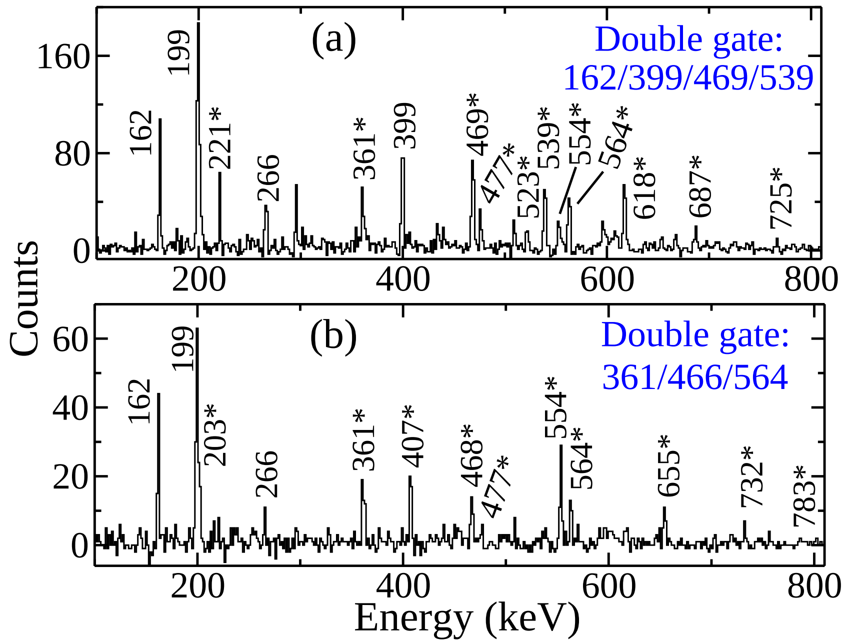

Figure 6.7: Double gated spectra coresponding to gate list of 162, 399, 469, 539 keV and 361, 466, 564 of band 4 from γ-γ-γ cube. New γ rays are marked by asterisks (*).

The band 5 has been newly observed in the present analysis. Most of the new transitions along with the new connecting transitions between band 4 and 5 have been confirmed in the single gated spectrum of 162 keV (Fig. 6.6) and also double gates on already known transitions of positive parity main band (Fig. 6.7). The band 5 has been extended upto the excitation energy of 3327 keV and the new intra and inter-band γ rays of band 5 have been confirmed in the single gate of a new 221 keV transition (Fig. 6.8). The band head spin and parity has been assigned as $15/2^+$ from the DCO ratio and polarisation asymmetry measurements of 638 and 476 keV transitions from 435 keV (pure E2) gated spectrum. The multipolarity of the new cross-over transition 435 keV, has been confirmed from the DCO ratio measurement in a previously known pure E2 (361 keV) gate and the type of 435 keV has been confirmed as the electric from the polarisation asymmetry measurement.

A new band 6 has been observed for the first time in the present analysis, with band head spin and parity $19/2^+$. Most of the inter-band transitions of band 6 and cross-over 574 keV transition have been confirmed in the single gate of 162 keV (Fig. 6.6). The multipolarity of newly observed 574 keV cross-over transition (pure E2) can be obtained using DCO ratio measurement in already known E2 gate at 399 keV and the electric nature has been confirmed form the polarisation asymmetry measurement. The band head spin and parity of band 6

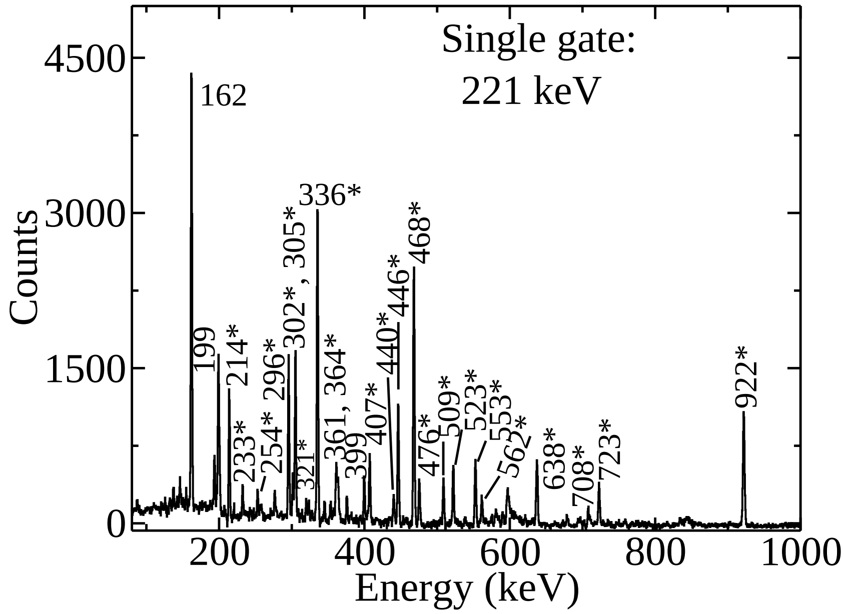

Figure 6.8: Single gate of 221 keV of band 6 from γ-γ matrix. New γ rays are marked by asterisks (*).

have been confirmed from the measurement of multipolarity and nature of the decaying 488 keV transition. This transition can be confirmed as a pure E2 in the DCO gate of 574 keV transition. All the inter and intra-band transitions of band 6 have been shown in the sum-gate of 246 and 308 keV transitions (Fig. 6.9(a)).

The band 7 has been found for the first time in the present analysis at an excitation energy of 2030 keV and band head spin and parity $25/2^+$. This band head spin- parity of this band has been assigned from the DCO and polarisation asymmetry measurement of the 468 keV transition. The E2 nature of the 468 keV transition has been obtained from the 466 keV pure E2 DCO gate and polarisation asymmetry measurement. The new γ rays of band 7 have been shown in the single gate of 221 keV (Fig. 6.8).

Another sequence of gamma rays (band 8) have been found from the present analysis which are in coincidance with each other as shown in Fig. 6.9(b) but the connection between this band structure with any other bands in ^{187}Os has not been observed yet. Therefore, the band head excitation energy and spin-parity is not possible to fix. It has been also checked that this sequence of gamma rays are not present in the neighbouring iostopes which are populated in this reaction.

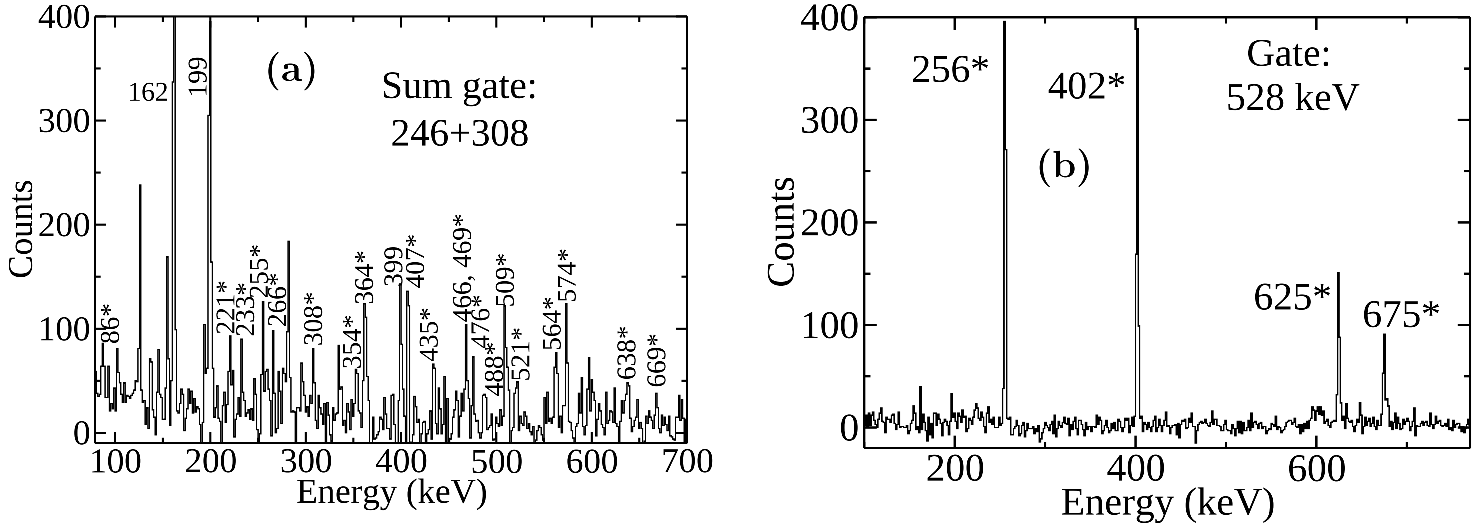

Figure 6.9: (a) Sum gate of 246 and 308 keV of band 6 from γ-γ matrix. (b) Single gate of 528 keV of band 8 from γ-γ-γ cube. New γ rays are marked by asterisks (*).

6.3 Discussions

The rotational bands based on $1/2^-$, $3/2^-$ and $7/2^-$ states of ^{187}Os indicate the occupation of odd-neutron in the single particle orbitals of $2f_{5/2}$, $3p_{3/2}$ and $1h_{9/2}$, respectively. The first excited state $3/2^-$, is an isomeric state [12], corresponding to the $\nu p_{3/2}$ orbital lying close to the neutron Fermi level. The $7/2^-$ state, corresponding to the odd-neutron in Ω=$7/2^-$ Ω component of $\nu h_{9/2}$ orbital, is an isomeric state in the Os isotopes [12]. Various deformed rotational bands in ^{187}Os isotopes could be understood from the coupling of the odd neutron with even-even gamma deformed ^{186}Os core [5].

The aligned angular momenta of the unpaired nucleon along the rotational axis (x) is obtained, in the cranked shell model [15], by substractting the rotational aligned angular momentum of reference configuration from the total aligned angular momentum $I_x(=\sqrt{I(I+1)-K^2})$ of the nucleus. Rotational alignments as a function of rotational frequencies of different bands in ^{187}Os have been done to understand the nature of the bands. In case of odd mass nuclei, the neighbouring even-even nucleus is considered as reference and the Harris parameter of j$_0$=$20\hbar^2 MeV^{-1}$ and j$_1$=$94\hbar^4 MeV^{-3}$ of the reference ^{186}Os can be obtained from the fitting of the ground state rotational band [5], as shown in Fig. 6.10(a).

The nearly degenerate bands 1 and 2 along with their signature partners were explained in the frame work of pseudo spin symmetry [9, 10]. Certain Nilsson orbitals with $\Delta\Omega = 1$ and $\Delta\Lambda = 2$ are nearly degenerate and remains parallel as a function of deformation (β_2) [16, 17]. These orbitals like $\Omega[Nn_z\Lambda-2]$ and $\acute{\Omega}[Nn_z\Lambda]$ can be transformed into Pseudo Nilsson quantum number of $\tilde{\Omega}[\tilde{N}\tilde{n_z}\tilde{\Lambda}]$, where $\Omega = (\Lambda-2)+1/2$ and $\acute{\Omega} = \Lambda$-1/2 and the pseudo-Nilsson quantum numbers can be written as $\tilde{N} = N - 1$, $\tilde{\Lambda} = \Lambda - 1$, and $\tilde{\Omega} = \Omega$. Accordingly, the bands 1 and 2 of Nilsson quantum numbers of 1/2[510] and 3/2[512] transform to the pseudo Nilsson quantum numbers of 1/2,3/2[$\tilde{4}\tilde{1}\tilde{1}$]. In this frame work, the two degenerate orbitals obey the relation of $\tilde{\Omega} = (\tilde{\Lambda}+1/2)$ and $\tilde{\Omega} = (\tilde{\Lambda}-1/2)$ similar to the orbitals spliting due to spin orbit interaction in spherical nuclei. The ideal degenerate bands in pseudo-Nilsson frame work follow all the properties of degenerate bands like similar γ-ray energies, closely spaced energy levels etc. Also the separtion between the particle aligned angular momentum will be $1\hbar$ [18] coming from the $\tilde{\Lambda}+1/2$ and $\tilde{\Lambda}-1/2$ of the two bands. In case of band 1 and 2, only one signature has been extended upto first particle alignment. The similar γ rays and level energies at the lower angular momentum for the two degenerate structures of bands 1 and 2 signify these two as twin bands in normal deformed region.

The aligned angular momentum (i_x) as a function of rotational frequency (ω) for the twin bands have been plotted and compared with the similar bands in ^{185}Os [19] as shown in Fig. 6.10(b). Similar large values of crossing frequencies indicate the pair breaking in $\nu i_{13/2}$ in the presence of N=110 deformed shell gap. It can be seen in Fig. 6.10(b), the aligned angular momenta of bands 1 and 2 in ^{187}Os are seperated by $1\hbar$ unit of angular momentum like all other pseudo-Nilsson doublets [20, 21]. The minimum level degeneracy for these two bands are 2-3 keV at lower spins but the degeneracy gets gradually lifted with increasing spin and attains a maximum value of 60 keV for the last known level. The large seperation between the level energies of bands 1 and 2 at higher angular momenta does not hold the twin structures well. Also, connecting transitions have been seen with the other negative parity band 3, which indicate configuartion mixing or structural similarities between band 3 and upper parts of bands 1 and 2.

The band 3, based on $\nu h_{9/2}$ configuration, has been extended upto first particle alignment frequency. This band is similar to the other neighbouring odd-A isotopes with a Nilsson config-

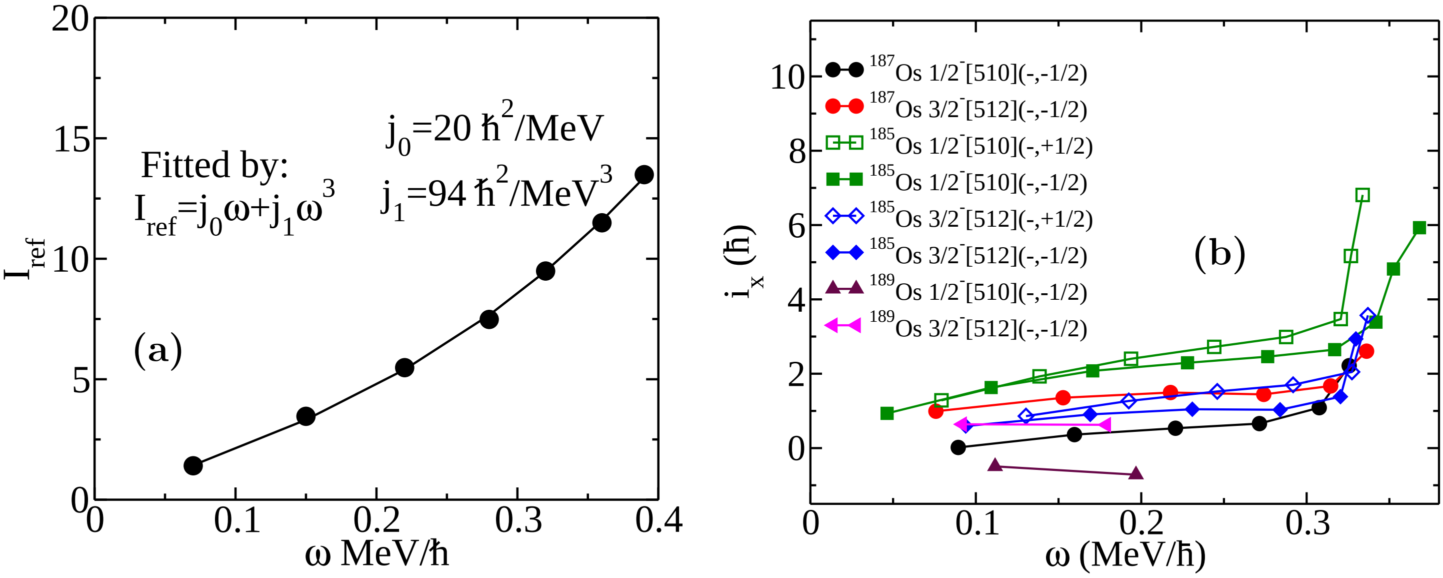

Figure 6.10: (a) Harris parameters (j_0 and j_1) estimated from even-even ^{186}Os ground state rotational band. (b) Aligned angular momentum i_x as a function of rotational frequency (ω) for the twin bands 1 and 2 in ^{185,187,189}Os.

uration of 7/2$^-$[503]. The aligned angular momentum (i_x) as a function of rotational frequency (ω) of the bands based on 7/2$^-$[503] has been plotted for ^{183}Os (N=107) [22], ^{185}Os (N=109) [4], and ^{187}Os (N=111) nuclei as shown in Fig. 6.11(a). The band based on 7/2$^-$[503] in ^{185}Os (neutron number N=109) shows delayed crossing at crossing frequency $\hbar\omega$=0.34 MeV as compared to ^{183}Os (N=107) which has a crossing frequency of $\hbar\omega$=0.23 MeV. The delayed crossing in ^{185}Os has been explained by the existence of N=108 deformed shell gap [4]. But the experimental data on the effect of next deformed shell gap at N=110 on an odd neutron nucleus was absent. As shown in Fig. 6.11(a), ^{187}Os (N=111) has a delayed crossing with a crossing frequency $\hbar\omega$=0.31 MeV. Therefore, the crossing frequency of band 3 in ^{187}Os is delayed compared to ^{183}Os but earlier than ^{185}Os. According to Ngijoi-Yogo et al. [8], the delayed crossings have been observed for the isotopes of Hf and W with neutron number 108 and 110 and crossing frequencies $\sim$ 0.4 MeV has been reported. The smaller crossing frequency for the same isotones in Os nuclei may be due to the the presence of gamma deformation. The energy staggering S(I) of a rotational band can be obtained by S(I)= E(I)-[E(I+1)+E(I-1)]/2 which will give better insight about the nuclear structure. Staggering vs. spin($\hbar$) has been plotted in

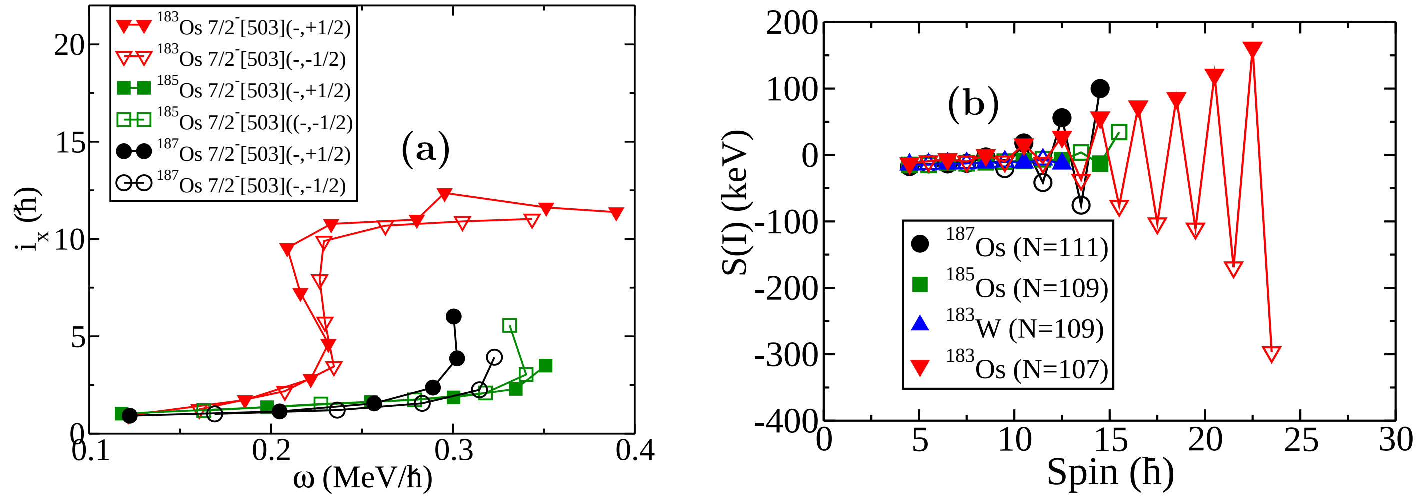

Figure 6.11: (a) Aligned angular momentum i_x as a function of rotational frequency (ω) for the $\nu h_{9/2}$ band in ^{183,185,187}Os. (b) Energy staggering (S(I))) vs. spin ($\hbar$) for the $\nu h_{9/2}$ band in ^{183,185,187}Os and ^{183}W.

Fig. 6.11(b) for different odd-A Os and W isotopes for the same band based on $7/2^-[503]$. All the isotopes show very similar behavior of S(I) with no staggering at lower spin (I). However, at higher spins, they differ for the Os isotopes. ^{183}Os (N = 107) and ^{187}Os (N = 111) have similar (large) staggering after I = 9.5$\hbar$. In case of ^{185}Os (N = 109), the staggering is small and in opposite phase to that of ^{183,187}Os. Data on W isotopes corresponding to the same neutron number are not known at higher spins for comparison. The large signature splitting of band 3 based on high Ω orbital ($\Omega = 7/2$) in ^{187}Os implies the presence of triaxial deformation.

In a triaxial odd-A Os isotope, the odd neutron hole can align along the long axis and generate a stable long-axis rotation of a triaxial core.

The intensity ratios between the ΔI = 1 and ΔI = 2 transitions, can be used to measure the ratio between M1 and E2 transition strengths [B(M1)/B(E2)]. It can be used to get the intrinsic quadruple moments (Q_0) for $11/2^-$ to $21/2^-$ states in band 3 using well known relation of equation 4.1 [23]. In this estimation the g_k value of 0.15 is taken, corresponding to the neutron in $\nu h_{9/2}$ from Ref. [24].

Total Routhian surface calculations (TRS) have also been performed for the configuration of band 3. The TRS plots in the (β_2-γ) plane are shown in Fig. 6.16. A stable triaxial minimum with $\gamma = -100°$ to $-90°$ has been obtained for this configurations and it indicates a stable

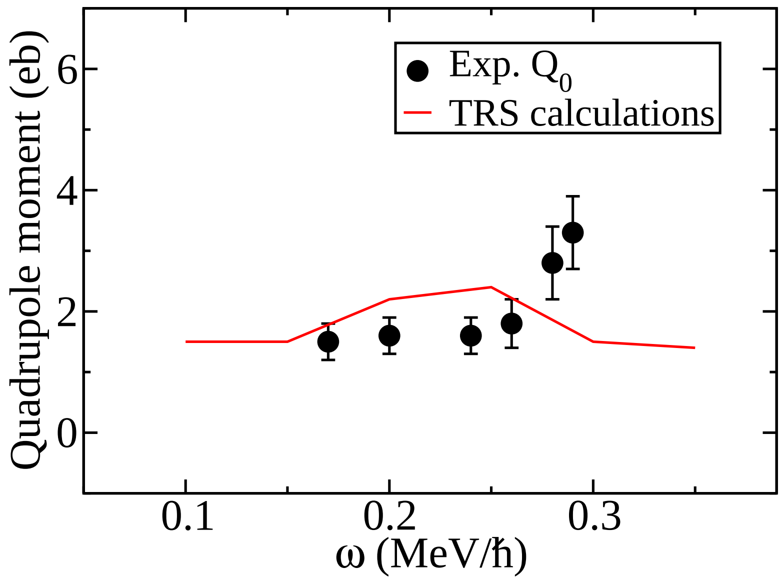

Figure 6.12: Intrinsic quadrupole moments vs rotational frequency (ω) for the $\pi h_{9/2}$ band in ^{187}Os. Experimental valus compared with the results of TRS calculations.

triaxial rotation around long axis (see Fig-2.1). TRS calculations have been performed for different values of rotational frequencies and the (β_2-γ) values corresponding to the minima at each $\hbar\omega$ have been obtained. The theoretical intrinsic quadruple moments can be calculated using these β_2 and γ values from TRS calculations for each $\hbar\omega$ using the equation [25]

$$Q_0 = \frac{6ZA^{2/3}r_\circ^2}{\sqrt{15\pi}}\beta_2(1+0.16\beta_2)\frac{cos(\gamma+30^\circ)}{cos30^\circ} \tag{6.1}$$

. The experimental intrinsic quadruple moments (Q_0) have been plotted with rotational frequencies and compared with the calculated Q_0 as shown in Fig. 6.12. A good agreement of experimental values with the theoratical once confirms the presence of stable long axis rotation in ^{187}Os.

The positive parity main band based on $\nu i_{13/2}$ has also been extended upto the first particle alignment. This band is similar to the $11/2^+$[615] band observed in the neighbouring isotope ^{185}Os [4]. The aligned angular momentum (i_x) as a function of rotational frequency (ω) of this band has been plotted for ^{187}Os (N=111) nucleus and compared with ^{185}Os (N=109) [4] as shown in Fig. 6.13(a). The energy staggering S(I) of the positive parity rotational band has also been plotted and compared with the positive parity band in the neighbouring odd-A ^{185}Os and has been shown in Fig. 6.13(b). The large energy staggering S(I) with spin in both

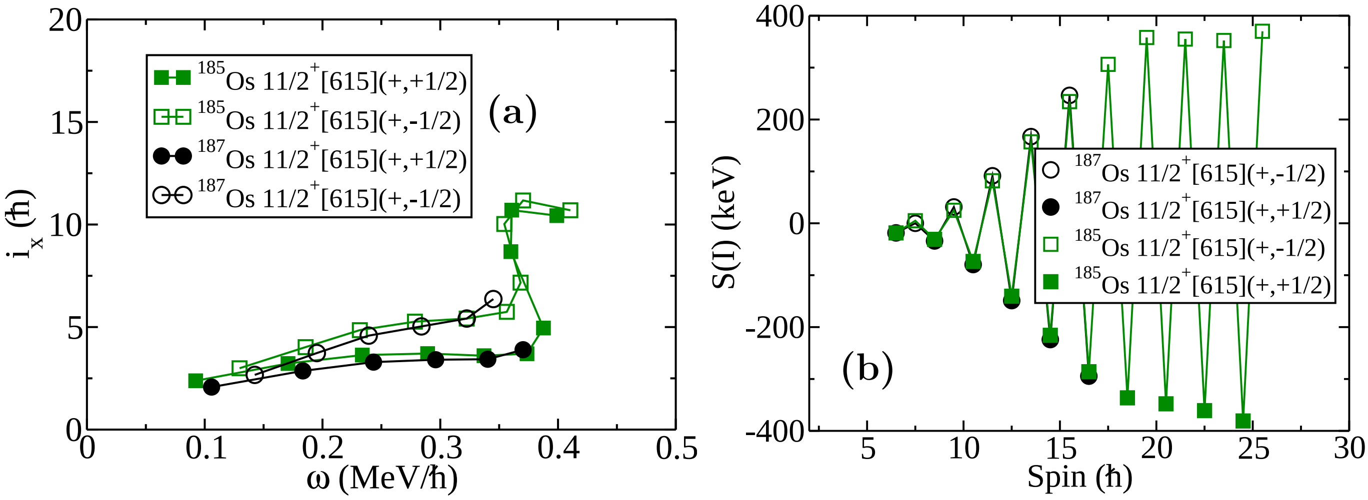

Figure 6.13: (a) Aligned angular momentum i_x as a function of rotational frequency (ω) for the $\nu i_{13/2}$ band in ^{185,187}Os. (b) Energy staggering (S(I)) vs. spin ($\hbar$) for the $\nu i_{13/2}$ band in ^{185,187}Os.

Table 6.3: The systematic comparison of γ and $\gamma\gamma$ band head excitation energies for ^{186,187,188}Os

Nucleus	$K_{1\gamma}$	$E_{1\gamma}$(keV)	$K_{2\gamma}$	$E_{2\gamma}$(keV)	$E_{2\gamma}/E_{1\gamma}$
^{186}Os	2^+	768	4^+	1353	1.76
^{187}Os	$15/2^+$	637	$19/2^+$	1125	1.77
^{188}Os	2^+	633	4^+	1280	2.02

the positive parity bands based on high Ω orbital in ^{185}Os and ^{187}Os can be a menifestation of triaxial nuclear shape.

The band head excitation energies of γ-band and γ-γ band in even-even neighbouring ^{186,188}Os [3, 5] isotopes are mentioned in Table. 6.3. It shows that the band head excitation energy of second 2^+ state of the γ band decreases for heavier Os isotopes. The decrease of band head excitation energy means that the heavier Os isotopes are much more γ deformed as discussed in details at chapter-1. In case of odd-A ^{187}Os, a new γ-band (band 5) and a new γ-γ band (band 6) at the excitation energy of 637 and 1125 keV have been observed with respect to the band head excitation energy of the positive parity main band 4. The generation of γ-band and γ-γ band in ^{187}Os can be represented by a coupling of odd neutron in $11/2^+$[615] orbital with the γ-band and γ-γ band at even-even ^{186}Os. The $11/2^+$ state in positive parity main band

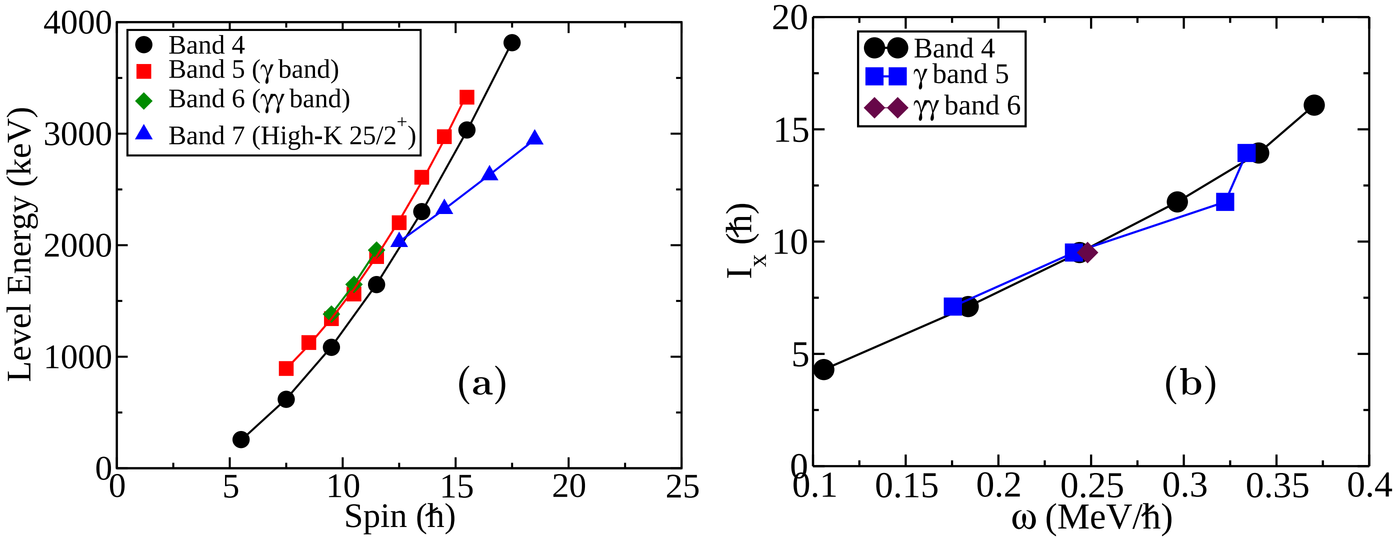

Figure 6.14: (a) Level energy vs. spin ($\hbar$) of the band 4, band 5, band 6 and band 7. (b) Total aligned angular momentum (I_X) vs. rotational frequency (ω)for the band 4, 5, and 6.

in ^{187}Os nucleus couple with the 2^+ and 4^+ state of the γ-band and γ-γ band in ^{186}Os and generate a γ-band and γ-γ band in ^{187}Os. The band head spin and parity of the γ and γ-γ bands are $15/2^+$ and $19/2^+$ respectively as observed in other γ and γ-γ bands in odd A nuclei [26, 27]. The band 5 follows all the signatures of a γ band (disscussed in chapter 1)

- Band 5 is a ΔI = 1 band with regular energy spacing [26].
- The band 5 strongly decays to positive parity main band 4 via M1+E2 and stretched E2 transitions as observed in other γ bands in odd-A nuclei [26, 27].
- The level energy vs angular momentum of positive parity main band, γ-band and γ-γ band have been plotted (Fig. 6.14 (a)) and fitted using second order rotational energy formula of

$$E(I, K) = E_K + A[I(I+1) - K^2] + B[I(I+1) - K^2]^2 \tag{6.2}$$

The inertia parameter A is determined from the fit. The inertia parameter A of positive parity main band, γ-band and γ-γ band are 13.33, 12.28, 10.03 keV respectively. The

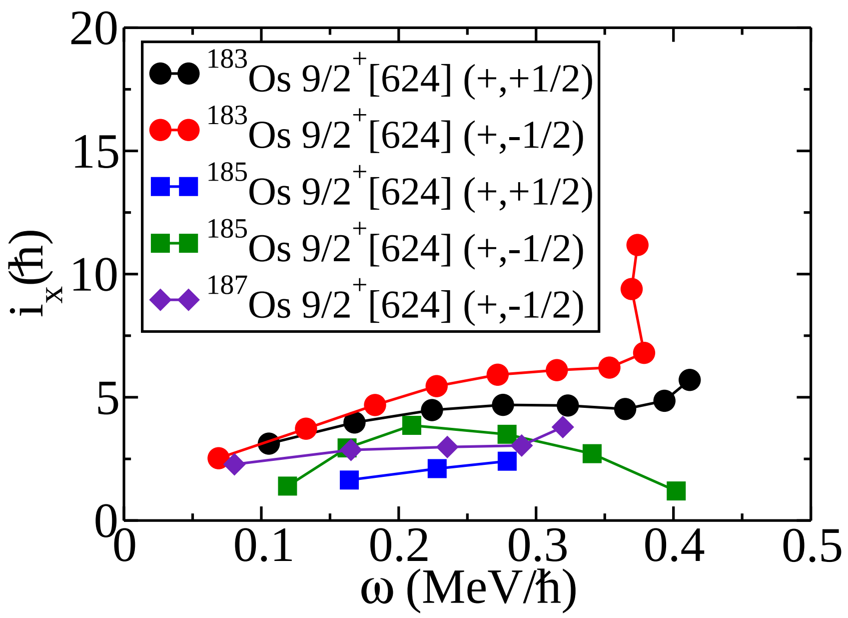

Figure 6.15: Aligned angular momentum i_x as a function of rotational frequency (ω) for the band based on $9/2^+[624]$ configuration in ^{183,185,187}Os.

similar values of inertia parameters of the bands indicate the similar configuration of these two bands.

- Fig. 6.14 (b), shows plots of the Ix (Equation-2.55) vs. rotational frequency for the positive parity main band and γ band. The slopes of the curves are the kinematic moment of inertia. From Fig. 6.14 (b), It can be seen that the slope of the newly observed γ band is similar to the positive parity main band. This is consistent with the expectation of a γ vibrational band.

The non-axial deformation parameter γ can be extracted from the Davydov model [28] using the energy ratio $E_{2_2^+}/E_{2_1^+}$ of the first two 2^+ states for even-even nuclei [25]. In case of ^{187}Os (odd-A), the deformation parameter γ can be extracted using the energy ratio $E_{15/2_2^+}/E_{15/2_1^+}$ of the first two $15/2^+$ states with respect to the band head excitation energy of the positive parity main band using the equation[25]:

$$\frac{E_{15/2_2^+}}{E_{15/2_1^+}} = \frac{1+X}{1-X}, \tag{6.3}$$

where,

$$X = \sqrt{1 - \frac{8}{9} sin^2(3\gamma)} \tag{6.4}$$

in this equation, γ is the non-axial deformation parameter. The deduced γ value for the γ band in ^{187}Os is $|\gamma| \sim 30°$ which agrees well with $\gamma \sim -35°$ obtained from the Total Routhian surface (TRS) calculations for the positive parity configuration (as shown in Fig. 6.17).

Similarly, the band 6 has been identified as a possible candidate of a γ-γ band in ^{187}Os by considering the following signatures

- The expected value of $E_{2\gamma}/E_{1\gamma}$ is 2.0 for two phonon γ vibrational state. In ^{187}Os, the ratio of $E_{19/2_2^+}/E_{15/2_1^+}$ comes out to be 1.77 which is very similar to the known γ-γ band in even-even ^{186}Os [3] as shown in Table. 6.3. The ratio is nearly 2.02 for the heavier ^{188}Os.

- The inertia parameter in case of γ-γ band is, also similar to the main and the γ bands in this nucleus, though it is slightly different than the other two (as shown in Fig. 6.14 (a)). This difference, however, may be due to the presence of hexadecapole deformation with the triaxial shape as reported in this mass region [29, 30].

- The decay out of the γ-γ band in ^{187}Os show similar behaviour as shown by the γ-γ bands in other odd A nuclei [26, 27].

This is the very first observation of γ-γ band in odd-A nucleus in mass 190 region.

Even-even ^{186}Os and ^{188}Os nuclei have positive-parity high-K bands [5, 31]. Similarly, in odd-A ^{187}Os, high-K bands of band-head spin and parity $25/2^+$ has been observed for the first time in the work. The level energy vs. spin of band 7 has been plotted (Fig. 6.14) and compared with the other collective excitations of positive parity main band, γ band and γ-γ band. The small value of inertia parameter A = 6.23 of band 7 (large moment of inertia), suggests that this band build on multi quasi-particle configuration which is differnt from band 4, 5, and 6 and the possible 3-quasiparticle configuration of $\nu(h_{9/2})^2_{8^+} \otimes \nu 9/2^+[624]$.

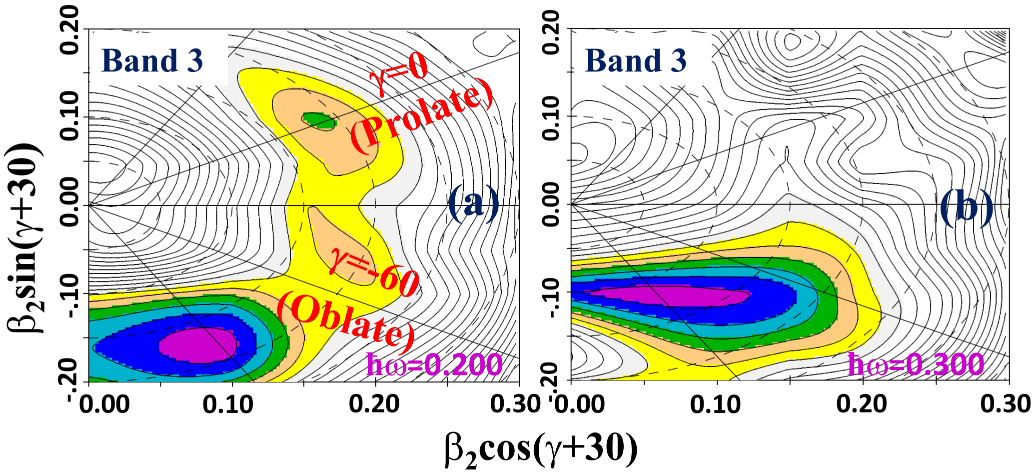

Figure 6.16: 1-qp configuration of $\nu h_{9/2}$ corresponding to the band 3 in ^{187}Os at rotational frquency ($\hbar\omega$) 0.2 (a) and 0.3 (b) MeV

The aligned angular momentum (i_x) as a function of rotational frequency (ω) of the band 8 (band head spin parity $9/2^+$) has been plotted for ^{187}Os (N=111) and compared with the bands based on $9/2^+$[624] configuration in ^{183}Os (N=107) and ^{185}Os (N=109). Similar values of their aligned angular momenta, i_x, as shown in Fig. 6.15, support the configuration assignment of the band 8 as $9/2^+$[624].

6.4 Theoretical Calculations

6.4.1 TRS Calculations

In order to understand the different shapes in ^{187}Os and the effects of the high-j active neutron orbitals (positive and negative) on shapes, the total Routhian surface (TRS) calculations have been performed, as discussed in Chapter 2.5 and 2.6. The formalism of Nazarewicz et al., as depicted in Ref. [32, 33], has been used and the detail technical procedure has been given in Ref. [34] (and references there in). As mentioned before, the deformation of a nucleus for a particular configuration at a particular rotational frequency corresponds to the minimum in the contour plots of the potential energies in β_2 and γ ($\gamma = 0^\circ$ = prolate and $\gamma = -60^\circ$ = oblate) mesh points. The energy minimization on β_4 was done for each value of β_2 and γ. Few TRSs have been calculated for different configurations and at several rotational frequencies

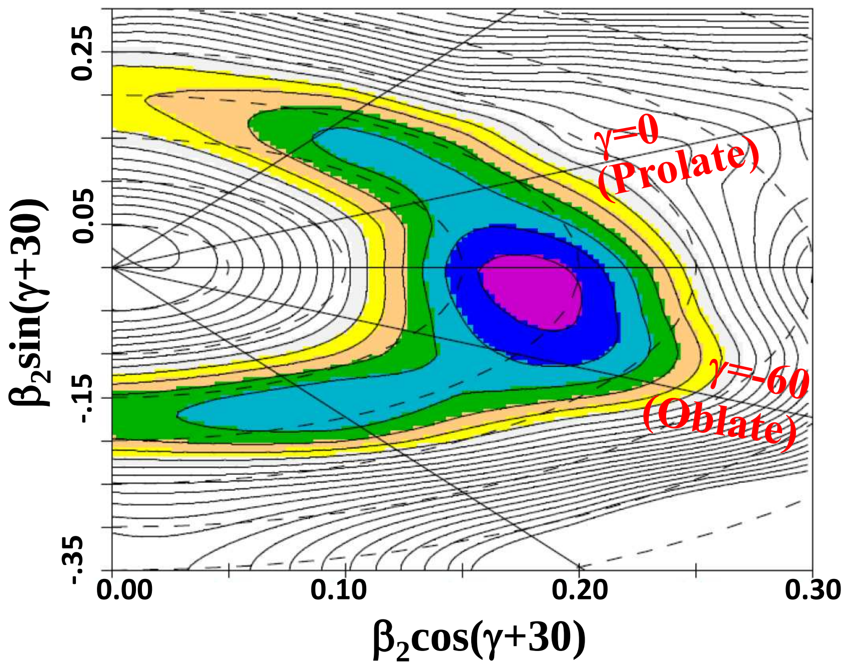

Figure 6.17: 1-qp configuration of $\nu i_{13/2}$ corresponding to the band 4 in ^{187}Os at rotational frquency ($\hbar\omega$) 0.1 MeV

($\hbar\omega$). The TRS calculations, performed for the configuration corresponding to the band 3 in ^{187}Os as shown in Fig. 6.16 for various rotational frequencies ($\hbar\omega$). The Fig. 6.16 show , a stable energy minimum at near-triaxial deformation with $\beta_2 \sim 0.18$ and $\gamma \sim -92°$ and $\beta_2 \sim 0.12$ and $\gamma \sim -90°$ at rotational frequencies $\hbar\omega$= 0.20 and 0.30 MeV, respectively. The triaxial minima at $\gamma \sim -90°$ indicate that the ^{187}Os has rotation axis around the long-axis of the triaxial core.

The TRS calculation was also performed for positive parity band 4 and is shown in Fig. 6.17. A triaxial shape with $\beta_2 \sim 0.18$ and $\gamma \sim -35°$ has been obtained for the positive parity band 4. The triaxial minimum obtained from TRS calculation supported the observation of γ and γ-γ bands couple with positive parity main band.

6.5 Summary

The excited states in ^{187}Os have been studied by γ-ray spectroscopic technique. The reaction ^{186}W(^{4}He,3n)^{187}Os at 36 MeV of beam energy from the K-130 cyclotron at VECC, Kolkata was used to populate the states and the INGA array with 7 Compton-suppressed clover HPGe detectors and one LEPS detector were used to detect the γ-rays. A new and vastly improved level scheme of ^{187}Os with the placement of 94 new γ-ray transitions has been proposed. The pseudo Nilsson doublet bands 1 and 2 have been extended upto first particle alignment and the level degeneracy has been observed to be lifted at higher angular momenta due to the possible presence of nuclear triaxiality. The band based on $\nu h_{9/2}$ has been identified as long-axis rotation of a triaxial nucleus. The positive parity main band has also been extended upto the first particle alignment and new γ-band, γ-γ band, and High-K band have been observed in the present work.

Bibliography

[1] Y. Lee et al., Phys. Rev. Lett. **38**, 1454 (1977).

[2] G. Baldsiefen et al, Nucl. Phys. **A 574**, 521 (1994).

[3] T. Yamazaki et al, Nucl. Phys. **A 209**, 153 (1973).

[4] T. Shizuma et al., Phys. Rev. **C 69**, 024305 (2004).

[5] C. Wheldon et al., Nucl. Phys. **A 652**, 103-131, (1999).

[6] J. Ndayishimye et al., Phys. Rev. **C 100**, 014313 (2019).

[7] H. Sodan et al., Nucl. Phys. **A 237**, 333-353 (1975).

[8] E. Ngijoi-yogo et al., Phys. Rev. **C 75**, 034305 (2007).

[9] A. M. Bruce et al., Phys. Rev. **C 56**, 1438 (1997).

[10] F. S. Stephens, et al., Phys. Rev. **C 57**, 1565(R) (1998).

[11] S. G. Malmskog,V. Berg, B. Fogelberg and A. Backlin , Nucl. Phys. **A 166**, 573, (1971).

[12] Karin Ahlgren et al., Nucl. Phys. **A 189**, 368-384, (1972).

[13] B. Harmatz, T.H. Handley and J.W. Mihelich, Phys. Rev. **128**, 1186, (1962).

[14] M. S. Basunia Nucl. Data Sheets **110**, 999, (2009).

[15] R. Bengtsson, S. Frauendorf, Nucl. Phys. **A 327**, 139, (1979).

[16] A. Bohr et al., Physica Scripta. **26**, 267-272, 1982.

[17] R. D. Ratna Raju et al., Nucl. Phys. **A 202**, 433-466, (1973).

[18] C. Baktash et al., Annu. Rev. Nucl. Part. Sci. **45** 485-541, 1995.

[19] C. Wheldon, et al., Eur. Phys. J. **A 19**, 319-325 (2004).

[20] D. E. Archer et al., Phys. Rev. **C 57**, 2924 (1998).

[21] Ts. Venkova, et al., Eur. Phys. J. **A 18**, 1-4 (2003).

[22] T. Shizuma et al., Nucl. Phys. **A 696**, 337-370 (2001).

[23] P.H. Regan et al, Nucl. Phys. **A 586**, 351 (1995).

[24] N. Perrin et al., Z. Phys. **A 359**, 373-376 (1997).

[25] R. F. Casten, *Nuclear Structure From A Simple Perspective* (OXFORD UNIVERSITY PRESS, New York 1990).

[26] Jian-guo wang et al., Phys. Lett. **B 675**, 420 (2009).

[27] H. B. Ding et al, Phys. Rev. **C 74**, 054301 (2006).

[28] A.S. Davydov and G.P. Filippov, Nucl. Phys. **8**, 237 (1958).

[29] D. L. Balabanski et al, Nucl. Phys. **A 563**, 129 (1993).

[30] D. L. Balabanski et al, Phys. Rev. **C 49**, 2843 (1994).

[31] V. Modamio et al, Phys. Rev. **C 79**, 024310 (2009).

[32] W. Nazarewicz et al., Nucl. Phys. **A 435**, 397 (1985).

[33] W. Nazarewicz et al., Nucl. Phys. **A 512**, 61 (1990).

[34] G. Mukherjee et al., Nucl. Phys. **A 829**, 137 (2009).

Experimental study of shape evolution in nuclei near Z=82

SOUMEN NANDI (PHYS04201504014)
Variable Energy Cyclotron Centre, Kolkata

ABSTRACT

The excited states and band structures in three odd-A nuclei, ^{197}Tl (Odd-proton), ^{183}Au (Odd-proton), and ^{187}Os (Odd-neutron), with atomic number Z< 82, have been experimentally investigated by conventional gamma ray spectroscopic technique. Such nuclei are predicted to be triaxial in shape. So, the study of these nuclei is important for our general understanding of evolution and manifestation of triaxial shape. One of the important findings in this study is different manifestations of triaxial shapes in nuclei, namely, wobbling motion (in ^{183}Au), γ and γ–γ bands and un-favored "long axis" rotation (in ^{187}Os) and transition from an aplanar chiral geometry of the proton-, neutron and core angular momentum vectors to a planar geometry of magnetic rotation (in ^{197}Tl). These were demonstrated with clear observation, identification and characterization.

Fusion evaporation reactions with light-ion (α) and heavy-ion (^{20}Ne) projectiles have been used to populate the excited states in the three nuclei using the reactions:

- ^{197}Au(α, 4n)^{197}Tl at 50 MeV of beam energy
- ^{186}W(α, 3n)^{187}Os at 36 MeV of beam energy
- ^{169}Tm (^{20}Ne, 6n)^{183}Au at 146 MeV of beam energy

The experiments were performed at the Variable Energy Cyclotron Centre (VECC), Kolkata and the beams were delivered from the K-130 cyclotron. The Indian National Gamma Array (INGA) and VECC Nuclear Spectroscopy (VENUS) array of clover HPGe detectors were used to detect the de-excited γ rays from the residual nuclei. The γ–γ coincidence relation (determined from γ–γ matrix and γ–γ–γ cube) and intensity argument were used to generate the level schemes in the nuclei. The spin and parities of the excited states were obtained from the multipolarity (λ), type (E and M) and the mixing ratios (δ) of the de-excited γ rays were determined from the combined measurements of DCO (Directional Correlation from Oriented states) ratio and polarization asymmetry ratio.

In this thesis work, a total of 136 new γ transitions have been observed and placed in the level schemes of the three nuclei. New aspects and important features of this thesis work are:

(1) In ^{197}Tl: Evolution of shape from chiral (^{195}Tl) to shears (^{197}Tl) geometry for the 3-qp and 5-qp bands (these bands are identified for the first time in ^{197}Tl) and observation of complete alignment of a $\nu i_{13/2}$ neutron pair in the $\pi h_{9/2}$ band for the first time.

(2) In ^{183}Au: The observation of multiple transverse wobbling bands in ^{183}Au nucleus is the first such observation in any atomic nuclei so far and a new concept of an angular momentum I_m has been introduced in order to distinguish between longitudinal and transverse wobbling bands.

(3) In ^{187}Os: Pair alignments have been identified in the pseudo-spin "twin bands" based on $1/2^-$[510] and $3/2^-$[512] orbitals, and in $11/2^+$[615], and $7/2^-$[503] bands. New γ and $\gamma\gamma$ bands have been observed for the first time in this work. Evidence of stable long-axis rotation and the effect of the N = 110 deformed shell gap on pair alignment have been observed in the band based on $7/2^-$[503] configuration.

The new results obtained in this work not only provide new insight in to the manifestation of triaxial shapes in odd-A nuclei but also opens up new avenues of future research.

Thesis Highlight

Name of the Student: SOUMEN NANDI

Name of the CI/OCC: VECC **Enrolment No.: PHYS04201504014**

Thesis Title: Experimental study of shape evolution in nuclei near Z=82

Discipline: Physical Sciences **Sub-Area of Discipline: Nuclear Structure**

Date of viva voce: April 19, 2021

The high spin states of ^{197}Tl (Odd-proton), ^{183}Au (Odd-proton), and ^{187}Os (Odd-neutron) nuclei with atomic number Z< 82 have been experimentally investigated by the conventional gamma ray spectroscopic technique. The nuclei near Z< 82 are known to be transitional nuclei and predicted to be triaxial in shape. Therefore, these nuclei are important to study for our general understanding of evolution and manifestation of triaxial shape. One of the important findings in these studies is that different manifestations of triaxial nuclear shapes in nuclei, namely, wobbling motion (in ^{183}Au) in nuclei, γ and γ–γ bands and unfavoured "long axis" rotation (in ^{187}Os) in nuclei and transition from an aplanar chiral geometry of the proton, neutron and core angular momentum vectors to a planar geometry of magnetic rotation (in ^{197}Tl) could be demonstrated with clear observation, identification and characterization. The excited states were populated by fusion evaporation reactions using light-ion (α) beam for ^{197}Tl & ^{187}Os nuclei and heavy ion (^{20}Ne) beam for the neutron deficient ^{183}Au nucleus. The experiments were performed at VECC. The INGA and VENUS clover HPGe detector arrays were used. In this thesis work, a total of 136 new γ transitions have been observed and placed in the level schemes of the three nuclei. The γ-ray coincidence relation, DCO ratio and γ-ray polarization asymmetry ratio were used to assign new levels, definite spin and parity of the excited levels. New aspects and important findings of this thesis work are: (1) Evolution of shape from chiral (^{195}Tl) to shears (^{197}Tl) geometry for the new 3-qp and 5-qp bands. A complete pair alignment of $\nu i_{13/2}$ in the main band based on $\pi h_{9/2}$ has been observed for the first time. (2) Observation of multiple transverse wobbling bands in ^{183}Au nucleus is the first such observation in any atomic nuclei so far and a new concept of an angular momentum I_m has been put forward in order to distinguish between longitudinal and transverse wobbling bands. (3) In ^{187}Os, the bands based on $1/2^-$[510] and $3/2^-$[512] "twin bands", $11/2^+$[615], and $7/2^-$[503] have been extended up to first pair alignment. New γ and $\gamma\gamma$ bands have been observed for the first time in this work. Evidence of stable long-axis rotation and N = 110 deformed shell gap have been found in the band based on $7/2^-$[503] configuration.

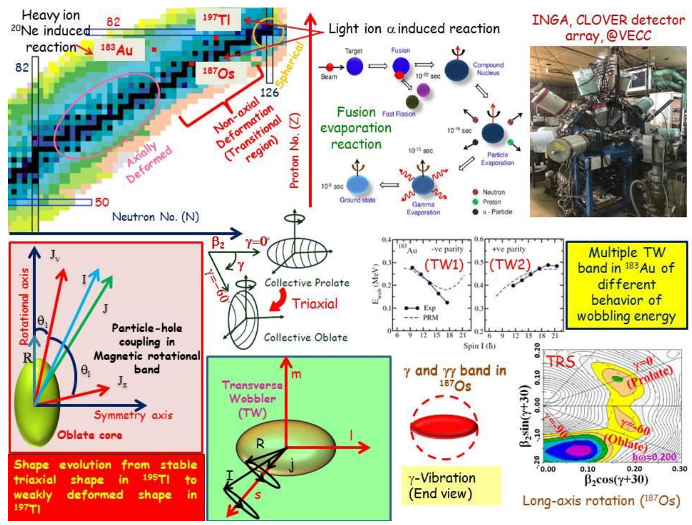

Figure 1. ^{197}Tl, ^{183}Au and ^{187}Os nuclei are shown in nuclear chart. Their structural phenomena like MR band, multiple transverse wobbling bands, γ band, $\gamma\gamma$ band, most unfavoured long-axis rotation are shown.

The new results obtained in this work not only provide new insight in to the manifestation of triaxial shapes in odd-A nuclei but also opens up new avenues of future research.